Atom-by-atom control and characterisation of molecular structures at surfaces

Leonardo Forcieri, MPhys (Hons)

Supervisor: Dr. Samuel P. Jarvis

A thesis submitted for the degree of
Doctor of Philosophy

LANCASTER UNIVERSITY
DEPARTMENT OF PHYSICS
August 2023

To my mum,
who would have deserved easier days.

Declaration

I declare that this thesis and the work presented in it are entirely my own, and has not been submitted in substantially the same form for the award of a higher degree elsewhere. I confirm that it does not contain, to the best of my knowledge and belief, any material published or written by another person, with the exception of where it is attributed in the text.

Acknowledgements

As my time as a student at Lancaster University comes to its end, there are a good many people without whom this thesis, and my PhD in general, would never have been possible. At the top of this list is my supervisor, Sam Jarvis, who has been essential to my progress as a scientist and continuously supported me through all the unpredictable events during these years. I must also thank Prof. Oleg Kolosov for his precious advice and contagious enthusiasm every time I needed a scientific opinion.
A special thanks goes to the guys of the mechanical and the electrical workshops, especially Phelton, Ashley, Graham, and Stephen, who have always been pleasant and helpful, and to Steviestores and Deborah Dunne, who have never hesitated a second to open their door every time I knocked.

Living and working on an island where people put beans on toast is not always easy, but I have met sensational people who turned this long journey into a memorable experience. For that, I am truly grateful to Angelino/Angelone, Josh my Gganbu, Martaja, Lil Sophie, Eva-TDC, Jamesino, Ash, CiCi, Sod Melissa, Eli, Ale, Edward, Dima, Ramon, and my British family - Fi&C and Andy the King of Primrose Street.

I must thank my mum and the old buddies who have always been there.

Finally, I would like to mention Anto and Bibi, to whom so much should be said, yet no words would ever be enough.

List of Publications

- Forcieri, L., Taylor, S., Moriarty, P., & Jarvis, S. P. (2021). Origin of C 60 surface reconstruction resolved by atomic force microscopy. *Physical Review B*, 104(20), 205428.
- Wang, X., Sangtarash, S., Lamantia, A., Dekkiche, H., Forcieri, L., Kolosov, O. V., ... & Robinson, B. J. (2022). Thermoelectric properties of organic thin films enhanced by π-π stacking. *Journal of Physics: Energy*, 4(2), 024002.
- Chen, Y., Wu, W., Gonzalez-Munoz, S., Forcieri, L., Wells, C., Jarvis, S. P., ... & Kolosov, O. V. (2023). Nanoarchitecture factors of solid electrolyte interphase formation via 3D nano-rheology microscopy and surface force-distance spectroscopy. *Nature Communications*, 14(1), 1321.
- Forcieri, L., Wu, Q., Quadrelli, A., Hou, S., Buceta, D., López-Quintela, M. A., ... & Jarvis, S. P., Extrinsic activation of 2D polymerization on inert surfaces using atomic clusters, (*under consideration*)
- Forcieri, L., Dunn, E., Young, R., Larsson, A., & Jarvis, S. P., Resolving sub-molecular chemical structure in ambient conditions with constant force AFM, (*manuscript in preparation*)

Contents

Chapter 1

Introduction

Aims and Motivations

The 2022 Nobel Prize in Chemistry, jointly awarded to Carolyn R. Bertozzi, Morten P. Meldal and K. Barry Sharpless, "for the development of click chemistry and bio-orthogonal chemistry", stands as the latest milestone on a pathway that roughly began sixty years ago when the physicist Richard Feynman in his lecture: "There's Plenty of Room at the Bottom" [1], considered the possibility of synthesis via direct manipulation of atoms. During this time frame, the concepts of nanoscience, and consequently of nanotechnology, as the general ability to control, manipulate, and understand the matter on an atomic scale, has seen a rapid expansion across large swathes of the scientific community, resulting in a radical paradigm shift of the nano-scale phenomena concept. The idea of a nano-scale system as a result of stochastic interaction of individual units was replaced with the view of a deterministic one where atoms and molecules could be precisely controlled like building blocks.

In this context, the idea of organised organic structures fabricated through directed molecular design rapidly took hold, enabling researchers to investigate the myriad possibilities of on-surface nano-architectures, including cross-covalent linked thin-films [2, 3]. In fact, the covalent-coupling reaction between molecules not only stabilises the structure of a polymer due to a stronger interaction but enables the growth of unique structures often otherwise impossible to synthesise, such as zig-zag graphene nanoribbons (GNR) [4], molecular wires [5], and nano-porous 2D layers [6]. To date, most publications on covalently linked assemblies show a reaction on metal surfaces. In fact, due to the catalytic behaviour of the substrate, the metal acts as a reaction mediator; however, as a negative consequence, it creates a strong surface coupling causing molecular distortion, orbital broadening, and electrical short-circuits that detrimentally affect or otherwise bypass molecular properties. Consequently, there is a substantial research interest in achieving polymerisation on inert substrates, however, this is exceptionally challenging. As it stands there are only a limited number of reports that

have demonstrated the polymerisation on insulators or have optimised lift-off methods to decouple the network from the surface including NaCl [7], iodine [8], or h-BN [9]. For this reason, one of the main aims of this work was the development and characterisation of a 2D polymer on inert substrates reaction-activated by the presence of atomic quantum clusters (AQCs) as extrinsic catalysts.

As previously mentioned, within the groundbreaking framework predicted by Feynman, the advent of nanoscience would never have occurred without the parallel advent of nanotechnology. In fact, the deterministic approach to nano-scale phenomena would have been possible only by developing new instruments and techniques capable of exploring and modifying matter on an atomic scale with such a level of accuracy. One of the main techniques that triggered this scientific revolution was scanning probe microscopy (SPM). With the invention of scanning tunnelling microscopy (STM) [10], first, and subsequently of the atomic force microscopy (AFM) [11], it was possible for the first time to reveal individual atoms [12, 13], and sub-molecular detail [14], to study the electronic configuration of frontier molecular orbitals [15] and determine intra- and inter-molecular chemical bonds [16, 17]. In addition, by the probe-sample interaction, SPM techniques could trigger chemical reactions [18–20], rearrange the atomic disposition of samples [21], and manipulate single atoms constructing new nanostructures [22, 23]. In this context, besides the extraordinary results obtained by the AFM, one of the most challenging aspects of this technique is the measurement under ambient conditions. The intrinsic environmental constraints, such as the water-film layer covering the surface of the sample and its progressive contamination, and the thermal, mechanical and acoustic noise, to mention some, entail lower resolutions and a more challenging atomic manipulation if compared with the results obtained under controlled conditions such as ultra-high vacuum (UHV) and at low temperatures. For this reason, the last section of this thesis is dedicated to the analysis and optimisation of the measuring technique, in particular a SPM acquiring data mode known as PeakForce Tapping [24], to demonstrate how a commercially available atomic force microscope, provided by conventional micromachined cantilevers, can achieve ultra-high resolutions at room temperature and under ambient conditions.

Chapters outline

Part I: Background

- **Chapter 1:** details the state of the art of the on-surface self-assembly, describing how nano-architecture growth is driven by intermolecular interactions for non-covalent and covalent coupled molecular arrangements. It also discussed the design role of the precursors, the influence of the substrate, and the application of metal adatoms for forming supramolecular structures. A brief overview of atomic quantum clusters (AQC) gives an insight into the recent use of AQCs as on-surface molecular catalysts.

- **Chapter 2:** shows the experimental techniques adopted in this research, presenting the methods to prepare, analyse, and characterize the samples. In particular, the first section describes the molecular deposition method for forming on-surface self-assemblies attained under ultra-high vacuum conditions. It also provides a description of the UHV apparatus and the experimental techniques to achieve these environmental conditions. The following section shows the sample analysis and characterisation methods utilised within this work, such as atomic force microscopy (AFM) and X-ray photoemission spectroscopy (XPS), covering the theoretical backgrounds and the working principle of the two experimental apparatus. In particular, the section provides an overview of the PeakForce Tapping mode for achieving high-resolution imaging and the temperature programmed XPS mode for the chemical region analysis as a function of the temperature.

- **Chapter 3:** retraces the pivotal phases of high-resolution imaging achieved by AFM techniques, from the first examples of lattice resolution to the latest 'true' atomic and sub-molecular ones. In particular, it analyses the state of the art of experimental evidence attained by implementing qPlus sensors and tip modification methods, both under ambient conditions and on organic samples. The fundamental results and the limits of this technique gave the motivations for one of the research studies of this thesis.

Part II: Experimental Results

- **Chapter 4:** shows the successfully controlled on-surface covalent-coupling reactions of Br_4TPP close-packed molecules using Cu_5 atomic quantum clusters (AQCs) as extrinsic catalysts on metal, inert and insulating substrates. The development and analysis of surface polymers are obtained by temperature-controlled X-ray photoelectron spectroscopy (TP-XPS) and high-resolution atomic force microscopy (AFM) and supported by the theoretical model within the interpretation of density functional theory (DFT).

- **Chapter 5:** investigates the limits of a commercial atomic force microscope operated under ambient conditions in PeakForce Tapping mode AFM. The research outcomes on C_{60}, Br_4TPP, BipyOPE3 and ZnTPP molecules prove single molecule and sub-molecular resolutions comparable with literature results achieved in UHV and low-temperature conditions. The results are interpreted within the framework of substrate-molecule interactions and packing disposition simulations.

Conclusion summarises the outcomes and conclusions from this thesis and outlines the potential for future research.

Part I

Background

Chapter 2

Molecular Assembly

Supramolecular chemistry is a field of research that aims to control the design and the characterisation of ordered surface structures grown on substrates. Generally, engineering nanoscale materials relies on one of two main pathways: the 'top-down' and 'bottom-up' techniques. The former covers methods that modify the structure of the sample to the desired pattern and configuration, such as etching, stamping, lithographing and printing, with precisions of the order of tens nanometers [25]. The latter, known as the 'bottom-up' technique, involves the process of on-surface organisation such as molecular self-assembly to pattern nanometric-sized elementary 'building blocks' in complex structures typically held together by non-covalent intermolecular forces.

2.1 Basic concepts of on-surface self-assembly

To efficiently and precisely control the assembly, molecular growth needs a controlled environment that can be in liquid, controlled gaseous atmosphere or ultra-high vacuum (UHV). UHV conditions provide ideal environments for the self-assembly of supramolecular architectures. The clean environments of UHV prevents side reactions with contaminants and guarantees longer sample preservation from ageing, ideal for characterisation and study. The most common method for molecular growth in UHV is via thermal deposition; molecules in their solid state are sublimated onto an atomically flat surface, where a balance between the intermolecular and interfacial interactions within the molecular-substrate system results in spontaneously organised structures. The specific design of molecule-surface systems can be controlled by varying several parameters, such as the precursor and the substrate materials, the control of the growth parameters and the environment, the supramolecular templating effect [26], and, in the case of surface chemistry, the choice of the activation method for on-surface reactions.
Considering a flux of thermally sublimed molecules deposited on a homogeneous substrate, once the elementary building blocks have landed, they tend to weakly bond to the

surface with an adsorption energy that exceeds the thermal desorption energy. Obeying a Maxwell-Boltzmann statistic, the desorption rate for an isolated monomer is described by:

$$\Gamma_{des} = \nu_0 exp[-\beta E^*] \tag{2.1}$$

where ν_0 is of the order of 10^{13} s^{-1}, $\beta = [k_B T]^{-1}$ and E^* is the corresponding energy barrier [27]. The prefactor ν_0 know as 'attempt frequency' represent the vibration frequency of the bond between the molecule and substrate, that is the periodic bond stretching as an attempt of the molecule to overcome the energy barrier and to desorp. As the adsorption energy depends on substrate reactivity, symmetry, and electronic properties of the species, its determination could be complicated. Generally, if the deposition is attained at room temperature (RT$\sim$300 K), the thermal desorption is considered prevented if the $E_{ad} > 1$ eV [27]. At this point, the clustering of the adsorbates, organised in surface structures, is ruled by the ratio between the diffusion rate, D, and the deposition rate, F.

Surface diffusion is a thermally activated process that describes the tendency of an adsorbed species to explore the surface, randomly hopping from one (meta-) stable configuration to another. The diffusion coefficient D represents either a collective process: chemical diffusion, that is, an ensemble of adsorbed species mutually interacting, or an individual process: tracer diffusion, described by the mean square displacement of one isolated random walker per unit of time [28]. Considering the ratio D/F, for small values of it, surface diffusivity shows a collective behaviour, and the growth of the pattern is ruled by kinetic processes leading to metastable configurations. For high values of D/F, even though the molecular vapour deposition is a collective process, the mean distances between two adsorbates are larger compared to the typical intermolecular interaction. Therefore, the surface diffusion is described by tracer diffusion coefficient [29], and the molecular self-assembly occurs in quasi-equilibrium condition: thermodynamic growth process.

The structural conformation of the substrate plays a crucial role in the migration/nucleation process. Considering a homogeneous material, the energy barriers of different substrate sites, such as kinks, step edges and atom vacancies, can vary a lot, making the nucleation preferable on these areas while the diffusion tends to be favoured on flat terraces, as shown by the terrace-step-kink (TSK) model of atomistic surface growth [30].Considering a homogeneous material, the energy barriers of different substrate sites, such as kinks, step edges and atom vacancies, can vary greatly, making nucleation preferable in these areas. At the same time, diffusion tends to be favoured on flat terraces, as shown by the terrace-step-kink (TSK) model of atomistic surface growth [30]. Furthermore, the substrate's nature, symmetry, and geometry can highly influence the migration/nucleation supramolecular process. Several geometries have been explored to mediate the molecular growth in organised structures, including trenches [31, 32], nanoholes [33], nanorods [34, 35] and nanojunctions [36]. The most common are planar surfaces, as atomically flat coinage metals like Au, Ag, Cu or less commonly Pt, Pd or Co; highly orientated semiconductor or semi-metal like HOPG (highly

oriented pyrolytic graphite), graphene and even insulators like NaCl and mica surfaces. In general, anisotropic surfaces with relatively large corrugation promote directional motion [37–39], whereas a 2D random-walk is more common on low-corrugation substrates where the surface-molecule interaction is weaker, even though there are examples of one-dimensional motion even on these types of substrates [40, 41].

The nature of the substrate can govern the type of growth due to physisorption or chemisorption. The first process concerns the weak adsorption lead primarily by van der Waals forces, and is commonly observed on weakly interacting substrates such as Au(111). The latter, a strong interaction between molecules and surface, involves strong chemical interactions, and is often observed on strongly binding substrates such as semiconductors and metals such as Ag and Cu, and often Au [42, 43].

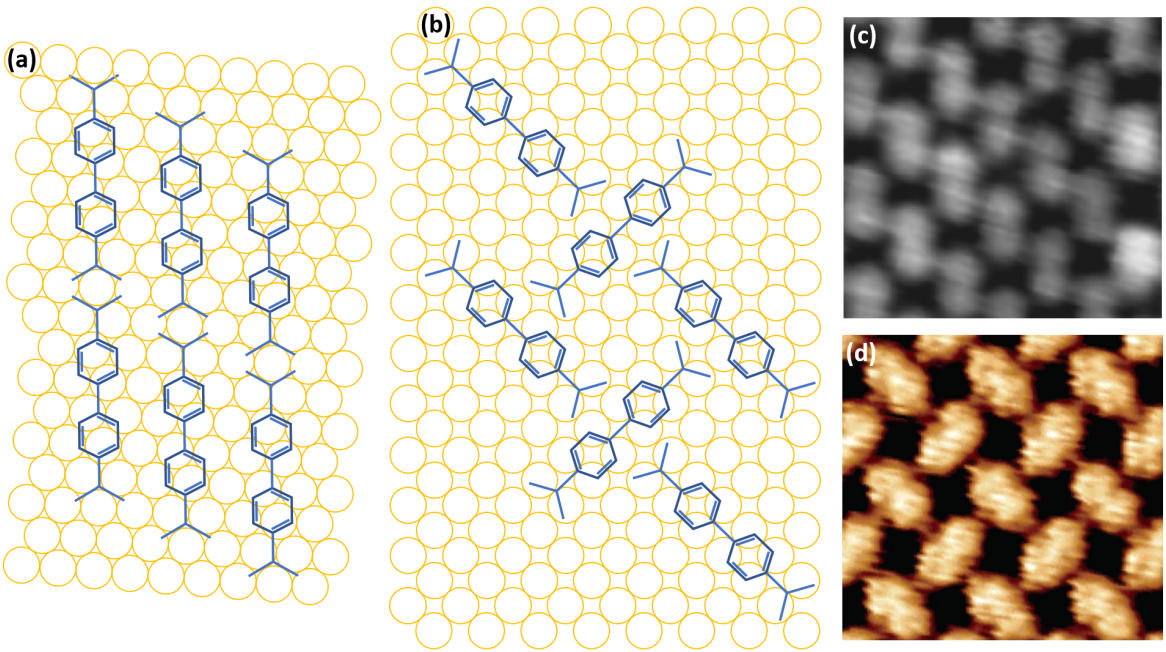

Figure 2.1: **Role of the substrate in molecular assembly.** Schematic representation and STM images of BDA arrangements deposited upon Au(111) (a, c) and Cu(100) (b, d) substrates. BDA arranges in 1D linear chains over Au(111) surface, while on Cu(100), it prefers a squared herringbone pattern. (a, c) Panels adapted with permission from ref [44]. (b, d) Panels adapted with permission from ref [45].

A clear example of the substrate influence was observed for 4,4-biphenyl dicarboxylic acid (BDA) molecules on either Au(111) or Cu(100) substrate. If BDA is deposited on the Au(111) surface, it arranges in one-dimension linear chains held together by hydrogen-bonding interactions and close-packed together in a parallel disposition [44], see (Fig: 2.1. a, c). By contrast, when the deposition is attained on a Cu(100) substrate, the interaction with the substrate becomes so strong that the carboxylic groups of BDA de-protonate, entailing a different arrangement. Each molecule is rotated by 90 degrees with

respect to the neighbouring two in the line, and the close-packing of the single rows forms a squared 'herringbone' crystal structure [45], see (Fig: 2.1. b, d).
In addition to the chemical nature of the surface, its crystallographic orientation can modulate the growth of on-surface structures due to the different symmetries that can assume the substrate, the coordination number of the surface adatoms, and their reactivity. For example, (111)-, (100)-, and (110)- are respectively hexagonal, square, and rectangular crystallographic orientation; the first is the densest but most inert, and the last is the least dense but most reactive. However, the TSK model gives a good description of surface migration depending on the different energy barriers of surface dislocations. Still, it does not consider crucial molecular features such as size, symmetry, and orientation that distinguish supramolecular growth from the surface reconstruction of intrinsic metal adatoms. In general, unlike a metal atom, the motion of a molecule is typified by both lateral and rotational movements. Considering the displacement of isolated species, if the unique migration energy barrier is present, the lateral motion and molecular rotation are thermally activated processes that follow an Arrhenius trend respectively described by

$$\Gamma_l = \nu_l exp[-\beta E_l] \tag{2.2}$$

and

$$\Gamma_r = \nu_r exp[-\beta E_r] \tag{2.3}$$

where $\beta = [k_B T]^{-1}$, the energy barriers $E_r \sim E_l$ are approximately (0.05 – 3) eV. The prefactors $\nu_l \sim \nu_r$ are in a range of 10^{10}-10^{14} s $^{-1}$[27] and represent the 'attempt frequency' of the adsorbate to diffuse to a neighbouring site by lateral or rotational movement, respectively.
In summary, the balancing between surface adsorption, lateral and rotational motion tuned by the indirect substrate mediation, and the direct molecular interaction between functional groups entail, near thermodynamic equilibrium, the supramolecular engineering on the surface. The weak, non-covalent interactions that hold such supramolecular structures are mainly: van der Waals, hydrogen-bonding and metal coordination forces.

2.1.1 Non-covalent interactions of molecular self-assembly

van der Waals (vdW) forces are non-directional intermolecular interactions typically acting at ranges $\leq$1 nm. They are usually weak interactions E_{as} $\sim$(0.02 - 0.1) eV [27]; nevertheless, contrary to the other ones, they are always present within all molecular systems. Generally, vdW forces are split into dipole-dipole, dipole-induced dipole, and instantaneous dipole-induced dipole. Permanent dipoles or quadrupole moments associated with organic adsorbates lead to the interaction/assembling of neighbouring molecules in ordered configurations (dipole-dipole contribution). The interactions between rotating permanent dipoles and the polarizability of atoms and molecules, or the charge transfer

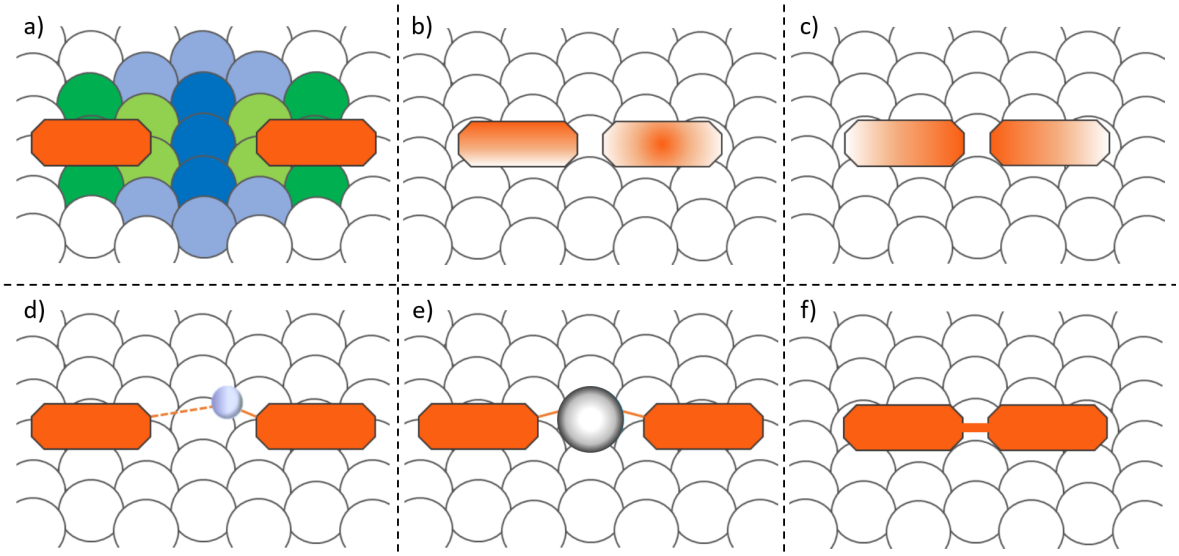

Figure 2.2: **Overview of intermolecular interactions at surfaces.** (a) Surface-assisted interaction between two adsorbed molecules (orange). The substrate mediation acts over comparatively long distances and varies depending on the adsorbant site (green - stronger, blue - weaker). (b) Charged molecules: on the right, the organic molecule-substrate interaction induces a charge redistribution and creates a dipole moment normal to the surface (induced dipole); on the left, a charged molecule (permanent dipole). (c) Dipole/quadrupole moment interaction between adsorbates leads to the molecules' distribution over the surface. (d) Hydrogen bonding between adsorbates: dipole-dipole attractive interaction (dotted orange line) between the H-atom covalently bonded to a very electronegative molecule (continuous orange line) and another very electronegative one. (e) Metal coordination interaction: a metal adatom residing on top of the surface (grey) forms coordination bonds with adsorbed organic molecules. (f) Covalent coupling bond between adsorbates induced at a surface. Panel adapted with permission from ref [46].

within a molecule, give rise to an instantaneous dipole that can, in turn, induce a different dipole. These two situations are the dipole-induced dipole and instantaneous dipole-induced dipole contributions, and they are weaker than the dipole-dipole situation. van der Waals forces scales as r^{-6}, where r is the intermolecular distance.
Hydrogen bonding (H-bonding) is a directional intermolecular force with a binding energy of E_{as} ∼(0.05 - 0.7) eV, acting in a range r ∼(1.5 - 3.5) Å[27]. This interaction is due to a hydrogen atom covalently bonded to a very electronegative one, usually ranging between 2.5 and 4.0, exerting its attraction to another very electronegative atom in a dipole-dipole interaction. It is generally represented by the interaction of the two polar groups Dn–H···Ac, respectively Dn and Ac, the donor and acceptor electronegative species.
Stronger than the H-bonding, metal coordination, also known as metal-ligand interaction, is a selective directional bonding, with a binding energy of E_{as} ∼(0.5 - 2) eV, exerted at distances of r ∼(1.5 - 2.5) Å. A metal adatom residing on top of the substrate acts as an 'electron pair acceptor' mediating in a coordination bond between organic ligands; usually, the metal adatoms belong to the transition metal group, that is, d-block metals. The d-type orbital electrons of these elements are shared with neighbouring molecules as valence electrons entailing the formation of covalent coordinated bonds. The shielding behaviour of the core electrons from the attraction of the nucleus yields the valence electronic configurations of the d-type orbital electrons.

2.2 Hydrogen-bonded networks

A typical example of a system characterised by hydrogen bonds (H-bond) can be found in the DNA structure, in which both the two strands of the helix are stabilised and held together by H-bonds.
Weaker than the other type of intermolecular forces, the H-bonding interaction is characterized by a particular electronic state of the molecular σ-system and by the π-system that indirectly contributes with a node orthogonal to the plane the hydrogen bond occurs in [46]. Due to its highly directional hydrogen donor/acceptor and its capability to form strong bonds [47], the carboxylic acid group is one of the main H-bonding organic compounds used and studied from the earliest stages of the field. One of the first experiments with carboxylic acid was done in 2002 by Griessl *et al.* [48]. They showed how 1,3,5-benzene tricarboxylic acid (TMA) deposited on HOPG in UHV conditions could assume open network arrangements either in a 'chicken-wire', commonly known as 'honeycomb' structure (Fig: 2.3. a, c), or in a 'flower' arrangement (Fig: 2.3. b, d), held together by hydrogen bonds. The honeycomb structure is a porous structure that exposes the atoms of the substrate in their cavities, which differs from the close-packed one in which the molecules are highly densely arranged and tend to cover the underlying area of the substrate fully. The two different assemblies can coexist on the HOPG surface; however, the most common TMA

configuration is the porous assembling pathway, while the closed-pack one occurs only at a higher molecular density of the surface. The alignment of the h-bonding lower the energy of the entire system, paired with the adsorbate-substrate interaction induces the formation of the 'flower' lattice; thereby, the mediation of the substrate is a parameter that influences the different configurations.

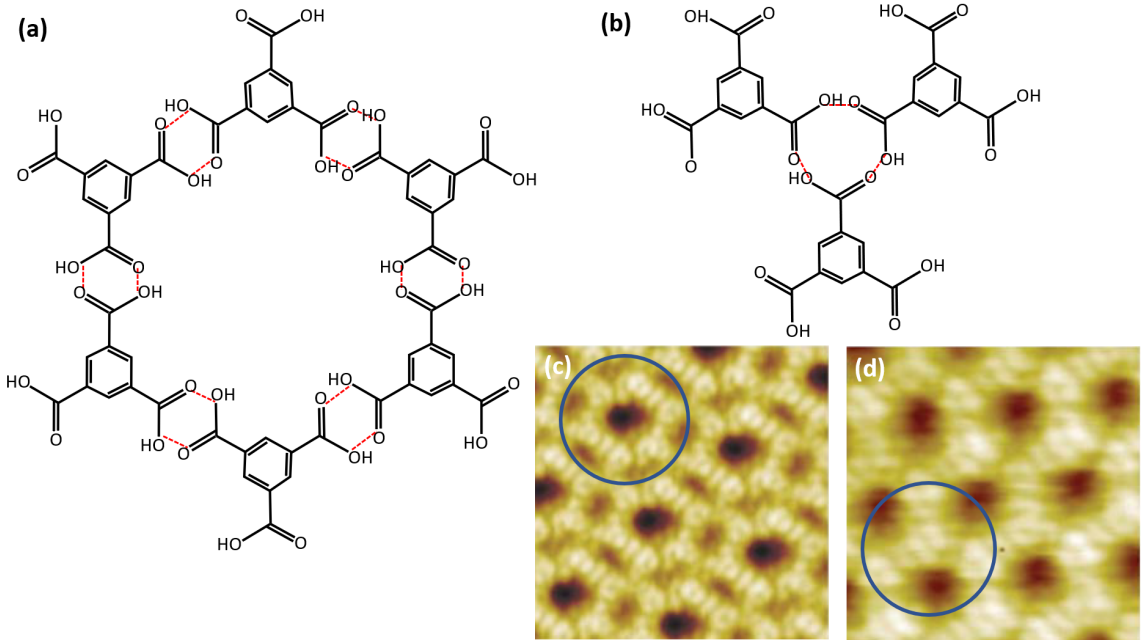

Figure 2.3: **Porous and close-packed structures held together by Hydrogen bonding.** (a, b) Schematic model of the chicken wire (honeycomb) and the flower structure of TMA networks on HOPG and their respective position (indicated by blue circles) in STM images (c, d). (c, d) Panels adapted with permission from ref [48].

Further studies showed how the temperature could yield molecular growth in different arrangements, as in the case of 1,3,5-tris(4-carboxyphenyl)Benzene, similar to a carboxylic acid, deposited on HOPG [49] (Fig: 2.4. a, b) or analogously the combination of temperature and concentration, as in the case of anthraquinone adsorbed on Cu(111) surface [50] (Fig: 2.4. c). In the former experiment, a honeycomb arrangement is obtained at low temperatures and more densely packed at high ones. In the latter case, if the substrate is kept at 80 K, the formation of close-packed anthraquinone arrays is prevented. At low temperatures, the combination of the long-range repulsive electrostatic interaction and the short-range attractive hydrogen bonding shield the isotropic vdW interaction. Furthermore, at low temperature, tuning the substrate coverage of anthraquinone molecules, the ordered structures could vary from one-chain arrays, eventually connecting in threefold symmetric systems, for low concentrations, to honeycomb formations for high ones [50].
Similarly, the network geometry can be controlled through a precise design of the precursor molecules, exploiting the high directionality of the hydrogen-bonding interactions.

Considering the case of homo-molecular structures, the two isotopes of the aromatic organic compound $C_6H_4(CO_2H)_2$ can have either a meta- or a para-conformation. The former is expressed as terephthalic acid, where two carbon atoms separate the two carboxylic acid groups. The latter is expressed as isophthalic acid, that is, when the two carboxylic acid groups are separated by only one carbon atom. As shown by Lackinger *et al.* [51], the deposition of the two isotopes on a flat surface of HOPG shows two different adsorbed assemblies, (Fig: 2.4. d, e). Both carboxylic acids tend to form close-packed chains arranged in parallel dispositions. The terephthalic acid forms one-dimension linear chains, while the isophthalic acid forms one-dimension zig-zag chains.

A remarkable example of precursor design for the formation of hetero-molecular structure [52] is the porous network obtained using Perylenetetracarboxylic dianhydride (PTCDI) and melamine as building blocks. The composition of a triple hydrogen bond between melamine molecules and the cyanuric acids at the ends of functionalised perylene cores by imide groups (CO, NH, CO) forms the honeycomb supramolecular structure. Nevertheless, the substrate influences the synthons arrangement; if the PTCDI-melamine mixture is deposited upon an Ag/Si(111) surface in UHV conditions [52], the self-assembly process forms a crystalline network with hexagonal pores, (Fig: 2.4. f). In contrast, on an Au(111) surface [53], two different topologies are developed and can coexist simultaneously. The preferential one is the honeycomb arrangement; however, if the sample is annealed at high temperatures, a parallelogram phase of growth is observed.

Contrary to the hetero-, homo-molecular systems are structures formed by only one type of building block. They generally prefer to arrange in a close-packed lattice, as observed for PTCDI and aphthalene tetra-carboxylic di-imide (NTCDI) on the Ag-Si(111) surface, and perylene-3,4,9,10-tetracarboxylic-3,4,9,10-dianhydride (PTCDA) [54, 55]. However, the formation of these structures is not always predictable, and different configurations can coexist in the same assembly. For example, as observed by Blunt *et al.* [56], a couple of p-terphenyl-3,5,3',5'-tetracarboxylic acid (TPTC) molecules can bond in 'parallel' and 'anti-parallel' configurations; therefore, a TPTC assembly grows on HOPG in a porous network that could have up to four different types of pores. Even though the TPTC system is characterised by orientational symmetry, the lack of translational one yields these nanoarchitectures belonging to the non-crystal structure group.

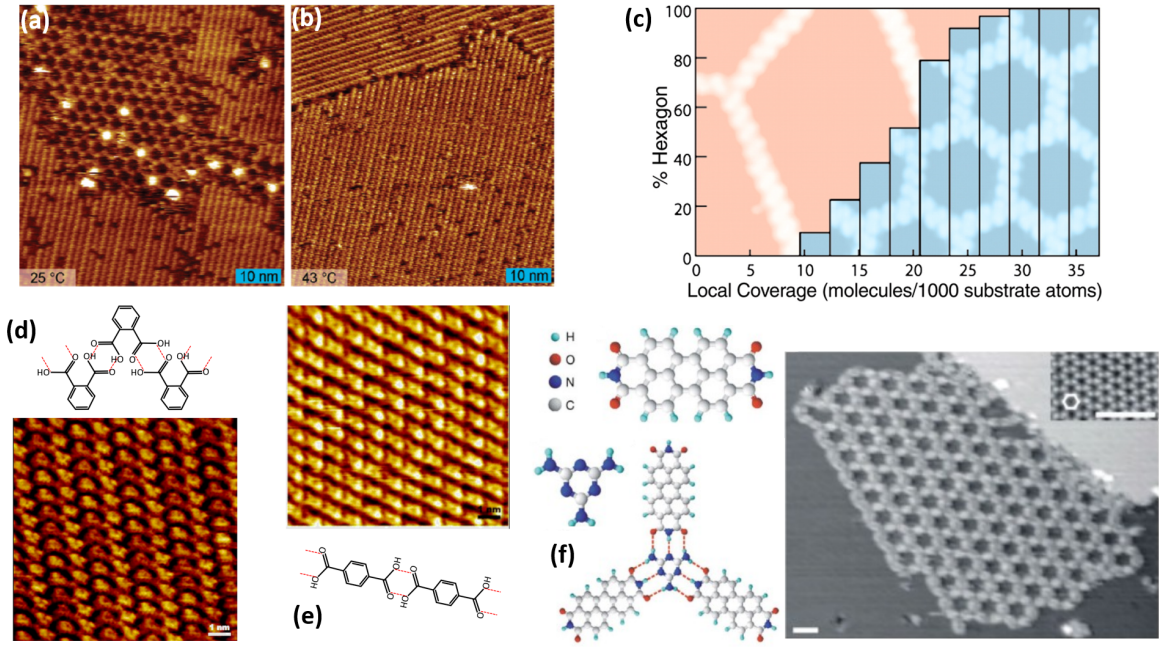

Figure 2.4: **Structures formed by hydrogen-bonding interactions.** (a, b) STM images of the two configurations of BTB assembles changing from honeycomb (a) to close-packed 1D chains (b) tuning the temperature of the sample. (c) Percentage of hexagon structure as a function of precursor concentration for anthraquinone formations. (d, e) STM and chemical models of the two aryl acid isotopes: 1D linear chains for terephthalic acid (d) and 'zig-zag' chains for isophthalic acid (e). (f) STM image of the hetero-molecular structure designed by a mixture of PTCDI and melamine building blocks and the molecular scheme of the triple h-bonds between the single melamine molecule and the three cyanuric acids. (a,b) Panels reprinted with permission from ref [49]. (c) Panel reprinted with permission from ref [50]. (d,e) Panel adapted with permission from ref [51]. (f) Panels adapted with permission from ref [52].

2.3 Metal covalent-coordination interactions

Metal covalent-coordination interactions have been highly explored because the formation of metal-organic coordination was already studied in solutions. Nevertheless, the properties of complexes in solutions and metal-organic frameworks obtained by wet chemistry reactions completely change if the structure is developed upon a surface due to the two-dimension growth confinement geometrically and, mainly, to the multiple interactions between the substrate, metal adatoms and ligands. Especially metal substrates can participate in the supramolecular assembly by providing charges to the coordination centres; this mediation allows the charge donation from adatoms to ligands impeding the charging of the adatoms themselves. Furthermore, naturally, metal substrates can provide intrinsic adatoms to the system; therefore, if the metal adatoms are adsorbed over the metal surface, the mean distance between them is generally reduced with respect to the substrate layer spacing, thereby the closer interaction induces the formation of a positively charged dipole moment normal to the surface itself [46].

The influence of the substrate on the formation of supramolecular architectures can be noticed by studying the geometry of the coordination networks. Generally, the geometry of the metal lattice is reflected by the adsorbed structure, in particular, three-fold for fcc(111) surfaces and two- or four-fold for fcc(100) surfaces.

The adatoms used as coordination centres can be either deposited or, for metal substrate, the surface itself can provide a few atoms that can migrate across the sample [57]. Generally, if the supporting metal is a soft substrate like copper, a few amounts of adatoms start diffusing even at 200 K; otherwise, simple thermal annealing can activate the process for harder metals.

Metal covalent coordination interactions are used to form and control 2D supramolecular architectures. Similarly to the H-bonding-based networks, they can assume porous and close-packed configurations that can be tuned by selecting different ligands. For example, a 4,4-biscyanoterphenyl/cobalt network preserves the geometry and symmetry of its honeycomb structure. Still, the dimension of the pores would scale with the length of the oligophenyl chain, in particular, using quaterphenyl or quinquinphenyl moieties in place of terphenyl [58], see (Fig: 2.5. a-c). The scale variation of the elementary structure, i.e. the pore, affects the global dimension of the whole system without being influenced by the periodicity or electronic structure of the substrate. Similarly, Tait *et al.* showed how the squared pattern formed by the metal coordination bonding of 5,5'-bis(4-pyridyl)(2,2'-bipyrimidine) (PBP) with copper atoms is preserved despite the interaction with the underlying substrate [59], see (Fig: 2.5. d).

Moreover, inducing the assembly on Ag(111), Ag(100) and Cu(100), that is, varying some prominent features such as the nature, symmetry, and the lattice constant of the substrate, the final networks did not show significant differences. That proved that the metal coordination bonding is strong enough to shield the molecular-substrate interaction.

Finally, one of the critical results of the on-surface metal coordination chemistry is the

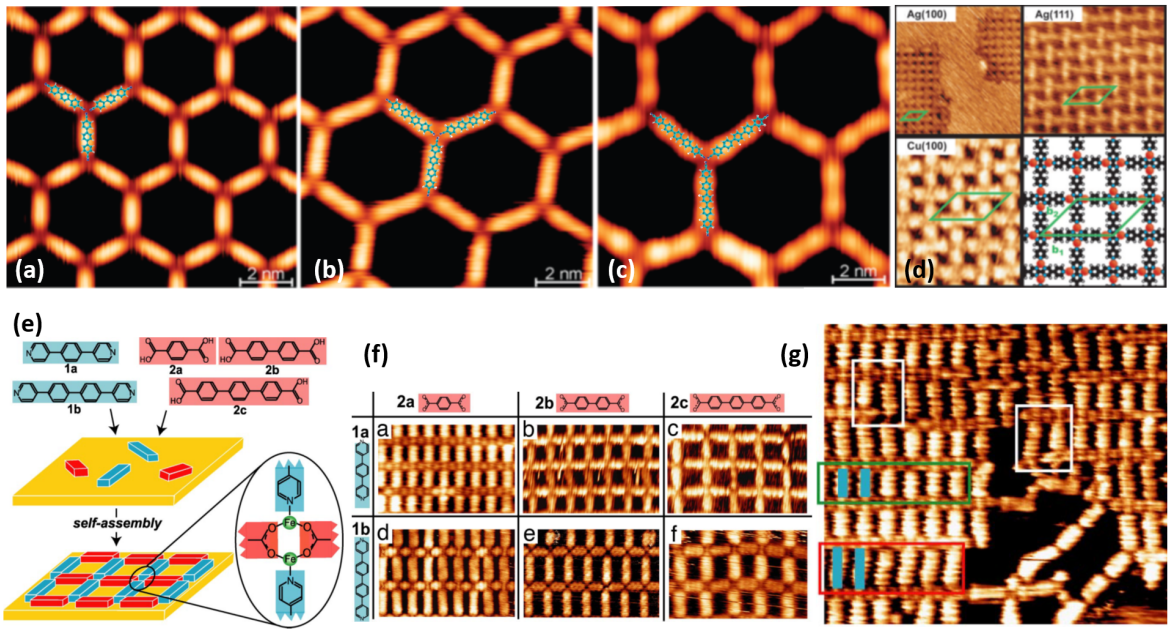

Figure 2.5: **Metal-organic frameworks.** (a-c) STM images of tunable metal-organic honeycomb lattice as a function of the designed linkers (partially superimposed on the structures). (d) PBP-Cu networks grown on Ag(100), Ag(111) and Cu(100), respectively, the network orientation and periodic spacings of the assemble are preserved for all the substrates and in close agreement with the theoretical model shown in the fourth quadrant. (e) Schematic illustration of the two series of organic ligands, linear bis-carboxylic acids and bipyridines (top) deposited with Fe atoms on Cu(100) (middle) self-assembling into regular rectangular arrays after annealing at 450 K (bottom). The metal coordination bond is shown in the inset. (f) Overview of the six possible network formations matching pairs of complementary molecular ligands. (g) STM image of a multicomponent metal-coordination supramolecular network. The self-recognition, self-selection, and dynamic self-organisation of the precursors lead to the growth of multiple subdomains coexisting in the pattern: 1a and 1b paired with 2a precursors are respectively highlighted in the green and red insets. Also, several defects exhibiting coordination of neighbouring bipyridine ligands of different lengths are shown (white boxes). (a-c) Panels adapted with permission from ref [58]. (d) Panel reprinted with permission from ref [59]. (e-g) Panels adapted with permission from ref [60].

property of self-selectivity and self-recognition of some structures. In a pioneering article, Langer *et al.* [60] proved the intermolecular interactions in a hetero-structure using two series of organic ligands, deposited on a Cu(111) surface, simultaneously with iron adatoms used as coordination centres, see (Fig: 2.5. e-g). The two sets of linear bis-carboxylic acid and bipyridine differed in length because of the number of benzene rings forming each chain. Hence, once the mixed deposition was completed, due to the restricted mobility of components at surfaces, self-recognition and cooperatively amplified self-assembly of ligands allowed the ordered bonding of non-crystalline networks. Areas of mixed sub-domains characterised the structure to preserve the right-angled pattern and avoid incomplete grids with unbonded ligands. Further self-repairing events proved how molecules could self-recognise and correct the mismatch in the design, snapping off and repairing the structural defects and replacing the ligand to reform the pattern configuration.

2.4 Isotropic molecular interactions: van der Waals forces

Contrary to hydrogen bonding and metal coordination, van der Waals interaction is characterised by non-directional molecular forces. Consequently, it is present in every supramolecular assembly, even though the other intermolecular forces almost always overshadow its action. For this reason, its relevance in the assembly of some molecular architectures is seldom unclear. Nevertheless, few examples of self-assemblies are held together only by non-directional forces. Historically, at the early stages of the field, Ulmann [61] was one of the firsts that showed the formation of self-assembled monolayers of alkane thiolates grown on metal surfaces held together by isotropic molecular interactions. Also, Cnossen *et al.* [62] studied molecular structures based on the sterically overcrowded alkenes that can be synthesised with 1,3,5-triethynylbenzene to create a threefold symmetric molecule. If deposited on HOPG, this molecule forms close-packed self-assembly characterised by recurrent porosity, stabilised exclusively by vdW forces, see (Fig: 2.6. a, b).
Finally, several studies of porous and close-packed lamellar structures of alkyl chains grown at solid-liquid interfaces proved that isotropic molecular interactions are the only factor that holds these structures together. Notably, Furukawa *et al.* [63] confirmed how the deposition on a HOPG substrate of planar organic molecules functionalised with chain-like hydrocarbon species could assume different patterns depending on the molecular structure, the density over the surface, and the concentration of the solution, see (Fig: 2.6. c, d). The dimension of the hexagonal pores formed by functionalised alkyl chains varies proportionally with the chain length of the alkyls themselves [64]. This behaviour is similar to the design achieved by metal-coordinated linear bis-carboxylic acids, even though the crystal structure of the network is invariant. Furthermore, the chemical synthesis of two similar alkyl chains: the triangular-shaped DBA (hexadehydrotribenzo[12]annulene) and the rhombic-shaped bisDBA (decadehydrotetrabenzo[12]annuleno[12]annulene), entails the coverage of the substrate with

two similar porous structures with different patterns. The dimension of the elementary hexagon that forms the pore is equal for the two networks. Still, in the first molecular arrangement, there is a triangular shape cavity between triplets of hexagons (Kagome's arrangement). In contrast, in the second assembly, there is no space between neighbouring ones (honeycomb arrangement). The geometry of the lamella structures is also dependent on the concentration solution. In fact, for low concentrations solutions, the self-assembly of the molecules in hexagonal pores; on the other hand, for higher concentrations, they prefer to assume a close-packed arrangement [65], see (Fig: 2.6. e-h).

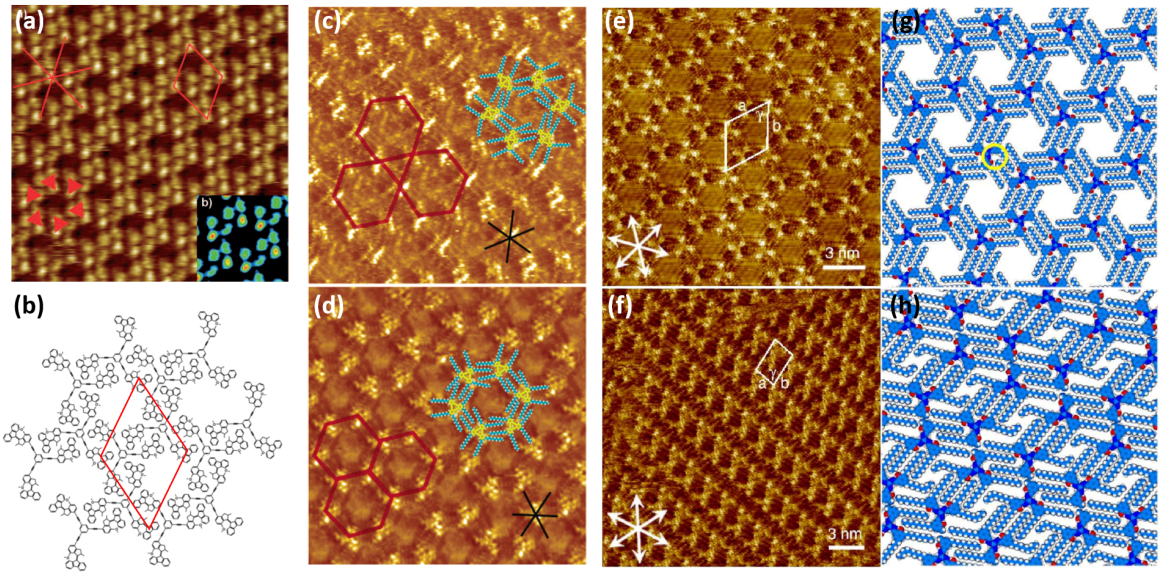

Figure 2.6: **Non-directional molecule-molecule interactions.** (a) STM image of the self-assembled monolayer based on the sterically overcrowded alkenes. The unit cell is indicated by a red rhombus, and the main crystallographic directions of the underlying HOPG lattice are marked by the three red lines. (b) Schematic representation of the proposed packing model of (a), the corresponding superlattice of brighter spots is evidenced with the red rhombus. (c, d) STM images (partially overlaid by the chemical model) of the Kagome and honeycomb arrangements of the two alkyls chains designs: triangular-shaped DBA and rhombic-shaped bisDBA, respectively (The directions of main symmetry axes of underlying graphite are indicated with black lines). (e-h) STM images and network models of the six alkyl compound assembled in porous and non-porous structures, respectively, due to the concentration of the molecular solution at the liquid-solid interface. The yellow circle highlights the space between the point end of the alkyl chain and the p-core. (White arrows and rhombus in (e) and (f) indicate the directions of the main symmetry axes of underlying graphite and the unit cell, respectively). (a, b) Panels adapted with permission from ref [62]. (c, d) Panels reprinted with permission from ref [63]. (e-h) Panels reprinted with permission from ref [65].

2.5 Covalent coupling bonds

The nanoarchitectures achieved with self-assembly described so far are relatively fragile, especially if considering applications where molecular layers require exposure to high temperatures or challenging conditions in catalytic, biological, and even ambient environments. The bonding interactions in molecular networks are usually reversible, and the supramolecular structures can easily be damaged or modified under a range of conditions. The spontaneous ageing of the sample often yields molecular clustering in disordered networks; furthermore, the actual process of measurement could transfer enough energy to the sample to induce a disruption of the ordered assembly or even desorption from the surface. For this reason, on-surface polymerisation through the formation of covalent coupling bonding between molecules had been, for years, a major goal for producing stable and functional molecular layers. However, even though Hla *et al.* [66] proved how a chemical reaction could be induced on a surface by a scanning tunnelling microscopy tip, only in 2007 Grill *et al.* [67] show the first self-assembly held together by C-C bonds. The formation of an assembly stabilised by covalent coupling is much more complicated than the supramolecular structures held together by weak forces. In fact, covalent polymers can't be evaporated due to their high molecular weight and the intrinsic limited thermal stability of most of them. Hence, the growth of the polymeric network must be achieved by the covalent bonding of precursor molecules deposited over the substrate. A well-known example of this was demonstrated by Grill, who showed how tetra(4-bromophenyl)porphyrin (Br_4TPP) molecules were deposited on an Au(111) surface under ultra-high vacuum conditions where they could polymerise after a process of activation/recombination. The aromatic backbone of the porphyrin was functionalised with four bromine atoms; therefore, thermal annealing was able to trigger the molecular activation process by dehalogenation, similar to the Ullmann coupling reaction. In the next step, following thermal diffusion, a recombination of the activated building block induces the covalent coupling formation, see (Fig: 2.7). Grill developed two methods to attain the activation. Method I: evaporating the molecules over the metal surface at a low temperature (550 K), the precursors have enough energy to diffuse and form close-packed islands stabilised by van der Waals interactions, hence annealing the substrate at temperatures over 590 K, the activation occurs. Method II: the precursors were evaporated at 610 K, inducing the debromination before the soft-landing on the metal substrate; consequently, the molecules would immediately connect by a C-C bond in an ordered pattern.

This pioneering study showed the potentialities of a new type of chemistry: the on-surface synthesis, which is the branch of heterogeneous catalysis confined to 2D templates. Furthermore, the rapid and newly developing field showed during the years the versatility of this kind of synthesis by a plethora of adjustable parameters that, if balanced, let to attain the growth of different covalent coupled architectures.

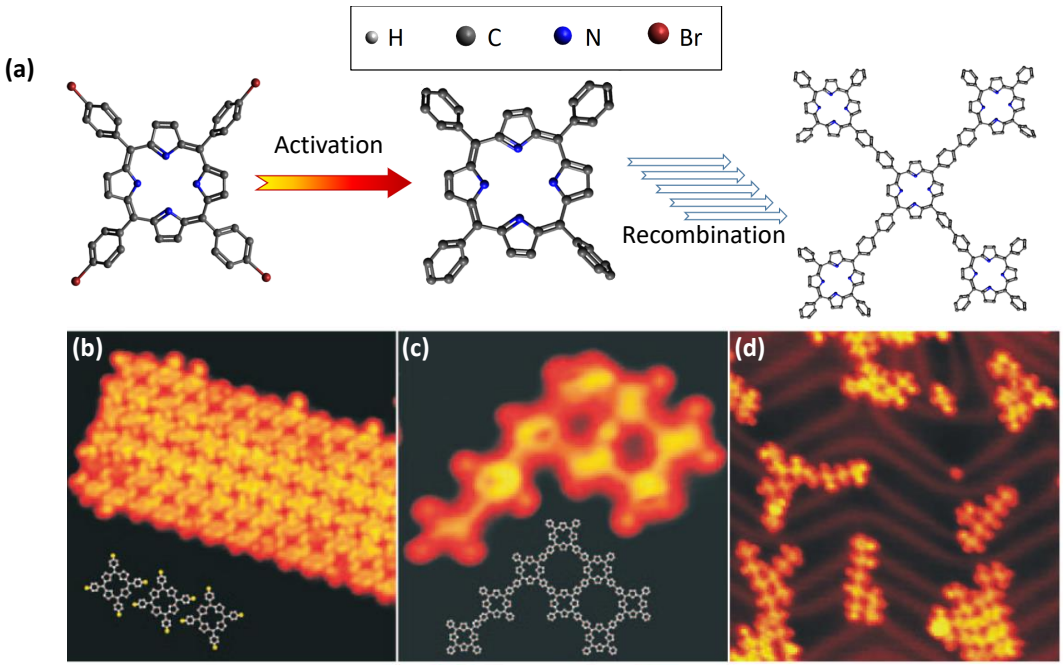

Figure 2.7: **Covalently bound network of tetra(4-bromophenyl)porphyrin (Br_4TPP) molecules on Au(111).** (a) Scheme of the two steps covalent bonding formation of Br_4TPP molecular building block: Thermal activation of the precursors by debromination, and recombination in a self-organised nanoarchitecture by covalent connection, here represented by the C-C assembly of five TPP molecules as a part of a polymer. (b) STM image (20 x 20 nm^2) of a molecular island after deposition at low evaporator temperatures of 550 K before being activated. The chemical structure is drawn in the inset. (c) STM image (8.5 x 8.5 nm^2) of a covalent-coupled network formed by eight molecules after the activation (annealing at 590 K) -recombination process. The inset shows the corresponding chemical structure of the network (Method I). (d) STM image (41 x 41 nm^2) of a covalent-coupled network formed in the gas phase during the deposition at an elevated evaporator temperature of 610 K (Method II). (b-d) Panels adapted with permission from ref [67].

2.5.1 Precursor design

The precursor design is one of the first features that can be tuned to control the self-assembly reaction pathway. The building block's size and symmetry profoundly influence the networks growth; as shown in his pioneering article, Grill [67] developed three different molecular arrangements simply varying the number and the position of the halogens. Using three monomers as precursors: BrTPP, trans-Br_2TPP and Br_4TPP, the number of feasible C-C bonds per building block was proportional to the number of its halogen. Hence, the recombination of BrTPP molecules yields only to BrTPP dimers (0D structure), activated trans-Br_2TPP forms linear chains (1D structure), and Br_4TPP a honeycomb structure characterised by squared domains (2D structure), see (Fig: 2.8. a).
Similarly to what has been described previously, the symmetry and the pore spacing scale with the size of the precursors; hence the change in network size could directly influence the extension of the conjugation of the aromatic system, thus providing an efficient way to tune the bandgap [68]. The precursors' dimensions also affect the quality of the network; in fact, the presence of defects in the pattern could increase or decrease proportionally to the scaling in size, depending on the molecules used for the reactions [69, 70].
As the quality and the dimension of the C-C network strictly depend on the diffusion of the precursor molecules [71], the activated monomers and the intermediate oligomers, hence their molecular adsorption geometry of them, could be tuned to promote or suppress the thermal migration of these species over the surface. As an illustrative example, chemisorbed molecules [72] or close-packed molecular monolayers [73, 74] can completely restrain the thermal diffusion, limiting the recombination. Furthermore, the quality of the network could be controlled by inducing sequential or hierarchical growth. Especially for small precursors, the low mobility of activated precursors and the high concentration of reacting sites could produce defective sequences of molecules [75]; thus, an efficient strategy to prevent chaotic recombination was to functionalised the monomers with one or more reactive groups. As showed by [76], a trans-Br_2I_2-porphyrin (trans-Br_2I_2TPP) has two different dehalogenation temperatures, therefore at 395 K the bond-cleavage of the Iodine atoms is completed, and the porphyrins can attain recombination in linear chains. At 525 K, further debromination leads to the connection of reactive chains in a second-growth direction, thereby establishing a porous squared network, see (Fig: 2.8. b). The functionalisation of aromatic molecules with halogen metals is not the only strategy to achieve sequential/hierarchical growth. Alkyne coupling, dehydration and condensation reactions, direct C-H activation, and intramolecular dehydrogenation can do common selective reactions. The last example represents a remarkable result for graphene nanoribbons (GNRs) preparation, especially because such nanoarchitecture seems inaccessible with other techniques. After the deposition

of 10,109-dibromo-9,99-bianthryl monomers over an Au (111) surface, the thermal annealing activates the precursors that undergo a radical addition reaction by covalent-connecting in linear chains. A further thermal activation step induces a cyclodehydrogenation of the polymer, forming an extended straight, fully aromatic GNRs system [77], see (Fig: 2.8. c). Using the hierarchical growth method, Cai *et al.* also showed that they could make straight GNRs from bianthryl monomers. It was also possible to make Chevron-type GNRs from tetraphenyl-triphenylene monomers [77].

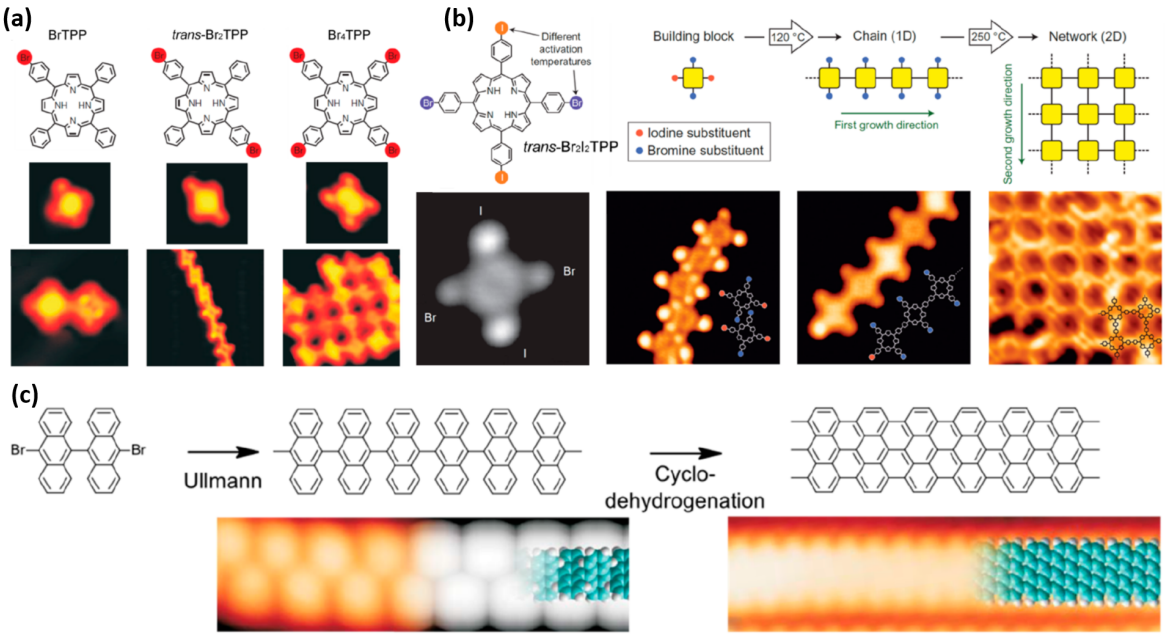

Figure 2.8: **Role of the precursors in the network dimensionality and topology.** (a) Chemical structure of molecular models designed as mono-, di-, and tetra-bromo functionalised porphyrins (first row) and corresponding STM images (all 3.5×3.5 nm^2) used as building blocks (second row) to grow 0D (dimers) (5×5 nm^2), 1D (linear chains) (10 x 10 nm^2), or 2D networks (8.5×8.5 nm^2), respectively (third row). (b) Chemical structure of trans-Br_2I_2-porphyrin (trans-Br_2I_2TPP) and its selective activation-covalent coupling recombination scheme (first row) and corresponding STM images of chemical molecular identification, trans-Br_2I_2TPP molecular island before the activation, 1D linear chain after the first deiodination-recombination process at 395 K, 2D network after the second debromination-recombination process at 525 K (second row). The chemical structures of the networks are drawn in the respective insets. (c) The reaction scheme of the two-step synthesis process from 10,109-dibromo-9,99-bianthryl monomers deposited on Au(111) to surface-assisted debromination-covalent coupling polymer to straight graphene nanoribbons (GNRs) after the final cyclo dehydrogenation-coupling step (first row). Overview of the respective phases: a polyanthrylene chain and a straight GNR represented by STM/DFT-based simulation of the STM (orange/grey) partially overlaid by the model of the polymers (blue, carbon; white, hydrogen) (second row). (a) Panels adapted with permission from ref [67]. (b) Panels adapted with permission from ref [76]. (c) Panels adapted with permission from ref [77].

2.5.2 Choice of the substrate

As previously described, the supramolecular structures are highly influenced by their orientation, and substrate template upon which they grow. In particular, the substrate's nature plays a crucial role in the thermodynamic and kinetic behaviour of supramolecular networks. It affects the diffusivity and the reaction kinetics of the precursors, mainly due to its molecule-surface interaction strength and the number of intrinsic adatoms adsorbed over the surface. Parallelly, the nature of the substrate influences the activation/recombination of the molecules acting as a catalyst, lowering the activation energy and the associated temperature, thus stabilising the structure during intermediate states. Several studies have been done to establish the role of surface nature in the competing events of surface adsorption and molecular diffusion. Comparing the covalent coupling formation from different precursors on Cu(111), Au(111) and Ag(111), it has been possible to determine the reactivity to diffusivity ratio of different substrates. For less reactive coinage metals such as Au (111), the interaction force with the adsorbed monomers is low (weak physisorption), so the molecular diffusion is highly enhanced; nevertheless, early molecular desorption frequently occurs. By contrast, on reactive surfaces such as Cu (111), the diffusivity is highly limited, and the molecules are strongly bonded to the substrate (strong chemisorption) [42, 43, 78]. The hexabenzocoronene (HBC) coupling on the two noble metal surfaces showed a rapid polymerisation after the deposition on Cu(111) due to its high catalytic properties. On the other hand, on Au(111), the coupling was highly inhibited at room temperature, and the molecules could be activated only due to thermal annealing [79], proving the inert nature of the metal. The comparison of the quality of the on-surface assemblies showed how Ag(111) is the most efficient substrate, able to achieve extended networks with a low presence of defects in the lattice [80–82]. Monte Carlo simulations for nanoporous graphene polymerization [82], see (Fig: 2.9. a-f), and a statistical analysis[83]: the Minimal Spanning Tree (MST) analysis for BDBA crosslinking also confirmed this feature of Ag(111) surfaces. Finally, the nature of the substrate plays a crucial role in the surface structure polymerisation, stabilising the activated precursors with the intrinsic adatoms provided by the metal surface. This organometallic intermediate phase leads the reaction pathway of the precursors, chemically selecting and modifying the distribution of the reaction products [84, 85]. With some exceptions, generally, organometallic bonding interphase is highly stable on silver, semi-stable on copper and almost prevented on gold. Hence the molecular recombination by C-C coupling quickly happens on gold, while on silver needs higher activation temperatures [84, 85], see (Fig: 2.9. j, k). An illustrative example is the study of the trisbromophenylbenzene precursor (TBB), crosslinked on Au(111), Ag(111) and Cu(111) surfaces (for the role of metallic adatoms in surface synthesis, see the next section).

In addition to its nature, the orientation of a metallic surface can influence the polymerisation by the substrate's catalytic activity of the substrate. As previously

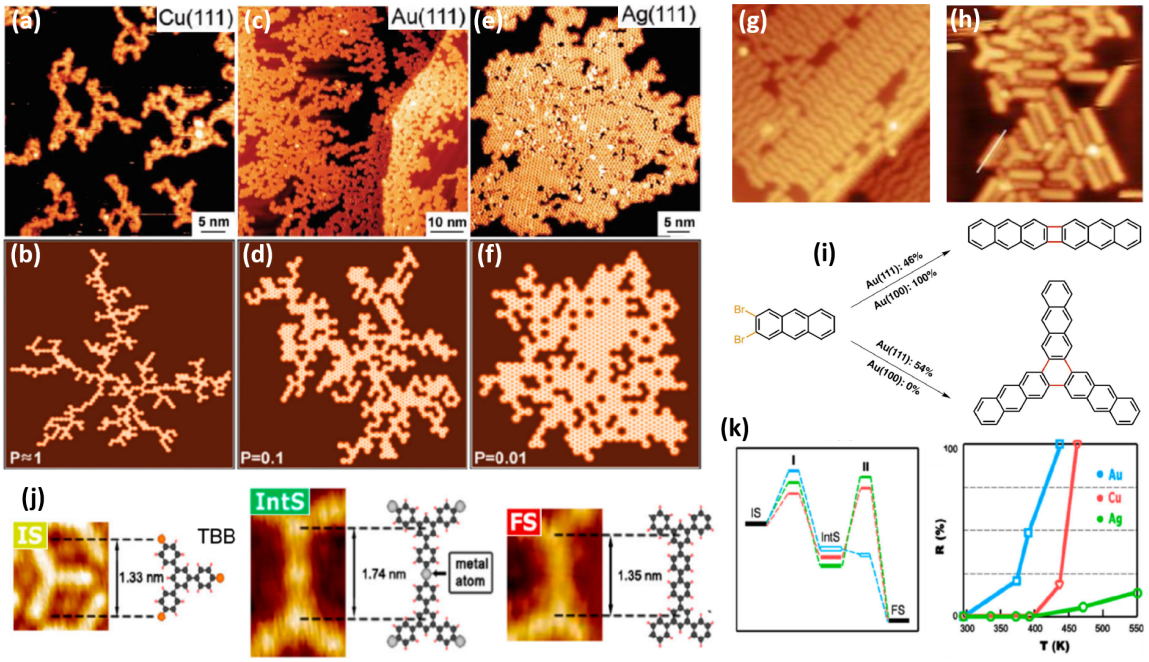

Figure 2.9: **Role of molecule-surface interactions.**(a-f) Comparison of on-surface phenylene polymerisation on different close-packed noble metal surfaces. The network dimension and quality depend on the nature of the substrate. (a, c, e) STM images and (b, d, f) corresponding results from Monte Carlo simulations with varying factor P corresponding to the ratio of reactivity to diffusivity. (g, h) STM images of the dimeric and trimeric formations of dBA deposited on Au(100) and Au(111) and (i) Representation of the two possible chemical reactions surface-orientation dependent. (j) STM images and corresponding chemical scheme of the three phases (IS: initial stage, IntS: intermediate stage, FS: final stage) of TBB coupling on metal surfaces: (IS) the initial steric repulsion of the precursors, (IntS) the metal-coordination interaction mediated by the intrinsic adatoms of the surface, (FS) the C-C coupling. (k) Comparative study for the three (111) surfaces of Au, Cu and Ag. The panels show, respectively, the energy state of the TBB coupling reaction process during the three phases, and the conversion ratios (R) of the precursors as a function of the activation temperature. (a-f) Panels adapted with permission from ref [82]. (g-i) Panels adapted with permission from ref [86]. (j, k) Panels adapted with permission from ref [85].

introduced, the orientation of the metallic surface modulates both the symmetry and the coordination number of the surface atoms. Generally, higher mobility of the adsorbed molecules and lower catalytic activity are observed on a low-index symmetry surface. Depositing 2,3-dibromoanthracene (dBA) molecules upon Au(111), the coexistence of dimeric and trimeric formations due to [2+2]cycloaddition and [2+2+2]cycloaddition reactions occurred. By contrast, the trimeric bonding is completely inhibited if the reaction is attained on an Au(100) surface [86], see (Fig: 2.9. g-i). Confirmations that the growth is orientation-dependent were also shown for Cu (e.g. the two different reaction pathways of DMTP on Cu(111) and Cu(110) [87]) and for Ag substrates (e.g. the Knoevenagel reaction and oxidative coupling promoted on Ag(111). On Ag(110) [88], it occurs at higher temperatures, and on Ag(100), it's even partially prevented.
Besides the orientation, both the surface reconstruction [5, 89, 90] and the surface structure [89, 91, 92] are intrinsic features of the substrate that can be tuned to produce different supramolecular networks.

2.5.3 Metallic adatoms

As previously described, the presence of intrinsic metal adatoms depends on the nature of the metal substrate and can influence the network synthesis process. Similarly, the concurrent deposition of extrinsic metal adatoms and precursors over the substrate can be used to entail two different supramolecular couplings. They can be used for covalent coupling bonding; metal atoms can catalyse the network synthesis, improving the monomer reactivity and lowering the system activation energy. The employment of extrinsic metal adatoms appeared useful on surfaces characterised by weak adsorption forces such as Au (111). In fact, the high molecular diffusion promoted by the substrate was combined with the enhanced precursor reactivity due to the adatoms, as in the case of Pd or Cu adatoms co-deposited with: porphyrin derivatives on Au(111) [93], or polyphenylene (BCCTP) on either Au(100) [94] or Au(111) [95], see (Fig: 2.10. a-d). Different reaction mechanisms were achieved with extrinsic adatoms compared with those generally obtained on the bare metal substrate [93]. Furthermore, sequential and hierarchical growth can take place either using hetero-depositions of adatoms [96] or depositing the metal atoms after a preliminary activation-reactivation process to get a selective reorganisation of the precursors [95].
A remarkable result is a network crosslinking on weakly interacting surfaces, such as graphite or bulk-insulating samples. Typically, the on-surface polymerisation is prevented on these substrates because the molecular activation energy is higher than the desorption energy [97]. Thus the precursors tend to leave the surface rather than crosslink. An illustrative example is synthesising hexagonal boron nitride networks on the Ni(111) surface. In contrast, deposition of Cu or Pd adatoms catalyses the activation-recombination process of tris-bromophenylbenzene precursors [98].

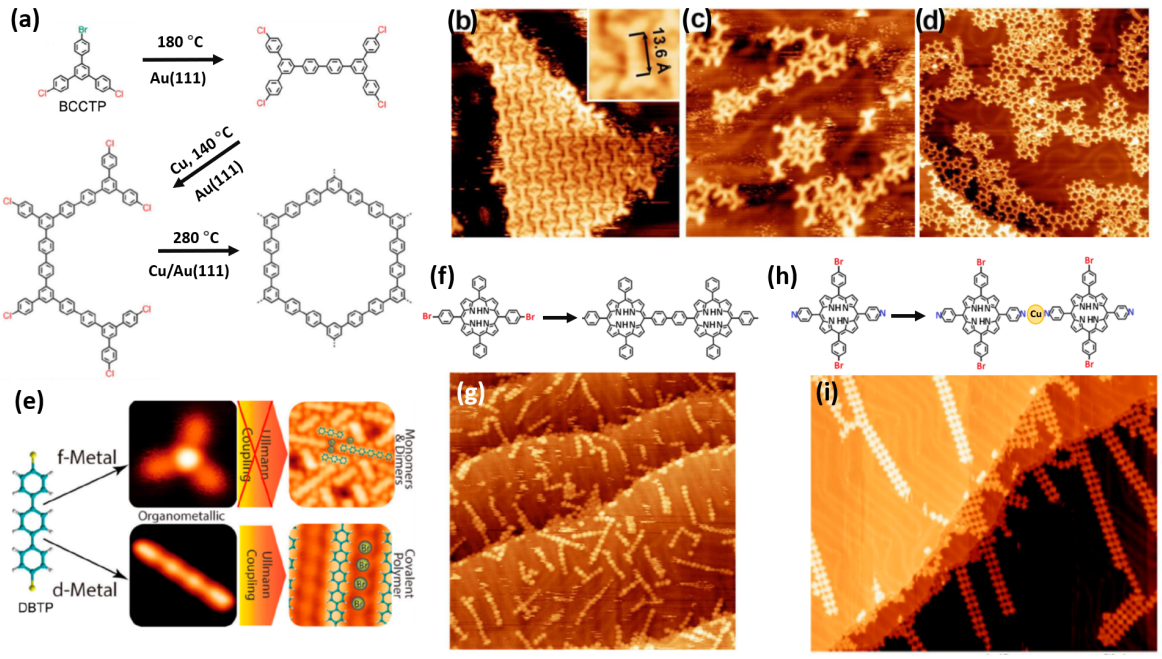

Figure 2.10: **Extrinsic metal adatoms for directional network formation.** (a) BCCTP reaction scheme catalysed by Cu adatom deposition on Au(111). (b-d) STM images of the BCCTP reaction phases: (b) close-packed island of thermal activated covalent-recombined BCCTP precursors, (c) deposition of the Cu atoms at 415 K (d) network formation after further annealing at 555 K. (e) Two possible pathway reactions of DBTP species deposited on Ag(111) either with Dy (f-block) or Ag(d-block) metal atoms. The former inhibits the reaction yielding a close-packed mixed assembly of monomers and dimers; the latter entails a debromination and a further 1D polymer chain formation. STM images and superimposed chemical schemes of the two reactions are shown. (f-i) Comparison of the two coupling intermolecular interactions yields by the Cu atoms depositions with similar porphyrin compounds: (f, g) chemical scheme and STM image of covalently coupled porphyrin compound chains (py-py) catalysed by the Cu adatoms, (h, i) chemical scheme and STM image of metal coordinated porphyrin compound and Cu chains (py-Cu-py). (a-d) Panels adapted with permission from ref [95]. (e) Panel reproduced with permission from ref [99]. (f-i) Panels adapted with permission from ref [100].

The second coupling strategy can be pursued using extrinsic metal adatoms in the metal-organic coordination bonding. The adatoms are incorporated into the molecular arrangement by non-covalent self-assembly. They can coordinate the precursors in an oriented growth, as happens for the porphyrin compound #1 [100] (shown in (Fig: 2.10. h)), where the monomers are held together by Cu adatoms in a 1D sequence of py-Cu-py. Otherwise, the metal-organic coordination bonding occurs as a mediator between the activation of the precursors porphyrin compound #2 (shown in (Fig: 2.10. f)) and the final recombination state, stabilising the structure during an intermediate phase [100], see (Fig: 2.10. f-i).
Finally, a peculiar use of the catalytic property of extrinsic metallic adatoms is as a coupling suppressor. An example is the inner transition metals (f-group) that can lower the thermal activation energy of the molecules catalysing the ligands cleavage even at room temperature but inhibit the uncontrolled covalent coupling reaction if the sample is annealed [99], see (Fig: 2.10. e).

2.5.4 Covalent coupling on insulators

The role of the substrate in the surface-assisted covalent coupling process has been deeply exploited in the previous sections; nevertheless, almost the totality of the C-C-based structures mentioned before was grown on metal surfaces. Metal substrates are characterised by strong adsorption energy that prevents molecular desorption and a high catalytic activity that lowers the activation energy of the precursors and initiates the coupling reaction; both features favour the formation of nanoarchitectures. By contrast, the realisation of covalent systems upon inert insulating surfaces or on low reactive semi-metals and semiconductors was critically challenging, even though some interesting results have been obtained. Relevant results have been reported for semiconductor surfaces. Olszowski *et al.* [101] showed on passivated Ge(001) the dimer growth of 10,10'-diiodo-9,9;-bianthryl (DIBA) from solution, and the formation of poly(p-phenylene) chains on TiO_2(110) by surface-confined debrominative homocoupling of 4,4"-dibromoterphenyl precursors [102]. Remarkable results were obtained for the molecular growth upon the semi-metal highly oriented pyrolytic graphite (HOPG), such as the honeycomb structure of a mixed phase of 1,3,5-Tris(4-aminophenyl)benzene (TAPB) and gaseous terephthaldicarboxaldehyde (TPA) activated by thermal annealing by Liu *et al.* [103], the surface covalent organic frameworks obtained either at a solid/liquid interface at room temperature or in a low vacuum with moderate heating by Xu *et al.* [104], and finally, the photochemical homocoupling of aryl-alkynes triggered by UV radiation at the liquid-solid interface by Colazzo *et al.* [105].
Further interesting results were reported on calcite substrate, a common insulator. However, in this case, the on-surface assemblies are constituted by a few oligomers formations, characterised mainly by the lack of symmetric pattern and surrounded by unactivated precursors [106–109]. Moreover, the strong chemisorption with the substrate prevents the

formation of a regular network; it constrains the diffusion of the precursors limiting the molecular reorganisation rather than contributing in terms of electron transfer [109].
Several strategies have been exploited to overcome the crosslinking limitations upon the non-metallic substrate. For example, the use of different polymerising techniques, such as the UV light irradiation [110], or STM tip atomic manipulation [111]; the co-deposition of metal adatoms as catalysts to reduce the activation temperature of the precursors [98]; or the design of a multilayer substrate characterised by an ultra-thin insulating layer between the organic network and a metal substrate, that aims to decouple the electronic and spatial interaction metal-organic film. Commonly, the molecular coupling is attained on the bare metallic surface, and then the insulator is intercalated under the polymeric network [7, 8, 112, 113].

2.6 Atomic quantum clusters in catalysis

To date, a more general strategy to activate and grow polymer networks using a much wider spectrum of functional molecules without the need for specialized structures is missing. As said before, extrinsic single-atom catalysts are promising candidates for activating coupling reactions on, in principle, any surface material; however, the major limitation of this method is that single-atom catalysts rapidly agglomerate, producing large clusters that disrupt molecular networks and remain trapped within molecular layers as unwanted byproducts. Identifying catalysts that activate coupling reactions whilst avoiding sintering, catalyst poisoning, and unwanted byproducts is, therefore, an essential criterion for realizing extrinsic catalyst activation of on-surface polymerization. Recently, metal clusters with dimensions ranging from sub- to a few nanometers have been considered a potential candidate for molecular activation. Even though the optical, electronic and magnetic properties of small metal clusters have been regarded as a research subject since the beginning of the '90s [114–117], only in the last decade their exceptionally high catalytic activity has provided a range of new capabilities and applications [118–120].
An atomic quantum nanocluster is considered a metal nanoparticle composed of a small number of atoms, generally $\leq$50, where the strong interplay between atomicity, geometry and size profoundly influence the behaviour of the cluster. In fact, if the cluster dimension is comparable to the de Broglie wavelength, it yields a quantum confinement effect that produces electronic levels discretization and localization in molecular orbitals. Hence, the electronic structure of the clusters in the sub-nanometer regime, rather than showing a full delocalization as in the bulk metal, is redistributed in a discrete frontier orbitals configuration with a non-zero band gap; for this reason AQCs are considered as non-metallic [121, 122]. In fact, similarly to the discretization of molecular orbital, the orbitals are labelled as HOMO/LUMO, respectively the highest occupied molecular orbitals and lowest unoccupied molecular orbitals. The energy difference between the HOMO and LUMO is

the HOMO–LUMO band gap. The HOMO-LUMO orbitals configuration generally consists of several lobes localized on the low coordinated metal atoms, whose size and energy level depends on the cluster morphology and atomicity [123], as shown in (Fig: 2.11. a). In fact, for each atomicity, clusters have multiple geometrical configurations whose relative stability varies from one element to another (Fig: 2.11. b).

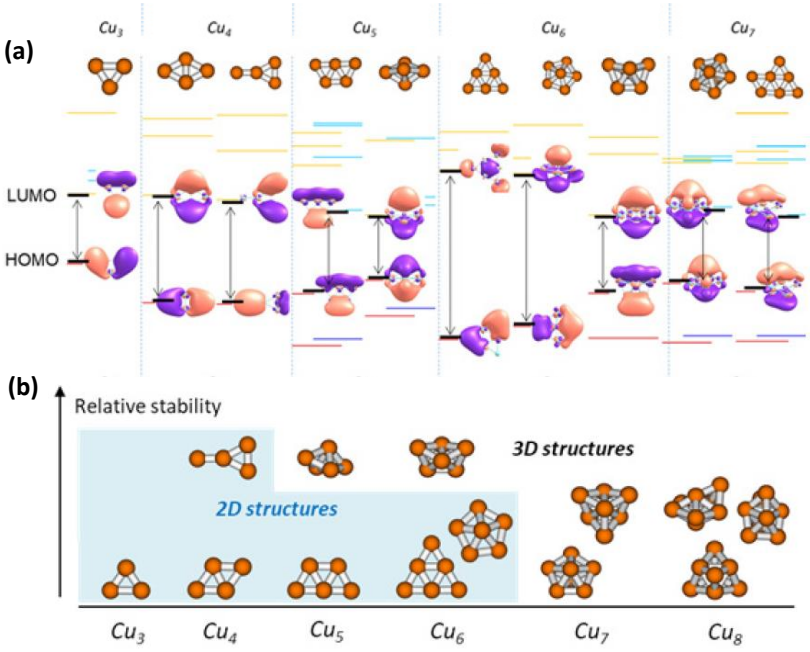

Figure 2.11: **Electronic and geometric properties of Cu_n clusters with 3 ≤n ≤8.** (a) Schematic depiction of the isosurfaces and energy levels of the lowest unoccupied (LUMO) and highest occupied (HOMO) orbitals. (b) Relative stability of Cu isomers for each atomicity. (a, b)Panels adapted with permission from ref [124].

Hence, as a result of the high tunability of the electronic structure through minor changes in nature, atomicity, and geometry, nanoclusters are a valuable method for increasing the selectivity and activity of catalytic reactions. In fact, sub-nanometer metal clusters have been applied to several critical catalytic processes, including O_2 activation [125], oxidation of hydrocarbons [126–128], and reduction of CO_2 [119], C–H bond cleavage [129], C–C bond scission [130, 131], C-X (X = C, N, S, P) bond forming reactions [132], and also for tuning surface states of TiO_2 [118]. This range of properties, including high resistance to cluster sintering and catalysis poisoning [124, 133], increased mobility, and thermal stability, make these atomic clusters ideal candidates for surface polymer synthesis and atomic scale study Recently, sub-nanometer copper-based materials have attracted much interest in the field of catalysis [118, 134, 135]. Due to their important catalytic properties, Cu_5 clusters have been employed throughout this experimental work. Although the text reference is made to the clusters, describing them in their pure form as Cu_5, theoretical [132] and experimental evidence [136] have proved that irreversible cluster oxidation occurs under ambient conditions. For this reason, a more accurate definition should be $Cu_5(O_2)_x$.

Chapter 3

Experimental Techniques and Methods

3.1 Isolab laboratory

Sample preparation and analysis were carried out in the IsoLab laboratory at Lancaster University. This facility has been designed to provide an 'ultra-clean' environment for measurement and characterisation. The laboratory sits on a 50-ton concrete block floating on air springs, accessible through a removable floor not connected with the block. The whole instrumentation: an ultra-high vacuum chamber, and an atomic force microscope are secured on metal frames positioned directly on the concrete block to shield the apparatus from the mechanical vibrations coming from the ground, and from the users working inside the laboratory. To reduce the acoustic noise, and the electromagnetic disturbance, the room is surrounded by a Faraday cage, and multiple layers of acoustic paddings. To further shield the AFM measurement, the instrument is housed in an acoustic enclosure with additional thermal insulation.

3.2 Ultra-high vacuum apparatus

The aim of this research is the development and study of ultra-thin layer of molecular assemblies on multiple surfaces: mainly Au(111), but also highly oriented pyrolytic graphite (HOPG) and mica. The growth needs to be carried out under ultra-high vacuum conditions that is at pressures lower than 10^{-9} mbar. This is a indispensable condition to keep the substrate contaminants free, preserve the ordered growth of supramolecular nano-structures and prevent its desorption and random clustering. In fact, the quality of the sample is directly proportional to the level of vacuum reached. Under ambient conditions, approximately in 3.2 ns a water layer fully covers the free-surface of the sample irreversibly impeding the molecular growth. In a range of few Atm to 10^{-3} mbar the level of vacuum is considered as

rough vacuum, the gas composition is mainly water vapour at percentage ranging from 75 to 85. Under high vacuum conditions (10^{-3} - 10^{-8}) mbar, gases are mainly H_2O, CO, N_2 and H_2, and the molecular growth start being achievable but the presence of the gases still limits the quality of the structures. Only under ultra-high vacuum conditions the supramolecular growth is fully controlled, the surface remains clean and the sample can last more than 24 hours.

3.2.1 Ultra-high vacuum set-up

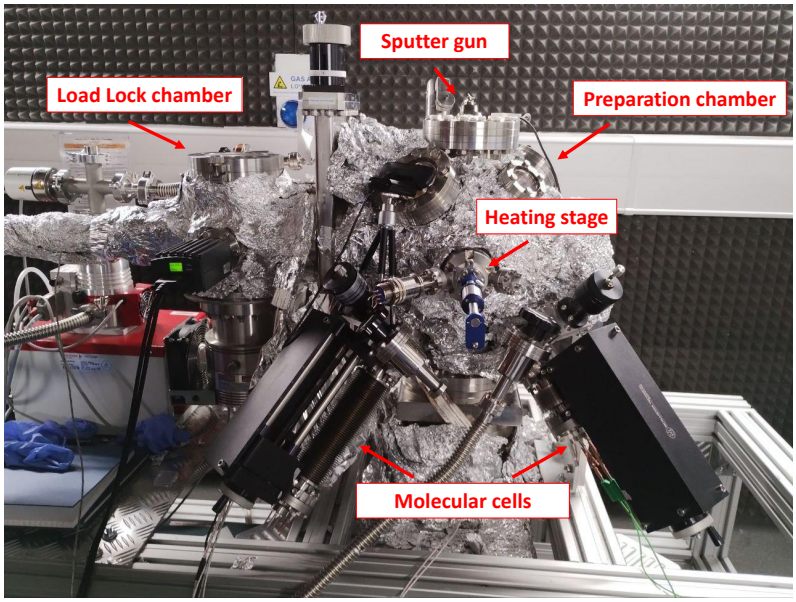

Figure 3.1: **Image of the IsoLab UHV chamber.**

This work has been conducted with a UHV apparatus constituted by two vacuum chambers: a load-lock chamber and a preparation chamber, separated by a gate valve, that can reach a regime of 10^{-10} mbar by a pumping system consisting of: a scroll pump, a turbo pump and an ion pump, see (Fig: 3.1).
The load-lock chamber is designated to the sample loading, and can reach a level of high vacuum of ($10^{-8} - 10^{-9}$) mbar (HV) by a combination of a scroll and a turbo pump. Once an HV condition is attained, a transfer arm moves the sample into the preparation chamber through the gate valve.
The preparation chamber is continuously kept pumped in a regime of 10^{-10} mbar (ultra-high vacuum) by the ion pump, equipped with: the sputter gun, the heating stage and several molecular cells known as Knudsen cells (K-cell). These pieces of equipments are designated to the sample preparation, respectively, in order: to clean the sample surface by Argon ions (Ar^+) bombardment, to reconstruct it by thermal annealing, and, the molecular cells, to allow the sublimation of molecules to form organic thin-film over the sample surface.

3.2.2 Ultra-high vacuum techniques

Here are resumed the general techniques related to an UHV chamber, as all the experiments were conducted in ultra-high vacuum conditions. However, the specific descriptions of the samples preparation will be analysed in a different section further on.

Achieving the UHV conditions: pumping and baking procedures

As previously described, the UHV condition is reached reducing the pressure to $<10^{-9}$ mbar, so, to achieve this result in a UHV chamber, the environment must be sequentially pumped down. The scroll pump shovels air from inside the chamber to outside, bringing the system from atmospheric pressure to a level of rough vacuum. The chamber volume and the pump speed determine the pumpdown time. In a rough vacuum regime gases move in viscous flow: the momentum transfers due to collisions between gas particles. The turbo pump paired with the scroll pump are used to reduce the presence of gases inside the chamber, which is mainly due to the water desorption from walls and surfaces. Once the high vacuum level is reached, the regime of the gas changes from viscous to molecular flow, that is the mean free path of the particles is higher than the chamber dimensions: gases are at thermal speeds. The molecular flow regime represents the intrinsic limit of efficiency of the displacements pumps, hence only the ion pump can further reduce the pressure letting the system reach the ultra-high vacuum condition. At this stage, surface area, material type, pump speed and temperature determine ultimate pressure and pumpdown times.
If the UHV chamber is exposed to the atmosphere, a thin water layer instantly covers all the surfaces. Hence, to drop the pressure to $<10^{-8}$ mbar, the whole UHV chamber needs to be baked at temperatures over 100 °C for several hours during the pumping down procedure, until the water molecules from walls and surfaces are fully evaporated and pumped away.

Molecular deposition using Knudsen cells

Molecular thin-film samples are prepared by thermal evaporation under UHV condition from a Knudsen cell. The K-cell consists in a borosilicate crucible cut and shaped from a glass tube in order to contain the molecules in the form of powder. Molecules are sublimated, by resistively heating, by a looped tantalum wire wrapped around the crucible. A Chromium-Aluminium K-type thermocouple, secured at the bottom of the K-cell, measures the temperature of the heating element.
A quartz crystal micro-balance (QCM) was used to determine the deposition temperature of the molecules. A QCM can detect any change from its resonance frequency, measuring the mass variation per unit area of material landed on the resonator. Quantifying the damping of the frequency, the deposition rate of the molecule, and its relative sublimating temperature can be extrapolated.
The growth of a molecular monolayer coverage over a surface can be done matching the

informations of the deposition rate for its sublimating temperature and the exposition time of the substrate to the molecular flux.

3.2.3 Substrate preparation

As previously described in section (Sec: 2.5.2), the role of the substrate is crucial for thin-film growth, influencing diffusion, orientation, bonding and molecular organisation in ordered structures. The molecular depositions performed in this work were attained on three types of substrates: Au(111), highly oriented pyrolytic graphite (HOPG) and mica, in particular, muscovite.
HOPG and mica are naturally atomically flat, so the sample preparation only involves the removal of contaminants from the surface. Substrates were exfoliated using scotch tape to make the surface contaminants free [137], then annealed in UHV condition at $\sim$ 250 °C for 15 minutes.
The Au(111) surface reconstruction [138] and the process required to obtain an atomically flat substrate are briefly described in the next section.

Au(111) surface preparation

The Au(111) used in this experiment, produced by Georg-Albert-PVD, was epitaxially grown (300 nm thick) on a mica substrate and flattened by thermal annealing at 1.5 $\times 10^{-8}$ mbar. Once the Au(111) on mica was trimmed to size, so that the sample holder could host the strip, it was introduced to the UHV chamber. In fact, the surface preparation requires a three-step procedure that can be achieved exclusively at UHV conditions. The first step is the removal of the thin water layer. As the strips of gold are stored under ambient conditions, water vapour condenses over the sample; hence, to remove the water layer from the surface, the UHV chamber was pumped down and baked overnight at $\sim$130 °C. Once the UHV regime was reached, the gold was moved to the preparation chamber to be subjected to a double cycle of sputtering-annealing, the second and third steps of the surface preparation. During this procedure, the majority of the contaminants are removed, and an atomically flat stepped gold surface is produced. The close-packed Au(111) reconstruction assumes the typical long-range herringbone pattern on scales of a few hundred nm [139]. Argon gas was poured into the preparation chamber by a leak valve until a pressure of 5×10^{-6} mbar was reached. A sputter gun ionised and accelerated the argon atoms over the Au(111) surface by a potential difference of $\sim$0.6 keV for 20 minutes [140]. The impacts of the ions mechanically knocked out all the impurities, such as oxygen, from the gold surface. As a drawback, the sputtering induces a surface flatness loss, as the collisions of the ions dig $\sim$25 nm deep holes all over the sample. The annealing of the sample at $\sim$250 °C for 20 minutes, then slowly ramped down to room temperature, induces a surface reconstruction. AFM measurements showed that a double cycle of sputtering-annealing reduces the mean roughness of the Au(111) surface to $\sim$20 pm.

Therefore the sample can be considered atomically flat.

3.3 AFM

Atomic force microscopy (AFM) is a technique that belongs to the wide category of microscopy methods generally classified by the umbrella term: scanning probe microscopy (SPM), a definition that covers all the detecting methods mainly characterized by two specific features: the feedback loop controller and the use of a sharp probe. Thanks to these two features, microscopies belonging to the SPM group can map and characterized surfaces at micro/nanoscopic level, 'feeling' the atomic interaction exerted between the probe and the sample.

3.3.1 AFM working principle

A standard AFM can generally be schematized in five main elements: the tip-cantilever system, the detection unit, the tip-sample motion unit, the feedback controller and the image processing and display unit, see (Fig: 3.2).
The tip-cantilever system is a device consisting of a micromachined tip with a radius of curvature that can reach dimensions of the order of few nanometers, attached to one end of a flexible cantilever. The manufacturing of the tip guarantees a sharpness of the apex that makes it sensitive to the single atom forces acting between the sample and the tip. The tip-sample interaction is transferred to the cantilever that deflects proportionally to its stiffness. The shape and material of the cantilever, for example silicon, has a characteristic spring constant and eigenfrequency of oscillation, allowing the user to detect and measure the range of forces felt by the tip. As a first approximation, the principle of operation of the tip-sample interaction F_{ts} could be described by the Hooke's law:

$$F_{ts} = -k_s d \tag{3.1}$$

where k_s is the spring constant, proportional to the stiffness of the cantilever and d is its displacement. Usually, a piezo-actuator is placed in the probe holder and it controls the oscillation of the tip at specific frequencies exciting the cantilever in the range of the kHz; this reduces the chances to damage or modify the sample during the measurement.
The second element is the detection unit applied to estimate the bending of the cantilever. Even though there are several methods to measure the cantilever deflection, the most common, also used in this work, is the optical beam deflection one, known also as optical lever technique [141]. A laser beam emitted by a solid state diode is deflected by the reflective back of the cantilever to a four quadrant position sensitive photodiode (PSD) that monitors in real-time its position, enabling the detection of both normal and lateral forces. The optical detector fundamentally operates by measuring the variation of the position of

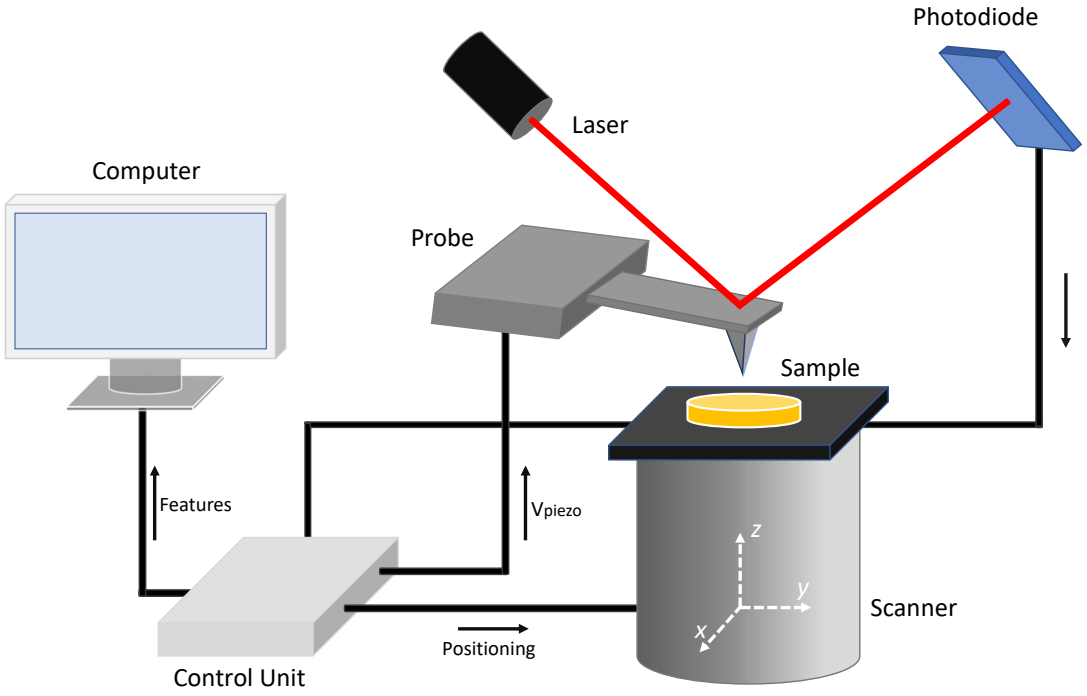

Figure 3.2: **Schematic diagram of the five main elements of an AFM.** The tip-cantilever system, the detection unit, the tip-sample motion unit, the feedback controller and the image processing and display unit.

the laser beam onto the photodiode, that is proportional to the vertical displacement of the cantilever, see (Fig: 3.3).

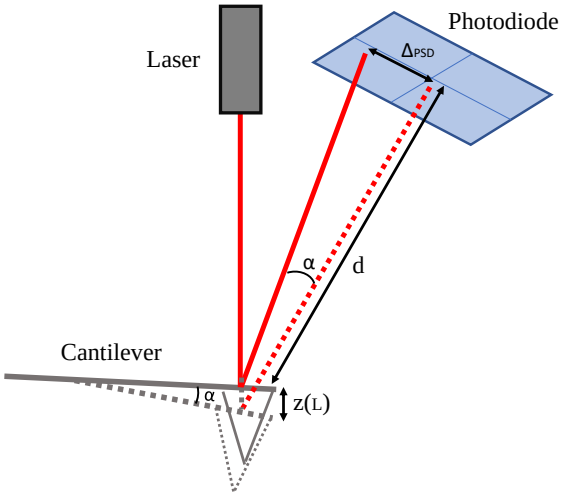

Figure 3.3: **Schematic representation of an optical bean deflection system to detect cantilever deflection.** Δ_{PSD} is the distance the laser spot moves on the photodector, d is the cantilever-photodetector distance, z(L) is the vertical displacement, and α is the laser beam angle variation.

When a force is applied to the tip, the cantilever bends and the reflected laser beam moves through an angle α equal to twice the cantilever change in slope $\frac{dz}{dx}$. Hence, the displacement of the laser spot on the photodiode, at a distant d far from the cantilever, is given by:

$$\Delta_{PSD} \approx 2d \tan \alpha \tag{3.2}$$

As the technique depends on the geometry of the cantilever, for a flat straight bar cantilever [142], applying the Euler-Bernoulli beam theory, the vertical displacement of the deflecting cantilever is described by:

$$z(L) = \frac{\Delta_{PSD} L}{3d} = \frac{2L}{3} \left. \frac{\mathrm{d}z}{\mathrm{d}x} \right|_L \tag{3.3}$$

where L is the length of the cantilever with a spring constant k_s and the deflection along the cantilever $z(x)$ caused by a force F, is defined by:

$$z(x) = \frac{F}{2k_s} \left[\left(\frac{x}{L} \right)^2 - \left(\frac{x}{L} \right)^3 \right] \tag{3.4}$$

see [141, 142] for a formal derivation of the equation. The thermal noise is the main source of error of the tip-cantilever system and yields to vibrations of the free end of the cantilever in the vertical direction proportional to:

$$\sqrt{\widehat{z^{*2}}} = \sqrt{\frac{4k_B T}{3k_s}} \tag{3.5}$$

where $\sqrt{\widehat{z^{*2}}}$ is the thermal fluctuation as the sum of the mean square deviations of each vibration mode, k_s is the spring constant, k_B is the Boltzmann constant, and T is the temperature [141]. If the end of the cantilever is supported by a hard surface the cantilever thermal noise is reduced by a factor of 2.
The next element is the tip-sample motion system, a piezoelectric actuator that controls the displacement of the sample in relation to the position of the tip. For the AFM used in this project, the piezoelectric actuator is the tube scanner placed underneath the sample that sets the x, y and z coarse position of the sample with an accuracy of the order of micrometer and a subnanometric precision when scanning. The sample displacement is controlled by the mechanical deformation of the actuator as a response of voltage inputs, but due to their non-linear relationship, it yields to hysteresis and creep as sources of error for large scan area scans and thermal drift for small ones. Generally, a close loop system is integrated in the microscope to compensate these sources of error, i.e. a system that measures in real-time the x-y-z position of the scanner and compares it to the nominal values. The generation of an error signal and its processing, minimize the instabilities.
The last two elements are the feedback loop unit and the imaging acquisition and display one. The first one compares the measured value of a specific parameter recorded by the detection unit to a reference setpoint. Usually, the setpoint is the deflection of the cantilever for Contact mode AFM, the amplitude or the frequency for Tapping mode AFM or the tip-sample force for PeakForce Tapping AFM. A voltage signal is sent as an output to the tip-sample motion unit to compensate the discrepancy between the measured parameter and the setpoint, withdrawing or approaching the sample from the tip. The minimization of the error signal between the real-time measurement and the value of the set point parameter is the goal of the feedback unit. Generally, the feedback unit is part of the control unit, that is the piece of the equipment that elaborates the input signals and generates all the outputs through its element. The imaging acquisition and display unit is the element of the control unit dedicated to the conversion of the raster voltage signal, registered by the detection unit, into 2D images displaying the sample features measured during the mapping.

3.3.2 Forces of interest in force microscopy

As the operation of force microscopy techniques is based on the quantification of the forces exerted by the sample to the tip, the knowledge and distinction of them are fundamental. This thesis does not study 'in liquid' measurements, but considers only forces present 'in air' or 'in vacuum' measurements, which are commonly grouped into two different categories: long-range forces and short-range forces. The former, such as: van der Waals (vdW), electrostatic, magnetic forces and capillary forces are most significant over a scale of 100 nm, the latter range forces are those arising from chemical bonding and Pauli repulsion between atoms and become dominant, overshadowing the long-range interactions, within 10

Angstroms [143].

The electrostatic interaction arises only either when there is a charge flow at the metal-metal interface when the tip approaches the sample during the transient phase at the equilibrium, or when there are spurious charges trapped in a dielectric material for either a dielectric-dielectric or dielectric-metal interface measurement [144]. For this reason, the electrostatic force could be minimized by applying a bias voltage between the tip and the sample. Similarly, the magnetic interactions are not always present but if they are, they can be nullified applying an opposite external field [145].

In most cases in air or vacuum, van der Waals forces are attractive forces, but in liquid they could have also a repulsive behaviour due to the dielectric constants and the refractive indexes at the interface. They are characterized by electric dipole-dipole forces between atoms and molecules and they are classified in Keesom, Debye and London dispersion forces [146], [147]. Keesom forces describes the interaction between two permanent dipoles of polar molecules, the Debye forces between a permanent and an induced dipole of respectively a polar and a non-polar molecule and the London dispersion force take place by the interaction of two induced dipoles within non-polar molecules. The three possible dipole interaction potentials scales with D^{-6}, i.e. are proportional to the distance D between the two objects, as showed in (Fig: 3.4).

In (Fig: 3.4. a), the ideal situation of two atoms or small molecules feeling the pair vdW potential and far from any other potential induced by a third body, however this is not a realistic representation of the tip-sample interaction in an AFM measurement. In fact, due to the mesoscopic dimensions of the objects involved, the number of atoms and the geometry of the physical bodies are element that must be taken under consideration. So, considering in first approximation, the net vdW potential as the sum of every pair interaction between two single atoms of the physical bodies, the foremost atom on top of a super-sharp tip feels a vdW interaction with the sample surface, equal to (Fig: 3.4. b). Furthermore, for a more accurate representation, the the last portion of the tip should be modelized either as a sphere or as a conical shaft capped with a halfsphere. The two van der Waal potential between the mesoscopic tips and the surface are showed respectively in (Fig: 3.4. c). Finally, assuming the dulling of the tip during the measurement, the vdW potential is equal to the one described by a surface-surface interaction, see (Fig: 3.4. d).

Under ambient conditions, vapour condensation on the sample surface results in the formation of a thin water layer. When studying these sample with an AFM, the water layer causes capillary forces between the probe and the sample, in particular a water meniscus could be formed in the gap between the tip and the sample, and it is dependent both to the environmental parameters such as the pressure and the temperature of the room, and to intrinsic physical features such as the dimension, the geometry and the hydrophilic of the tip or the sample. The capillary force between a spherical tip and a flat surface is equal to

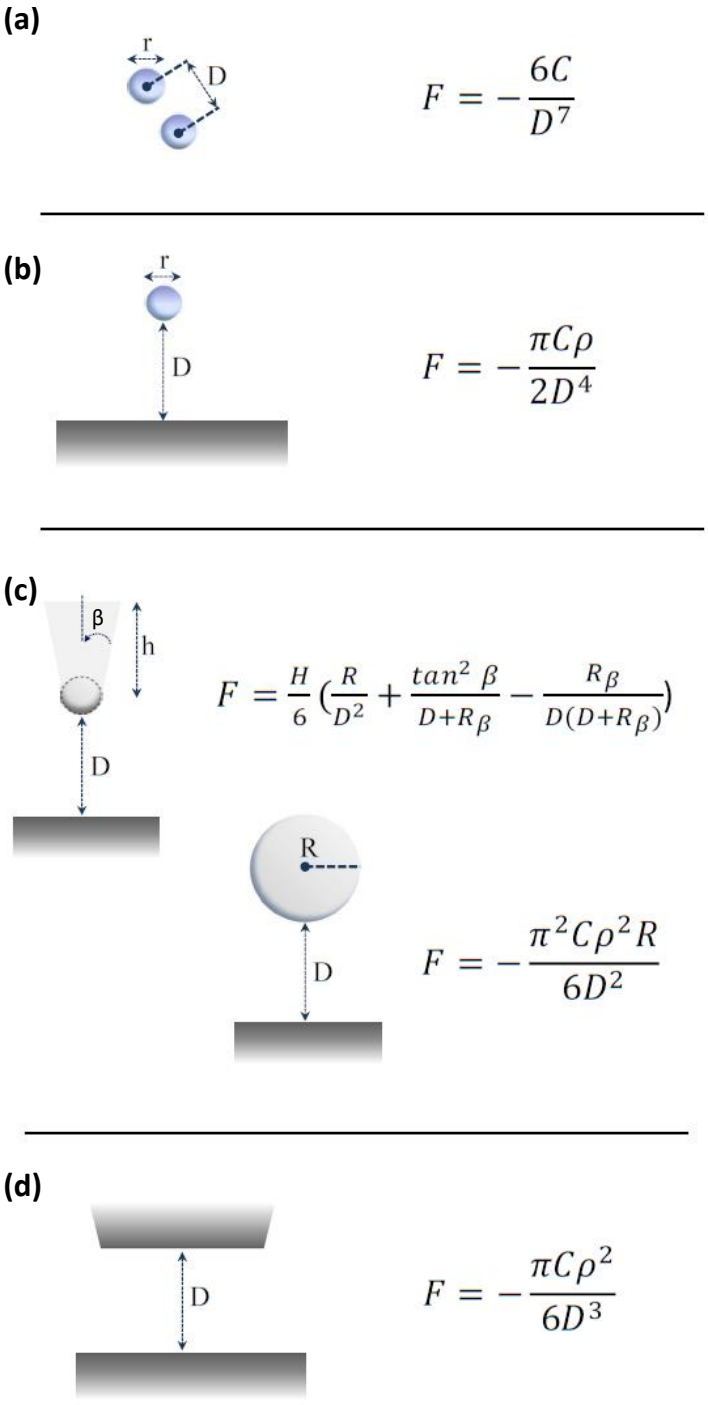

Figure 3.4: **vdW forces between bodies of different geometries**. (a) Interaction between two single atoms . (b) Single atom-surface interaction (ideal situation of an one-atom terminating tip). (c) Respectively, conical shaft capped with a half sphere flat and sphere flat-sample interaction (models of realistic tip surface geometry). (d) Interaction between two flat surfaces (realistic model of a blunt tip). Where F is the vdW force, D is the distance between the two bodies, C is a coefficient that considers the contribution of induction, orientation, and dispersion forces to the net van der Waalsthe interaction, ρ is the number density of particles in the solid, R and R_β is the radius of the sphere and the conical tip, respectively, and H is the Hamaker constant.

the capillary force associated to the water meniscus and it is proportional to:

$$F_{cap} = \frac{4\pi R\gamma_L \cos\theta}{1 + D/d} \tag{3.6}$$

where R is the tip radius, γ_L is the surface tension of liquid, d is the depth at which the tip is merged in the liquid surface, and θ is the angle between the meniscus and the tangent to the tip in the air-liquid interface point and D is the tip-sample distance [147], see (Fig: 3.5).

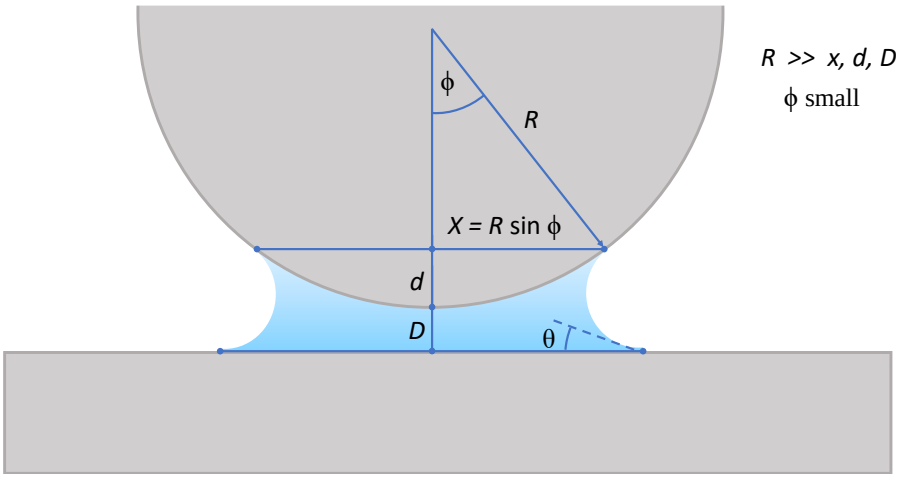

Figure 3.5: **Depiction of the capillary force acting on a cantilever tip interacting with a liquid layer during the meniscus formation.** Schematic representation of the physical quantities acting in a capillary force between the end of the tip an the thin layer of the sample. Panel adapted with permission from ref [147].

Considering the equation (Eq: 3.6), the maximum capillary force occurs at contact, that is if D=0:

$$F_{cap_{MAX}} \overset{D\to 0}{=} 4\pi R\gamma_L \cos\theta \tag{3.7}$$

where $F_{cap_{MAX}}$ is the max value that the capillary force can reach [147], that corresponds to the adhesion force.

Considering the intermolecular distance a_0 as the length that discriminates between long-range and short-range forces, if the tip-sample separation r_{ts} is lower than a_0, the chemical forces, that is the ionic and the Pauli's interaction that origin between the foremost tip atoms and the nearby sample ones, are the best physical interpretation of the tip-sample interaction rather than the van der Waals force. In fact, as it showed by the plot in (Fig: 3.6), the total force curve as a function of the distance, is described by the overlap of the two short and long range forces regimes.

Conventionally, when the tip is at a distance much higher than the intermolecular distance, even though also the chemical forces have an attractive behaviour, their contribution to the

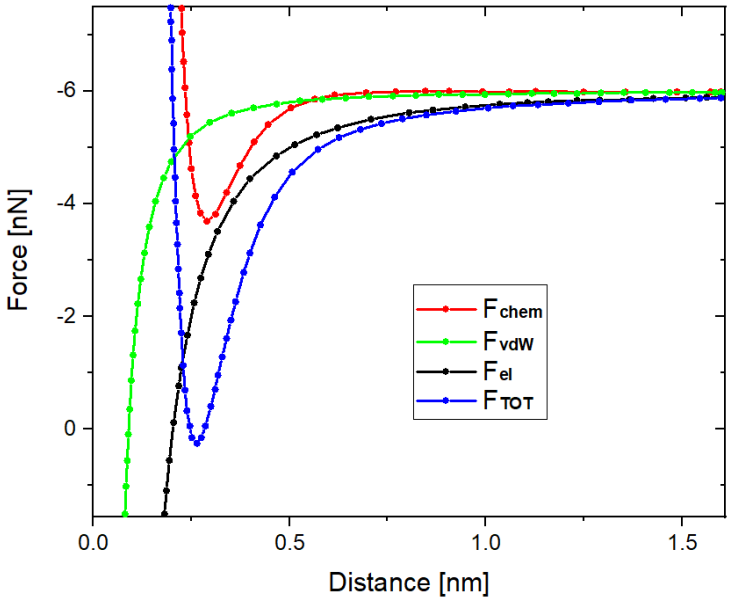

Figure 3.6: **Depiction of the common force contributions.** (Red curve) chemical interactions: ion and Pauli's repulsion, (Green curve) van der Waals interactions, (Black curve) attractive electrostatic interaction, (Blue curve) sum of all the attractive and repulsive forces.

tip-sample interaction can be considered negligible, vice versa for $r_{ts} < a_0$, the repulsive behaviour of the chemical forces overshadows the attractive one. As previously described, both the van der Waals and the capillary forces are tip geometry dependent, hence the long-range forces originate in the full volume of the tip and the interaction is due to the sum of all tip's atoms contribution, on the other hand, short-range forces occurs when tip and sample orbitals overlap. A qualitative description of the the chemical forces is given by the Morse potential, that uses the H_2^+ ion as a model for the covalent bond [148], even though it is not completely exhaustive because doesn't consider the anisotropy of the potential [143]. Summarizing, these interactions are often simplified into two key components, the long range interactions acting on the probe is a mesoscopic and involving collective behaviour involving multiple atoms over a large radius at the tip apex, whereas the short range one is site-specific and limited to the only foremost atoms of the tip. The Lennard-Jones potential provides a good approximation of the tip-sample interaction forces:

$$U_{LJ}(r) = +\frac{A}{r^{12}} - \frac{B}{r^6} = 4\varepsilon\left[\left(\frac{\sigma}{r}\right)^{12} - \left(\frac{\sigma}{r}\right)^{6}\right] \tag{3.8}$$

where ε is the depth of the potential well, σ is zero-potential distance and r is the distance between the particles.

In literature it has been widely documented the importance of the discrimination of short-range forces, as the only relevant forces in most high-resolution NC-AFM measurements, thereby several methods have been developed. The first ones were based on the calculation of the contribution of the long-range forces from the measured total one.

However, if in principle the subtraction of long-range forces from the measurement of the total one seems straight forward, practically the process is much more complicated. In fact, as showed in (Fig: 3.4) the force estimation is dependent by the shape and the radius of curvature of the tip, hence the correct modelling of it becomes crucial. However, this a-priori estimation of the tip geometry was affected by large uncertainties, adding a significant error to the force calculation. Another method involves the extrapolation through the direct measurement of the forces using the same tip for both short- and long-range regimes, i.e., the so-called 'on-minus-off' method [149]. Two are the main situation: for spatially coherent and periodic single atom surfaces the search of site-specific locations characterized by singularities such as vacancies, dopants or adatoms could entail the orbital pair interactions tip-sample at short regime and discriminate it from the long one measured in an 'null' area without chemical or structural singularities. The other case, the adsorbate-specific one, foresees thin-film molecular samples deposited on the substrates. In these situations, the short-ranges forces are defined by the specific adsorbate-tip interaction, even though clouded by the contribution of the nearby atoms of the substrate. So, in this case, the comparison of a spectrum taken on an adsorbed molecule and consisting of the sum of both regimes of interactions with the one taken off a molecule, therefore only characterized by collective long-range forces of substrate atoms, entail the measurement of the short-range contribution.

3.3.3 PeakForce Tapping Mode (PFT-AFM)

As previously described, the development and optimization of the AFM technique directly contributed to the achievement of high-resolution images. At the very beginning Contact mode AFM, also known as Static Mode AFM, was applied and immediately it was evident that the technique could easily resolve flat periodic lattice structures, but 'true' atomic resolution was achievable only in few and specific situations. In fact, during the measurement, the AFM tip is always in contact with the surface [150, 151] hence its lateral scanning induces large shear forces to the sample, increasing the chances to significantly deform or destroy the sample, or to collect some material on the tip compromising its sharpness, therefore prejudicing the resolution. In order to overcome these issues, especially for soft samples such as biological [152], polymers [153, 154], thin organic film [155], Dynamic AFM techniques were proposed. Also known as resonant mode techniques, these are low force technique, typically in the range of few hundred pN up to a few nN's, in which the cantilever forced to oscillate close to its resonant frequency 75 kHz $\Rightarrow$300 kHz [156] feeling intermittently the interaction with the sample surface. The three main resonant techniques are: Tapping mode (TM), non-contact mode [157] (NC-AFM) and multifrequency mode [158] (MF-AFM). Even though NC-AFM is the mode mostly used for the functionalized tip measurements, as it described in the next chapter, this section will focus on the TM mode because the working principle of PeakForce Tapping Mode (PFT-AFM) is based on this scanning mode.
In TM, the probe periodically oscillates tapping the surface, minimizing the shear lateral

forces exerted on the sample, but as a drawback, the vertical force acting orthogonally to the surface, is hard to control. In fact, as previously described, the true sub-molecular resolution has more chances to be achieved when the tip-sample interaction is in the short-range regime, but in order to do that, the imaging force has to be precisely controlled in a range high enough to detect changes in the characteristics of the surface, but low enough to not damage or modify the sample. However, for TM-AFM, the feedback control parameter is usually the amplitude or the frequency, therefore the estimation of the force acting on the sample is not a direct quantitative measurement, but an indirect calculation based on the feedback parameter itself. Moreover, the force calculation is not instantaneous, but the feedback parameter is averaged in the whole cycle of interaction, that is in all the positions of the tapping tip during its approaching-retracting trajectory. A further challenge concerning this technique is the control of both the setpoint and the gain of the instrument. As previously described, the Setpoint is the reference value at which the feedback refers to and the Gain (Integral and Proportional), is the sensitivity of the feedback loop, because it determines how much the vertical position of the tip must change in response to a given amount of error (the difference between the measured value and its Setpoint reference). High gains could induce feedback oscillations noise in the height output data due to the overshooting of the positioning tip-sample, or it reduces the tracking capability if the gain is too small. The challenge occurs because the same Setpoint can be related to high or low tip-sample interactions, proving that there is no monotonous relation between the force and the Setpoint parameter, but also as the feedback needs to be stable and optimal, both the I and P Gain needs to be correctly set at the beginning of the measurement, but also needs to be adjusted every time a discrepancy from the Setpoint is detected. For this reason, it appears clear that the control of the Dynamic AFM for true atomic resolution measurements becomes tricky even for an expert user and relies too much on trial and error. Finally, if the measurement is performed under ambient conditions, the probe oscillation could drop to zero every time the tip undergoes the attraction of the superficial capillary force, thereby introducing a feedback instability. For this reason, in order to avoid that, the spring constant of the cantilever must be chosen high enough that the kinetic energy of the tip, converting in static elastic energy every time it penetrates the superficial water layer, can overcome the capillary force of the sample. Usually, cantilevers for Tapping mode under ambient conditions have a spring constant of tens of N/m, narrowing the range of materials that can be scanned to whose are characterized by a Young's modulus high enough to bear the force impressed by the tip. To overcome the drawback of this technique, off-resonance mode, that is a mode that works at frequencies far from the eigenmode of the cantilever, was developed. Belonging to these group are: force volume (FV) mode [159–161], Digital Pulse-Force (DPT) mode [162, 163], Hybrid mode [164], QI mode [165], and PeakForce Tapping mode (PFT) [166], a method proposed in 2016 by Chanming Su *et al.* for Bruker Nano Inc. [24]. Sharing the advantages of the intermittent orthogonal tapping of the Tapping mode, PFT mode operates at frequencies, in the range of 0.5 $\Rightarrow$ 4kHz, higher than the cantilever eigenfrequency, but

contrary from the Dynamic mode, it uses as a feedback parameter the interaction force between the tip and sample, keeping the system at a stable state peak force recorded in the short-range repulsive regime of interaction. In PFT mode, the force is not the result of an average, but it is its direct measurement collected instantaneously at any interaction cycle; using a no/minimum interaction force as a reference value, the system moves the tip far from the sample re-establishing the non-interacting baseline and calculating the peak force. Due to this process, the imaging is a collection of force curves calculated at each pixel of the raster, so that the resultant scan is a map of topographical and mechanical information, see (Fig: 3.7. a, b).

Furthermore, the direct control of the force implies that the Setpoint value for the measurement is not the phase, the amplitude or the frequency as for the Tapping Mode, but the interaction force itself allowing the sample detection maintaining the peak repulsive interaction force at minimum values in the order of the pN. These very low interaction forces prevent any kind of sample modification, yielding the technique extremely functional for very soft samples, but at the same time, the force control allows the use of cantilevers with spring constants that span from 0.01 N/m to 1000 N/m, enabling the collection of mechanical data for sample with Young's modulus between 100 kPa to 100 GPa.

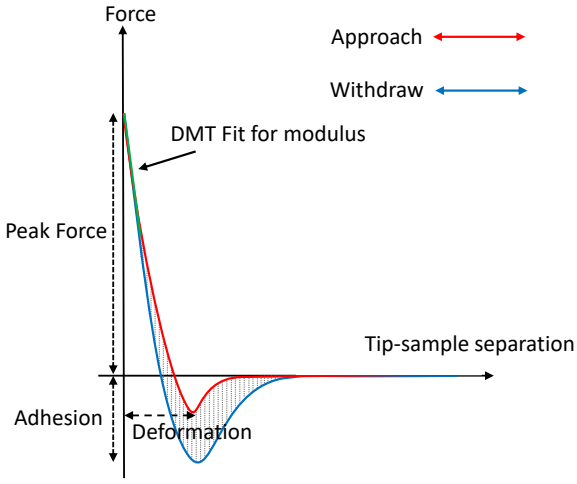

(a)

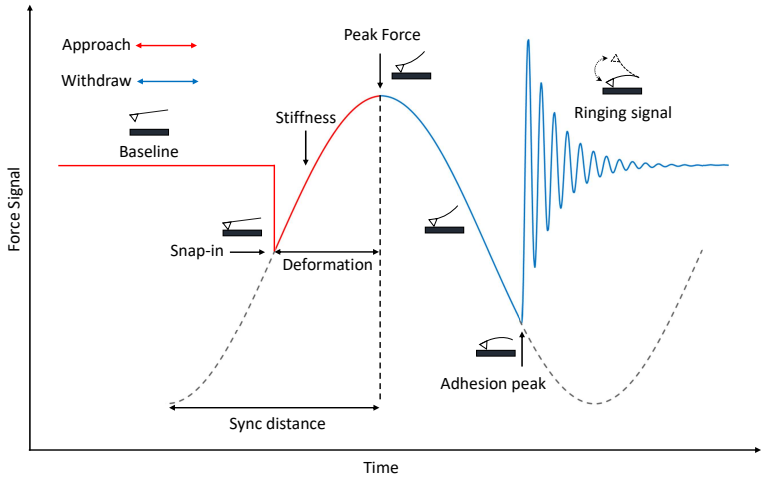

(b)

Figure 3.7: **Force curves for a PeakForce Tapping AFM measurement as function of Distance and Time.** (a) During every cycle: (red line) tip approaching the sample and (blue line) tip retracting from the sample, the curve can quantify: the surface forces, the mechanical deformation of the sample and its adhesion forces, and derive the elastic modulus (green curve) fitting the retract curve using the Derjaguin, Muller, Toropov (DMT) model, and energy dissipation (shadowed area). (b) Principle of PeakForce Tapping operation in a single tapping cycle with the tip trajectory depicted with the superposition of the tip displacement per every phase.

3.4 X-ray Photoelectron Spectroscopy (XPS)

X-ray Photoelectron Spectroscopy (XPS) is a technique that utilises the photoelectric effect to investigate the chemical composition of surfaces. It was developed in the mid-1960's by Prof. Kai Siegbahn and his research group at the University of Uppsala, for this technique Siegbahn obtained the Nobel Prize in 1981. XPS is a surface analysis method based on Einstein's Photoelectric law in which a monoenergetic X-ray source excites core-energy states of the sample entailing an inelastic scattering emission of electrons. From the analysis of the emitted electrons it is possible to identify the elements, their concentration in the sample composition and to get information about specific chemical environment where the species are.

3.4.1 Light-matter interaction

When multiple atoms combine chemically into a molecule, electrons of each atoms can be identified as core electrons or valence ones. The first ones belong to electronic orbitals close to the nucleus and are tightly bonded to this. As they are not involved in the interaction with the atoms participating in the chemical bond, they are considered associated to a specific atom. The latter ones, termed valence electrons, belong to the external electronic orbitals and contribute to the interaction and the bonding of atoms in the molecule. For this reason, the chemical bond involves a combination of valance orbitals between interacting atoms, described as a linear combination of atomic orbitals (LCAO) of the molecule: molecular orbitals are delocalized throughout the entire molecule rather than associated to single atoms. The discretization of the molecular orbitals due to the interaction of different atoms is described by the Frontier Molecular Orbitals Theory (FMOT), the orbitals are labelled as HOMO/LUMO, respectevely the highest occupied molecular orbitals and lowest unoccupied molecular orbitals. Considering both as sets of energy states, the closest filled levels to the Fermi level are conventionally labelled by a decreasing progression as HOMO, HOMO-1, HOMO-2 as the first empty unoccupied valence level termed by an increasing progression as LUMO, LUMO+1, LUMO+2. For a molecule, the Fermi level is conventionally considered as the energy level halfway between the HOMO and LUMO energy levels, as depicted in (Fig: 3.8).

In order to identify a type of atom and its concentration in the sample, the photoelectric emission has to occur from core level orbitals that is the only ones associated to that single atom. Thus, when a photon of energy $h\nu$, where h is the Planck's constant and ν is the photon frequency, interacts with a core level electron of an atom, if the energy transferred from the photon to the electron is high enough to excite the electron through the work function into free-electron-like states of the vacuum, the electron will be emitted with a kinetic energy of E_K. From the measurement of the E_K by a photoelectron spectrometer, the Binding Energy E_{BE}, regarded as the difference between the (n-1)-electron final state and the n-electron

initial state (Koopman's theory), can be calculated by the equation:

$$E_K = h\nu - E_{BE} - \phi_s \tag{3.9}$$

where energy $h\nu$ is the energy of the photon, ϕ_s is the work function of the surface that is the difference between the highest occupied state at the Fermi energy E_F and the free-space vacuum energy E_{vac}. As every chemical element has a unique set of binding energies between final and initial states, with their relative cross-sections, the analysis of the different kinetic energies determines the species and the concentration of each type of atom in the system.

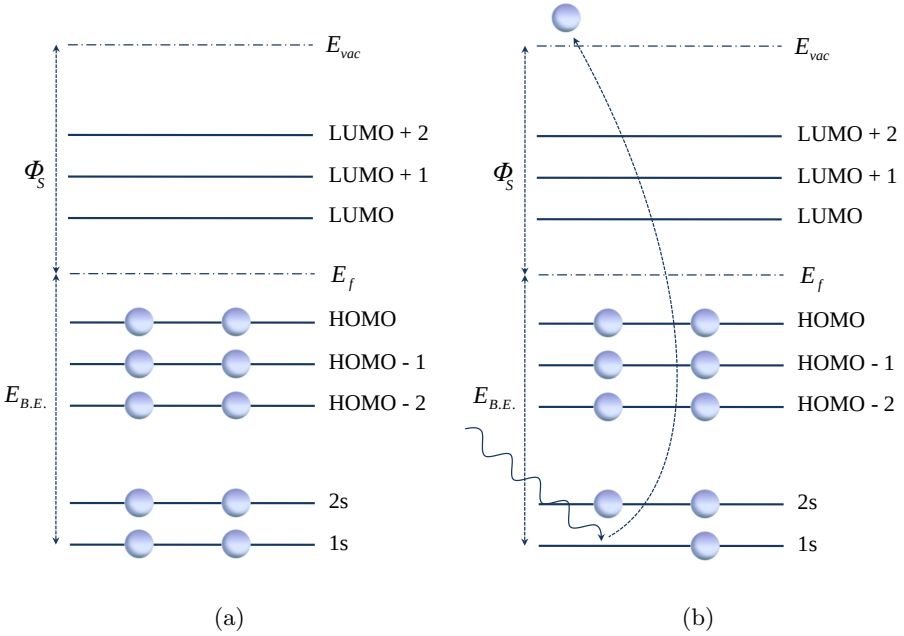

Figure 3.8: **Light-matter interaction in a molecule.** (a) Energy level diagram of a molecule. HOMO/LUMO orbitals, respectevely the highest occupied molecular orbitals and lowest unoccupied molecular orbitals, are due to the overlapping of neighbouring atoms orbitals, core levels belong to the specific atom. (b) Schematic depiction of a X-ray photoelectron emission from a molecular core-orbital.

3.4.2 XPS as a surface sensitive technique

The detection of a photoelectron can be prevented either by the kinetic energy loss of the photoelectron, due to inelastic scattering within the material, or through emission away from the photodetector. Considering inelastic mean free path (IMFP) of electrons the average distance travelled by an electron through a solid before it is inelastically scattered, the photoemission can be described as the probability of an electron not being inelastically

scattered while it reaches the surface and it is defined by the equation:

$$P(d) = e^{-\frac{d}{\lambda(E_K)}} \tag{3.10}$$

where d is the electron travelling distance and $\lambda(E_K)$ is the IMFP for the electrons of kinetic energy E_K which is usually displayed by the empirically derived plot, see (Fig: 3.9). The minimum of the plot is in a energy range of around (50 - 100) eV, so, according to the equation (Eq: 3.9), it is evident that the probability of an electron emission is maximized when the energy of the photon exceeds the free-space vacuum energy of ∼50 eV. For this reason X-rays, with a frequency range of (0.1 - 10) keV and (10 - >100) keV, respectevely for soft and hard X-rays, are the most common frequencies used for photoelectron spectroscopy.

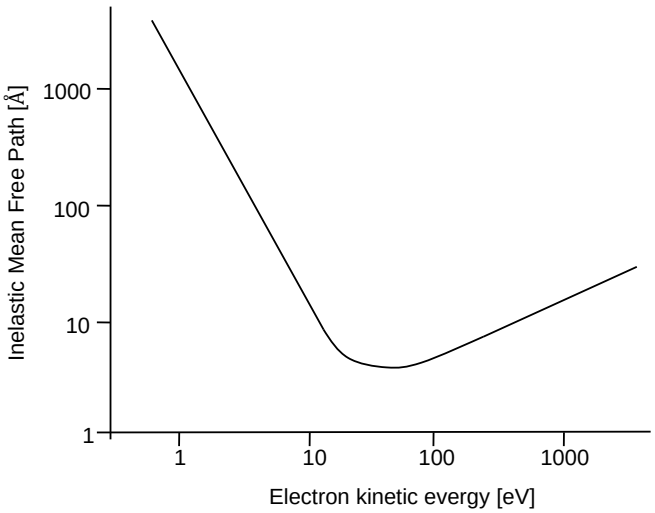

Figure 3.9: **Empirically derived "universal curve" of the dependence of the Inelastic Mean Free Path of a photoelectron in solids.**

According to the Equation (Eq: 3.10), the probability of an electron to escape from a material decreases with the photoelectron travelling distance, so even though the X-rays have a penetration depth in a solid of a few microns, only electrons ionized to depth of tens of Amstrongs can leave the surface without energy loss. For this reason XPS can be considered as a surface sensitive technique because, as surface electrons have the highest probability to be emitted, they are the main contribution to the XPS signal. In fact photoelectrons generated few atomic layer beneath the surface, still have enough energy to reach the free-electron-like states of the vacuum but they are detected as a background signal due to the energy loss for the high number of inelastic scattering events undergone,

consequently the probability of photoelectron emission of bulk material electrons is very low and the energy transferred from the X-ray photons to the electron is fully released in the solid either between electron-electron inelastic scattering or as phonon/plasmon excitation (the latter is the main scattering mechanism in metals).

3.4.3 X-Ray Photoelectron Spectroscopy

As discussed above, the ionization of a photoelectron from a core orbital of an atom due to a X-ray photon of energy $h\nu$ gives information about the binding energy E_{BE} of atom if the kinetic energy of the photoelectron E_K exceeds the free-space vacuum energy E_{vac} of the sample, see (Fig: 3.8: b) as described by the equation (Eq: 3.9). As in a real experiment the spectrometer that analyses the kinetic energies of the photoelectron is grounded with the sample, as shown in (Fig: 3.10), the spectrometer workfuncion must be taken into account and Einstein's photoelectric law becomes:

$$E_K = h\nu - E_{BE} - \phi_{sp} \tag{3.11}$$

where ϕ_{sp} is the workfunction of the spectrometer.

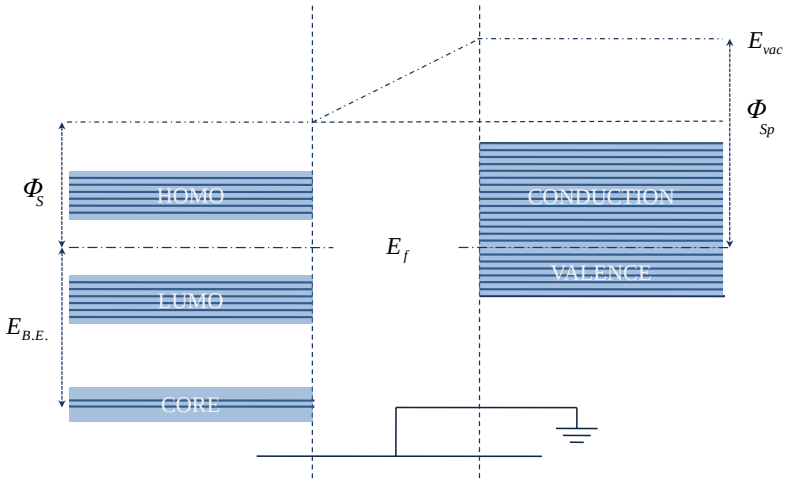

Figure 3.10: **Schematic depiction of the energy level structure of a molecular sample grounded with a X-ray spectrometer.** The photoelectron emission occurs only if the kinetic energy of the photoelectron is higher than the spectrometer work function, thus in the Einstein's Photoelectric law, spectrometer workfunction becomes more relevant rather than the sample one.

The XPS spectra of a sample is a series of sharp peaks according to the set of possible final states of ions associated to the binding energies of each element. The peaks are spaced as a function of their binding energies, taking the Fermi Energy as a reference: Fermi

level corresponds to the energy where the probability of an electron being present is $\frac{1}{2}$, by definition, and the height of the peaks are correlated to the abundance of the material present, and to the different cross-section of each final state that is the ionization probability of that type of atom. Since the mutual interaction of the electrons in an orbital, the atomic energy state is characterized by a total angular moment J as a combination $J = L + S$ of the orbital angular moment L and the spin S, the emission of an electron from an orbital causes a degeneration of the state (except for the s orbitals where L=0). In fact, depending on the value of the spin ($+\frac{1}{2}$ or $-\frac{1}{2}$) of the photoelectron, the total angular moment of the orbital could assume two different energies, such as $p_{\frac{1}{2}}/p_{\frac{3}{2}}$ for p orbital, $d_{\frac{3}{2}}/d_{\frac{5}{2}}$ for d orbital and $f_{\frac{5}{2}}/f_{\frac{7}{2}}$ for f orbital.
As described above, the XPS technique is a surface analysis able to identify the element and determine the concentration of each species in the sample. Moreover it gives information about the specific chemical environments that these type of atoms are in. In fact, the XPS measurement for a pure element is the analysis of the binding energy of core-level electron due to the nucleus attraction. For this reason, the XPS spectra of a pure element can be considered as the reference one. By contrast, the interaction of an atom with neighbouring different species clearly shows in the XPS spectra a chemical shift, that is an energy shift of the position of the peak respect to the reference one. In fact the atom affected by the electronegativity of the neighbouring species that changes the chemical potential and the polarizability of the compound, in the table (Tab: 3.1) are shown how different chemical enviroments can cause an energy shift of carbon peak 1s.

Species	**Binding Energy**
	[eV]
C=C	284.2
C-N	285.9±0.3
C-OH	286.5±0.2
C=O	287.8±0.2
C-F_2	292.6

Table 3.1: Chemical shift of the binding energy of C 1s peak as a function of the chemical environment [167].

A competitor process of the core level emission is the Auger electron emission, that is a relaxation process in which an electron is emitted to conserve energy released after a previous X-ray adsorbtion-ionization. It roughly occurs 10^{-14} s [168] after a previous event and it is observed in two different forms: the Auger spectator decay and the Auger partecipator decay. The first is the most common and it occurs after a X-ray photoelectron emission. The hole in the core level is filled by an electron dropped down from a higher energy level. The energy released during the process is absorbed by an unpaired electron of the same orbital

entailing the emission of the electron itself to the free-space vacuum.
If an electron, after a photon absorption, doesn't have enough kinetic energy to escape from the sample, an orbital transition from a core to a LUMO level occurs. Then, either similar to

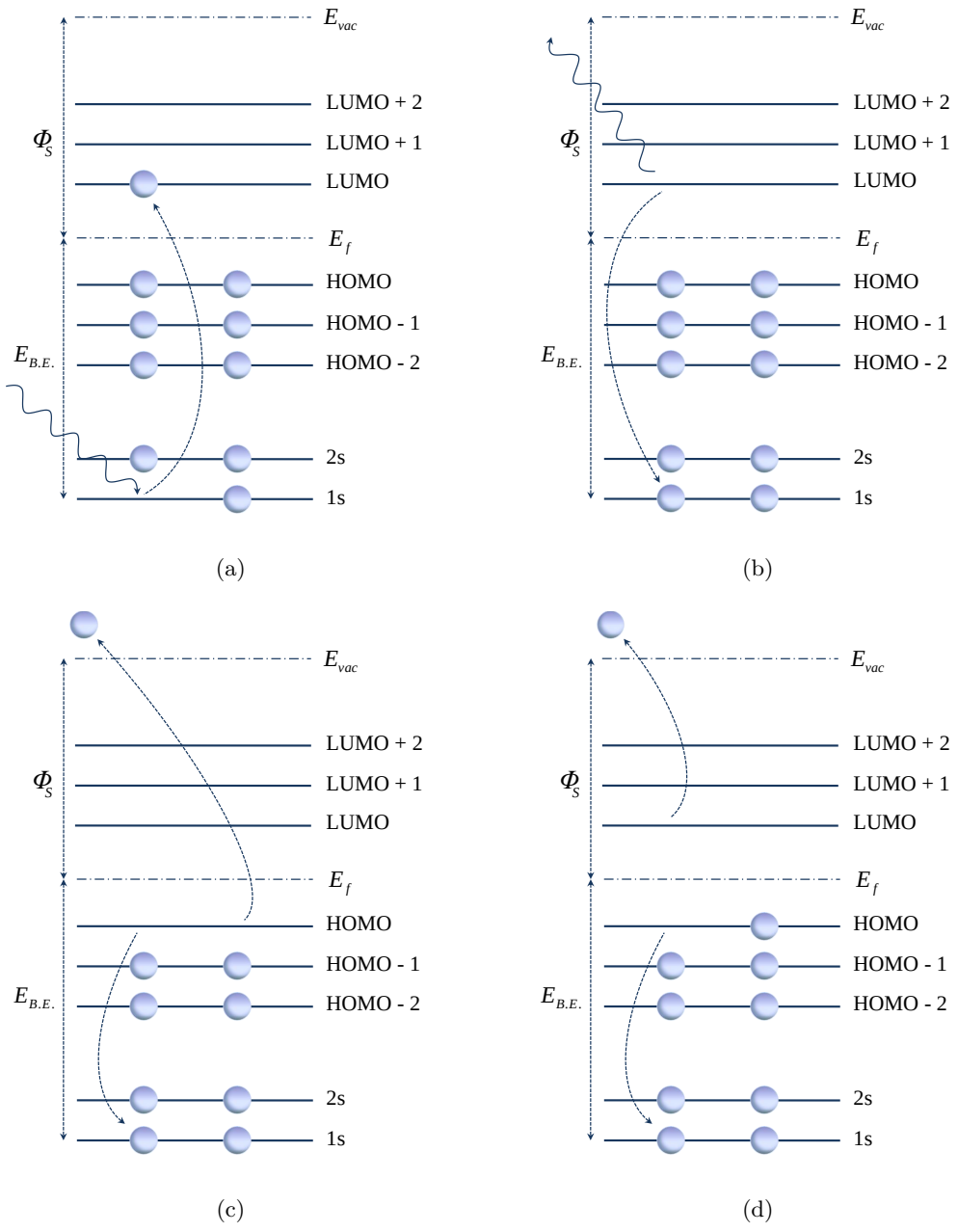

Figure 3.11: **Scheme of the different recombination paths.** (a) To a core level of an electron excited by a hν energy photon to a LUMO level. (b) The fluorescent X-ray emission . (c) The Auger spectator relaxation. (d) The Auger partecipator relaxation.

the Auger spectator relaxation, a HOMO electron drops down to the core hole and its energy released excites the electron from the LUMO level to the free-electron vacuum level or the

original electron does the reverse transition from the LUMO to the core level, resulting in a fluorescent emission. The processes are shown in (Fig: 3.11). These events are competing emissions but as light elements have a low cross-section the probability of an Auger electron emission is more common for element with a small atomic number rather than an X-ray photon emission which becomes predominant for elements with an atomic number > 35, see (Fig: 3.12).

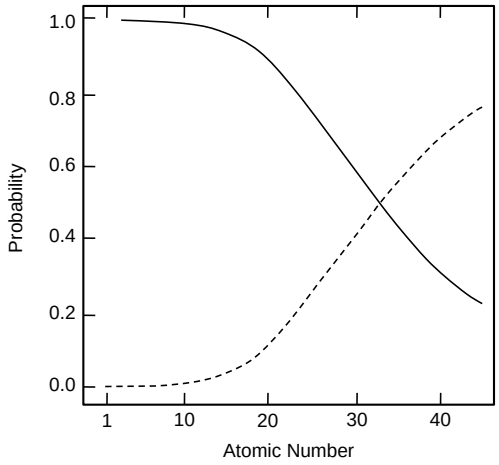

Figure 3.12: **Comparison of the probabilities of the Auger photoemission (continuous line) and the X-ray photoelectron emission (dotted line) as a function of atomic number of an atom.**

3.4.4 XPS setup

A Kratos AXIS instrument was used in this work for the XPS measurements. The schematic depiction of the three main components of the instrument is shown in (Fig: 3.13). The system uses two X-ray sources: an aluminium anode and a silver anode. Via thermionic emission, a filament emits electrons that are accelerated by a potential of approximately 15 kV on one of the anodes entailing an excitation of the its core-level electrons. The orbital recombination in the anodes causes a photon emission in the X-ray frequency range. The emission is monocromatic and has an energy of 1487 eV and 2984 eV respectevely for the aluminium and for the silver anode. The X-source is collimated on the sample entailing a photoelectron emission. The electrons are focused into the analyser by a lens column setup. The signal passes through a charge neutraliser which provides a source of low energy electrons to neutralise eventual positive charge built up on the surface of insulating samples, a set of apertures: (15, 27, 55, 110) μm used with a set of fixed sizes iris to perform selected

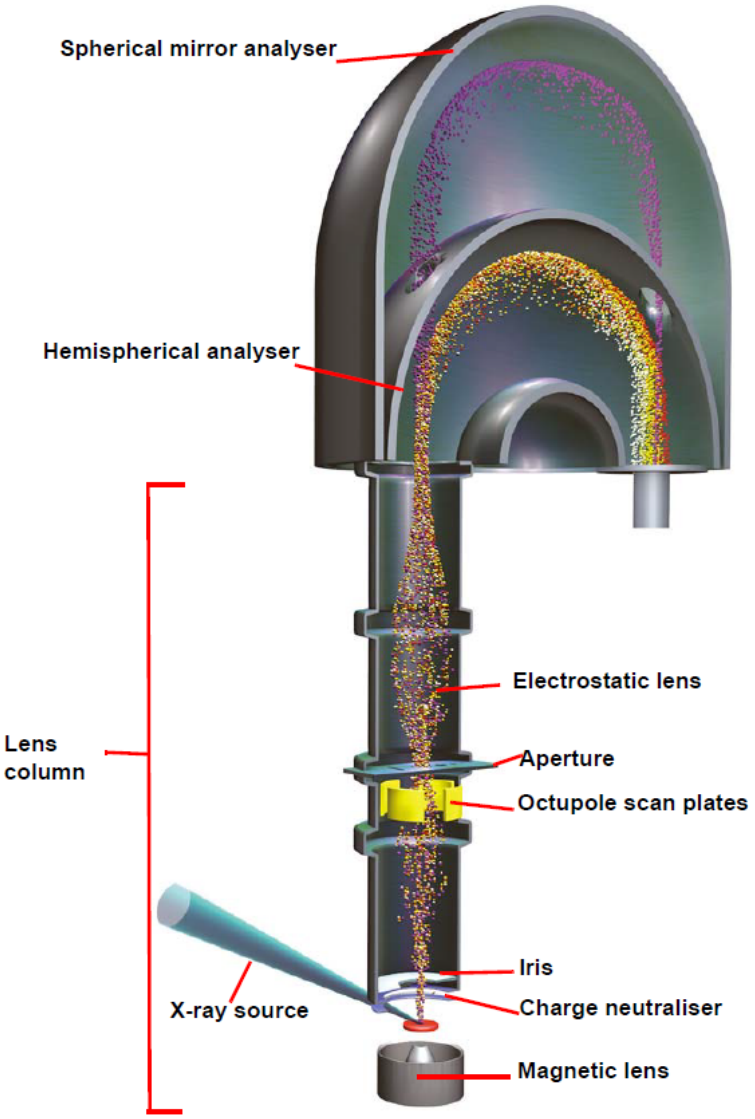

Figure 3.13: **Schematic depiction of a X-ray photoelectron analyser.** The three main components of a XPS analyser comprises: lens column, hemispherical analyser (HSA), spherical mirror analyser (SMA). Panel reproduced with permission from Kratos Axis Ultra XPS System manual.

area spectroscopy, an octupole scan plates that deflect the signal and are used to change the area of the sample analysed, an electrostatic lens which collimates the signal to the Hemispherical/Spherical mirror analyser. The Spherical mirror analyser gives information about the energy and the spacial 2D position of the photoelectron coming from the sample, for the measurements conducted in this work, this analyser wasn't used because all the data were collected by the Hemispherical analyser (HSA). HSA is biased by a potential positively in the inner emispheric plate and negatively in the external one in order to bend the electron path from the slit at the end of the lens column to the slit in front of the Delay Line Detector and preventing the collision with the walls of the HSA. The HSA works at a number of defined pass energies, so only photoelectron with energies higher than a threshold are effectively detected. Generally a small pass energy leads to spectra with a better energy resolution but a lower intensity. Conversely a higher pass energy leads to spectra with a wider energy spread with a lower resolution but a higher signal intensity. The delay-line detector linearly disperses the electron over its surface like a energy gradient as a function of the position, higher energy electrons are counted at one end of the DLD and to progressively lower energy to the other end. The counting of the electron events and their energy gives the spectra of the XPS signal.

3.4.5 Temperature programmed XPS measurement (TP-XPS) and data processing

In this research, XPS was mainly utilised to analyse the chemical regions of different elements as a function of the temperature. This kind of measurement, known as Temperature Programmed XPS (TP-XPS), consists of repeated sequences of spectroscopic acquisitions collected while the system ramps the sample temperature until a set value is reached. To perform this analysis, the sample is mounted on a Peltier stage, which, by thermoelectric effect, can cool/heat the sample in a temperature range of (-100 - +400) °C. Once the sample is in place, it can be loaded by a magazine into the first XPS vacuum chamber, the flexi-lock. In fact, to prevent any chemical contamination due to the ambient conditions, the XPS measurements are performed inside the main chamber exclusively under ultra-high vacuum conditions, in a pressure regime $< 10^{-10}$ mbar. To prevent the exposure of the main chamber to the ambient conditions, this environment is permanently pumped in a UHV regime by a scroll, turbo and ion pumps system similar to the one described in section (Sec: 3.2); it is separated from the flexi-lock by a gate valve. Hence, lowering the pressure in the flexi-lock until it reaches values $<10^{-9}$ mbar, the gate valve can be opened, and the sample transferred to the main chamber to start the measurement. In fact, it is inside this chamber that the analyser components: lens column, hemispherical analyser (HSA) and spherical mirror analyser (SMA) are allocated.
The actual TP-XPS measurement concerns a two-step settings procedure: the spectroscopic acquisition and the temperature program. The first step regards the preliminary instrument

setting by selecting the type of excitation source and its specific tuning mode, for example, which anode face is used, the X-ray size of the spot, and the emission current. Hence, as soon as the instrument is set, the actual measurement can be planned by choosing: the sample locations to examine, the chemical regions to inspect, therefore their energy range, and the resolution of the spectral peaks based on the sampling, the dwell time and the number of sweeps per region.

The next step is the temperature program setting, which requires choosing the starting and final temperatures and ramp rate. Generally, survey spectra that cover the whole energy region are collected at the beginning of every repeated sequence.

Once the measurement is completed, every spectral peak is firstly fit to determine its peak value and then processed by applying an energy correction to compensate for an eventual energy shift due to the sample charging. Generally, the standard uncharged binding energy of C 1S is taken as the reference to charge correct the other peaks. For the measurement attained on mica, the reference peak used was the Al 2p.

To better visualise the chemical variation as a function of the temperature, all the repeated acquisition per energy regions were plotted in a 3D colour map, where the abscissa axis displays the binding energy, and the ordinate axis, the temperature and colour variation represents the counts per second, that is the events per second measured by the detector, corresponding to the height of the peak, as it can be seen in (Fig: 3.14).

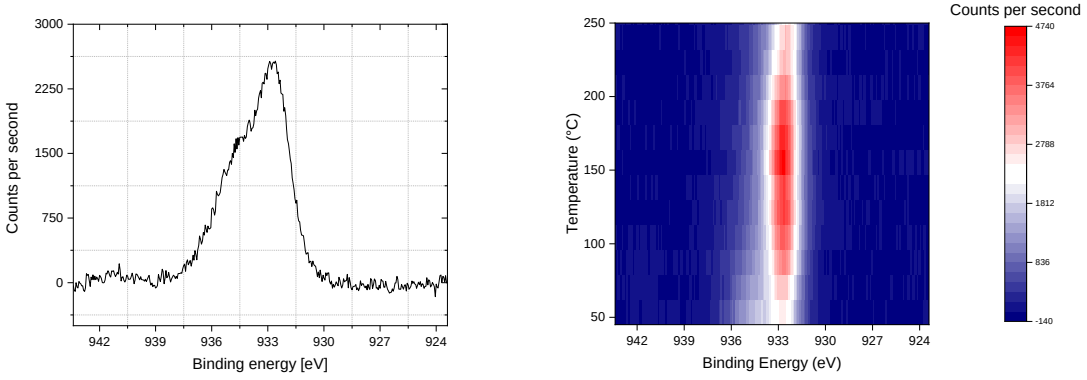

(a) (b)

Figure 3.14: **Examples of TP-XPS data.** (a) Single spectrum of the Cu 2P energy region collected at 50 °C. (b) 3D colour map of the whole set of repeated acquisitions collected in the Cu 2P energy region, ranging from 25 °C to 250 °C.

Chapter 4

'True' atomic resolution with AFM

Historically, the development of the AFM technique closely followed that of atomic resolution scanning tunnelling microscopy (STM), driven by the desire to obtain new information that STM can not provide. Hence, according to the definition of Gan [169], the ultimate goal of the AFM technique was to obtain resolution capable of resolving single or multiple atomic-scale features separated by atomic-scale distances. Achieving this goal required years of research pushing the limits of this technique to finally obtain sub-molecular and atomic resolution, which it is summarised here.

4.1 First steps of atomic force microscopy: lattice and atomic resolution in contact mode AFM

Almost ten years after the invention of the scanning tunnelling microscope (STM) by Binnig and Rohrer [10], the atomic force microscope (AFM) was developed to overcome the limitation of STM to conductive samples [11]. Soon afterwards, two different groups claimed for the first time the achievement of atomic resolution showing, with this new scanning technique, perfect crystal lattices [170, 171]. However, these results were quickly disproved, as the perfect crystal lattice images were due to tip-flattening artefacts. Scanning the sample in contact mode operation, the tip-sample interaction results as the average of the forces between the several atoms at the interface. Consequently, individual atomic features can't be detected. For this reason, these are identified as pseudo-atomic or lattice-resolution images. An analogy to picture the blunt tip artefact of lattice resolution is the pulling of a Lego® brick over another identical one except for a missing pin. The vacancy cannot be identified by the perfect brick sliding over the defective one, even though the lattice can be identified, see (Fig: 4.1).
However, there are a few cases where contact mode AFM can attain atomic resolution. In 1993, Binnig and Ohnesorge, scanning a layer of (10$\bar{1}$4) calcite in water, resolved the individual unit cells at the step edge of two monoatomic terraces. Working in the

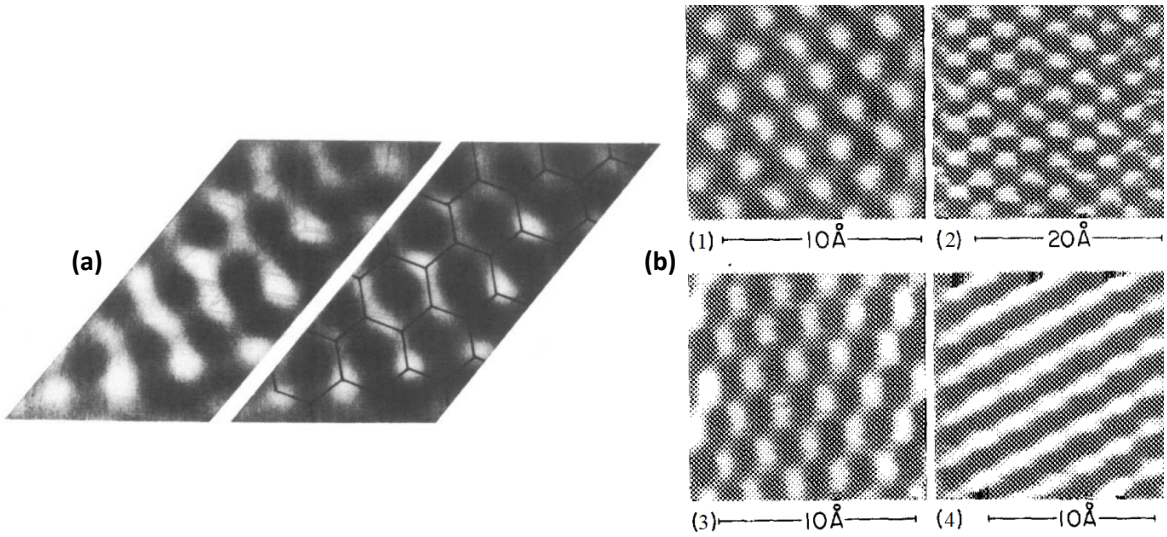

Figure 4.1: **Pseudo-atomic or lattice resolution images.** (a)Thermal drift corrected AFM image of a graphite lattice, partially superimposed to highlight the pattern. (b) AFM images of (1) graphite, (2) molybdenum disulfide, and (3) boron nitride. (4) Lattice resolution disappearance of boron nitride due to a tip-sample multiple contact effect. (a) Panel adapted with permission from ref [170]. (b) Panel adapted with permission from ref [171].

attractive-force regime, at tip-sample forces of the order of 10^{-11} N, they proved that an atomic force microscope could achieve atomic resolutions. Due to this, they coined the definition *'True' atomic resolution* [12]. Similar results were achieved a few years later in air, on the (0001) cleavage plane of 2H-$NbSe_2$ by Schimmel [172], see (Fig: 4.2). Almost at the same time with Binnig and Ohnesorge, the true atomic resolution was also demonstrated for a KBr crystal in UHV condition by Giessibl [13].

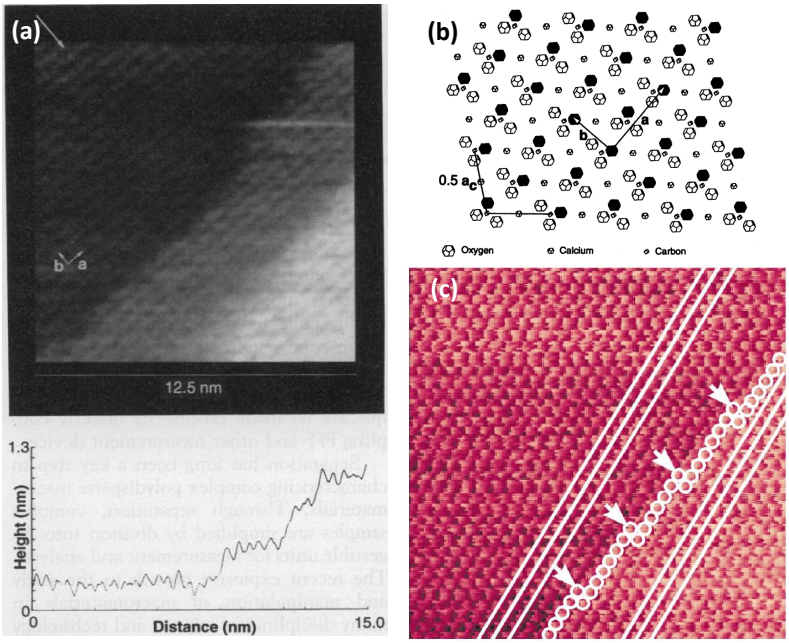

Figure 4.2: **First evidence of 'true' atomic resolution.** (a) AFM image of monoatomic and diatomic steps of calcite, and its line profile, measured along the direction of the arrow, from the left upper corner to the lower right one. The heights of the monoatomic kinked steps are in a range of (2.7-3.3) Å; this matches the theoretical value of 3.316 Åsingle unit cells. (b) Schematic representation of the $(10\underline{1}4)$ cleavage plane of the calcite imaged in (a). (c) AFM image of the (0001) cleavage plane of 2H-$NbSe_2$: the white lines and circles indicate the atomic rows and the position of the step edges, respectively. In both AFM images, the presence of kink sites (white arrows in (c)) at the step-edge represent point defects, which is evidence of true atomic resolution. (a, b) Panels adapted with permission from ref [12]. (c) Panel adapted with permission from ref [172].

4.2 True atomic resolution: the limitation of NC-AFM technique

Even though the initial results obtained by the AFM operated in contact mode, the technique showed several limitations: the impossibility of using the method with soft samples, the high chances to blunt or contaminate the tip, the infeasibility of discriminating long and short-range tip-sample interactions. However, with the introduction of the non-contact atomic force microscopy (NC-AFM) operation, a technique capable of detecting short-range interaction forces, most of these issues were overcome. The major drawback of the technique was the achievement of an atomic-level resolution possible only under UHV conditions. In fact, the lateral resolution is highly reduced in ambient, as the tip needs to be kept relatively far from the surface to prevent the capillary effects due to the adsorbed water layer over the sample. The first key articles on true atomic resolution with the NC-AFM technique were by Giessibl [173], by Kitamura and Iwatsuki [174], and by Ueyama [175]. Published less than a week apart, the first two studies aimed to prove the effectiveness of NC-AFM under UHV conditions, showing the atomic resolution of Si(111) reconstructed surface, measured by a Frequency Modulation AFM technique. Modifying the cantilever: Giessibl reduced the tip beam, and Kitamura increased the stiffness, performing true atomic resolution. In particular, they could measure the ∼1 Ådeep corner-holes of silicon(111)-(7×7) unit cell. On the other hand, Ueyama showed the vacancies in a quasi-one-dimensional zig-zag chain of an InP(110) surface.

Three different regions characterised the original image of Giessibl. The first one showed the crystalline structure of the surface (lattice resolution) due to the average between long and short-range forces interacting probably with multiple apexes tip. The second one was completely blurred, and the third one detected the 7×7 dimer-adatom-stacking fault (DAS) reconstructing the surface of Si(111). However, due to the limit of the technique, the true atomic resolution was possible only in the vertical direction but prevented in the lateral one: [6 Ålateral resolution, 0.1 Åvertical resolution] [173], similarly for Ueyama, the atomic defects were well resolved, but the alternating of In and P atoms in the quasi-one-dimensional chain was not, see (Fig: 4.3).

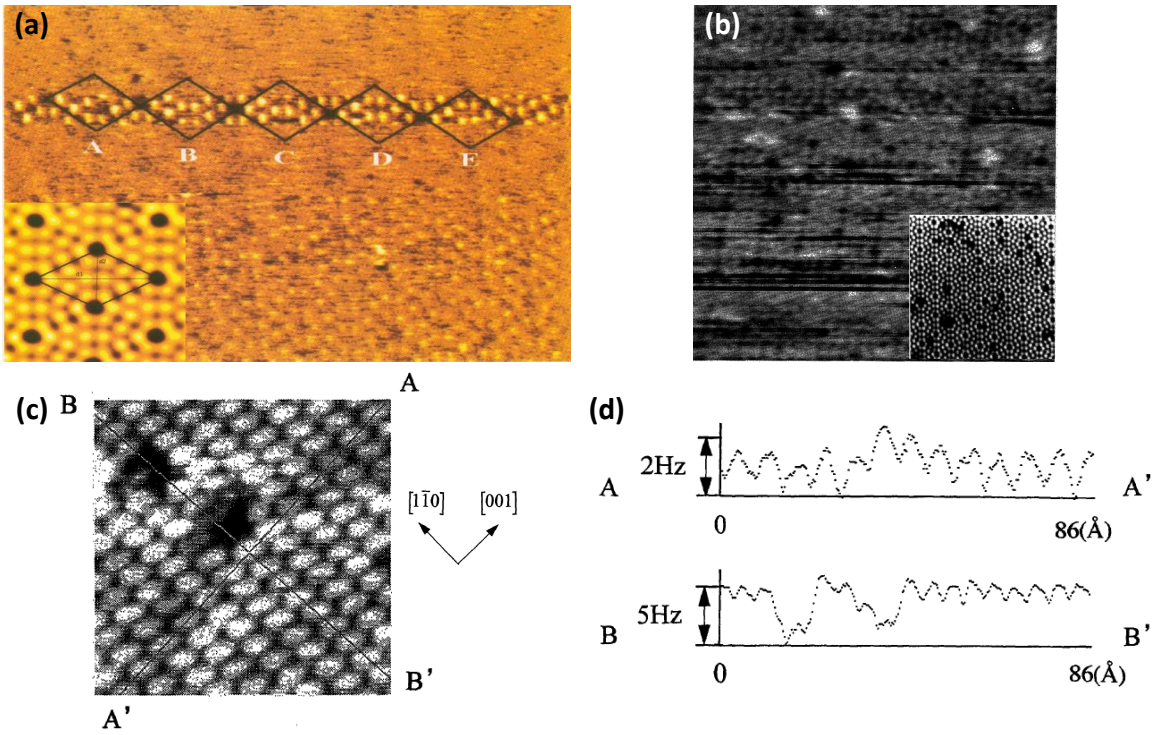

Figure 4.3: **True atomic resolution with NC-AFM in UHV conditions.** (a) True atomic resolution of silicon(111)-(7×7) unit cells corner-holes. The dimensions of the unit cell are comparable with the STM image pictured in the sub-panel. A multiple apex tip phenomenon could cause the resolution loss of the lower part of the image due to surface contaminants. (b) Besides the image results being blurred, few areas reproduce the Si(111)-(7×7) structure shown in the STM image sub-panel. The presence of the central corner holes surrounded by the Si atoms proves the true atomic resolution. (c) Atomic defects image of an InP(110) surface (dark spots), the two vacancies are highlighted by the frequency shift differences between the (d) two line profiles along the cross-sections A-A' and B-B'. (a) Panel adapted with permission from ref [173]. (b) Panel adapted with permission from ref [174]. (c, d) Panel adapted with permission from ref [175]

4.3 How to achieve atomic resolution

With the advent of the first atomically resolved images, many researches were focused on determining the conditions, establishing the criteria necessary for realising and replicating true atomic resolution, and overcoming the limitation of the scanning technique up to date. Heuberger *et al.* showed how the tip-sample elastic deformation limits the AFM capability to image at true atomic resolution and how elastic deformations can be used to measure local elastic properties of a sample [176]. Buldum *et al.* investigated the nature of tip-sample forces giving an interpretation of long-range van der Waals interatomic interaction calculated for different types of tip apex [177]. Weih *et al.* also studied methods for improving the lateral resolution as a function of applied force, tip radius, adhesive force, and tip and film properties, particularly for soft samples [178]. Based on the hypothesis of Giessibl that the short-range covalent bonding was responsible for the true atomic resolution of his images, the theoretical confirmation of this assumption occurred two years later by Perez *et al.* [179, 180]. Furthermore, Sokolov *et al.* developed model simulations for the correct interpretation of raw atomically resolved images gained by a commercial AFM under non-vacuum conditions [181], and derived a critical force of single nanonewtons for atomic resolution confirmed by experimental evidences [182, 183].
This new theoretical background laid the groundwork for future research about atomic resolution, whose major results are ascribed to: the performance of atomic force microscopy in frequency mode operation (FM-AFM) using a force sensor based on a quartz tuning fork (qPlus sensor), and the tip functionalisation by the atomic or molecular mediator for the study of organic samples.

4.4 Experimental evidence of true atomic resolution based on the implementation of a qPlus sensor in FM-AFM

Rather than using an optical sensor to detect the cantilever deflection, Giessibl, in his precursory research [173], decided to use a force sensing cantilever (CL) based on a quartz tuning fork [170]. Different from the micro-machined silicon cantilevers, the detection method of a qPlus sensor is self-sensing due to the intrinsic piezoelectricity of the material. The working principle of a frequency mode AFM integrating a qPlus sensor is based on the signal-frequency shift from the cantilever natural driving eigenfrequency as a function of the tip-sample interaction. Therefore, the deconvolution of the forces, particularly the short-range interactions, from the frequency shift and the calculation of the different noise contributions: thermal, deflection detector, oscillator, and frequency shift noise, let to determine the signal-to-noise ratio. The maximisation of the signal-to-noise ratio that can be expressed as a function of three parameters: stiffness k, eigenfrequency f_0 and quality factor Q [184], improves the spatial and the force resolution. Hence, as demonstrated in

1997 by Giessibl [185], in first approximation, high values of Q and spring constant and the minimisation of the oscillation amplitude are fundamental conditions for atomic-resolved imaging.

As the three key parameters are intrinsically dependent on the characteristics of the qPlus sensor and its integration in an FM-AFM operation, the majority of the studies to improve resolution by this setup were mainly focused on exploring the potentiality of the microscope, such as the design and the fabrication of different generations of cantilevers, the improvement of the electronic, the signal amplification and the sensor excitation for attaining low detector noise and reduce the creep, furthermore the theoretical and experimental calculation of noise sources and their minimisation. However, as an accurate review of these technical aspects of the instrumental improvement and development would fall outside the aim of the chapter, please refer to [186] for an exhaustive analysis of the topic.

Since the preliminary studies, the implementation of self-sensing devices, such as the qPlus sensor, seemed to embody the ideal tool to study matter at its atomic level. Due to its versatility, it can get atomic resolutions in UHV and liquid/ambient, even with highly different environmental conditions. In fact, considering a sample under UHV conditions, the Q factor is high and doesn't change during the measurement. By contrast, under ambient conditions, the presence of a water layer covering the sample causes a damping effect on the cantilever entailing a significant variation of the Q factor; while in liquid, where the Q factor is generally low, its variation, even though present, it is highly reduced. Furthermore, in ambient the presence of contaminants, due to the absorption/desorption of atoms and molecules over the surface in a time scale shorter than the AFM imaging time, often prevent the detection of atomic features.

Besides, in ambient, the oscillating amplitude of the cantilever needs to be higher, often by orders of magnitude, to let the tip penetrate through the water layer over the sample, increasing the measurement instability. Furthermore, due to the environmental conditions in which the measurement is carried out, the thermal fluctuations are an additional noise source. However, contrary to liquid and ambient measurements, the possibility of cooling down a sample to ultra-low temperatures in a UHV chamber using liquid nitrogen massively reduces any thermal noise augmenting the chances of true atomic resolution.

So, as said before, the qPlus sensor integrated into an FM-AFM achieved atomic resolution under UHV, liquid and ambient conditions. In fact, in the last 20 years, over 1000 publications showed important results about atomic resolution obtained by this technique. In 2000, only two years after the development of the qPlus sensor development, Lantz *et al.* [187] reported the resolution of a Si(111)-(7×7) unit cell in an ultra-high vacuum at liquid helium temperature (4 K), see (Fig: 4.4. a,b). The result was confirmed in 2002 by Eguchi [188], and one year later, Hembacher *et al.* resolved the unit cells of graphite [189], showing a better resolution than STM measurements used in the same conditions. In addition to this, the resolution of the unit cell achieved by Lantz *et al.* was also obtained in UHV conditions and at room temperature by Giessbl *et al.* [190], see (Fig: 4.4. c). Other room temperature

UHV experiments reported significant results examining insulators such as $CaF_2(111)$ [191] and NiO(100) [192].

The first example of true atomic resolution achieved in liquid with a qPlus sensor used

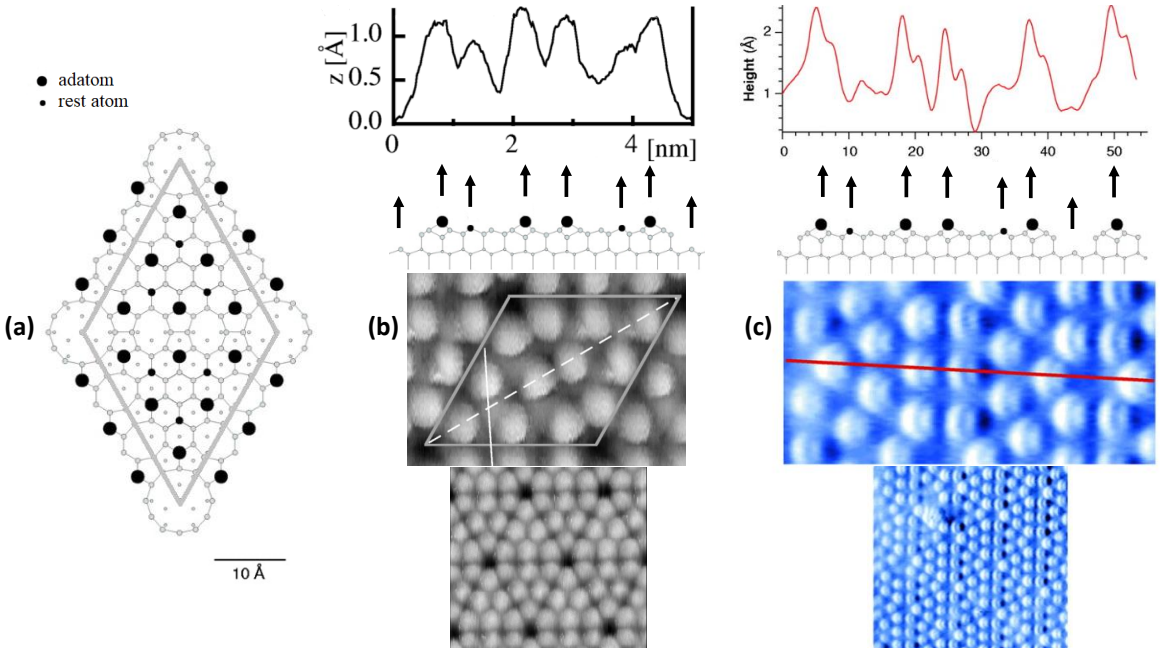

Figure 4.4: **True atomic resolution under UHV condition of a Si(111)-(7×7) surface acquired by qPlus sensor.** (a) Schematic representation of dimer-adatom-stacking fault (DAS) model of the Si(111)-(7×7) surface (top view) [193]. (b, c) AFM topographies and line profiles from the researches [187], and [190], respectively. The side views of (a) underneath the plots are an eye guide for the respective positions and height differences of corner holes, rest atoms and adatoms represented by the line profile features. (b) The measurement was carried out at 4 K, registering a corner-hole depth of ∼120 pm using an amplitude of A= 5 nm. (c) The measurement was carried out at room temperature, registering a corner-hole depth of ∼180 pm using an amplitude of A= 0.8 nm. This result is similar to the value recorded by Uchihashi *et al.* of ∼180 pm [194]. (a) Panels adapted with permission from ref [187]. (b) Panels adapted with permission from ref [190].

in FM-AFM operation was demonstrated by Ichii *et al.* scanning a mica surface in KCl aqueous solutions, and ionic solutions liquids [195]. However, other atomic evidence had been demonstrated before: by Ohnesorge and Binnig in 1993, using quasi-static AFM for a muscovite mica surface in water [12], by Hoogenbooma performing quantitative dynamic-mode scanning force microscopy measurement on the same sample in water [196], and by Rode *et al.* operating an FM-AFM on a calcite ($CaCO_3$) cleavage plane in 1M KCl solution, and Milli-Q water [197].

Using high stiffness cantilevers allows driving the tip at small amplitudes, implying, therefore, high Q factors. This method produces high-definition imaging and reduces the chance of damaging or deforming the sensitive surface of the samples. Hence, by a high stiffness qPlus sensor, Purckhauer *et al.*, both showed molecular resolution of lipid bilayers immobilised on mica and measured in buffer solution, and imaged of triangular shaped DNA origami [198, 199]. Similar results on the biological sample were obtained with soft silicon cantilevers

and optical detection [200–202], see (Fig: 4.5).

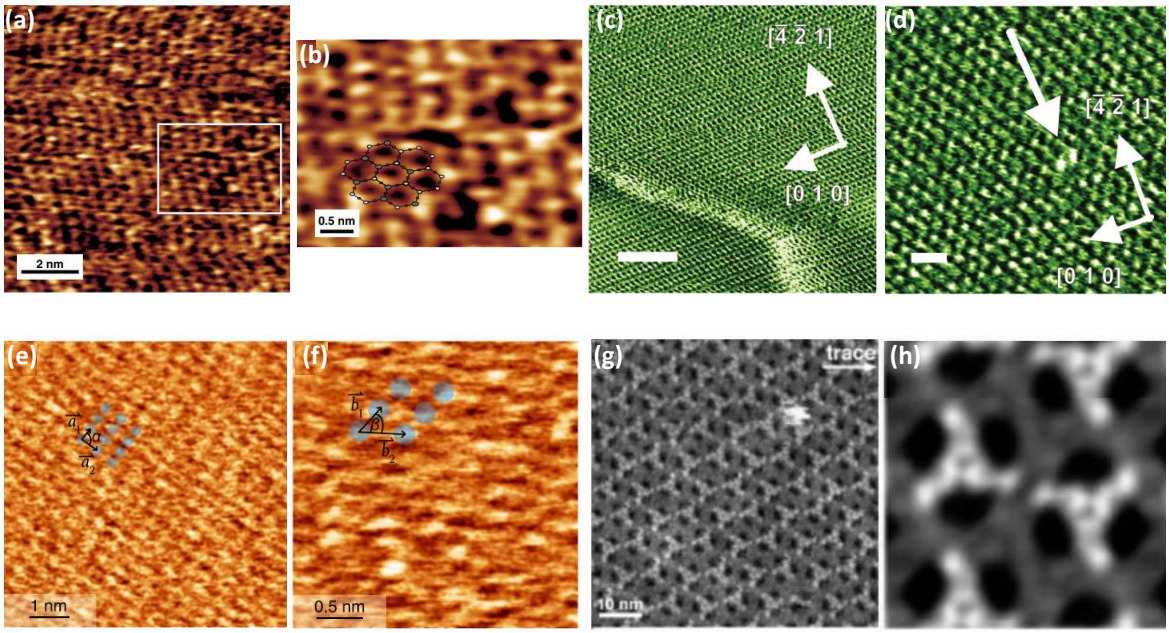

Figure 4.5: **True atomic resolution in liquid performed by force sensing (a-d) and by optical detection (e-h).** (a) First evidence of an atomically resolved image of a cleaved mica surface in ionic liquid (EMI-AcO). (b) Enlarged image of the white rectangular area from panel (a), a schematic model of the side view of the mica crystal lattice is superimposed to highlight the structure resolved. (c, d) Topography of (10$\underline{1}$4) calcite in Milli-Q water. The kink sites at the step edges in panel (c) and the atomic-scale defect on the surface in panel (d) demonstrate the true atomic resolution. (e, f) High-resolution image of a lipid bilayer adsorbed on mica and measured in buffer solution. The superimposed blue dots highlight the headgroup positions of the lipids.(g, h) High-resolution AFM image of the periplasmic surface of native OmpF porin in solution. The symmetrised image highlights the sub-molecular resolution. (a, b) Panels adapted with permission from ref [195]. (c, d) Panels adapted with permission from ref [197]. (e, f) Panels adapted with permission from ref [198]. (g, h) Panels adapted with permission from ref [202].

More recently, the true atomic resolution of samples in liquid has been proved by implementing different techniques, such as bimodal AFM. Exciting the qPlus sensor simultaneously at the fundamental and second flexural mode, Ooe *et al.* attained atomic resolution images of KBr(100) for both of the modes [203]. Furthermore, by the application of the 3D-AFM scanning method, Uhlig *et al.* analysed the crystal lattice of WSe_2, hBN, and HOPG in water [204], see (Fig: 4.6).

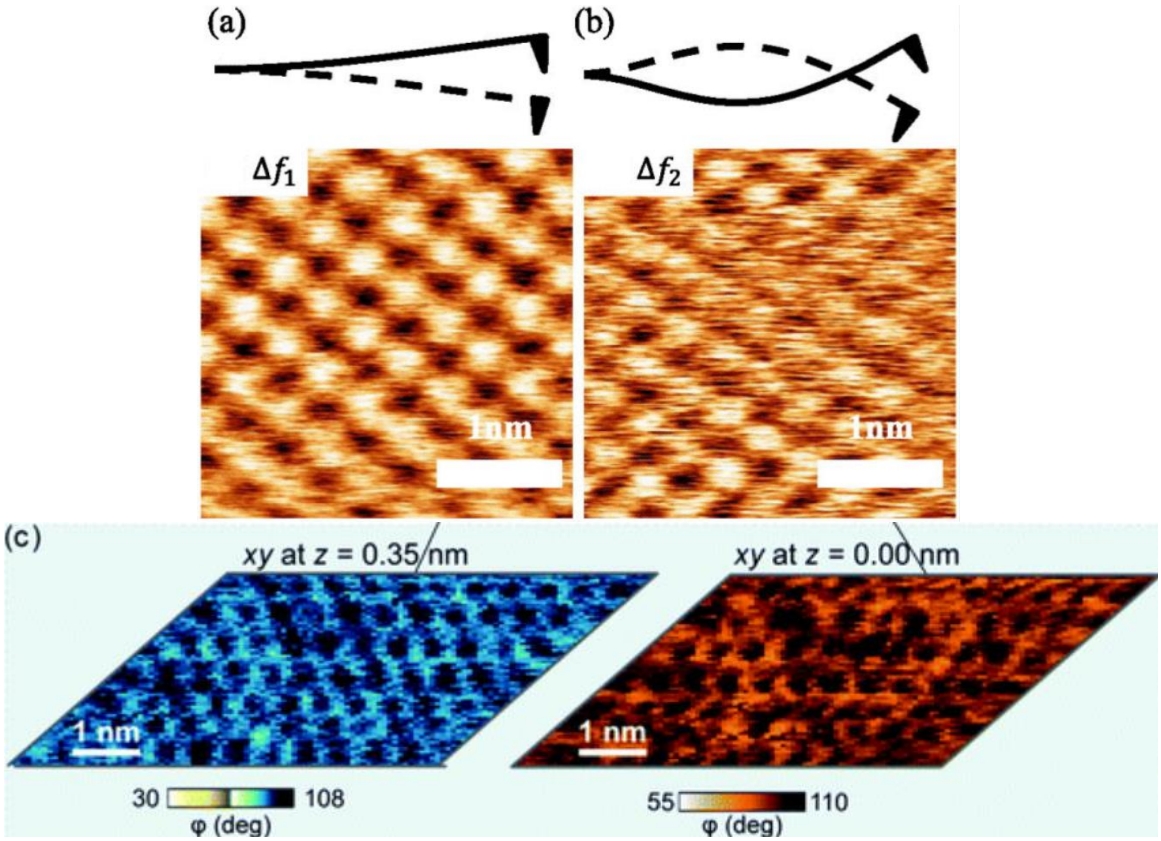

Figure 4.6: **True atomic resolution at solid-liquid interfaces performed with alternative techniques**. (a, b) KBr(100) images operating bimodal AFM mode. The height maps obtained decoupling the (a) first and (b) second flexural mode. A schematic motion of the tip for each flexural mode is placed upon the topographies. (c) 2D maps of the mica–water interface acquired by the 3D AFM technique. The maps represent the phase shift of the tip as a function of the its position, and imaging of the sample in the x-y plane (parallel to the mica surface) was carried out at different heights. For the blue map, z= 0.35 nm, and the orange one at z= 0.00 nm. (a, b) Panels adapted with permission from ref [203]. (c) Panel adapted with permission from ref [204].

More than a decade after the first results in UHV, a true atomic resolution was also obtained under ambient conditions. Calculating how the frequency shift and the drive voltage versus distance changes as a function of the water layer adsorbed over the sample, Wastl *et al.* determined the atomic resolution of the KBr lattice [205]. Similar high-resolutions were obtained few years later for graphene [206], calcite [207], and mica [199] surfaces in ambient, see (Fig: 4.7).

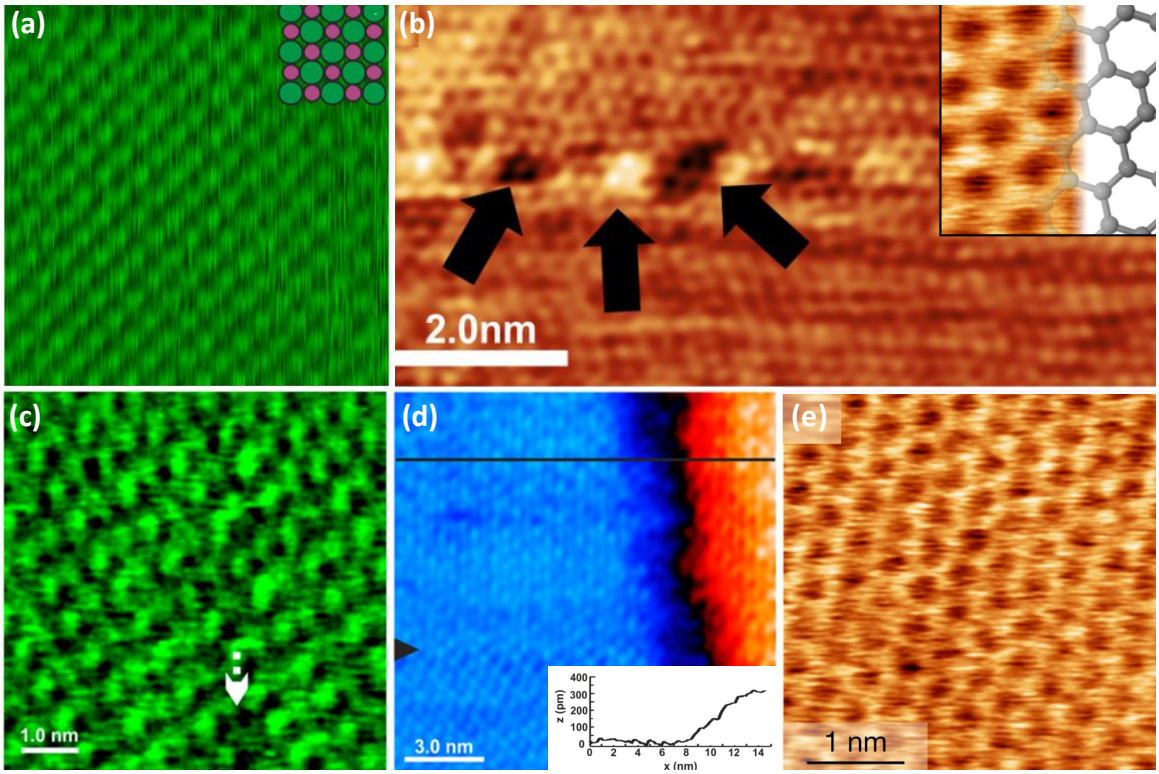

Figure 4.7: **True atomic resolution under ambient condition acquired by qPlus sensor**. (a) Atomically resolved topography of a KBr(100) cleavage plane measured with a bulk sapphire tip. The model of the crystal lattice in the inset box shows Br^- (green) and K^+ ions (purple). (b) Atomic-size defects resolution of a HOPG surface acquired by a silicon tip. In the inset box, a higher resolution of the HOPG lattice compared with its schematic model of the crystal lattice. (c, d) Height maps of $(10\underline{1}4)$ single calcite terrace and diatomic steps (see the line profile in the inset box), respectively. The vacancy of an oxygen atom, highlighted by the white arrow, in the zig-zag structure and the kink sites at the step edges confirm the atomic resolution of the topographies. The black arrow in (d) marks a tip change. (e) True atomic resolution of the honeycomb lattice of muscovite mica. (a) Panels adapted with permission from ref [205]. (b) Panels adapted with permission from ref [206]. (c, d) Panel adapted with permission from ref [207]. (e) Panel adapted with permission from ref [199].

Albeit the crucial results attained since the early '90s, the research of high-resolution images of molecular systems was almost completely unexplored for almost 20 years. This, until the first image of a pentacene [14] was resolved at the sub-molecular level, that is, the corresponding true atomic resolution capability for molecular samples, i.e. adsorbed molecules deposited on a substrate.

4.5 Theoretical and experimental evidence of short-range interactions based on tip modification: the sub-molecular resolution of organic structures

As previously described by Ohnesorge and Binnig, imaging atomic defects in the lattice is evidence of true atomic resolution. Their research was ascribed to a single atom protruding from the rest of the tip, attaining a short-range interaction with the atoms of the surface. The interpretation of the relationship between true atomic resolution and the protruding atom was explained by Perez, who simulated the interaction of a four silicon atoms tip with a Si(111) surface [179]. Comparing the density functional theory (DFT) of a four atoms tip with another one in which additional hydrogens terminated the external atoms in the base of the tip, the result of this saturation showed how the Si-H bonds hybridised the four atoms tip to a state similar to the bulk sp3, yielding the protrusion of a dangling bond from the apex of the tip directed towards the Si(111) surface. Covalent bonding would form, entailing a strong vertical tip-sample interaction, by positioning the tip directly above the highly reactive unsaturated bonds of the substrate adatoms pointing out of the surface. Only the strong localisation of the electronic density for a dangling bond terminated tip could trace the atomic corrugations of the sample, overcoming the contribution of long-range interaction in this way. The DFT simulations of the AFM tip [180] corroborated by the preliminary experimental studies based on these simulations, showed the potentiality of the tip modification for high-resolution AFM measurements, exploring the interaction of the dangling bond tip with several materials such as metals [208, 209], insulators [210, 211], polar surfaces [212–214] and graphene-like structures [215].

Hence, in 2009, Gross *et al.* combined capability of the qPlus sensor with the potentiality of a dangling bond terminated tip and demonstrated the first sub-molecular AFM image. Functionalising with a CO molecule the metal tip of a qPlus tuning force integrated into a non-contact AFM, Gross could resolve the intermolecular structure of a pentacene molecule at a temperature of 5 K and under UHV conditions [14], see (Fig: 4.8).

This discovery opened a new field covering insight into molecular geometry, aromaticity, chemistry, bond length, and connectivity.

The working principle of the measurement was based on two main features: the geometrical dimensions of the tip and its chemical passivation. Placing a CO molecule at the apex of the standard silicon tip, the CO-mediator can be considered a single-atom tip due to its very sharp termination. Its radius of curvature is akin to the atom of oxygen. Contrary to the very reactive dangling bond tip reported by Perez, the CO-terminated tip is essentially chemically inert. Its passivation enables it to bring the tip so close to the adsorbed molecule, passing through the attractive interaction regime without bonding and reaching the short-range regime, which is the repulsive one. Long-range forces are still dominant compared to Pauli's repulsion. However, the attractive force components tend to vary much more slowly than

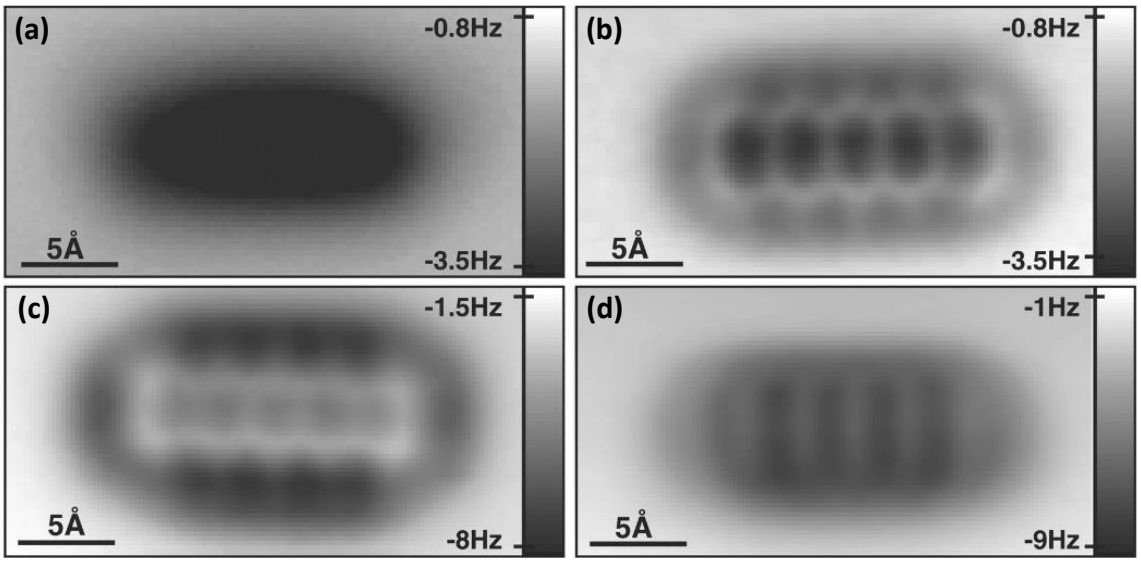

(a)

Figure 4.8: **First sub-molecular resolution images obtained by tip-mediator technique.** Topographies of pentacene on NaCl(2ML)/Cu(111) in UHV condition at 4 K, different resolutions are due to the kind of mediator used for the measurement: (a) Ag tip. (b) CO tip. (c) Cl tip. (d) Pentacene tip. (a-d) Panels reprinted with permission from ref [14].

the repulsive ones and only contribute an attractive background force.

After this fundamental milestone, in the last ten years, the functionalised tip technique massively evolved: other atoms or molecules were used to terminate the AFM tips, such as Ar/Au, Cl, I, Br, O, N or more complex molecules such as breitfussin A and B [216]. It was also showed that the method is practicable at a higher temperature; noteworthy results are the images of C_{60} and pentacene molecules at 77 K attained by Moreno *et al.* [217], the resolution of intramolecular and intermolecular force contrast of NTCDI molecule at 78 K by Sweetman *et al.* [149, 218], of the PTCDA molecules adsorbed on an Ag/Si(111)-($\sqrt{3} \times \sqrt{3}$) surface at Room Temperature by both Iwata *et al.* and Huber *et al.* a[219, 220]. Further high-resolution evidence was demonstrated on different substrates such as highly-reactive Si(111)-7×7 [149, 221], and chemical passivated Ag:Si(111) [218], see (Fig: 4.9).

Finally, the sub-molecular resolution was also achieved for non-planar molecules and molecules during a chemical reaction. The technique capability was limited to the high resolution imaging of the adsorbants, and evidence of chemical and structural model identification of the molecules was reported. Gross *et al.* showed how it is possible to identify the type of order for intramolecular carbon-carbon bonds based on their length or, in some cases, on their brightness [222] — the longer or brighter the bond within aromatic hydrocarbons, the higher the order of the bonds. Mohn *et al.* showed how the covalent bond between a gold atom and a molecule of PTCDA could be reversed by changing the molecule geometry and using the metal-molecule complex as a molecular switch [17]. Clearly there has been remarkable progress in high resolution imaging with this technique, however, one of the major remaining barriers appears to be conducting measurements under ambient conditions.

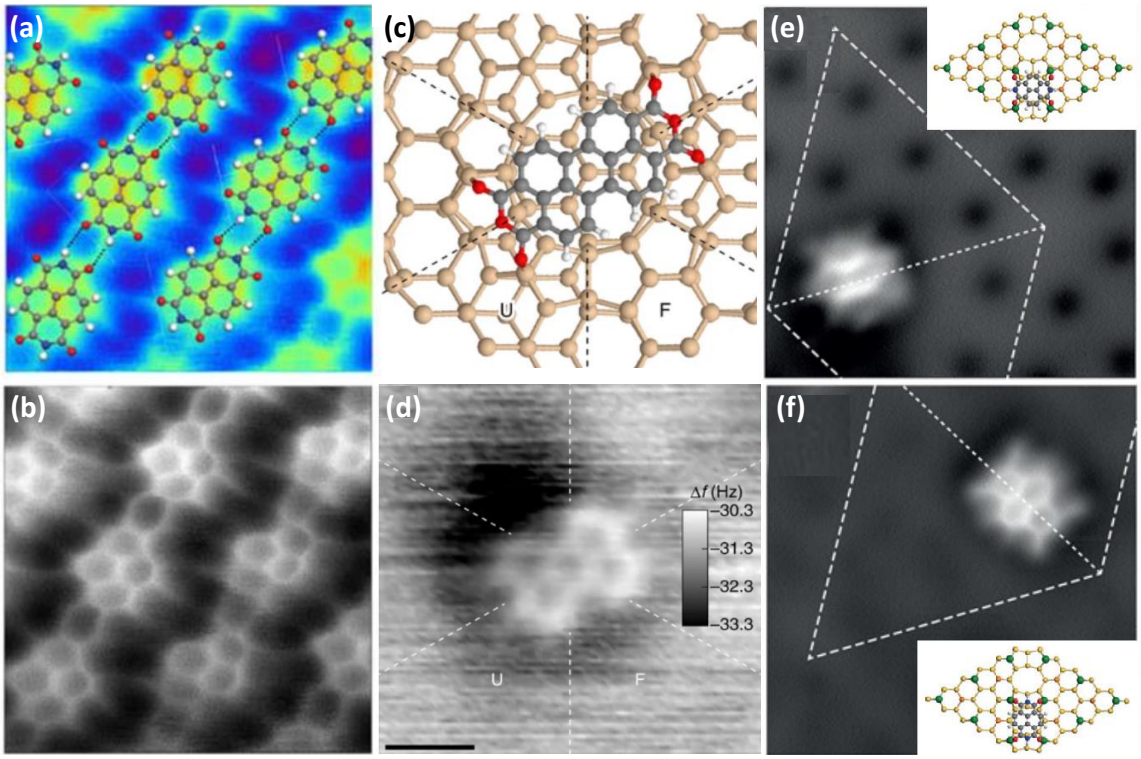

Figure 4.9: **High-resolution topographies of molecules resolved by mediated-tip at higher temperatures and on reactive substrates.** (a) Molecular model of NTCDI molecule superimposed over the contrast-adjusted sub-molecular resolution image, showed in panel (b), obtained at 78 K. (c) Molecular model of PTCDA molecule adsorbed on an Ag/Si(111)-($\sqrt{3} \times \sqrt{3}$ observed at Room Temperature (d). (e, f) The two primary stable configurations of NTCDI molecule adsorbed on highly-reactive Si(111)-7×7. Schematic representation of the model in the inset boxes. (a, b) Panels reprinted with permission from ref [218]. (c, d) Panels reprinted with permission from ref [220]. (e, f) Panels reprinted with permission from ref [221].

In fact, so far, there is no evidence of sub-molecular resolution attained in the air with a functionalised tip used in NC-AFM mode, and only a few studies reported true atomic resolution at room temperature, limiting the use of the technique just to Ultra-high vacuum conditions. It seems evident how, in air and at room temperature, many factors such as the water layer condensed over the surfaces, the presence of contaminants and the thermal noise make extremely challenging any kind of control of the AFM atomic tip termination.
Due to the limits of tip control in ambient, different approaches of molecular imaging in ambient conditions were recently explored. In particular, Korolkov *et al.* performed molecular resolution on 3 Melamine cyanurate (CA.M), trimesic acid (TMA), 1,2,4,5-tetrakis(4-carboxyphenyl)benzene, and terephthalic acid (TPA), imaging at the second or third harmonic of the eigenfrequency in Amplitude Modulation AFM (AM-AFM) mode [223, 224]. Liiró -Peluso *et al.* used the same technique to perform sub-molecular resolution images of P3HT:PCBM [225]. Furthermore, the high spatial resolution imaging of syndiotactic polypropylene (sPP) was performed by driving the microscope in bimodal tapping AC mode. Exciting the cantilever at its eigenfrequency and an additional resonant one, topographical and nanomechanical information can be observed [226]. Finally, even though they were performed on non-organic samples, three alternative imaging methods demonstrated promising results in ambient conditions that can further expand the horizons of high-resolution microscopy. Severin *et al.* operating at high-eigenmode and subnanometer amplitudes, an AFM in Amplitude Modulation mode, imaged single sulfur vacancies at MoS_2 crystal surface at temperatures ranging from room temperature to 250 °C, graphite, arachidic acid layer on a graphite surface and potassium ions on hydrophilic and highly adhesive muscovite mica surfaces [227]. Sumaiya *et al.* reported true atomic-resolution surface imaging via conductive atomic force microscopy (C-AFM) performed at high scanning speeds of HOPG and MoS_2 crystals [228]. Eichhorn *et al.*, applying the recently published methodology named AMFlex2-FMTor1-FMFlex3 mode [229] with a slightly modified setup (AMFlex2-FMLat1-FMFlex3), managed to resolve a HOPG structure. The technique combines in-plane and out-of-plane multifrequency excitations of the cantilever, particularly the second flexural eigenmode for the topographical feedback in amplitude modulation and the first torsional, first lateral and third flexural mode in frequency modulation. Operating at small amplitudes setpoint, high-resolution images were obtained [230], see (Fig: 4.10).

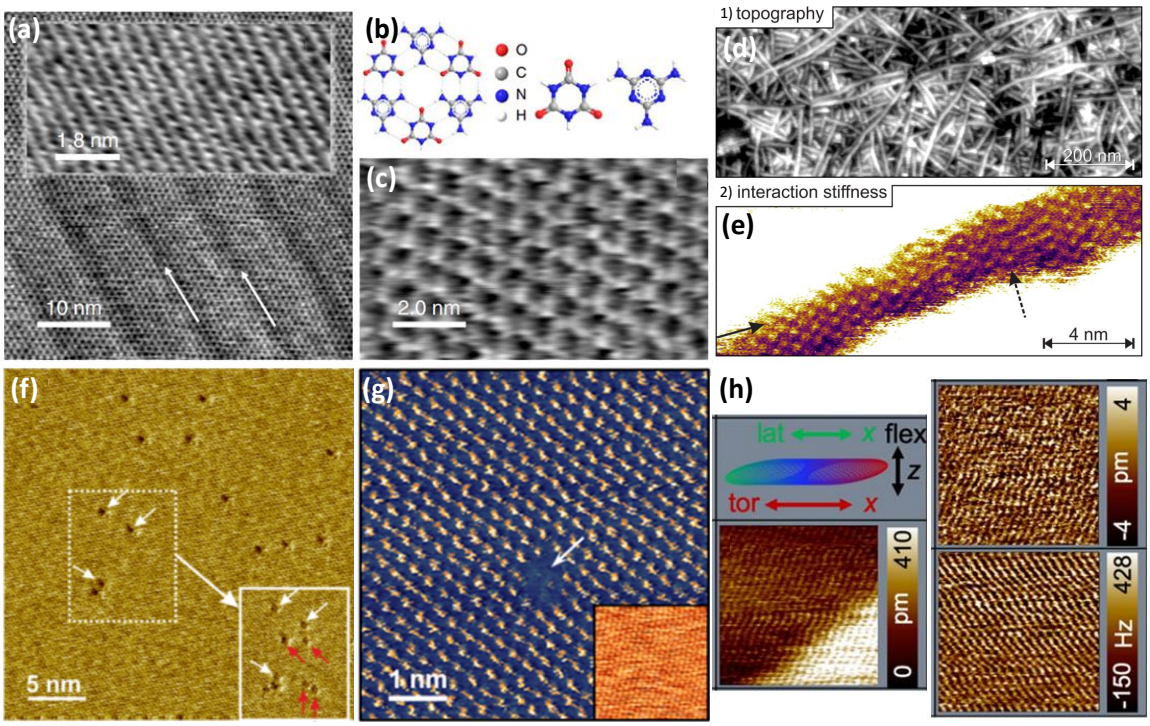

Figure 4.10: **Further approaches for the atomic/sub-molecular resolution imaging.** (a) Melamine cyanurate (CA.M) growth on black phosphorus surface resolved using the third harmonic. The arrows indicate the principal growth direction of CA.M, aligned with the black phosphorus rows. In the inset box, a higher resolution of the sample. (b) Schematic representation of melamine cyanurate complex and of the two molecules that constitute it, melamine and cyanuric acid, respectively. (c) Sub-molecular resolution of CA.M. (d, e) Topographical and nanomechanical imaging of a random syndiotactic polypropylene (sPP) arrangement in AM-FM mode. Operating in bimodal tapping mode, individual methyl groups of the sPP backbone are resolved in the modulus map, panel (e). (f) Vacancies resolution of a cleaved MoS_2 surface imaging the sample using higher eigenfrequencies. The full rectangle is a following scan of the dashed rectangle area; use the white arrows as references. The red arrows indicate further defects (knocked-off atoms)caused by the hard-tapping scanning. (g) Imaging of a cleaved MoS_2 surface in height (inset box) and current (C-AFM) mode in ambient. The resolution of defects is evident only in the current map, white arrow. (h) True atomic resolution of HOPG under ambient conditions, operating the AFM in AMFlex2-FMLat1-FMFlex3 mode. The scheme shows the movement of the tip as a convolution of flexural, torsional and lateral trajectories. The images are height, first torsional-eigenmode amplitude error, and lateral frequency-shift channels, respectively. (a-c) Panels reprinted with permission from ref [223]. (d, e) Panels reprinted with permission from ref [226]. (f) Panel reprinted with permission from ref [227]. (g) Panel reprinted with permission from ref [228]. (h) Panels reprinted with permission from ref [230].

Part II

Experimental Results

This part of the thesis shows all the experimental results relating to the controlled on-surface polymerization and the ultra-high resolution of molecular nano-architectures. In the first chapter, the surface polymers are studied as a result of atomically precise growth on inert and insulating substrates. However, in the absence of a surface catalyst, on-surface covalent coupling reactions become energetically unfavourable, so molecules often desorb from the surface before they can polymerize. The results show for the first time the controlled on-surface polymerization on bulk inert surfaces using Cu_5 atomic clusters as extrinsic catalysts. The second chapter describes how the optimization of the imaging method performed with an atomic force microscopy, using the constant force PeakForce mode in a noise-suppressed environment, improved the resolution of SPM measurements. A new approach to achieve lattice, single-molecule and sub-molecular structural identification of simple molecules was demonstrated under ambient conditions.

Methods

The Au(111) surface was prepared by repeated cycles of Argon sputtering before annealing at a temperature of 475 °C under UHV conditions, while HOPG and mica surfaces were prepared by mechanical exfoliation, followed by annealing at 130 °C under UHV conditions to remove contaminants. Molecules were deposited via standard thermal sublimation, calibrated using a quartz crystal microbalance, under Ultra-high vacuum conditions (lower than 10^{-9} mbar) using a homemade quartz crucible with integrated thermocouple (further details can be found in [231, 232]. Cu_5 clusters were spin-coated on flattened surfaces from either 4 mg/L or 0.4 mg/L Cu_5 dispersed solutions in Milli-Q water. Sample preparation and characterization were attained in a noise-suppressed environment: the IsoLab laboratory of Lancaster University.
Scanning probe atomic force microscopy was carried out on a Bruker MultiMode 8 equipped with a Nanoscope V controller housed in the IsoLab facility. To ensure minimal sample interaction and achieve high-resolution images, the AFM was operated in PeakForce mode using NuNano Scout 70 probes (f_0 ~70 kHz; nominal spring constant 2 N/m). Its design enables the resolution of specific molecular features resembling the topographies collected at low temperatures by CO-mediator tip NC-AFM imaging.
X-ray photoelectron spectroscopy was performed using a Kratos Analytical AXIS Supra spectrometer with monochromatic Al K_α 1486.7 eV X-ray source, operating at 15 kV, 15 mA, and equipped with an electron gun for charge neutralization. Temperature-programmed XPS was carried out at pressures ~10^{-10} mbar using an integrated sample heater with a temperature ramp of 0.4 K/min. A pass energy of 80 eV was typically used for Br 3p spectra in order to maximize the count rate when running TP-XPS over extended periods. All the spectra were analysed using CASAXPS (Casa Software Ltd, UK). The TP-FXPS transition temperature uncertainty is estimated based on data resolution on the temperature axis.
Density function theory, as geometrical optimizations and adsorption energy calculations for molecule-cluster interactions, were carried out with spin-polarized PBE calculation plus

the Becke-Jonson (BJ) damping function in Grimme's D3 method [233] to include van der Waals corrections due to the accuracy for reproducing the binding or adsorption energies. Bader analysis method [234, 235] is applied to the results of spin-polarized calculation for atomic charge distributions. In order to find the transition state (TS), a damped molecular dynamics algorithm was performed combined with the climbing-image nudged elastic band (CI-NEB) method [236, 237]. During the CI-NEB calculation, the structural optimization was considered complete when the maximum forces on all atoms were smaller than 0.02 eV/Å. Dimer [238, 239] is further utilized based on the results of CI-NEB to search for the transition state. Finally, only one imaginary frequency was checked and confirmed for the transition state. All the optimized structures were visualized by VESTA [240].

The following formula calculates binding energy E_b: $E_b = E_{AB} - E_A - E_B$ where E_A and E_B are calculated for the geometries directly obtained from geometrically relaxed composite AB by deleting B and A part, respectively.

Density functional theory calculations for ZnTPP high-resolution imaging interpretation were carried out using vdW corrected functionals implemented within the VASP code. This follows methods previously developed when modelling Br_4TPP:Cu(111) [231, 232]. The AFM simulations were carried out using a modified version of the Probe Particle Model [241], modelling constant height NC-AFM tip as two particles with a relationship which can be described by Hooke's law. One particle, the 'probe particle', interacts with the object to be imaged via the Lennard-Jones potential and, as a result, imparts a force to the particle representing the tip. This allows for the simulation of images created by functionalized tips and nano-asperites [242, 243]. The Lennard Jones potential is calculated from a set of atomic coordinates as a 3D grid of points, each with a calculated force it would impart onto the tip if it were in that location.

Chapter 5

On-surface polymerisation using atomic quantum clusters

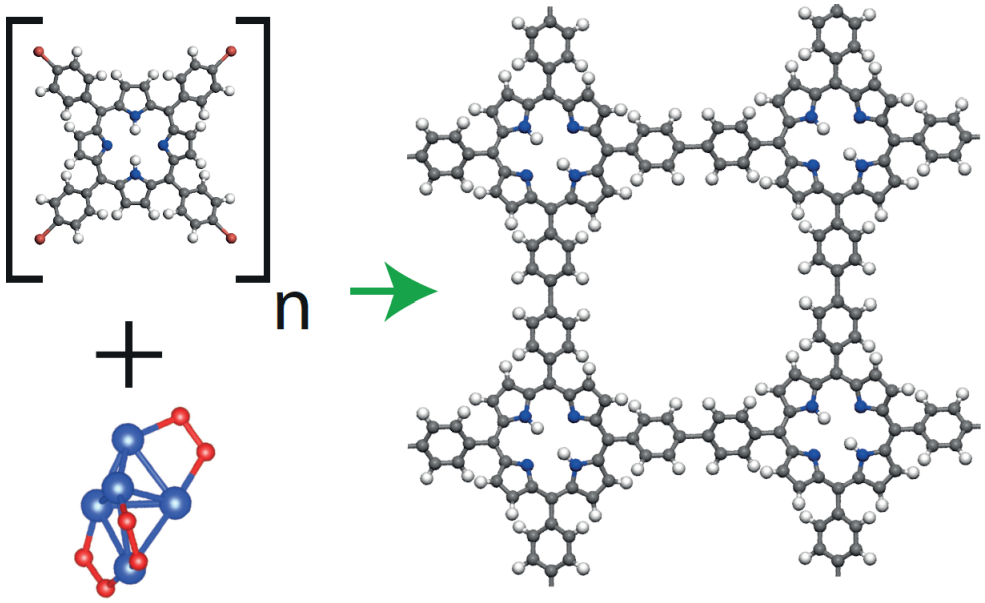

Figure 5.1: **Schematic representation of the on-surface polymerization of tetra (4-bromophenyl) porphyrin (Br_4TPP) catalysed by $Cu_5(O_2)_x$ atomic quantum clusters.** The presence of Cu_5 clusters, here represented in its partially oxidised (red balls) 3D diamond shape configuration, catalyses the dehalogenation of Br_4TPP molecules, entailing the formation of covalent coupled TPP networks.

This chapter reports the development and analysis of controlled on-surface polymerization of Br_4TPP molecules using for the first time the AQCs clusters as extrinsic catalysts, see (Fig: 5.1). Using temperature-controlled X-ray photoelectron spectroscopy (TP-XPS) and high-resolution atomic force microscopy (AFM), it was demonstrated that Cu_5 clusters reduce the activation temperature for on-surface polymerization by as much as (150±25) °C, resulting in stable surface covalent structures on inert graphite and mica surfaces. Moreover,

TP-XPS suggests that the dehalogenation process begins at, or below, room temperature, providing a route to overcome the 'desorption problem' that limits thermal activation on inert substrates. Through the collaboration with Prof. Lambert's group, results are interpreted within the framework of density functional theory (DFT), and climbing image nudged elastic band (CI-NEB) and dimer analysis, which reveal a strong dependence between the catalytic activity of Cu_5 clusters and their stabilizing oxygen layer, highlighting the potential further to tune the catalytic activity of atomic scale catalysts.

5.1 Growth and stability of unreacted and polymerized close-packed Br_4TPP:Au(111) assemblies

Initial experiments were carried out on the Au(111) surface to provide a comparison to previous reported results, and to determine the additional effect of Cu_5. The Au(111) reconstruction was prepared, as previously described, by a double sputtering-annealing cycle; hence (4-bromophenyl) porphyrin (Br_4TPP) molecules were deposited by thermal evaporation from a K-cell under UHV conditions onto the atomically flat surface. A low temperature molecular flux, approximately 275 °C for 15 minutes, enables the growth of a full Br_4TPP monolayer on the Au(111) surface.

Samples were first prepared under UHV conditions before subsequent exposure to air to test the stability of the Br_4TPP islands. High-resolution ambient-AFM images, see (Fig: 5.2. a), show unreacted Br_4TPP close-packed layers, retaining the highly ordered island structure typical in UHV environments [244]. The almost complete absence of contaminants across the surface confirms that the ambient exposure doesn't influence the sample; however, further measurements over time revealed that unreacted Br_4TPP:Au(111) samples survive atmospheric conditions only for up to 24 hours, see (Fig: 5.2. b). Any sample kept overnight in air showed a complete deterioration of the ordered structure in favour of a random molecular distribution over the Au(111) surface.

Furthermore, evidence of the weakly bonded Br_4TPP assemblies was proved by the molecular diffusion and structure modification entailed by the AFM scanning; imaging at (200 - 250) pN set point forces could drag molecules over the sample, disrupting the ordered island. For this reason, the following measurements were conducted at (100 - 120) pN, see (Fig: 5.3).

This work aims to measure the efficacy of clusters as a catalyst material in the process of Br_4TPP assemblies polymerization. Hence, considering the process of activation-recombination of the Br_4TPP precursors deposited on a substrate, as previously demonstrated by Grill *et al.* [67], a temperature reduction induced by higher reactivity of copper compared to gold and the higher coordination of the clusters, catalysis was expected during the process of molecular C-C coupling. For this reason, it was therefore chosen to use a combination of temperature-programmed X-ray photoemission spectroscopy (TP-XPS)

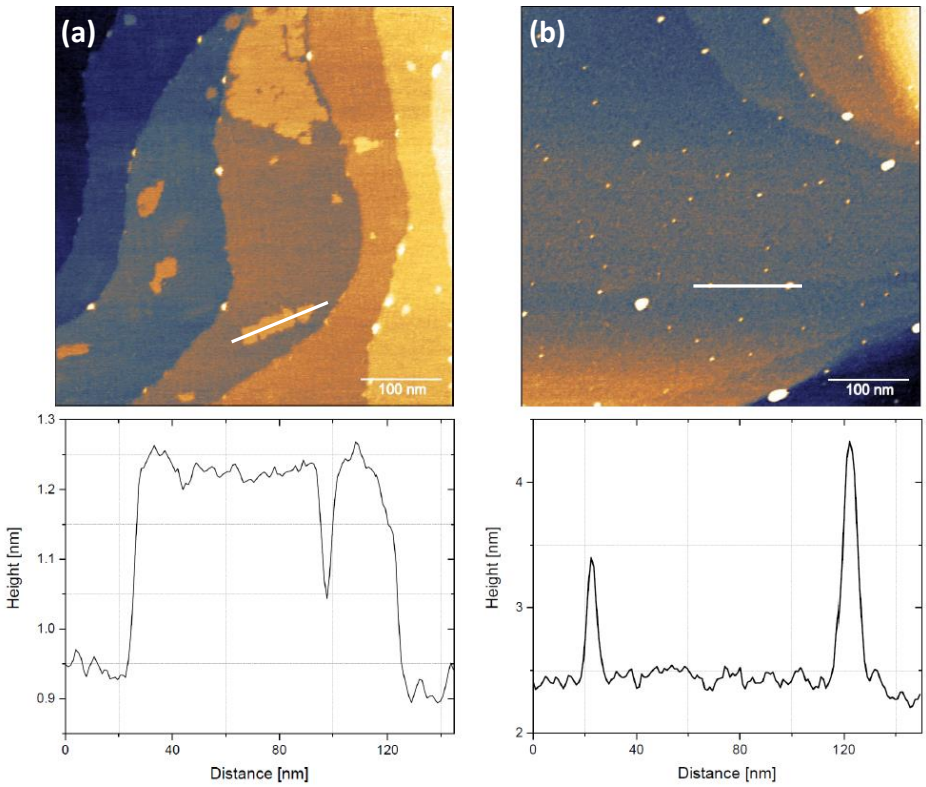

Figure 5.2: **Material stability in ambient conditions.** (a) AFM image of sub-monolayer Br_4TPP close-packed assembly on Au(111) collected on the same day as preparation in UHV. The line profile of the Br_4TPP island shows a topographic height of $\sim$ 200 pm in agreement with the Ultra-Low Temperature STM images of [231]. (b) AFM image of a Br_4TPP:Au(111) sample collected one day after preparation. The ordered structures are completely lost, and molecules diffused over the surface in a random configuration. Nanometric pillars, shown by the line profile plot, are reasonably due to contaminants and molecular clustering.

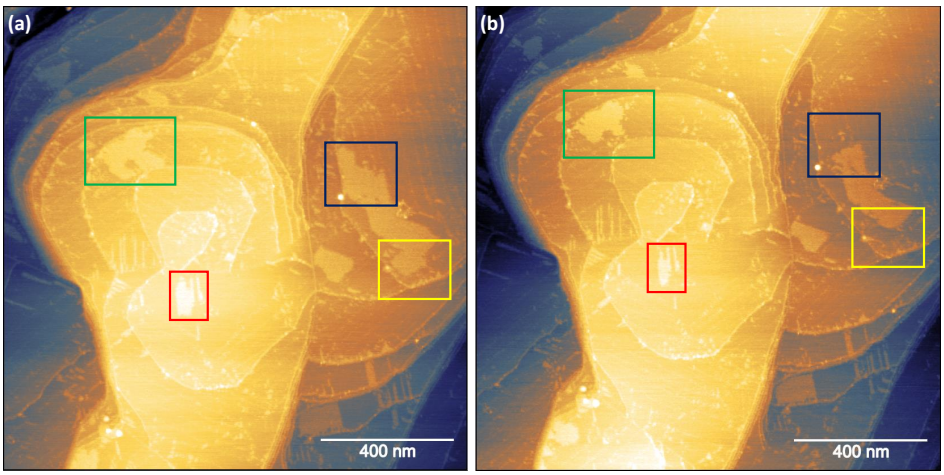

Figure 5.3: **Stability of Br_4TPP:Au(111) during AFM measurements.** (a) AFM image of Br_4TPP close-packed islands and (b) subsequent scan with coloured boxes highlighting the damage to the structure induced by weak binding and AFM tip interaction during the raster scanning. Scans were collected at 250 pN set point force.

and AFM scanning to analyze and characterize the samples.

To demonstrate the actual polymerization of Br_4TPP:Au(111) samples and measure the activation temperature of the molecules, Grill *et al.*'s experiment [67] was replicated. Hence, immediately after the molecular deposition over a reconstructed Au(111) substrate, the sample was exposed to a temperature annealing at ∼150 °C/min for 10 minutes, which it followed a slow cool down (∼10 °C/min) to allow the covalent-coupling connection to form networks. The high-resolution ambient AFM images exhibited the disordered structure typical for TPP covalent networks [67, 76]. Also, for the polymerized Br_4TPP:Au(111) samples, the presence of contamination from ambient exposure was very little, see (Fig: 5.4).

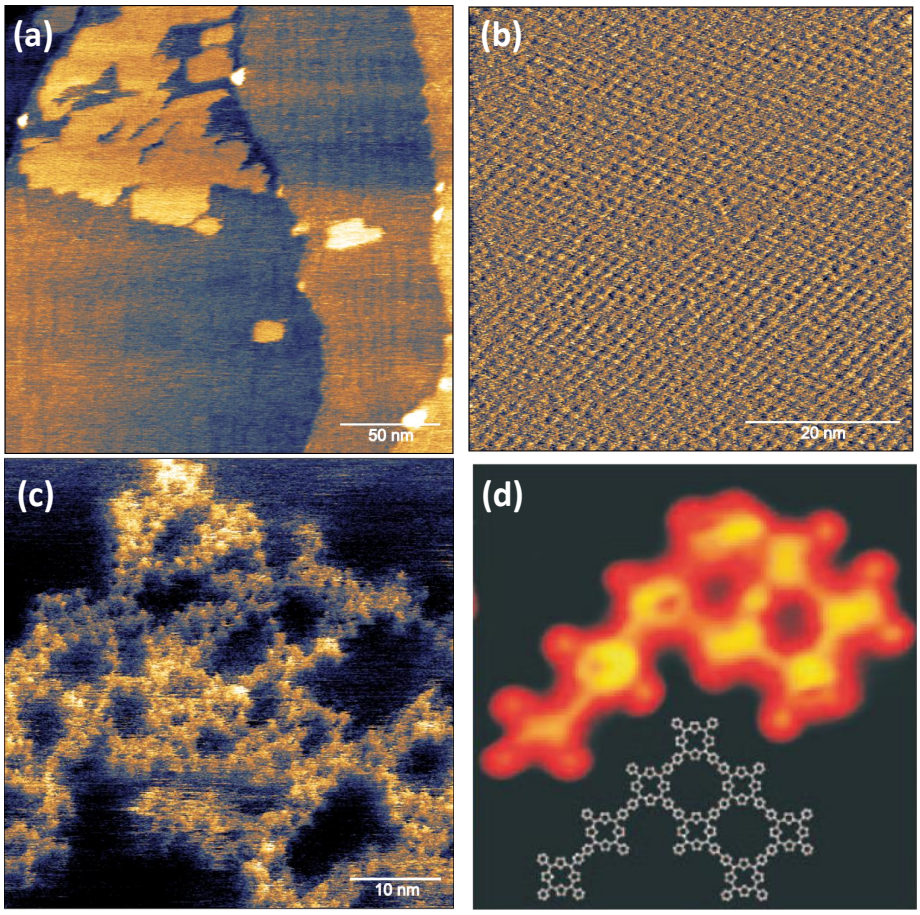

Figure 5.4: **Br_4TPP assemblies on Au(111) surface as a function of the temperature.** (a) AFM image of a close-packed Br_4TPP sub-monolayers characterized by a weak bonding between molecules. (b) AFM lattice resolution of the Br_4TPP widest island of panel(a) processed with a 1D FFT. (c) AFM lattice resolution of a covalent coupled Br_4TPP superstructure obtained under UHV condition by thermal activation and recombination replicating the Method I described in [67]. The image was processed with a 1D FFT filter. Even though the presence of contaminants trapped in the chains (lighter spots), the C-C structure replicates the (d) 8 cross-linked TPP molecules bonding, and the relative schematic representation obtained by Grill *et al.* with Method I. Ultra-Low Temperature STM obtained the image. (d) Panel adapted with permission from ref [67].

To precisely measure the activation temperature and explore the effect of ambient exposure

on the close-packed unreacted molecules, a sample of Br_4TPP:Au(111) was first prepared in UHV and then exposed to ambient conditions for one hour. The following XPS characterization was conducted under UHV conditions. In all XPS measurements, the spectra were collected on the Br 3p and N 1s photoemission signal, referenced to the Au 4f doublet, see (Fig: 5.5). As shown in (Fig: 5.5. a, b), at room temperature Br 3p spectra appeared as a doublet at 183.7 eV and 190.0 eV, characteristic of the C-Br bond [245]. Similar to previous reports [245–248], a downshift in the energy of the Br 3p doublet to 182.5 eV and 188.8 eV was observed, indicating scission of the C-Br bond, and formation of Au-Br due to the bromine atom binding to the Au(111) surface. This downshift was observable as a gradual splitting of the Br 3p peaks into two clearly identifiable components starting at a temperature of ∼50 °C, with full conversion by (200±20) °C, see (Fig: 5.7. a, d). At (200±20) °C, the Br 3p signal was undetectable, suggesting complete desorption of bromine from the surface, with only the reacted TPP molecules remaining, as confirmed by a measurement of the N 1s peak. Between 350 °C and 400 °C (the upper-temperature limit of the XPS instrument), the N1s peak was still detectable even though diminished; this result testified the lack of full desorption of the molecules from the substrate, see (Fig: 5.5. c, d). The shift in the Br 3p peak was remarkably consistent with those reported by Batra *et al.* [247], suggesting that ambient exposure of the Br_4TPP:Au(111) has minimal effect on the coupling reaction. Both these AFM images and the TP-XPS spectra will be used as control measurements and standard references for further analysis with the Cu_5 cluster catalysts.

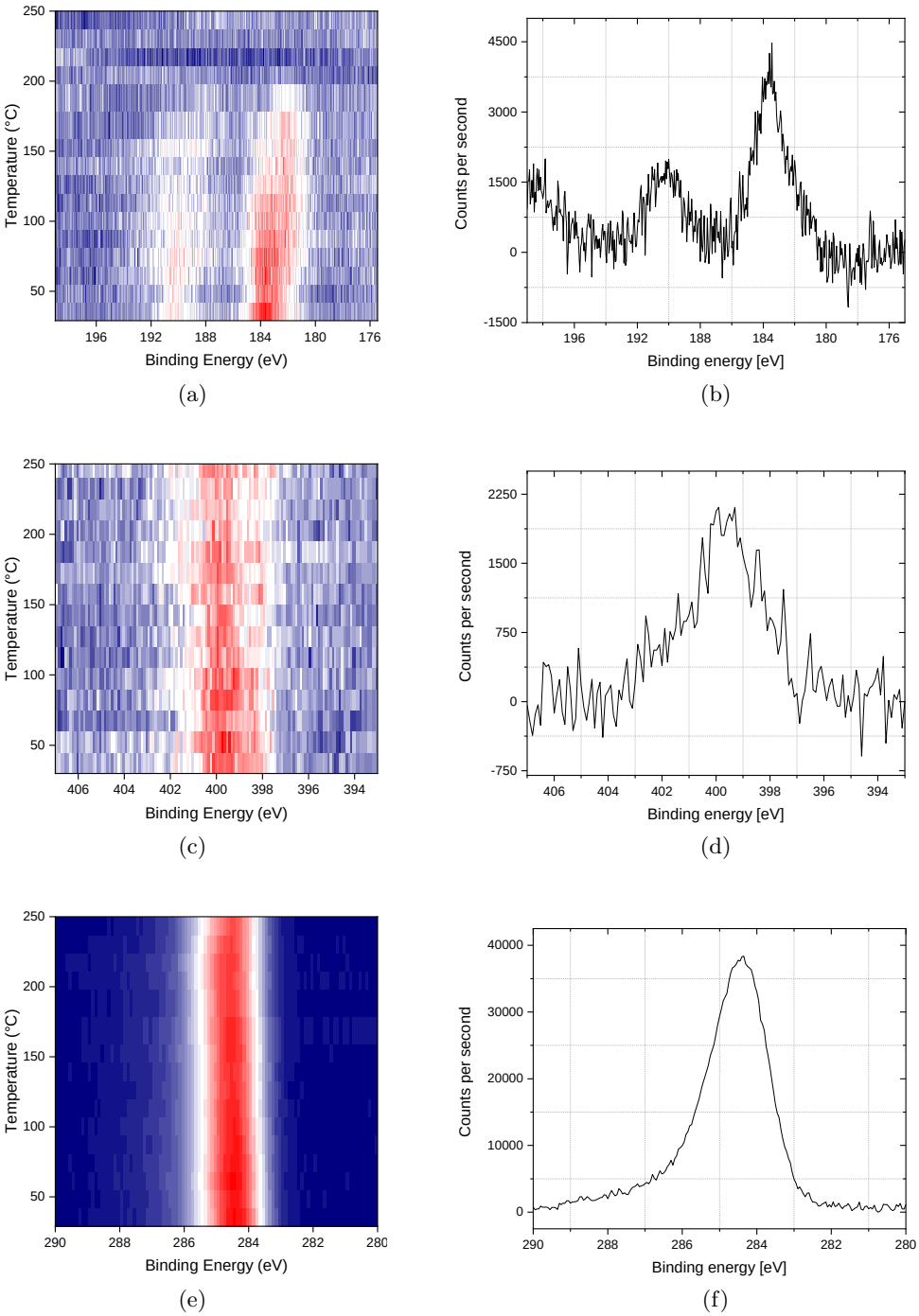

Figure 5.5: **Temperature programmed XPS of Br_4TPP:Au(111) sample.** Analysis in the (a) Br 3p (c) N 1s and (e) C 1s regions with their (b), (d) and (f) respective room temperature spectra. Au 4f region was used as the reference energy.

5.2 Stability of atomic quantum clusters

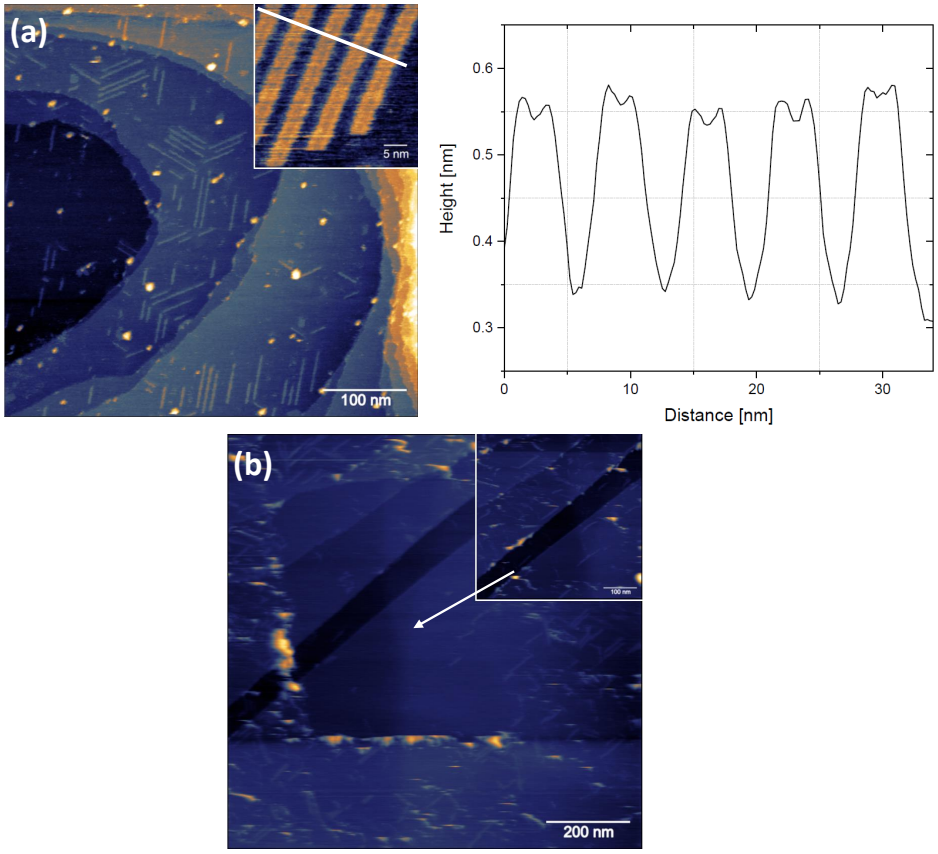

Figure 5.6: **Weakly bound superstructures and diffusion of Cu_5 AQCs on Au(111).** (a) AFM image of Cu_5 islands following a preferential alignment along Au(111) herringbone reconstruction. In the inset box, a higher resolution image of the ∼200 pm height M shape Cu_5 stripes, see the line profile plot. (b) AFM Image showing a 100×100 nm^2 region of "swept" Au(111) surface created by prior AFM imaging dragging away the weakly bound Cu_5. In the inset box, the (100×100) nm^2 AFM scan relative to the "swept" Au(111) area.

To explore the behaviour of Cu_5 in the absence of molecules, 4 mg/L or 0.4 mg/L Cu_5 clusters solutions in Milli-Q water were initially prepared using the method previously reported by Huseyinova *et al.* [249]. Following dispersion by ultra-sonication, clusters were immediately deposited via spin coating onto Au(111). Ambient AFM revealed preferential alignment of the clusters along with the herringbone of the Au(111) surface, with islands measuring (200±50) pm in height, suggesting a single layer structure, see (Fig: 5.6. a). Closer inspection of the islands using an increased force set point of ∼ 120 pN revealed that the islands were easily disturbed, with small clusters often observed diffusing across the surface, see (Fig: 5.6. b). These results provided good evidence that Cu_5 clusters are highly mobile, survive the atmosphere, and, unlike single atoms, resist chemically binding with one another at room temperature, retaining their single cluster structure. Similarly to the Br_4TPP:Au(111) samples, deposited Cu_5 clusters lasted less than 24 hours. Imaging

Cu_5:Au(111) samples kept overnight under ambient conditions showed the loss of the stripes alignment to a random clustering arrangement, due to the presence of the water layer over the Au(111) substrate.

5.3 Atomic clusters as extrinsic catalysts on Au(111)

Catalyst material affects each coupling reaction step, including dehalogenation, molecular diffusion, and covalent linking [82, 250], as previously described in section (Sec: 2.5.2. Hence, to measure the catalytic effectiveness of Cu_5, clusters were tested by preparing a sample of Br_4TPP:Cu_5:Au(111). First, the Au(111) was prepared as previously described, but before the molecular deposition, the substrate was unloaded from the chamber to undergo a spin-coating cycle of 4 mg/L Cu_5 cluster solution. Hence, the Cu_5:Au(111) sample was immediately reintroduced into the UHV chamber, and the system was pumped down for 4-5 hours until the load-lock pressure was in a range of low 10^{-8} mbar. The deposition of Br_4TPP molecules over the Cu_5:Au(111) substrate was performed following the method previously reported. The final sample was Br_4TPP:Cu_5:Au(111). As it could has been already noticed, the convention implemented to describe a sample considers labelling by sample preparation steps, following a chronological order, from the latest to the oldest procedure, and not a morphological specimen stacking order.
AFM imaging of Br_4TPP:Cu_5:Au(111) samples after the activation-recombination process carried out under UHV conditions didn't give the expected results. In fact, presumably due to contaminants, wide C-C networks couldn't be resolved, in contrast with a small fraction of reacted molecules gathered together in disordered agglomerations. For this reason, to study the catalyst mechanism expected by the AQCs cluster, temperature programmed XPS measurements were performed on Br_4TPP:Cu_5:Au(111) samples. The XPS spectra analysis revealed that at (125 ± 20) °C, the Br 3p signal was nearly undetectable, signifying a substantially reduced activation temperature for the dehalogenation process upon the addition of the Cu_5 clusters of $\Delta T_{Au} = (75 \pm 20)$ °C, see (Fig: 5.7). Furthermore, partial dehalogenation had already begun at room temperature, observable as a clear splitting of the Br 3p doublet, and the peak downshift was attributed to either Au-Br or Cu-Br bonds formation. The partial dehalogenation at RT suggested that the catalytic effectiveness of Cu_5 was greater than what can be measured on Au(111).
The detection of the N 1s peak at temperatures up to at 400° C, confirmed that TPP remains on the surface, as expected for a covalent network, see (Fig: 5.8. c, d).
To test if the deposition order affects the coupling reaction, samples were prepared following a different procedure than Br_4TPP:Cu_5:Au(111). On a sample of Br_4TPP: Au(111) firstly prepared in UHV, a 4 mg/L dispersed solution of Cu_5 clusters was immediately deposited via spin coating. The final Cu_5:Br_4TPP:Au(111) was hence analyzed following the TP-XPS procedure previously described. The XPS spectra showed full dehalogenation

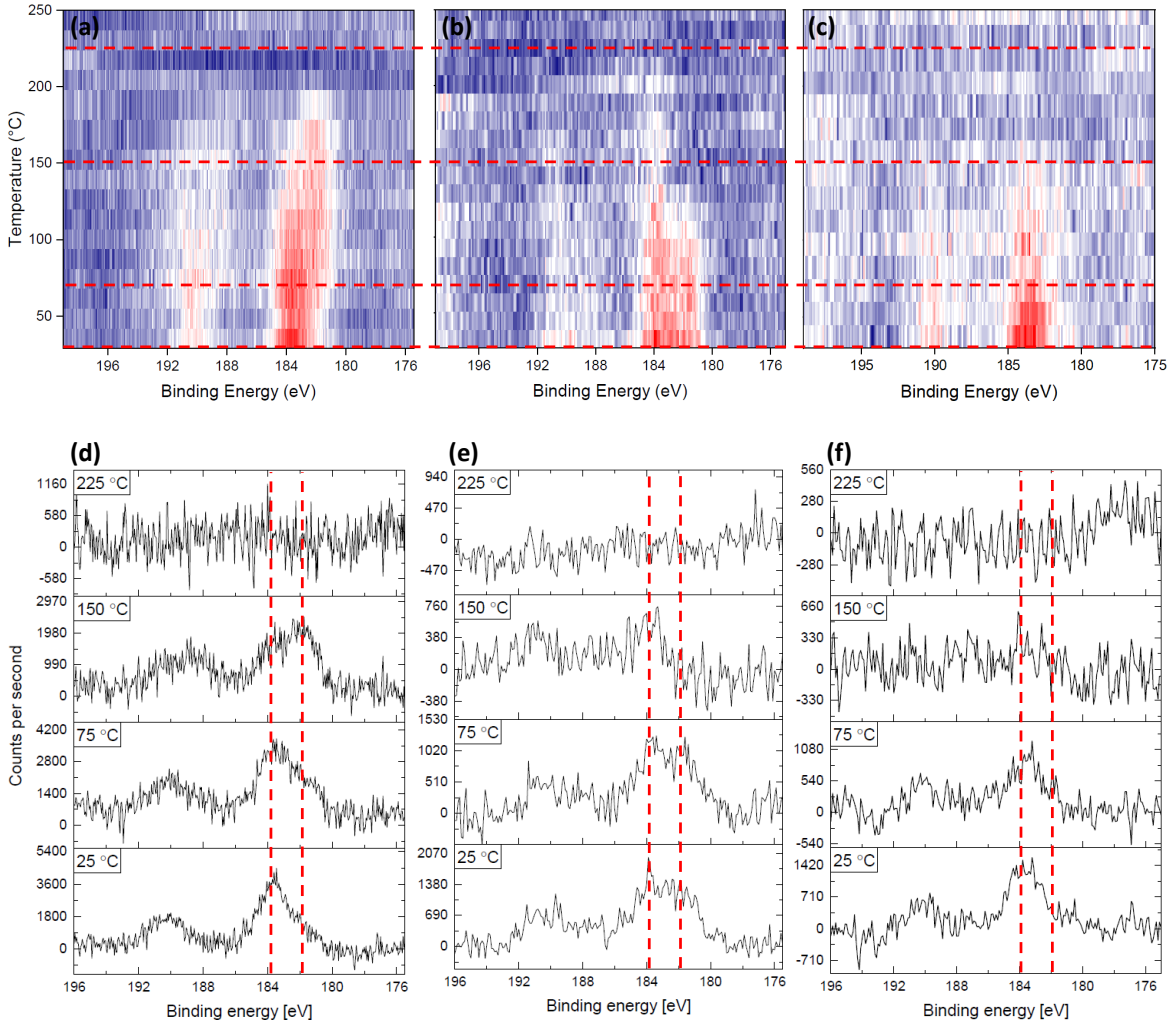

Figure 5.7: **Cu_5 induced activation temperature reduction for Br_4TPP:Au(111) samples.** (a) 2D TP-XPS plot of the Br 3p region for Br_4TPP:Au(111) in the absence of Cu_5, showing complete dehalogenation by (200±20) °C. (d) Line profile XPS spectra highlighting key steps of the coupling reaction at temperatures marked by the dashed lines in (a). (b) and (c) show the 2D TP-XPS data and their line profile: (e) and (f), respectively, for the Br 3p region on Br_4TPP:Au(111) in the presence of Cu_5 clusters, prepared by the two different processes: (b) Br_4TPP:Cu_5:Au(111) and (c) Cu_5:Br_4TPP:Au(111). The dehalogenation temperature reduction to (125±20) °C caused by the Cu_5 catalysis is present in both samples. The Br 3p peak downshift was detected only in Br_4TPP:Cu_5:Au(111) sample.

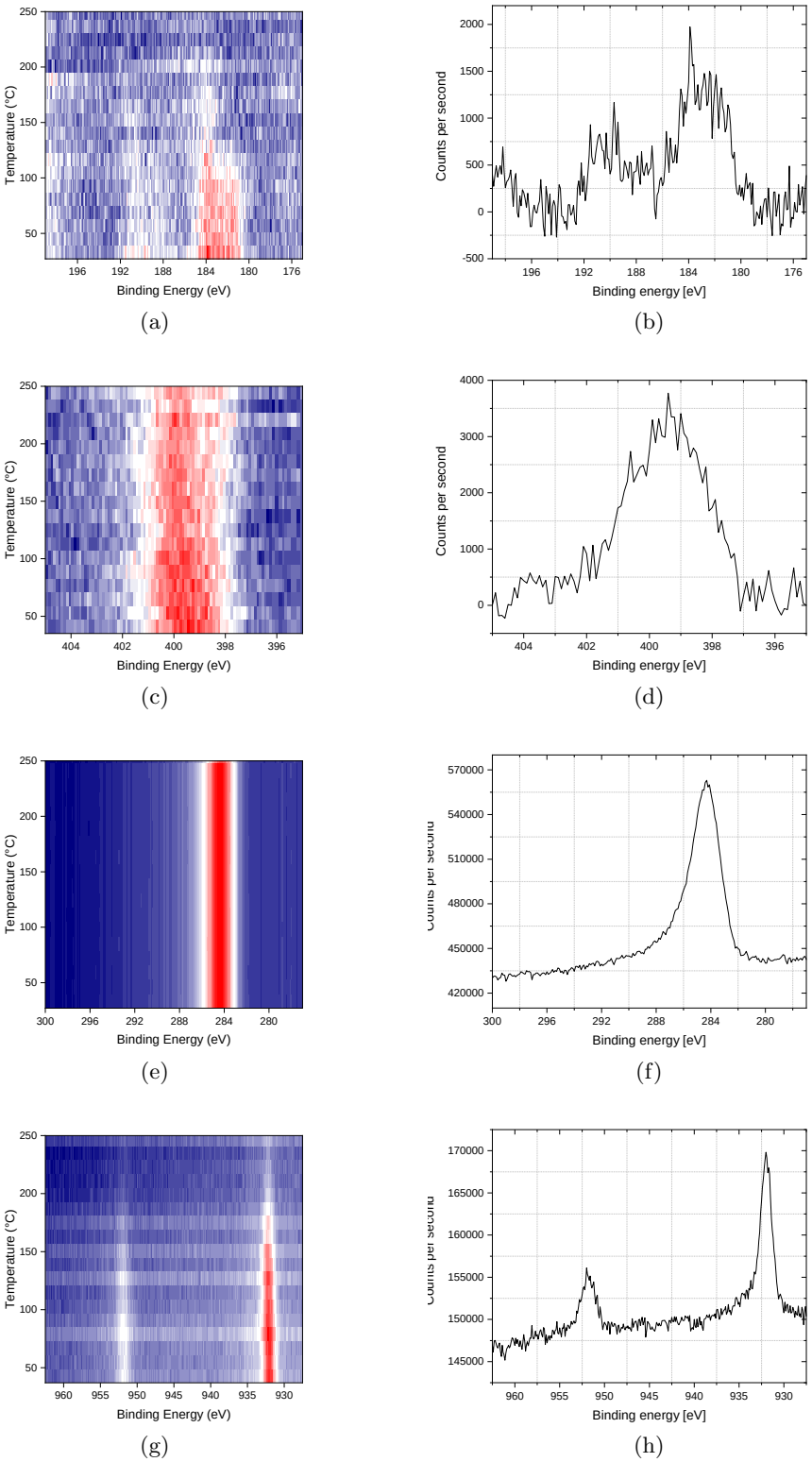

Figure 5.8: **Temperature programmed XPS of Br_4TPP:Cu_5:Au(111) sample.** Analysis in the (a) Br 3p, (c) N 1s, (e) C 1s and (g) Cu 2p regions with their (b), (d), (f), (h) respective room temperature spectra. C 1s region was used as the reference peak

below (150 ± 20) °C, and the presence of TPP covalent network on the surface at 400° C demonstrated by the N 1s spectra. However, the splitting of the Br 3p doublet was not detected; this proved that the Cu_5 reduced the activation temperature for the dehalogenation process, acting as a catalyst, but the oxidation of the metal surface and the cluster, prevented the Au-Br or Cu-Br formations, attributed to the peak downshift, see (Fig: 5.7. c-f).
The proof of the nano-cluster catalysis provided encouragement to test the clusters on inert substrates; however, besides the good results achieved by both deposition procedures, the molecules:clusters:substrate method was assumed as the preferential, considering the lower presence of oxide over the sample. In particular, to eliminate the effect of the catalytic substrate, the polymer formation, activated by Cu_5 clusters, was studied on highly oriented pyrolytic graphite (HOPG) and muscovite mica substrates as naturally atomically flat, non-catalytic, and readily available surfaces.

5.4 Surface polymer activation on a non-metal substrate

The choice of HOPG as a substrate for the growth of organic 2D structures was due to its semi-metal material properties, which are intermediate between those of metals and solid non-metals/semiconductors-like, due to the small overlap between the conduction and valence band. However, conversely, from the traditional semiconductors, on which the high presence of unsaturated dangling bonding at the free surface tends to reduce the diffusivity of the molecules, anchoring them to the substrate, the interaction between the molecules and the HOPG is ruled by weak interaction such as van der Waals forces. Furthermore, as said before, the choice of HOPG as a semiconductor-like substrate was due to its stability under ambient conditions and the ease of obtaining atomically flat and clean surfaces by mechanical exfoliation.
The molecular deposition was pursued following the same procedure optimized for the metal substrate samples to achieve Br_4TPP sub-monolayer islands and prevent the full coverage of the HOPG surface. After a mechanical exfoliation to expose a new atomically flat surface, the HOPG was annealed under UHV conditions to eliminate the contaminations collected in ambient. A comparison of AFM images of a clean surface at RT and after a ∼ 300 °C annealing confirmed the stability of the surface at these temperatures and a mean roughness of 30 pm that can be considered atomically flat.
In ambient AFM imaging of an UHV-prepared Br_4TPP:HOPG sample showed an arrangement characterized by both 2D layer and 3D island growth known as Stranski-Krastanov growth mode. This growth process for porphyrin molecules on a semi-metal surface was already demonstrated by Bussetti *et al.* for H_2TPP:HOPG samples [251, 252]. In particular, the preferred Br_4TPP arrangement was the close-packed 2-layers islands in proximity to substrates defects, such as kinks, holes or steps, leaving most of the HOPG substrate clean, see (Fig: 5.9. a).

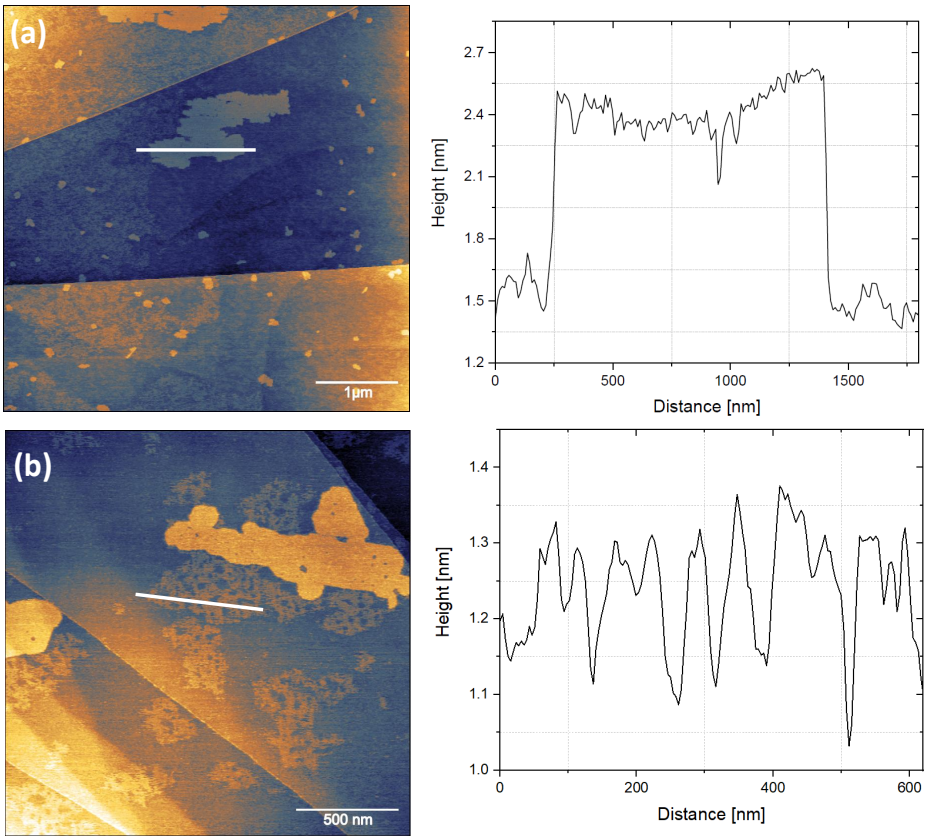

Figure 5.9: **Br_4TPP assemblies on the HOPG surface as a function of the temperature.** (a) AFM image of 3-layers Br_4TPP close-packed islands kept at room temperature. As shown by the relative line profile plot, the preferential Br_4TPP molecular assembly follows a Stranski-Krastanov growth mode (b) AFM image of a Br_4TPP:HOPG sample annealed at (250±20) °C. The different island conformation is due to a partial dehalogenation-recombination that occurred during the annealing due to the coexistence on the sample of unreacted 3-layers Br_4TPP close-packed and sub-monolayer islands; see the relative line profile plot.

The TP-XPS measurement of an UHV-prepared Br_4TPP:HOPG sample showed, in the Br 3p region, a full debromination temperature between (225 ± 25) °C, and as expected, the absence of a peak-shift demonstrated that bromine doesn't interact with the surface and instead desorbs, see (Fig: 5.10. a, b). The presence of the N 1s peak at higher temperatures (up to 300° C) confirmed the presence of TPP molecules at high temperature, which is most likely due to C-C formation, see (Fig: 5.10. c, d). Using 225 °C as a debromination temperature reference, a Br_4TPP:HOPG sample was annealed inside the UHV chamber immediately after the molecular deposition. Further AFM analysis of the surface under ambient conditions presumably showed a coexistence of close-packed multi-layers island (∼0.8 nm high) and C-C coupled molecular assemblies. The annealing was not efficient enough to trigger a complete thermal activation-recombination reaction, except for the different sub-monolayer structures (∼0.2 nm high), see (Fig: 5.9. b).
Before determining if the nano-clusters activate catalysis, AFM images of HOPG free-surface coated only in Cu_5 clusters were collected to determine the dimensions and the stability of the AQCs structure. The Cu_5:HOPG samples were prepared by a 4 mg/L dispersed solution of Cu_5 clusters deposited via spin coating on a freshly cleaved HOPG substrate. The AFM imaging under ambient conditions showed a high coverage of AQCs, packed together in up to 2 nm high clumps, presumably due to the oxidation of the clusters and the lower binding energy with the substrate rather than between them, see (Fig: 5.11. a). Furthermore, if the AFM measurements were collected after a light-annealing in UHV (120±20 °C), the Cu_5 clusters deposited on the HOPG mostly desorbed from the surface or diffused due to the thermal energy transferred and aggregate at the surface discontinuities, like kinks, crack and especially at the step edges, see (Fig: 5.11. b).

To determine how the molecular architectures evolve by the simultaneous presence on the surfaces with the AQCs, Br_4TPP:Cu_5:HOPG samples were prepared. Like the process developed for Au(111) samples, AQCs clusters were spin-coated on a mechanically exfoliated HOPG substrate; so, pumping down the sample until the high vacuum regime was reached, porphyrins were evaporated onto Cu_5:HOPG substrate. The following TP-XPS analysis of Br_4TPP on HOPG showed a substantial reduction in the activation temperature for dehalogenation from around (225±25) °C, for Br_4TPP:HOPG samples, down to (75±25) °C, for Br_4TPP:Cu_5:HOPG ones, resulting in a reduction of ΔT_{HOPG} = (150±25) °C. Unlike on Au(111) and as previously observed, Br is expected to immediately desorb from the HOPG surface following dehalogenation, with the disappearance of the Br 3p peak signalling completion of the dehalogenation process. As shown in (Fig: 5.10), once again a clear broadening of the Br 3p peak upon the addition of Cu_5 clusters was observed, suggesting a second chemical environment due to Cu-Br bonding indicative of an intermediate organometallic phase. TP-XPS in the Cu 2p region (Fig: 5.12. e, f) supported this assignment, with a clear shift in the Cu 2p peak from 932.7 eV close to 50 °C, to 933.0 eV above 100 °C. This shift coincided with the temperature at which Br leaved the substrate, indicating a chemical change in the Cu_5 due to the presence of Br. Similar to

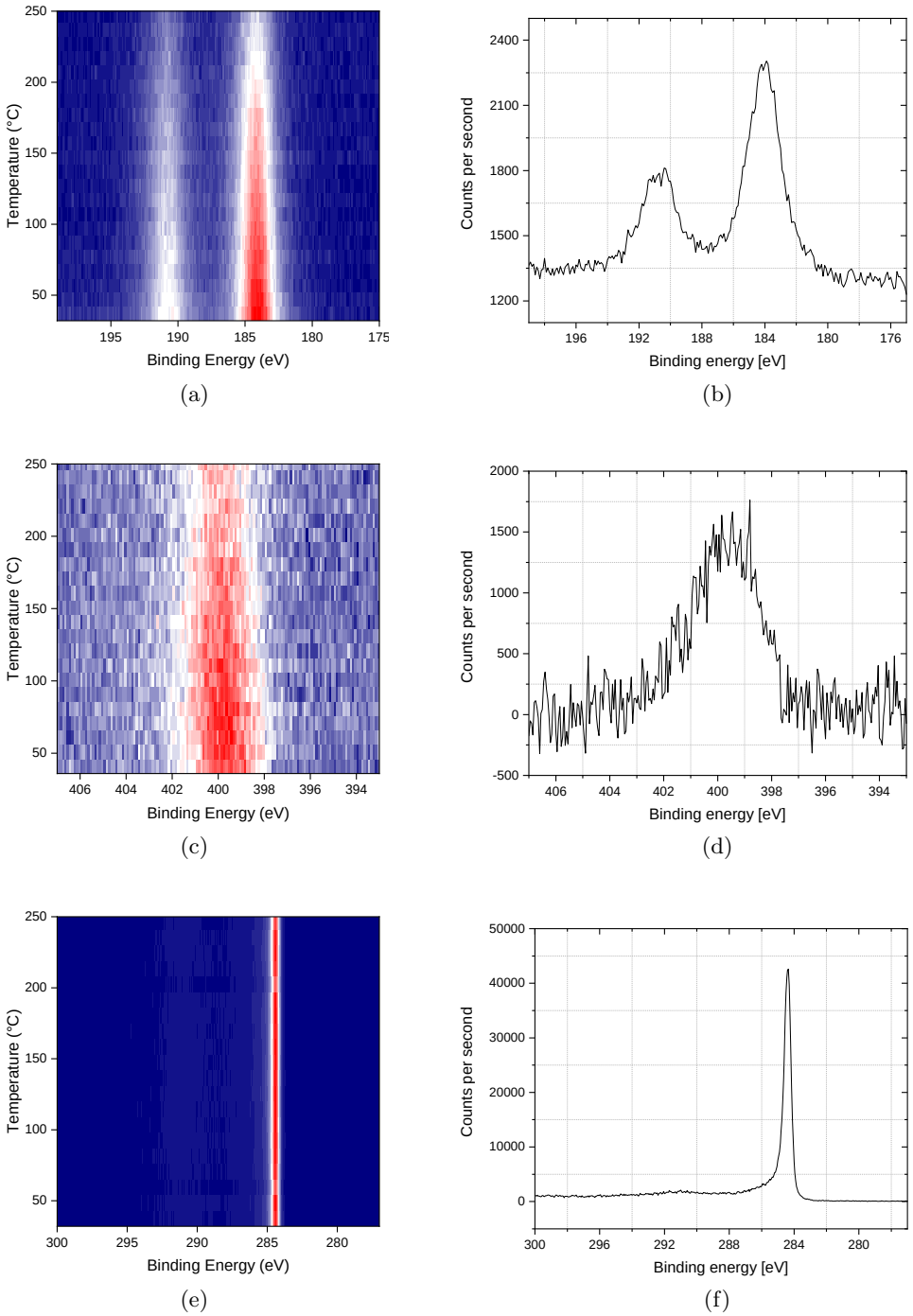

Figure 5.10: **Temperature programmed XPS of Br_4TPP:HOPG sample.** Analysis in the (a) Br 3p, (c) N 1s and (e) C 1s regions with their (b), (d), (f) respective room temperature spectra, confirming that covalently bound TPP remains on the HOPG following desorption of Br. C 1s region was used as the reference peak.

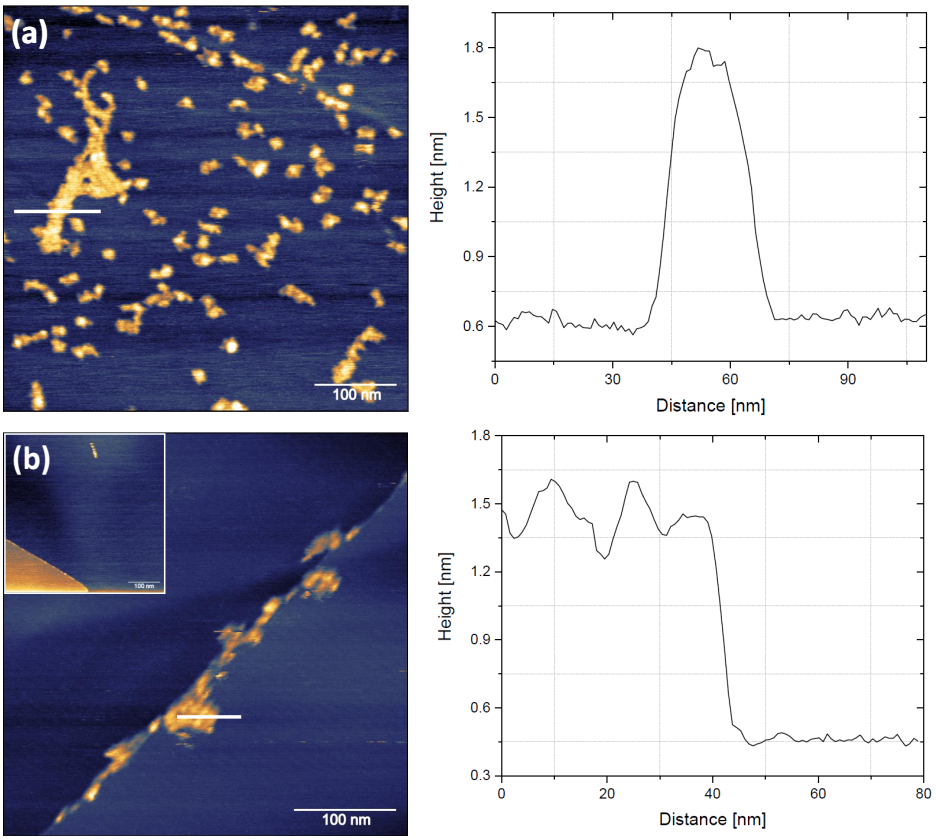

Figure 5.11: **Cu_5 clusters deposition on HOPG as a function of the temperature.** (a) AFM image of AQCs collected immediately after the clusters spin-coating deposition. Differently from the Cu_5:Au(111) samples, AQCs are packed together in chaotic structures up to 2 nm high; see the line profile plot. The aggregation is due to the presence of oxygen trapped in the clumps and the higher binding energy with the substrate (b) AFM image of thermal annealed AQCs under UHV conditions packed together at a HOPG step edge in ∼1 nm high structures, see the line profile plot. As the sample was annealed at (150±20) °C, most clusters were desorbed during the process. In the inset box, an AFM image of a diffusive Cu_5 clump, dragged by the probe during the scanning, proves the weak interaction with the substrate.

data on Au(111), TP-XPS in the N 1s region with and without Cu_5, see (Fig: 5.12. c, d) confirmed that the TPP molecules remained on the surface following dehalogenation.
The ambient AFM measurement of Br_4TPP:Cu_5:HOPG samples kept at room temperature didn't show a C-C network formation because the catalysis had not been thermally activated yet. However, the lack of broad and flat porphin islands despite more extensive, close-packed clumpy features proved that a meta-architecture made by metal-coordinated and metal-organic bonds was achieved, see (Fig: 5.13. a). Conversely, the annealing of Br_4TPP:Cu_5:HOPG samples to complete the debromination showed once the sample was cooled down at RT, the presence on the surface of new chaotic structures, see (Fig: 5.13. b). Considering the dimension of these features, comparable with the one of the Br_4TPP-only sample, it was presumable that a C-C coupling between a few molecules was achieved. Still, the presence of Cu_5 cluster on the surface and the higher binding energy with the substrate inhibited the network formation. Furthermore, the high diffusivity of the porphins on the surface prevented the high resolution of these features.

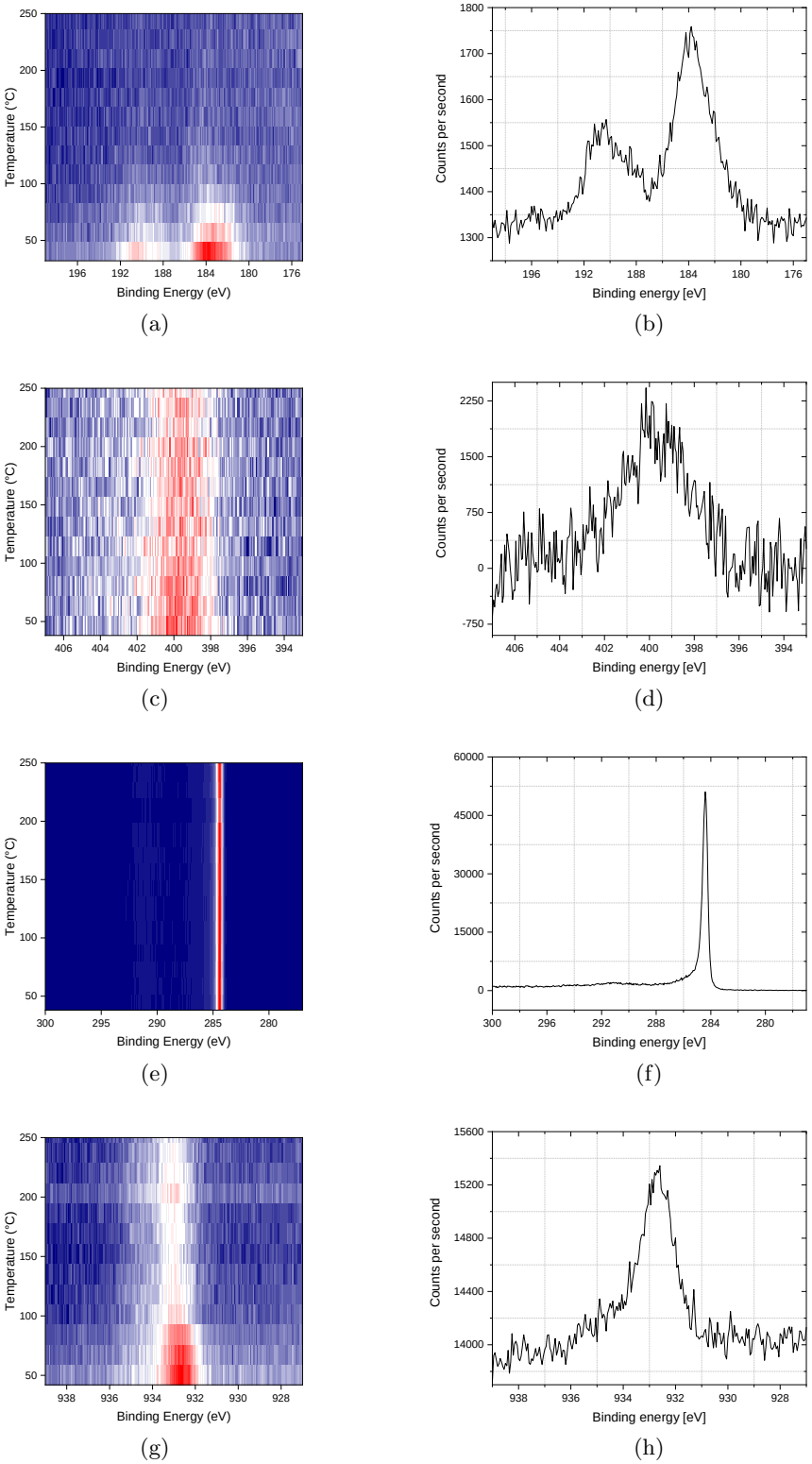

Figure 5.12: **Temperature programmed XPS of Br_4TPP:Cu_5:HOPG sample.** Analysis in the (a) Br 3p, (c) N 1s, (e) C 1s and (g) Cu 2p regions with their (b), (d), (f), (h) respective room temperature spectra, confirming that covalently bound TPP remains on the HOPG following desorption of Br. C 1s region was used as the reference peak.

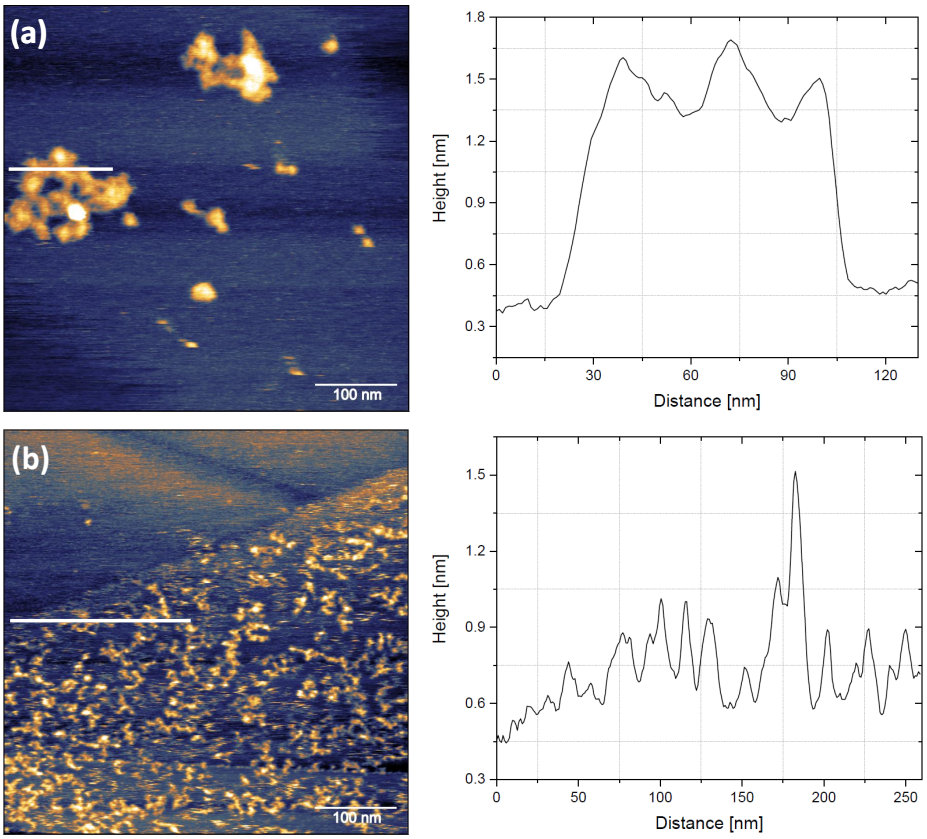

Figure 5.13: **$Br_4TPP:Cu_5$:HOPG sample as a function of the temperature.** (a) AFM image of a $Br_4TPP:Cu_5$:HOPG sample kept at room temperature. The concurrent presence of AQCs, Br_4TPP molecules and Oxygen contaminants, shows a chaotic structure highly different from the Br_4TPP close-packed island of (Fig: 5.9. a). (b) AFM image of a $Br_4TPP:Cu_5$:HOPG sample annealed a ∼200 °C under UHV condition. The complete disaggregation of the assemblies shows a unique structure with an average high of 200 pm tall, similar to the TPP networks. This image cannot be considered strong evidence of cross-linking.

5.5 Surface polymer activation on an insulator

In addition to the semiconductor substrates, Br_4TPP was deposited on an insulator, a mica (muscovite) substrate, to monitor the evolution of the molecular architecture with a further more weak binding energy with the surface. The choice of mica was motivated by its stability in air, the high wettability, and the ease by which a clean flat surface can be obtained by mechanical exfoliation. The stability analysis at RT and after a $\sim$ 300 °C annealing showed no unexpected results; the mica surface preserves an atomically flat roughness of <50pm and doesn't exfoliate at high temperatures.

The UHV-evaporation of porphyrins on mica surface kept at RT, showed the formation of chaotic structures of packed molecules and contaminations, ranging from 400 to 1200 pm height, see (Fig: 5.14. a). The annealing of Br_4TPP:mica didn't show an expected rearrangement of the molecules; due to the weak interaction with the substrate, most of the molecules desorbed and only a small amount clumped in packed pillars few nm high, see (Fig: 5.14. b). Due to this specific behaviour, it was not possible to determine if a C-C coupling occurred.

To test if a network cross-linking occurs for UHV-prepared Br_4TPP:mica samples, TP-XPS measurements were carried out. The analysis in the energy region showed the disappearance of the Br 3p peak at (200±25) °C, see (Fig: 5.15. a, b). As expected, similarly to the Br_4TPP:HOPG sample, the absence of Br 3p peak-shift demonstrated the immediate halogen desorption after the C-Br cleavage, instead of following recombination with the atoms substrate as occurred on the metal surface. The presence of the N 1s peak at higher temperatures, confirmed that TPP molecules were still on the surface most likely due to C-C formation, see (Fig: 5.15. c, d). Due to the surface charging during XPS analysis of the insulating sample, the spectra were affected by spurious peaks; for this reason, the Al 2p region was used as the reference energy, see (Fig: 5.15. e, f) and the Br energy region was narrowed around the 184 eV peak, to avoid interference related to the nearby Si 2p peak.

Finally, the standard reference sample of mica substrates covered exclusively with Cu_5 clusters showed, for samples kept at room temperature, a high presence of packed AQCs agglomerations and pillars up to 1 nm high, see (Fig: 5.16. a). In fact, the AFM analysis of the Cu_5:mica samples, after annealing in UHV at ∼150 °C, showed a shrinkage of the clumps presumably due to the partial oxide degassing. The rare Cu_5 features measured 0.4 nm high on a mostly empty free surface of mica, see (Fig: 5.16. b).

The preparation of Br_4TPP:Cu_5:mica was pursued following the procedure adopted for Br_4TPP:Cu_5:HOPG samples; however, the RT-AFM imaging under ambient condition didn't show distinguishable features, and the surface resulted covered in chaotic structures of partially reacted molecules and AQCs agglomeration, as the activation temperature was not reached and the debromination didn't fully take place, see (Fig: 5.17. a). By contrast, entailing the molecular debromination by thermal activation of the AQCs catalysis at ∼150 °C, the following recombination of the precursors occurred in ordered arrangements, typical

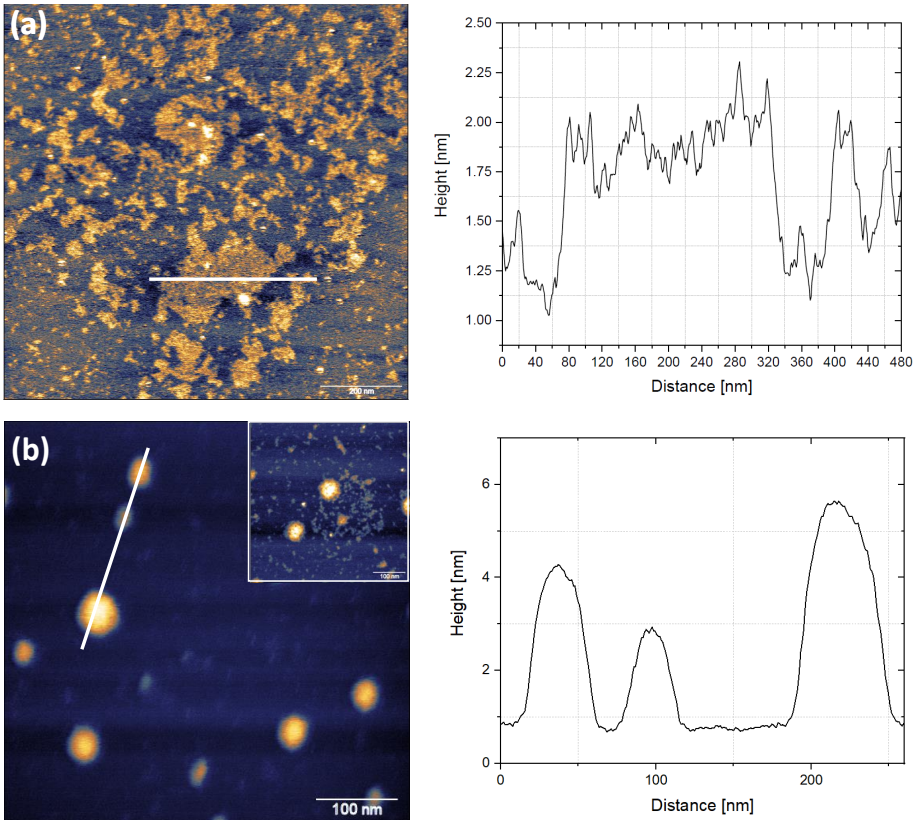

Figure 5.14: **Br_4TPP assemblies on mica surface as a function of the temperature.** (a) AFM image of Br_4TPP deposited on mica before the annealing. Molecules aggregate in disordered multi-layer islands, as the line profile plot shows. (b) AFM image of a Br_4TPP:mica sample annealed at (200±20) °C. The weak interaction with the surface entails a high molecular diffusion and aggregation in clumps ranging from 1 to 6 nm high; see the relative line profile plot. There is no evidence that dehalogenation-recombination occurred during the annealing. In the inset box, an AFM image of a Br_4TPP:mica sample annealed for a shorter time shows the intermediate phase between the multi-layers island of the panel (a) and the pillar formations of panel (b).

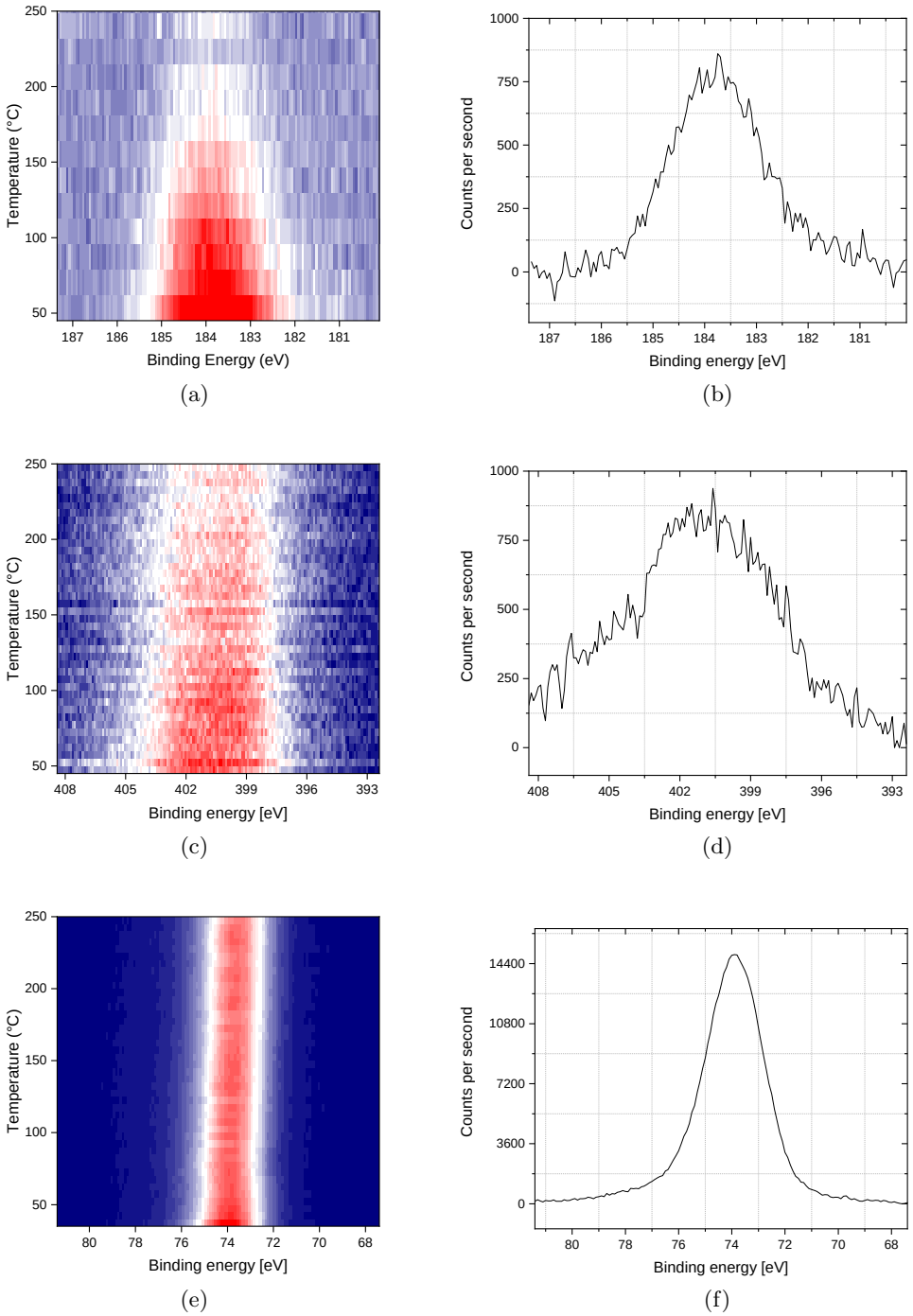

Figure 5.15: **Temperature programmed XPS of Br_4TPP:mica sample.** Analysis in the (a) Br 3p, (c) N 1s and (e) Al 2p regions with their (b), (d), and (f) respective room temperature spectra. Al 2p region was used as the reference energy

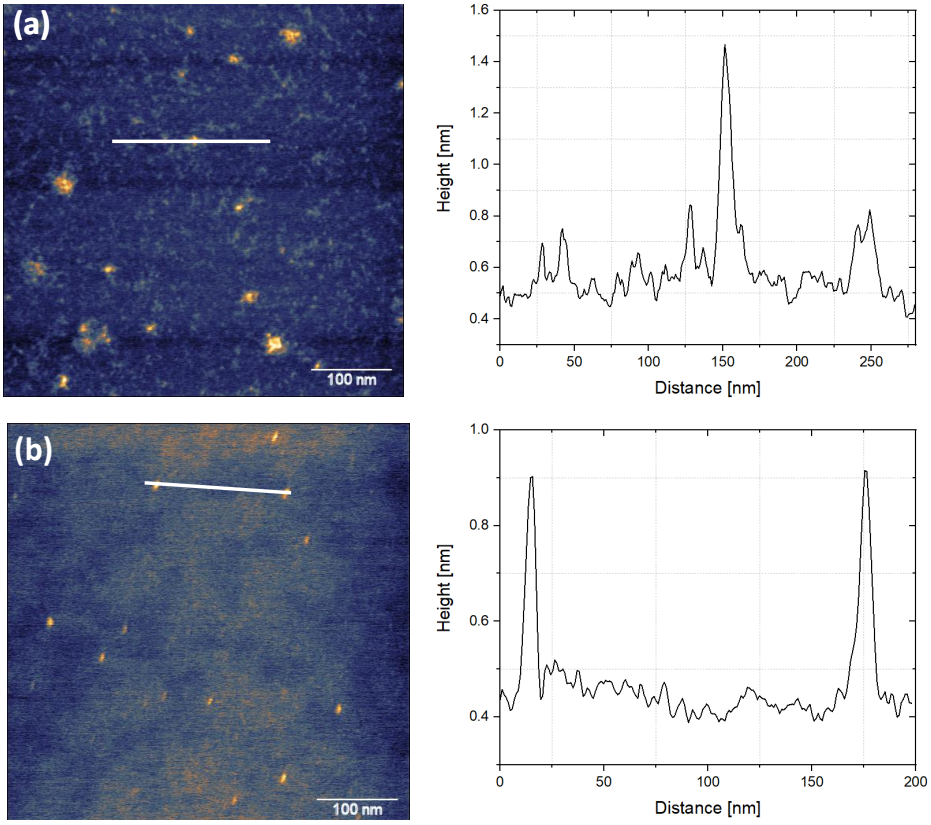

Figure 5.16: **Cu_5 clusters deposition on mica as a function of the temperature.** (a) AFM image of AQCs collected immediately after the clusters spin-coating deposition. Similarly to the Cu_5:HOPG samples, AQCs tend to cover the whole surface aggregating in disordered structures. Reasonably, the tallest structure, up to 1 nm high, see the line profile plot, is due to the presence of Oxygen trapped in clumps. (b) AFM image of thermal annealed AQCs under UHV conditions. The weak interaction with the substrate entailed almost full desorption of the cluster from the mica surface except for the few 2-layers clusters pillars. As a confirmation of the cluster desorption, the background mean roughness of the Cu_5:mica sample is comparable with the 30 pm of clean mica.

of polymerized molecular layers, see (Fig: 5.17. b). The shape and the height of the islands resolved by the ambient-AFM imaging induced to hypothesize a C-C coupling with some discontinuities in the morphology. The defects could be due to the presence of metal-organic coordination bonds and oxide AQCs agglomerations trapped in the island. Comparing the Br_4TPP:Cu_5:mica cross-linked islands with all previous control samples revealed very different topographies distinct from that observed. Moreover, similar to previous studies [67], the 2D network was significantly more stable and resistant to manipulation than the unreacted Br_4TPP.

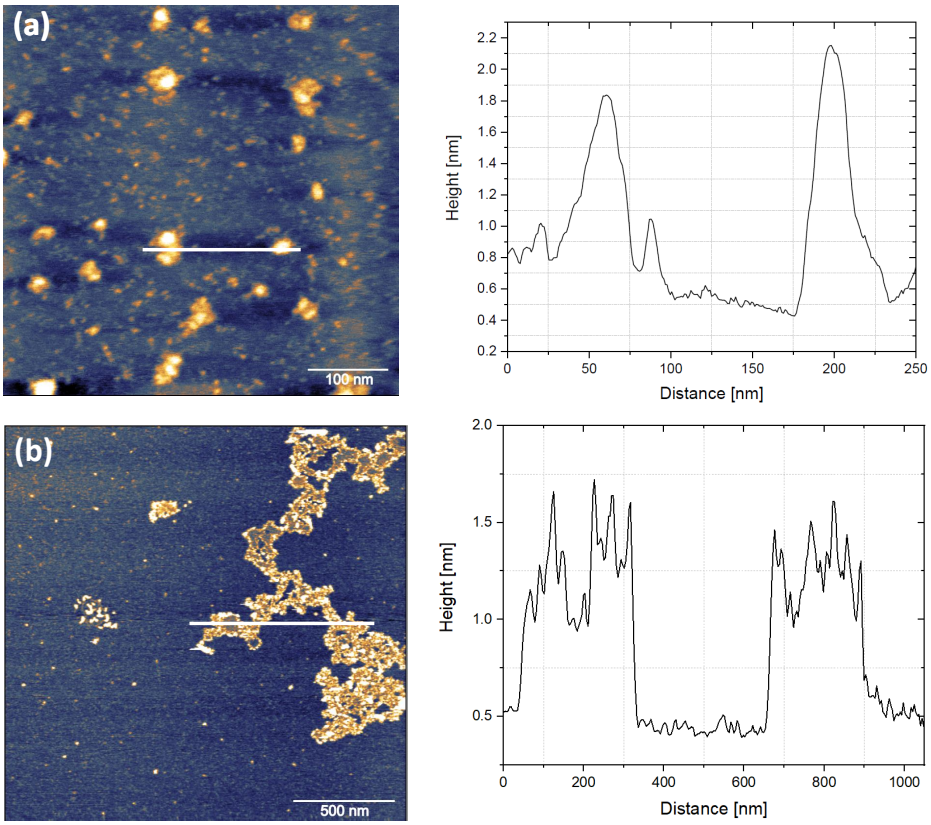

Figure 5.17: **Br_4TPP:Cu_5:mica sample as a function of the temperature.** (a) AFM image of a Br_4TPP:Cu_5:mica sample kept at room temperature. Similarly to the Br_4TPP:Cu_5:HOPG sample, see (Fig: 5.13. a) AQCs, Br_4TPP molecules, and Oxygen contaminants, tend to cluster in 3D chaotic clumps rather than multi-layers assemblies detected in (Fig: 5.14. a). (b) AFM image of a Br_4TPP:Cu_5:mica sample annealed a ∼200 °C under UHV condition. Even though the lattice resolution wasn't reached to resolve the covalent coupled TPP network, the unique shape and dimension of the 2-layers island led to assuming the activation-recombination process was successfully obtained, besides the high presence of feature defects.

The observations of a stable surface structure on the inert surfaces, combined with XPS data of N 1s peak at temperatures higher than full debromination one, suggested that C-C coupling likely took place. Ongoing experiments are trying to confirm these first evidences. Also, for samples prepared on mica, the TP-XPS analysis showed a similarity with the TP-XPS HOPG data. In fact, the Br 3p data, collected in a narrower region around the

184 eV Br 3p peak, showed an activation temperature of (75±25) °C, see (Fig: 5.18. a, b), demonstrating a substantial reduction in the activation temperature of ΔT_{mica} = (120±30) °C. The In addition, the presence of the N 1s peak at a temperature higher than 300 °C, see (Fig: 5.18. c, d), and also the observed chemical shifts for Cu 2p, were most likely due to a C-C coupling, see (Fig: 5.18. g-h).

Finally, in a previous report, TP-XPS measured on the C 1s peak confirmed C-C coupling [245, 247] and, therefore, complete polymerization of the layer. In the present study, however, a combination of resolution limitations from lab-based XPS and the presence of advantageous carbon from ambient sample exposure limited the ability to detect such small shifts.

The results on Au(111), HOPG and mica surfaces provide good evidence that the Cu_5 activated coupling reaction proceeds similarly on both inert substrates, suggesting that coupling is predominantly driven by the Cu_5 and not by the surface, see (Tab: 5.1). Furthermore, as expected, the Br 3p peak downshift and the higher full dehalogenation temperature for Br_4TPP:Cu_5:Au(111) samples confirmed the formation of Br-Cu and Br-Au bonds after the molecular activation.

Surface	$\mathbf{T}_{activation}$ **without** $\mathbf{Cu_5}$	$\mathbf{T}_{activation}$ **with** $\mathbf{Cu_5}$	Δ**T**
	°C	**°C**	**°C**
Au(111)	200±20	125±20	75±20
HOPG	225±25	75±25	150±25
mica	200±25	75±25	125±25

Table 5.1: Analysis for different substrates of the Br_4TPP activation temperature as a function of the Cu_5 AQCs.

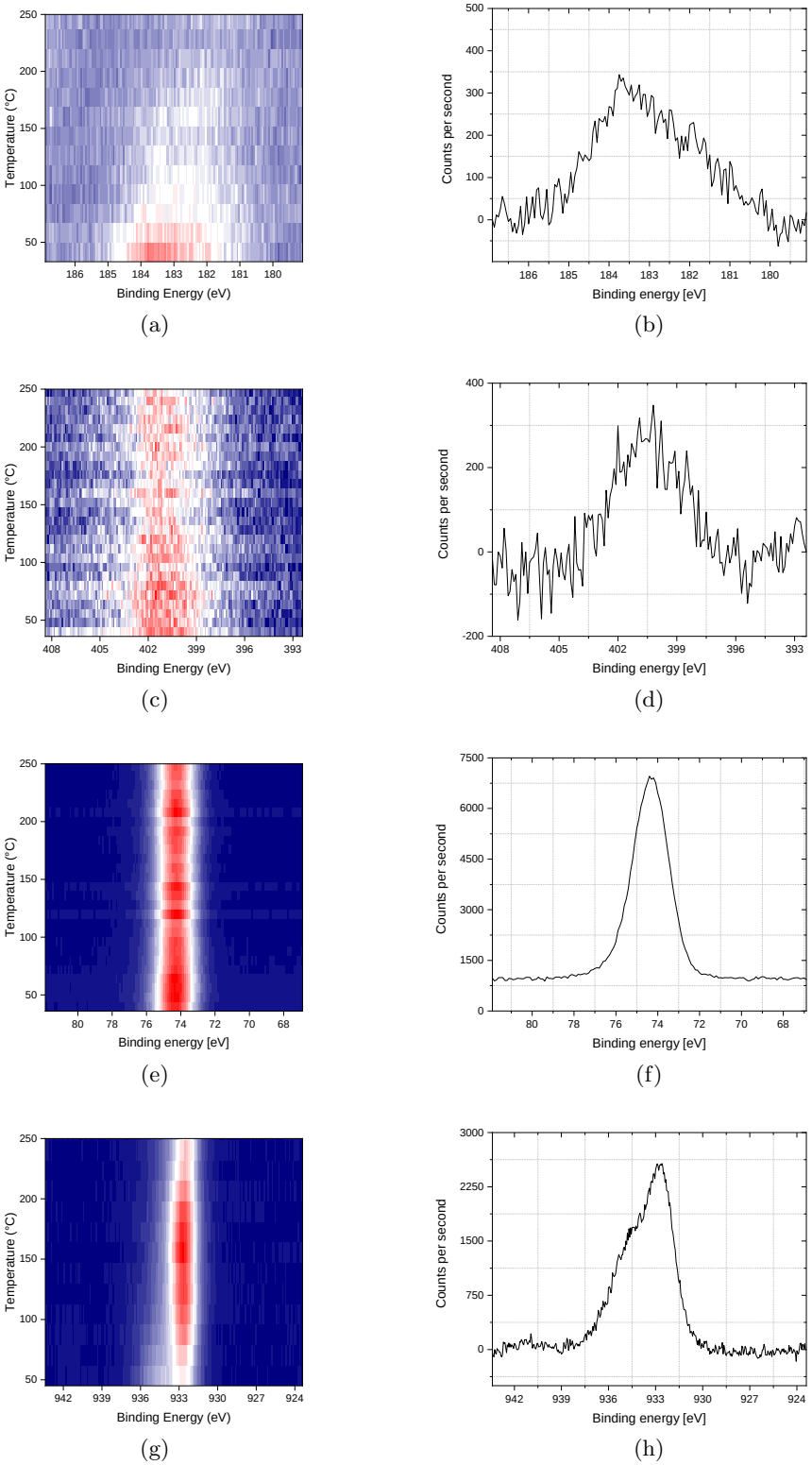

Figure 5.18: **Temperature programmed XPS of Br_4TPP:Cu_5:mica sample.** Analysis in the (a) Br 3p, (c) N 1s, (e) Al 2p and (g) Cu 2p regions with their (b), (d), (f), and (h) respective room temperature spectra. Al 2p region was used as the reference energy.

5.6 Density Functional Theory calculations

This section of the work was achieved by the precious contribution of Dr Wu and Dr Hou in Prof. Lambert's group. Their research is included in this thesis as the theoretical interpretation within the framework of Density Functional Theory (DFT) of my experimental results. To understand the origin of the variation in activation temperature on different substrates, the dehalogenation of bromobenzene was investigated using density functional theory and climbing image nudged elastic band (CI-NEB). Bromobenzene was chosen to reduce the size of the simulation cell. Firstly the dissociation of bromobenzene deposited on the Au(111) surface was demonstrated. The adsorption configurations, charge distributions, binding energies (Eb) for molecular and dissociated bromobenzene, and energetics are shown in (Fig: 5.19). Furthermore, the activation barrier of 1.07 eV and a C-Br distance in the transition state of 2.33 Åon an Au(111) surface were demonstrated. Furthermore, as shown in (Fig: 5.19. d), dehalogenation on Au(111) is found to be an exothermic process, i.e. Br gains more electrons from the substrate when it is split from the phenyl ring, in agreement with previous reports [250]. To model the catalytic activity of Cu_5 clusters, dehalogenation

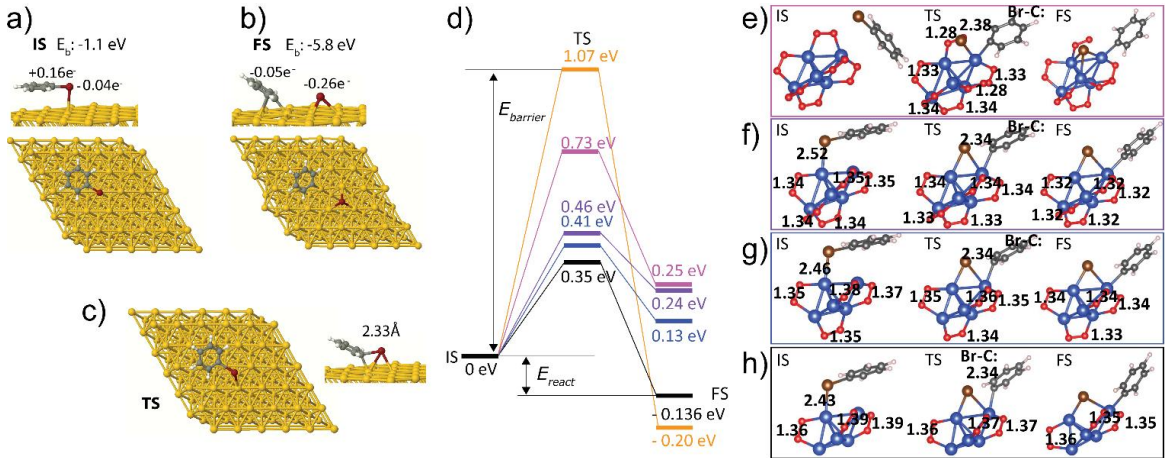

Figure 5.19: **Reaction pathways for dehalogenation of bromobenzene.** (a) Binding energy and charge distribution for molecular bromobenzene adsorbed on an Au(111) surface in the initial state (IS). The binding energy of the entire bromobenzene to the substrate is E_b = -1.1 eV, where the phenyl loses 0.16 e^- and the Br gains 0.04 e^-. (b) Final state (FS) configuration where E_b= -5.8 eV is the binding energy for the dissociated phenyl and Br. The phenyl gains 0.05 e^- while the Br gains 0.26 e^- after the dissociation. (c) Transition state (TS) with Br-C bond length 2.33 Å. (d) Activation barriers and reaction energies for the dehalogenation process catalysed by Cu_5 clusters with different numbers of oxygen dimers. Barriers are compared to that of the Au(111) substrate (yellow). (e-h) The corresponding configurations of the initial state (IS), transition state (TS), and final state (FS) structures with labelled O-O and Br-C bond lengths. Cu, O, Br, C, and H atoms are presented by blue, red, brown, black, and white balls in the configurations.

activated by a single Cu_5 cluster in the absence of any substrate was simulated. This is motivated by the assumption that the inert substrate has negligible influence on the geometrical or electronic structure of the Cu_5 clusters, as supported by the similarity

between experimental measurements on graphite and mica.
In (Fig: 5.19) simulated results for dehalogenation with Cu_5 clusters with increasing adsorbed oxygen molecules, and similarly in (Fig: 5.20) binding energies and bond lengths between O_2 and Cu_5 atoms are shown. It was determined that the binding energy per $O_2(E_b)$ decreases from -2.8 eV for $Cu_5(O_2)_3$ to 1.3 eV for $Cu_5(O_2)_6$, and as shown in (Fig: 5.21), the tightly adsorbed series is more energetically preferred than the loosely adsorbed series, with energy differences ranging from 0.4 eV to 1.0 eV. The tightly adsorbed series was therefore used to simulate the catalytic process for dehalogenation using clusters $Cu_5(O_2)_n$ (n=3, 4, 5, 6) with a 3D bipyramidal geometry.

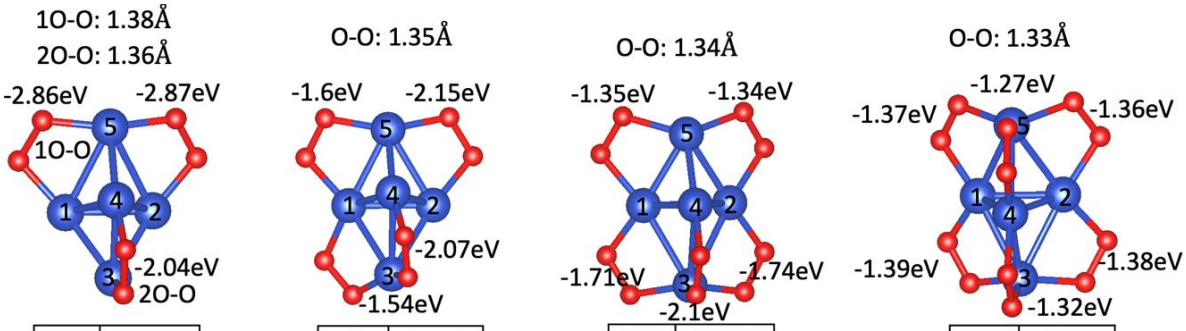

Cu	charge
1	+0.3e⁻
2	+0.3e⁻
3	+0.3e⁻
4	+0.4e⁻
5	+0.6e⁻
Sum	+1.9

Cu	charge
1	+0.55e⁻
2	+0.3e⁻
3	+0.6e⁻
4	+0.33e⁻
5	+0.6e⁻
Sum	+2.3e⁻

Cu	charge
1	+0.55e⁻
2	+0.54e⁻
3	+0.8e⁻
4	+0.3e⁻
5	+0.55e⁻
Sum	+2.7e⁻

Cu	charge
1	+0.52e⁻
2	+0.53e⁻
3	+0.77e⁻
4	+0.5e⁻
5	+0.74e⁻
Sum	+3e⁻

Figure 5.20: **Binding energies and bond lengths of adsorbed O_2 dimers and charge distributions on Cu atoms.**

A series of reaction pathways are shown in (Fig: 5.19) for each of the simulated $Cu_5(O_2)_n$ clusters, compared to Au(111). The reaction path catalyzed by $Cu_5(O_2)_3$, as shown in (Fig: 5.19. h), possesses the smallest energy barrier 0.35 eV and is an exothermic process with a reaction energy of -0.136 eV. For the transition state, the distance between Br and the phenyl ring is 2.34 Å, which is increased by 0.4 Åcompared with the initial Br-C bond. The O-O bond length decreases a little due to the stronger binding of Cu_5 to the dissociated Br and phenyl ring in the final state, which is also observed in the clusters with more Oxygen adsorbed. As shown in (Fig: 5.19. f, g), as the number of O_2 dimers increases, the activation barrier increases to 0.41 eV and then to 0.46 eV. It was also noted that the reaction energy increases to 0.13 eV and then to 0.24 eV for $Cu_5(O_2)_4$ and $Cu_5(O_2)_5$ respectively.
The binding energies E_b and charge distributions of molecular and dissociated bromobenzenes were calculated to understand these phenomena. It was proved that Eb decreases from -0.9 eV to -0.73 eV, which agrees well with the weakening Br-Cu bond length from 2.43 Åto 2.51

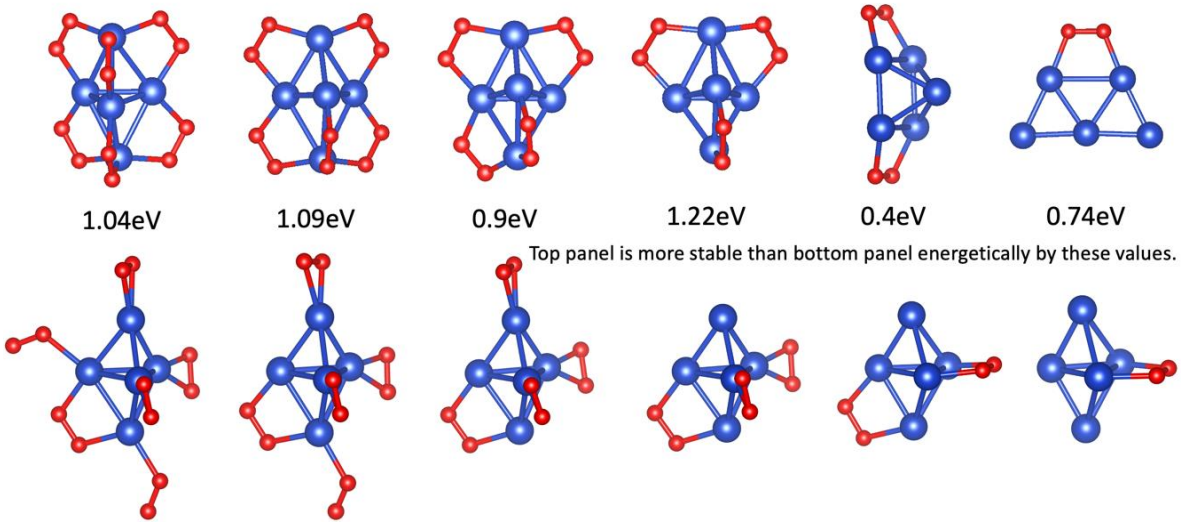

Figure 5.21: **Energetics of the Cu_5 clusters with different numbers of adsorbed O_2.**

Åfor molecular bromobenzenes in the initial state shown in (Fig: 5.22). The E_b decreases from -4.95 eV to -3.96 eV in the final state due to the decreasing charge transfer to the Br adsorbed on the cluster (-0.45 e^- to -0.36 e^-), see (Fig: 5.22). Charge distributions of molecular and dissociated bromobenzenes on Au(111) are shown in (Fig: 5.19. a-c).

To summarize this oxygen adsorption analysis, it was found that as more oxygen dimers adsorb to Cu_5, fewer electrons are transferred to the dissociated Br atom leading to a weaker coupling between the Cu_5 and the bromobenzene. The decreased charge transfer and weakened binding energy lead to a larger activation barrier and reaction energy.

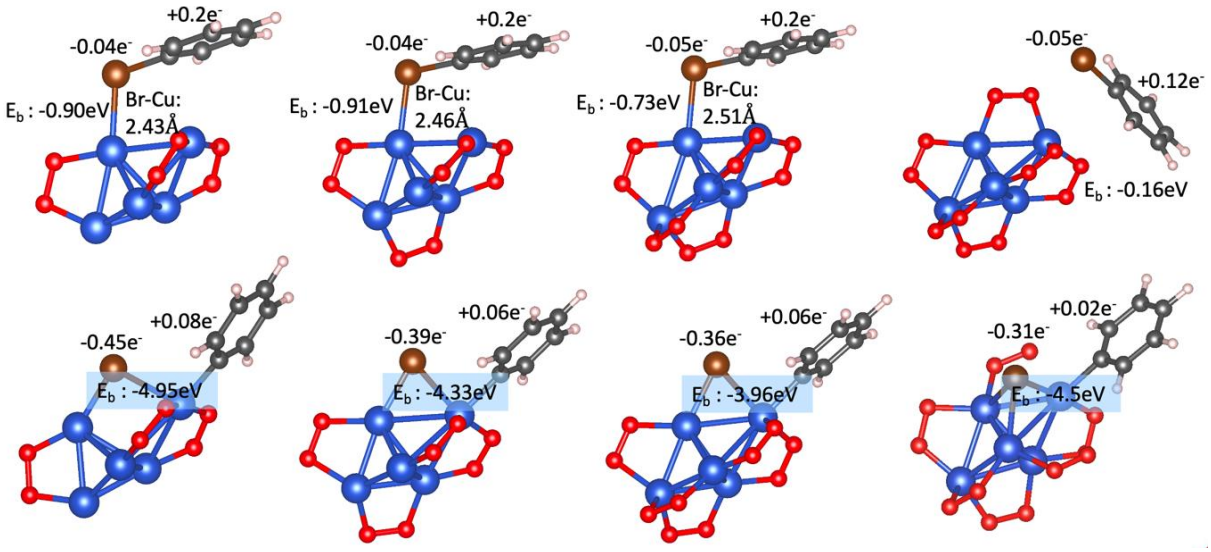

Figure 5.22: **. Binding energies and charge distributions for the molecular and dissociated bromobenzenes**. E_b is the binding energy for both the molecular and dissociated bromobenzene to the substrate. A positive charge denotes that the phenyl loses electrons, while a negative one represents that the Br gains electron.

5.6.1 Appendix

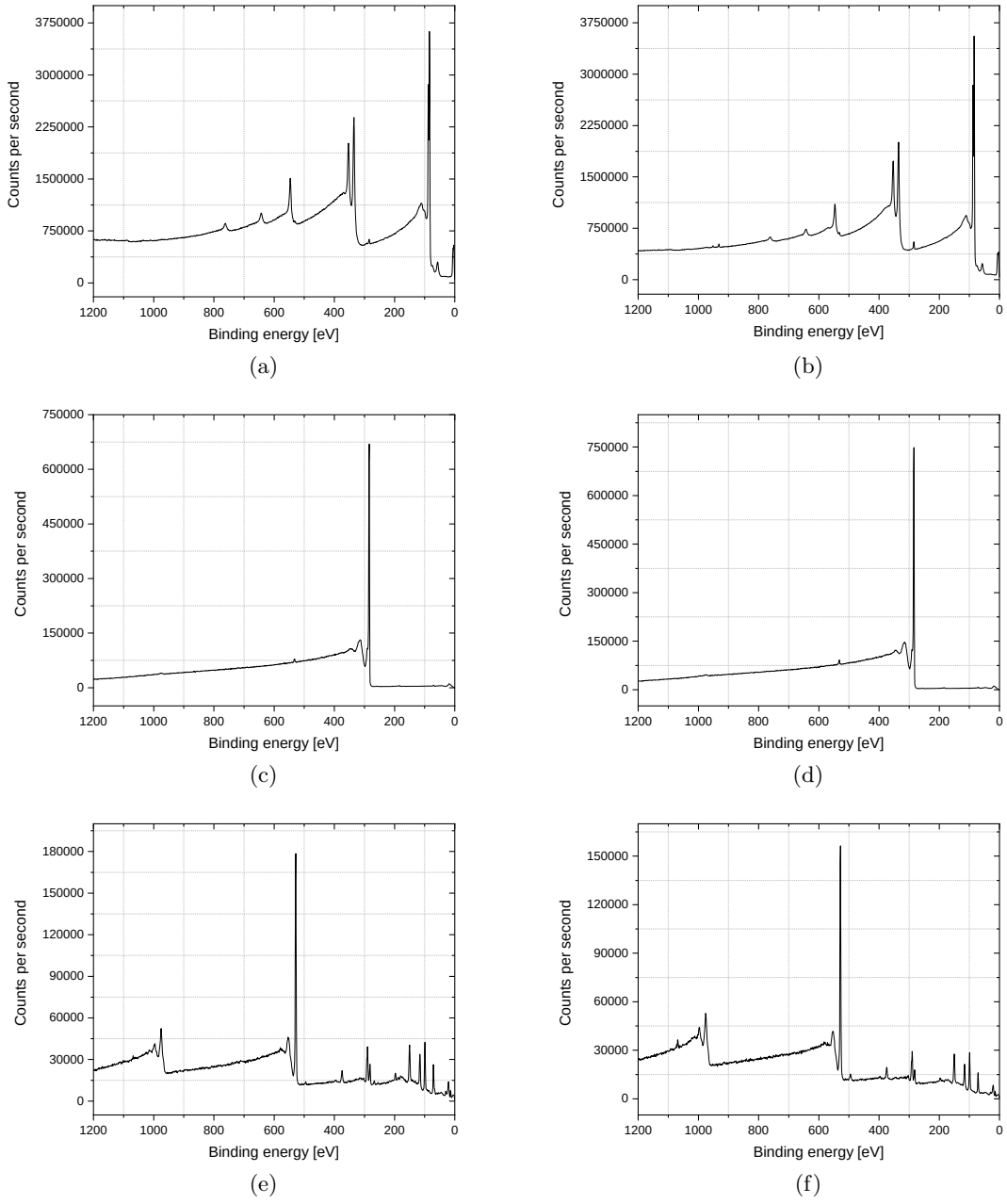

Figure 5.23: **XPS survey wide scan spectra of the samples analysed in the previous figures.** (a) Br_4TPP:Au(111), (b) Br_4TPP:Cu_5:Au(111) (c) Br_4TPP:HOPG, (d) Br_4TPP:Cu_5:HOPG, (e) Br_4TPP:mica, and (f) Br_4TPP:Cu_5:mica samples.

Chapter 6

Resolving sub-molecular structure with ambient AFM

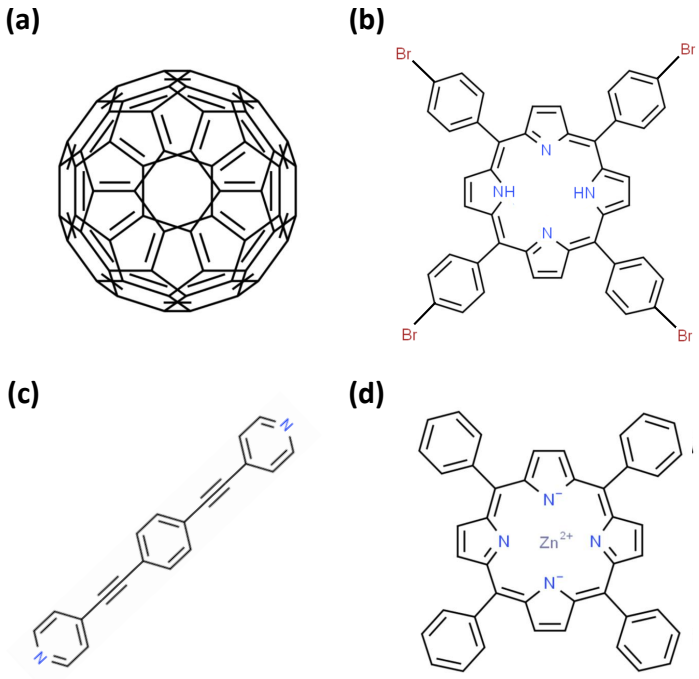

Figure 6.1: **Schematic representation of molecular chemical structures** (a) Buckminsterfullerene (C_{60}). (b) Tetra (4-bromophenyl)-porphyrin (Br_4TPP). (c) 4,4'-(1,4-Phenylenedi-2,1-ethynediyl)dipyridine (BipyOPE3). (d) Zinc tetraphenyl porphyrin (ZnTPP).

This chapter describes how an atomic force microscope (AFM), operated at room temperature and under ambient conditions, can achieve molecular and sub-molecular resolution resolving lateral features <1 nm. These results utilise PeakForce Tapping mode (PFT) performed on a Bruker MM8 housed in the ultra-low-noise IsoLab facility. The IsoLab environment suppresses acoustic, mechanical, electronic and thermal fluctuations.

This environment, combined with a sensitive 'low-contact' method of operation, whereby tip-sample forces never exceed 1 nN, allowed to obtain single molecule and sub-molecular resolutions comparable with results achieved with non-contact AFM under LT-UHV conditions. The images, interpreted in conjunction with density functional theory (DFT) simulations, yield new insights into the achievable limits of microscopy techniques in ambient. The molecules used in this study are: Buckminsterfullerene (C_{60}), Tetra (4-bromophenyl)-porphyrin (Br_4TPP, $C_{44}H_{26}Br_4N_4$), 4,4'-(1,4-Phenylenedi-2,1- ethynediyl)dipyridine (BipyOPE3, $C_{20}H_{12}N_2$), Zinc tetraphenylporphyrin (ZnTPP, $C_{44}H_{28}N_4Zn$), see (Fig: 6.1). Molecules were deposited via standard thermal sublimation on an atomically flat Au(111):mica surface, prepared by repeated sputtering-annealing cycles as previously discussed in the methodology section.

6.1 Exploring single molecule resolution of 2D molecular architectures

A collection of molecular samples were prepared to investigate the limits of resolution of a commercially available Bruker MultiMode 8 equipped with a Nanoscope V operated under ambient conditions. The criteria adopted to test the atomic force microscope was progressively increasing the sample complexity level at each step, analysing the resolution achieved every time in order to confirm 'true' molecular resolution.

6.1.1 Single molecules and rotational domains observed in C_{60}:Au(111) with ambient AFM

The first self-assembly structure explored was a monolayer C_{60} islands surface deposited on an atomically flat Au(111) substrate. As previously reported, a double sputtering-annealing cycle performed the Au(111) flattening under UHV conditions and C_{60} molecules were deposited by thermal sublimation. A 12 minutes deposition at 410 °C formed compact monolayer islands with preferential binding at lower step edges and some small regions of double layer growth, as can be seen in (Fig: 6.2. a). The measured height value of ∼0.7 nm for a C_{60} monolayer matches the one reported in published works [253],
As extensively reported in the literature, the close-packed direction of the fullerene island on Au(111) can adopt four different arrangements [253–256]. The "in phase structure" when the direction of the C_{60} close-packed domain is aligned along $< 1\bar{1}0 >$ direction. This arrangement is also known as 38 × 38 R0°, which stands for a unit cell of 38 × 38 gold atoms, or 11 × 11 C_{60} molecules, and R0° is the angle between the molecular and the substrate directions. Further configurations are: the 7 × 7 R14°, 3 × 3 R34° and $2\sqrt{3} \times 2\sqrt{3}$ R30°. From the analysis of the image of (Fig: 6.2. b), it was not possible to identify each C_{60} close packed island orientation; however three main growth directions (labelled in

blue, red, and green) are visible, and consequently, the pattern discrepancies at the edges of two different domains. The resolution of sharp lattice transitions between two domains and the honeycomb structure of a single C_{60} island, see (Fig: 6.2. c), are the evidence of a single molecule resolution imaging. Furthermore, as a confirmation of the high resolution of the imaging, the topographical line profile of the fullerene pattern (Fig: 6.2. d), where the ∼1 nm mean distance between two peaks matches the literature values [257–259], proves that the feature shown are due to the C_{60} lattice and not because an artefact.

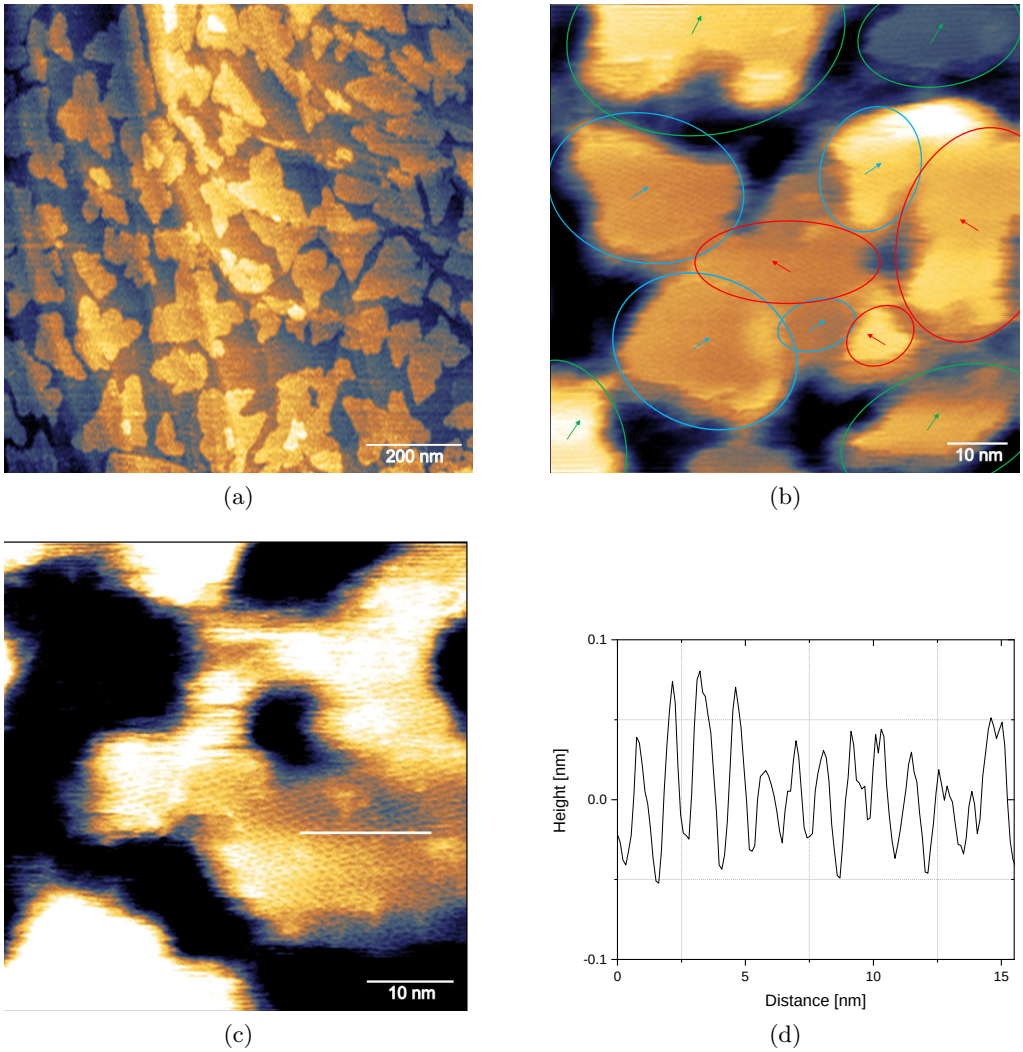

(a) (b) (c) (d)

Figure 6.2: **PeakForce AFM of C_{60}:Au(111) sample.** (a) Close-packed monolayer islands of C_{60} deposited on Au(111). (b) Crystal orientation resolution of different molecular domains labelled in blue, red and green. Superimposed arrows indicate the individual growth directions. (c) Lattice resolution of a C_{60} island. The image was processed using a Fast Fourier Transformation filter to highlight the molecular honeycomb structure. (d) The line profile peak-to-peak distance matches the literature values, confirming the lattice resolution imaging.

6.1.2 Molecular resolution observed in mixed molecular layers of ZnTPP and BipyOPE3

To further confirm the molecular resolution observed and preclude the possibility of 'lattice imaging' effects, samples were prepared with two different lattice sizes. In particular, the molecules chosen to be deposited on an atomically flat Au(111) surface were BipyOPE3, a bipyridine derivative, and ZnTPP, a porphyrin, characterised by a linear and a square structure, respectively, see (Fig: 6.1. b, c). The different chemical structures motivated the choice of the molecules; the expected close-packed superstructure should have different lattices.

The metal surface was prepared as previously described under UHV conditions; hence, molecules were deposited separately to prevent a meta-configuration of the superstructures. First, ZnTPP powder was thermally sublimated at ∼220 °C for 10 minutes; then, a 15 minutes/∼75 °C deposition was performed for the BipyOPE3 molecule. The deposition rate of both of the molecules was determined by a quartz crystal microbalance (QCM), and the deposition time was optimised to have a sub-monolayer coverage of the metal surface for each molecule in order to prevent, or at least reduce as much as possible, molecular stacking. The final result revealed a sample constituted by rectangular islands of ZnTPP surrounded by a close-packed BipyOPE3 background that thoroughly covers the Au(111) substrate, see (Fig: 6.3. a). Due to the low sublimation point of bipyridine, and the intrinsic delay K-cell heating-thermocouple response, the control of the BipyOPE3 deposition was affected by a high margin of uncertainty, sometimes causing clustering of the molecules over the sample. However, the quality of the resolution seemed not affected by the presence of these contaminations, compare panels (a, c) of (Fig: 6.3).

The PeakForce AFM measurements reveal exceptionally clear molecular resolution that are distinct for each molecular species. In wide scans such as (150×150) nm^2, not only the two lattices are clearly distinguishable, see (Fig: 6.3. b), but also the growth directions of different close-packed molecular domains are resolved. More specifically, the different molecular domain orientations are shown in (Fig: 6.3. b) for BipyOPE3, and in (Fig: 6.3. c, d) for ZnTPP, respectively. Furthermore, the highly-ordered nano-porous network of a single-layer island of ZnTPP is perfectly resolved, even though the image needs to be processed to highlight the lattice. The raw AFM data already shows a regular pattern. Still, filtering the noise component by a fast Fourier transformation (FFT), that is, the square units of the porphyrin network, can be resolved, as shown in the progressive filtering steps of (Fig: 6.3. e, f). As expected from the literature, the molecular assembly matches the morphology of the porphyrin space-filling model where the TPP macrocycle face-on and the phenyl groups are rotated due to the interaction with the metal substrate.

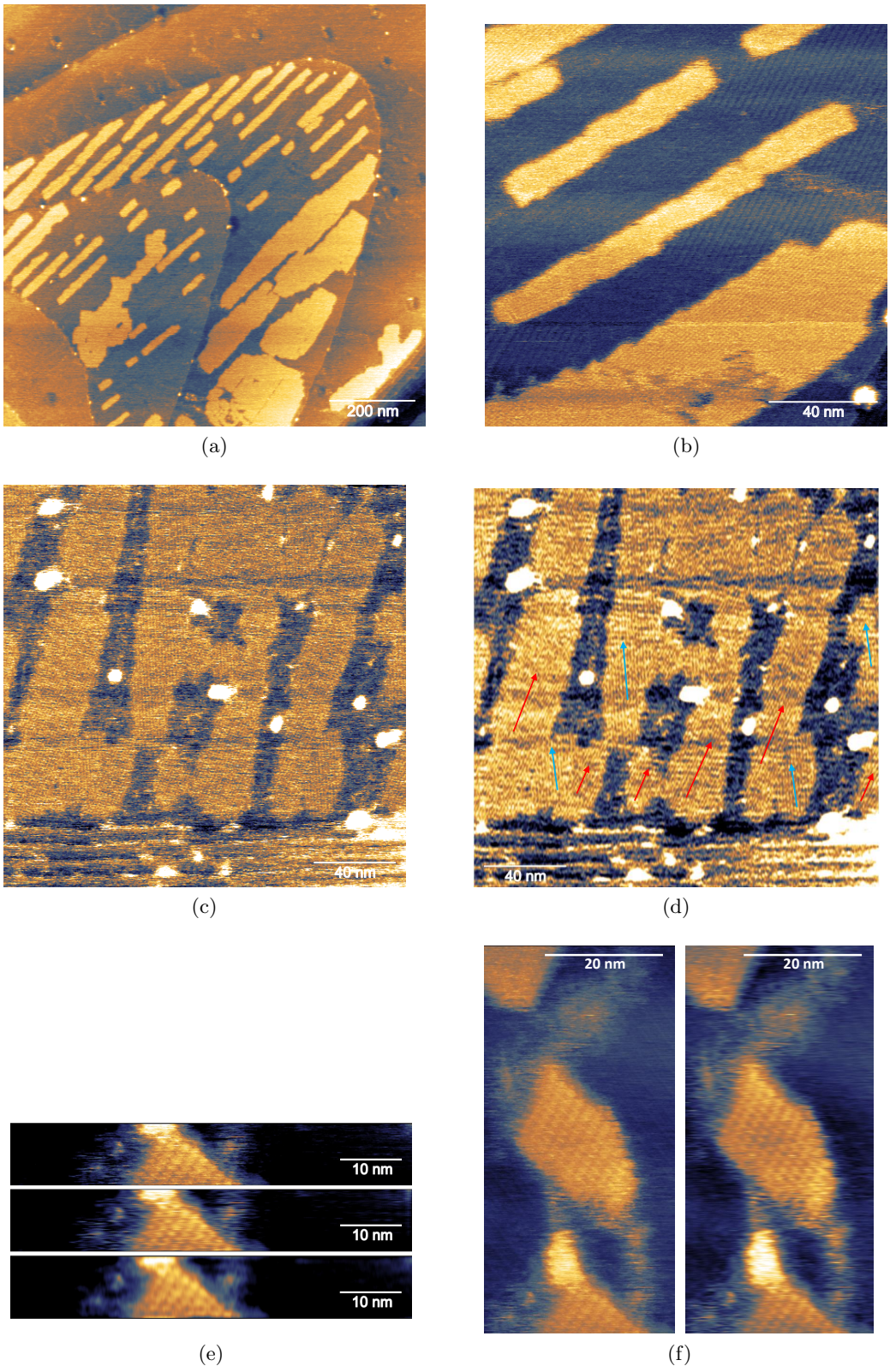

Figure 6.3: **PeakForce AFM of BipyOPE3:ZnTPP:Au(111) sample (1).** (a) Overview of the double deposition occurred as a formation of ZnTPP narrow islands surrounded by a close-packed BipyOPE3 background. (b) Both the crystal lattice of each molecule and the BipyOPE3 growth directions of different domains are resolved. Proving both lattice and evidence of single-molecule resolution. (c, d) Raw and Fast Fourier Transformation filtered images of an area mainly covered by ZnTPP. The crystal orientation of different packing is perfectly resolved. Superimposed arrows indicate the individual growth directions. (e, f) Raw and FFT filtered images of a ZnTPP island. The progressive process of filtering highlights the regular pattern of the lattice.

The deposition rate was improved to prevent molecular stacking and obtain a ZnTPP semi-monolayer adsorbed onto the Au(111) surface, by reducing the temperature to 210 °C and increasing the time to 20 minutes. Hence, following a Stranski–Krastanov growth, molecular structures lost their rectangular shape covering wide substrate areas. As before, the following bipyridine deposition covered the metal surface between the ZnTPP islands and, due to a long deposition time, clustered in a few nm high structures, see (Fig: 6.4. a). However, even for wide scans, both the lattices are clearly resolved, showing a higher quality resolution than before, see (Fig: 6.4. b). Both the space-filling porphyrin arrangement and the packing formation of BipyOPE3 are resolved both individually see (Fig: 6.4. c) and (Fig: 6.4. d), respectively, and at the same time see (Fig: 6.4. e, f), showing the nano-porous ZnTPP network and the bipyridine stripe arrangements. The strong vdW interactions and bonding between the Nitrogen atoms of the BipyOPE3 and the metal surface are expected to constrain the molecules to lie flat on Au(111) rather than stand upright. The distance between two consecutive peaks of these stripes is measured at approximately 4 nm, and according to the literature, a single bipyridine molecule is ∼1.6 nm long; therefore, each line is likely formed by pairs of BipyOPE3 molecules end-to-end interacting. The mismatch between the measured value (approximately 4 nm) and the theoretical one (∼3.2 nm) is reasonably due to the thermal drift of the imaging.

Furthermore, the single molecule resolution allows the imaging of small features perpendicular to the stripes due to the BipyOPE3 packing assemblies. According to Izzouihda *et al.* [260, 261], pyridine superstructures tend to assume two different conformations. Considering top, bridge and hollow as the common adsorption sites for bipyridine onto an Au(111) surface, the molecular arrangement is likely to be formed either by a four rows BipyOPE3 formation aligned by the Nitrogen anchor groups (∼2 nm wide) or by a three rows where the Nitrogen atoms are misaligned (∼1.5 nm wide), see (Fig: 6.5). Besides, as said before, bipyridine molecules tend to pack as a couple; hence each row is formed by two pairs of molecules, labelled as A and B in (Fig: 6.5), where the peak-to-peak distance from the middle of the two is approximately 4 nm length. Therefore, the feature perpendicular to the stripes resolved by the imaging is the gap between the A and B couples of bipyridine. That the two species can clearly be resolved with multiple orientations excludes the possibility of 'lattice' type imaging, providing good evidence for single molecule resolution.

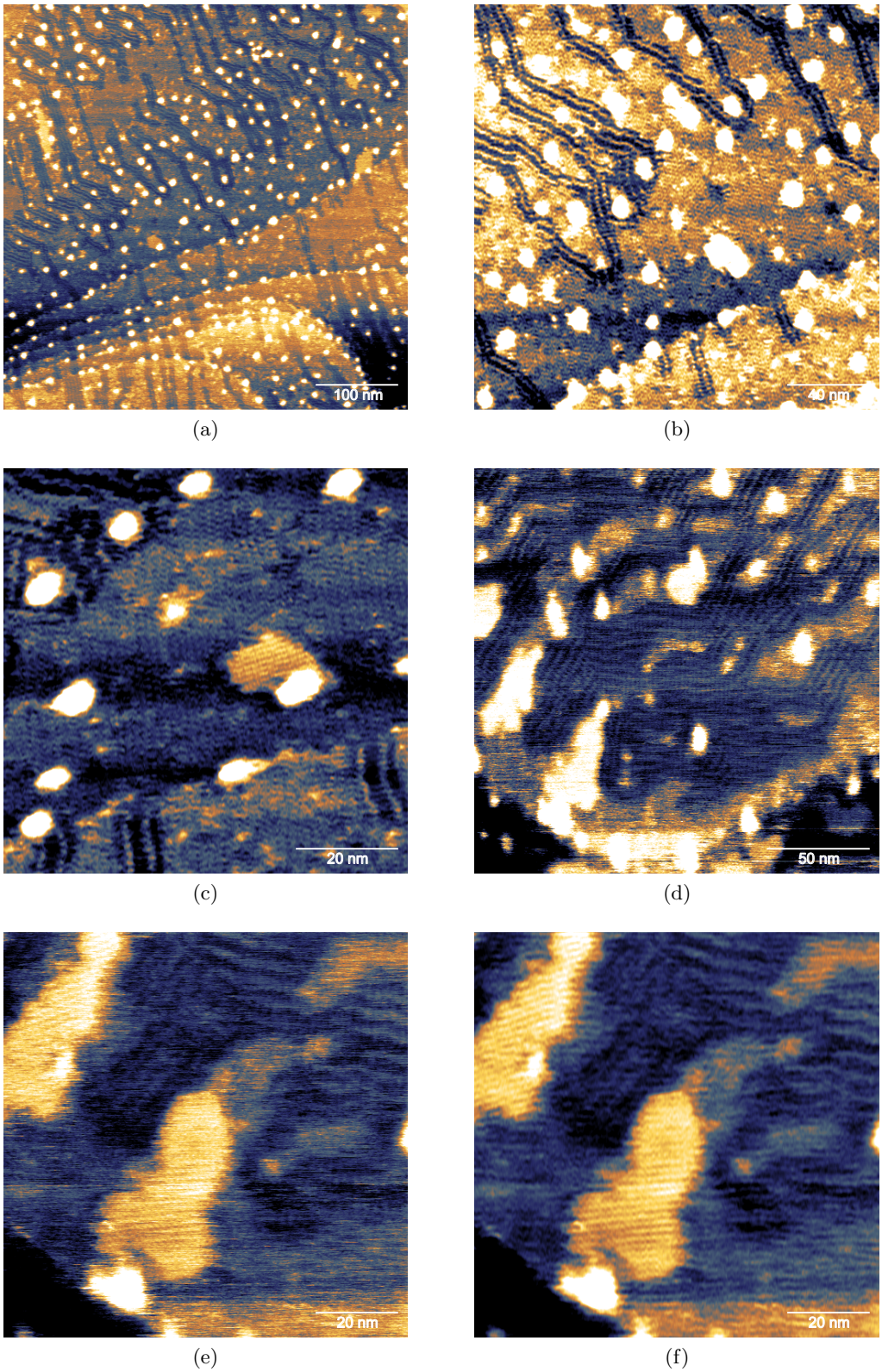

(a) (b) (c) (d) (e) (f)

Figure 6.4: **PeakForce AFM of BipyOPE3:ZnTPP:Au(111) sample (2).** (a) Overview of the double deposition. A high amount of defects characterises the sample due to the BipyOPE3 clustering. (b) Lattice resolution of both molecules. (c, d) FFT filtered images of a main ZnTPP and BipyOPE3 domains, respectively, showing single molecule resolution. (e, f) Raw and FFT filtered images of an area characterised by the coexistence of mixed molecules. Both the lattices are simultaneously resolved.

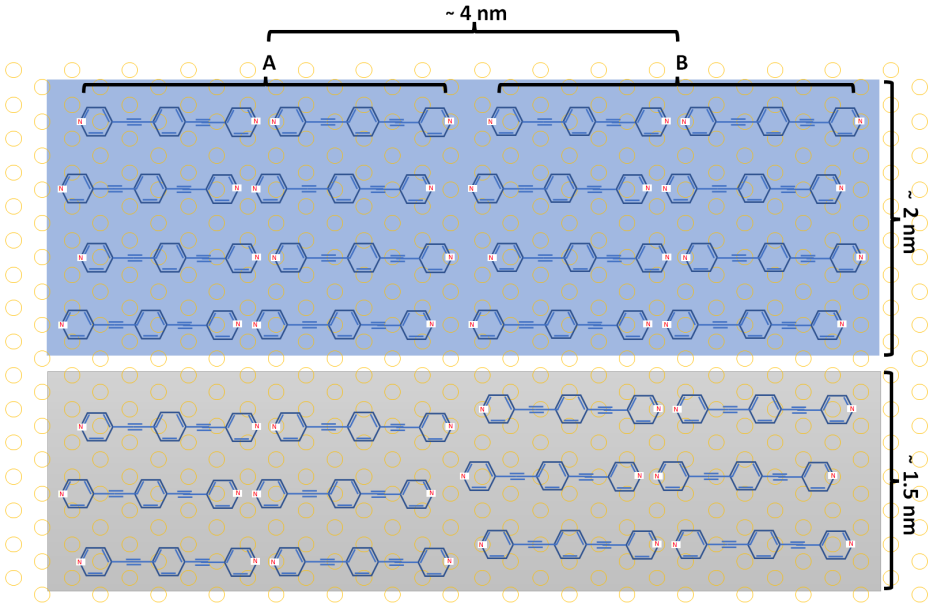

Figure 6.5: **Schematic representation of BipyOPE3 molecules adsorbed on a Au(111) surface.** Bypiride tends to be arrangements formed by a couple of molecules; see columns A and B. The molecular pairs could pack either in four rows disposition aligned by the Nitrogen atoms (blue panel) or in a staggered three rows disposition in which the Nitrogen of the different columns are misaligned (grey panel).

6.1.3 Single molecule details of a TPP polymer

Further evidence of single molecule resolution under ambient conditions was found by imaging a covalently linked molecular polymer.

For this, we used Tetra (4-bromophenyl)-porphyrin (Br_4TPP) deposited on Au(111). Prior to surface annealing, the molecules arrange into islands up to 400 nm wide, that were likely to nucleate at the step edges, see (Fig: 6.6. a). The characterisation of these molecular islands exhibited close-packed nano-structures, which minimised the intermolecular distances due to molecular diffusion on the gold substrate. The lattice resolution of AFM topography show hints of molecular detail already demonstrated by Grill *et al.*, both for the raw and the FFT filtered image, see (Fig: 6.6. c, e) respectively.

As already seen in the previous chapter, if a Br_4TPP:Au(111) sample is annealed in UHV at 150 °C, for 10 minutes, porphyrin is subject to the cleavage of carbon-halogen bonds, followed by molecular recombination to form a covalent-coupling network. Different from Grill's nano-structure, the high-resolution AFM in ambient showed a TPP polymer characterised by a disordered packing, with a low presence of contaminants trapped in the chains. Nevertheless, this chaotic arrangement demonstrates high-resolution imaging. In fact, the utter absence of a regular and periodic pattern proves that a lattice resolution is not possible; hence, not only the position and the orientation of some molecules is resolved, confirming single-molecule resolution imaging, and also hints of sub-molecular details (e.g. the observation of small features in the corner of each molecule).

In conclusion, the orientation images of C_{60} and ZnTPP islands with highlights for different crystal directions, the resolution of mixed molecules with completely different packing of BipyOPE3:ZnTPP:Au(111) samples, showing details of both molecular arrangements, and the resolution of a C-C network, after the activation of Br_4TPP islands, are the evidence that a commercial AFM, even though operating under ambient conditions, can achieve single molecule resolution in a facility such as IsoLab. Furthermore, the sub-molecular details resolved in the polymer data gave hints that sub-molecular resolution is feasible.

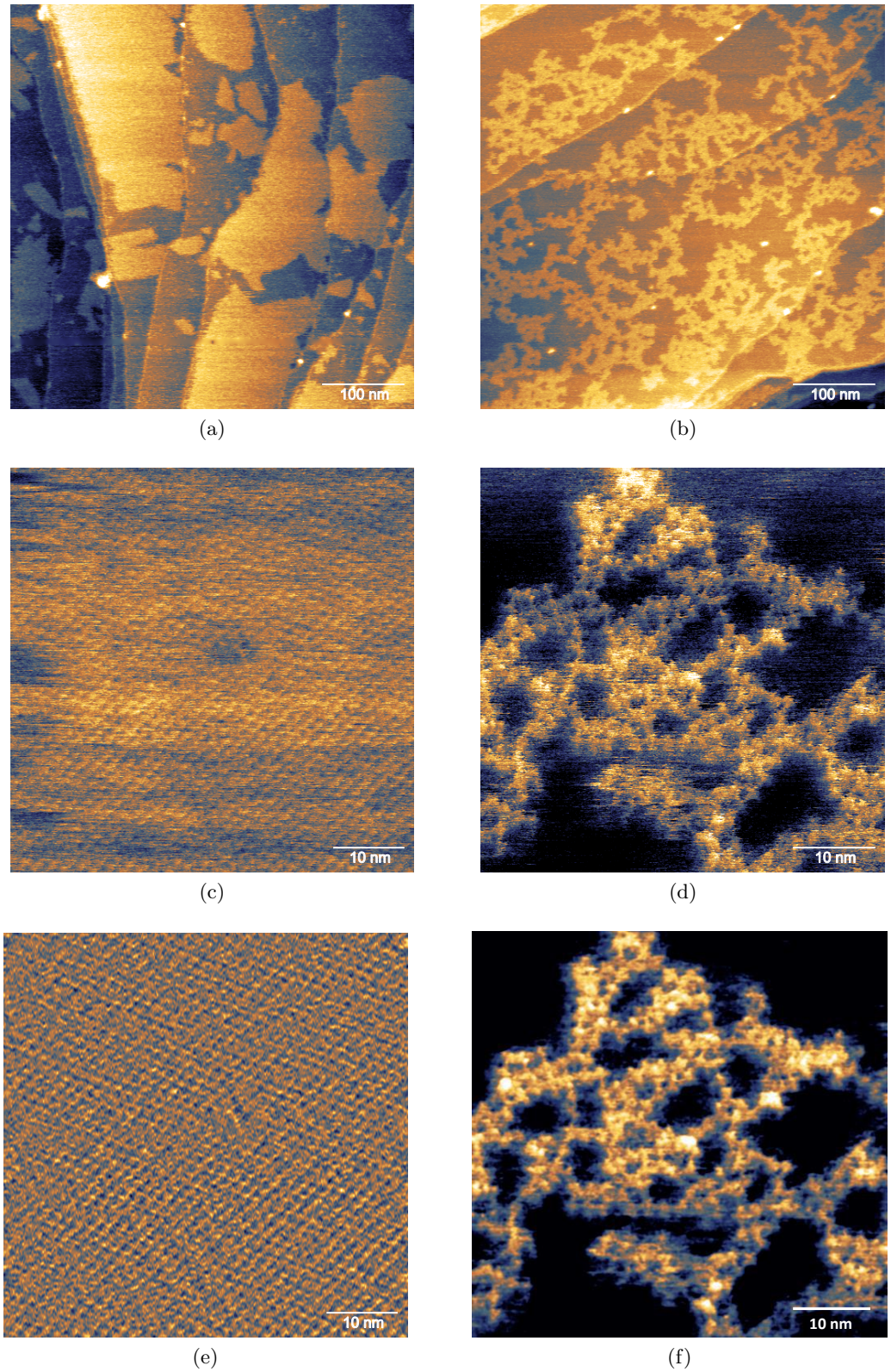

Figure 6.6: **Br_4TPP molecules before and after the activation/recombination reaction.** (a) Overview of the close-packed Br_4TPP superstructures grown on Au(111) surface. (b) Overview of the crosslinked Br_4TPP molecules after the thermal activated debromination. (c-e) Lattice resolution of raw and FFT filtered images of the close-packed molecular arrangement. The defects, such as the blue area in the centre of the (c) panel, give hints of single-molecule resolution. (d-f) Single-molecule resolution of raw and FFT filtered images of the C-C TPP polymer, justified by the absolute lack of lattice periodicity and symmetry. Especially panel (f) shows hints of corner structures suggesting a sub-molecular resolution.

6.2 Sub-molecular structure observed with ambient atomic force microscopy

Thus far, molecular resolution has been demonstrated and, in some cases, hints of undefined sub-molecular detail observed. Here this part of the research shows that is possible to resolve and interpret features within a single molecule, which can be assigned to specific moieties within the molecular structure (sub-molecular resolution).

6.2.1 Instrument optimisation for sub-molecular resolution

As described below, PeakForce mode, implemented in the Nanoscope V, enables a high degree of control of the instrument, allowing to approximate conditions similar to that used for high resolution imaging with qPlus NC-AFM. These details are described here, rather than in the methodology section, as they are non-standard and their development was key to enabling the molecular resolution imaging described in this chapter.

One of the primary factors to achieving higher resolution is measurement optimisation during tip approach, in addition to the actual scanning. In fact, to reduce the chance of damaging the sample or contaminating the tip collecting material from the surface, the probe must be approached as softly as possible. For this reason, the Peak Force Engage Setpoint was reduced to the lowest possible value which could be measured on the instrument (i.e. just above the noise floor of the instrument). To improve the responsiveness during approach, the Engage integral gain was also set to a higher value than usual. Furthermore, to reduce the chances of crashing the tip onto the sample and increase the control of the sample approach, the default value of Peak Force Engage Amplitude of 100 nm was reduced to 0.3 nm, and the Step Height, that is, the distance the probe is moved downward without encountering the sample was reduced from 200 nm to 20 nm. The last two values let to increase the control of tip amplitude oscillation. However, as a result, the approach becomes extremely slow, and it can take several minutes to engage the sample; furthermore, the high Gain and the low Setpoint can cause a series of false engages that can further slow down the process of sample approaching. To partially overcome these issues, the tip was manually brought in proximity to the surface, monitoring its position by an optical magnifier set up in front of the AFM probe holder.

The scan settings should be adjusted depending on the scan size, particularly the Z limit, that is the maximum allowable vertical scan range to achieve higher digital resolution in the Z direction. In general, for large topographies taken to check the molecular deposition and the packing arrangement (higher than (200×200) nm^2), the Z limit was set at 500 nm, for mid range scans (between (50×50) nm^2 and (200×200) nm^2) the value was between 200 nm and 300 nm, and for small range scans (lower than (15×15) nm^2) it was possible to use 100 nm. A low Z limit increases the scan control as the probe displacement is reduced; however, the chances to disengage or crash the tip on the sample substantially increase. Therefore, it

should be changed only in homogeneous, flat and contaminant-free regions of the surface. Similarly, for large and mid scans, the standard values of PeakForce Tapping Control section, respectively: Peak Force Amplitude: 20 nm, Peak Force Frequency: 2 KHz, and Lift Height: 40 nm, were enough for lattice and single molecule resolutions; the sub-molecular resolution, for small scans, was possible only setting the values as Peak Force Amplitude: 5-3 nm, Peak Force Frequency: 4 KHz, and Lift Height: 10-6 nm. Low values of the Lift height parameter, that is, the distance that the Z piezo is retracted from the sample, reduce the chances of piezo-creep during the measurement; furthermore, the reduction of Peak Force Amplitude, that is, the zero-to-peak amplitude of the cantilever drive in the Z axis, increases the contact time during each tip-tapping cycle, which, in combination with a higher Peak Force Frequency, and a very low Peak Force Setpoint (between 50 and 25 pN) are the very key-factors for sub-molecular resolution. In contrast, for large and mid scans, a Peak Force Setpoint of 125-200 pN were enough for lattice and single molecule resolution. Still, the resolution of some molecular features was feasible only by reducing the force, prolonging the tip contact, and augmenting the number of tip-sample interactions. Finally, Feedback Gain, Scan Rate and Sample/Line were adjusted to increase the signal-to-noise ratio and compensate for the measurement drift. Generally, the values ranged from Feedback Gain: 12-8, Scan Rate: 0.5-1 Hz, and Sample/Line: 512-1024. As a rule of thumb, to minimise the noise and the drift, the higher the Sample/Line value, the higher the Scan Rate and the lower the Feedback Gain.

To reduce the thermal drift and acoustic noise, in addition to housing the AFM within the ultra-low noise IsoLab facility, the AFM was further enclosed in a custom shield with inner walls covered in sound-absorbing foam, carrying out the measurements 20-30 minutes after the sample positioning in the AFM, waiting for the stabilisation of the thermal fluctuation inside the box.

6.2.2 Evidence of Sub-molecular resolution measuring close-packed ZnTPP superstructures

Applying the optimised PeakForce AFM method on ZnTPP:Au(111) samples, a resolution improvement was immediately observed, even for a wide scan. The preparation was carried out using the procedure already developed for the BipyOPE3:ZnTPP:Au(111) sample; however, due to the low sublimating temperature of pyridine that caused the growth to be difficult to control, it was chosen to use the porphyrin exclusively. In this case the ZnTPP deposition was longer than before to create a full monolayer over the atomically flat Au(111) substrate, to reduce as much as possible molecular diffusion. As can be seen in Fig: 6.7. a), the sample was homogeneously covered, with low levels of contaminants. Even at large scan sizes of (150×150) nm^2 scan, not only the close-packed monolayer crystal lattice was recognisable, but also the presence of kink sites at the edges of two neighbouring islands, as it can be observed in (Fig: 6.7. b).

As expected, the smaller the scanned area was, the higher the resolution became, showing clear single molecule resolution for a (50×50) nm^2 scan and (41×32) nm^2 scan of (Fig: 6.7. c, d). Both images are FFT filtered to highlight the features. In (Fig: 6.7. c), the single molecule resolution is indirectly demonstrated due to the pattern resolution disappearance at the defects as the central cluster or the trough at the edges of the island. As this behaviour cannot justify a lattice resolution. On the other hand, in (Fig: 6.7. d), the evidence is direct as the disposition and orientation of the single molecules is clearly resolved. As a further evidence of single molecule resolution, the (30×30) nm^2 raw and FFT filtered images of (Fig: 6.7. e, f) showed the molecular arrangement at edges of the islands.

To test the limit at which the microscope resolution could be pushed, a defect-free area of the molecular arrangement of (Fig: 6.7. d) was chosen to attempt a 15 × 15 nm^2 scan. Two consecutive topographies, top-to-bottom (Fig: 6.8. a, b), and bottom-to-top (Fig: 6.8. c, d) showed, for the raw and the FFT filtered data, sub-molecular features. At first glance, it appears that a square central feature is visible, with four smaller spots at each corner. This is more clearly visible in a smaller area of (5×5) nm^2 wide. However, as it can be noticed from both the top-to-bottom (Fig: 6.9. a, b), and bottom-to-top scan (Fig: 6.9. c, d), the measure started to be unstable. The first two panels, raw and FFT filtered data, were affected by an evident drift due to the Scan Size reduction, which was compensated in the second two; however, all four images were altered by a periodic noise (parallel lines). To overcome the issue, the Scan rate was increased from 1 to 2 Hz, and the Sample/Line doubled from 512 to 1024, achieving a higher-quality sub-molecular resolution in ambient conditions with a commercial AFM, see raw and FFT filtered topographies of (Fig: 6.9. e, f).

To give a correct interpretation of the image, and confirm that the sub-molecular resolution wasn't affected by any measuring artefact, my colleague and PhD student Edward Dunn in collaboration with the group of Prof. Andreas Larsson from the LuleåUniversity of Technology in Sweden, contributed to this research by simulating the molecular interaction and packing of ZnTPP complete with simulations of constant force AFM that can be directly compared to the PeakForce mode used in this study.

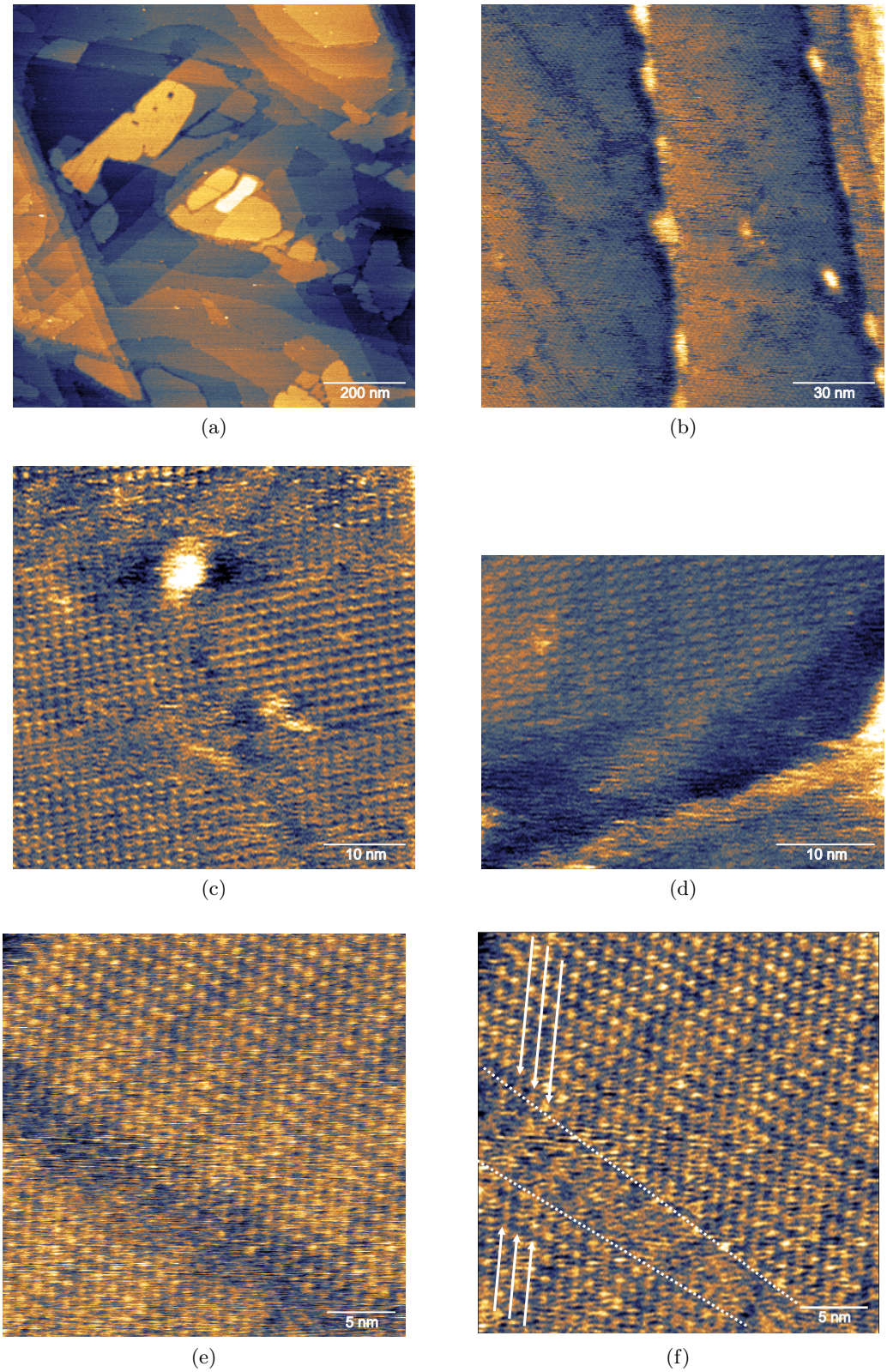

Figure 6.7: **PeakForce AFM of a ZnTPP:Au(111) sample.** (a) Overview of the close-packed ZnTPP full monolayer, with some areas characterised by multilayer structures. (b) Lattice resolution of a fully covered area. (c) Single-molecule resolution indirectly demonstrated by defects interrupting the lattice periodicity and symmetry. The image was FFT filtered. (d) Single-molecule resolution directly observed of an FFT filtered topography. (e-f) Single-molecule resolution of a raw and FFT filtered topographies at the edges of the islands. The dotted lines show the island edges, the arrows indicate the molecular arrangement.

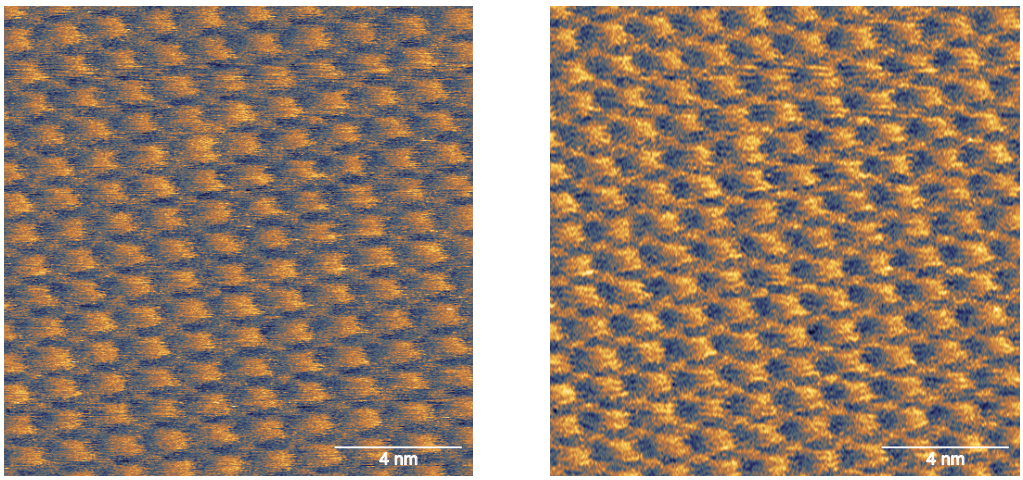

(a) (b)

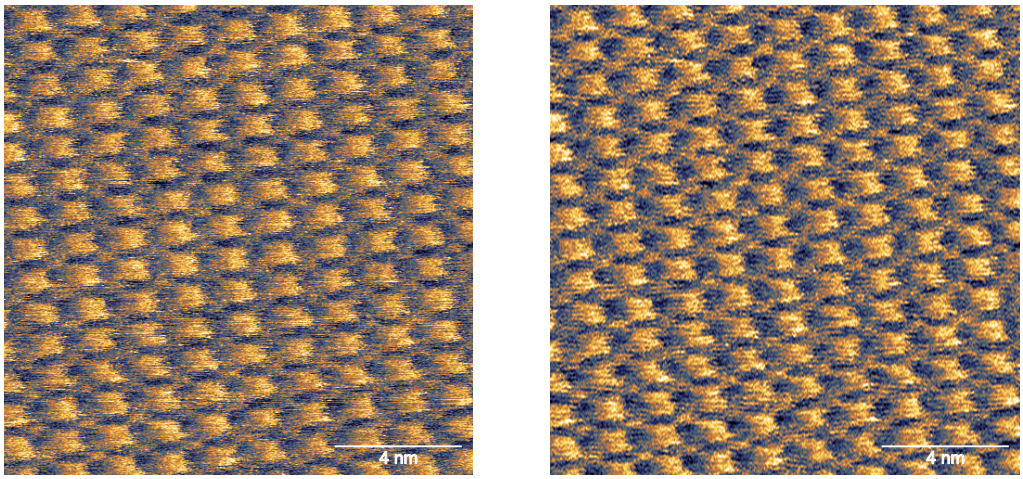

(c) (d)

Figure 6.8: **Single molecule resolution of a defect-free ZnTPP arrangement.** (a, c) Raw and (b, d) FFT filtered topographies of a top-to-bottom and bottom-to-top scans, respectively. The central body and the four phenyl groups are defined for most of the molecules of the images.

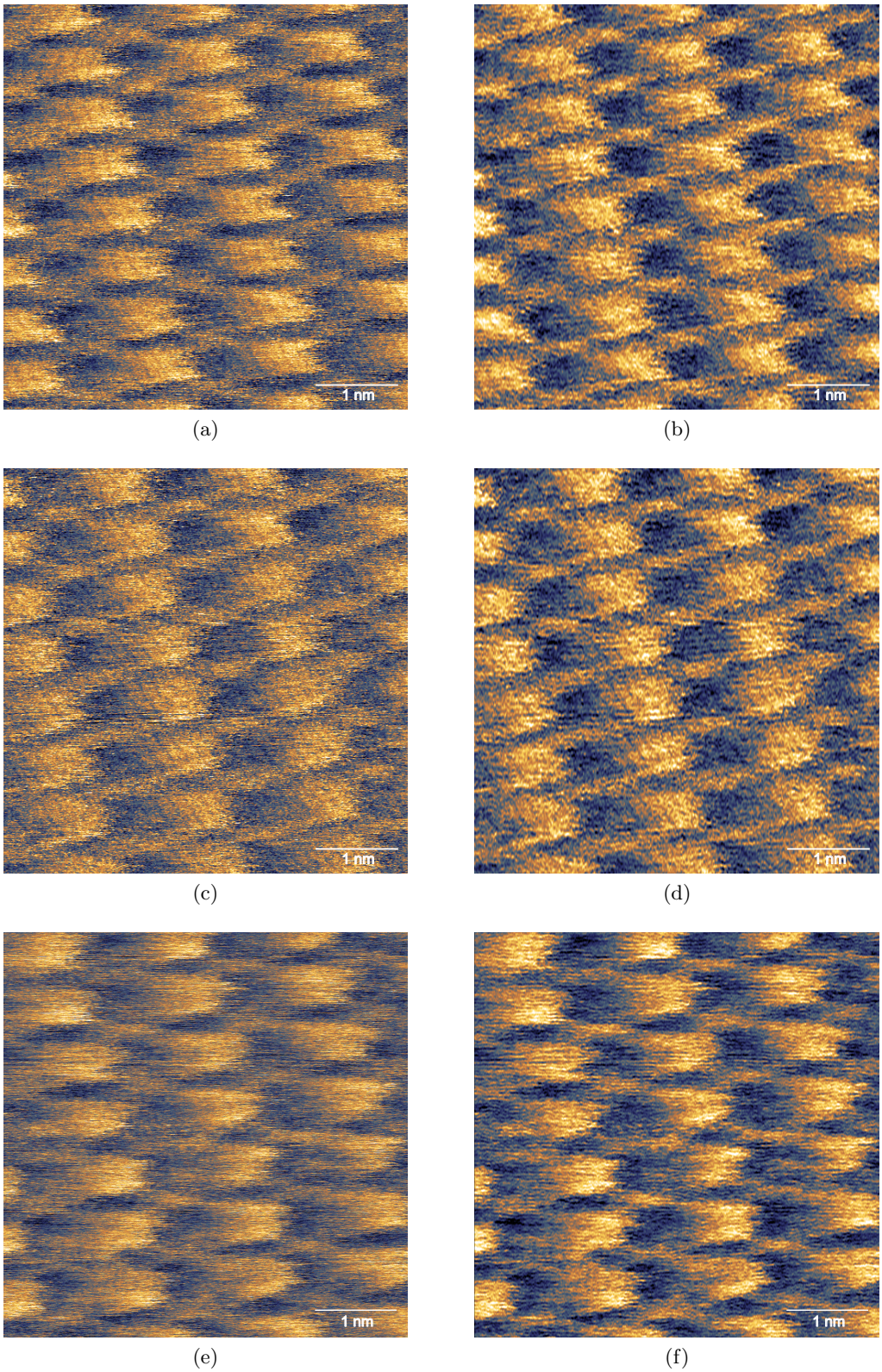

(a) (b) (c) (d) (e) (f)

Figure 6.9: **Sub-molecular resolution of a defect-free ZnTPP arrangement.** (a, c) Raw and (b, d) FFT filtered topographies of a top-to-bottom and bottom-to-top scans, respectively. The measurement was performed using a Scan rate of 1 Hz and a Sample/Line of 512. (e) Raw and (e) FFT filtered of a higher-quality topography, where sub-molecular features are resolved. The acquisition parameter used are Scan rate of 2 Hz and a Sample/Line of 1024.

6.2.3 Constant force simulations of sub-molecular AFM

Density functional theory calculations were carried out by the group of Prof. Andreas Larsson from the LuleåUniversity of Technology in Sweden using vdW corrected functionals implemented within the VASP code. This follows methods previously developed when modelling Br_4TPP:Cu(111) [231, 232]. Due to the lattice mismatch between the ZnTPP overlayer and the underlying Au(111) surface, the simulations modelled three Au(111) cell sizes with the overlaid ZnTPP. This includes a [-1 5] [5 -2] cell, [-1 6] [6 -2] cell, and a 'stretched' Au(111) unit cell, based on an initial cell size of [-1 5] [5 -2] stretched by <1% such that the ZnTPP-ZnTPP spacing was 14 Angstroms as previously determined with LT-STM studies. The [-1 5] [5 -2] cell and [-1 6] [6 -2] cell are specifically included as they result in molecular spacings that are too small or too large, respectively, and therefore provide insight into the effect of molecular spacing on simulated AFM images.
AFM simulations were carried out using a modified version of the Probe Particle Model [241]. This simulation models constant height NC-AFM by modelling a tip as two particles with a relationship which can be described by Hooke's law. One particle, the 'probe particle', interacts with the object to be imaged via the Lennard-Jones potential and, as a result, imparts a force to the particle representing the tip. This allows for the simulation of images created by functionalized tips and nano-asperites [242, 243]. The Lennard Jones potential is calculated from a set of atomic coordinates as a 3D grid of points, each with a calculated force it would impart onto the tip if it were in that location. Then the simulated tip is moved across the x-y plane at a specific z value. At each point, the probe particle is relaxed so that the force is minimized and the position of this particle is recorded along with the z component of the force it applies to the cantilever particle. Repeating the process for a range of z values allows the user to observe the images one could observe from AFM measurements at different heights above the molecule. The data provided from the planes of force measurements is then converted into another 3D grid representing the force experienced by the tip after the particle representing the CO particle has relaxed. By arranging the data into this cube one can think of the data as lying in columns, each positioned at an x-y co-ordinate. In order to simulate a constant force measurement: a threshold force is chosen and the force at each z value in a column is considered, starting at the top and moving downwards. The first point where the force first exceeds the threshold force is chosen and the height of this point can then be plotted as the value for that x-y co-ordinate. The process is depicted in (Fig: 6.10) (kindly provided by Prof. Andreas Larsson and my colleague and PhD student Edward Dunn), where the recorded z value can be seen to follow the shape of the surface from above. Repeating the process at each x-y co-ordinate builds up a topographic image of the surface. The ball and stick diagrams in (Fig: 6.10. a, b) show the minimum energy configuration for ZnTPP molecules bound to the stretched [-1 5] [5 -2] surface cell, rotated consistent with previous results from STM measurements [241]. As can be seen in the ball and stick structure, the phenyl rings interact with one another causing

the rings to rotate such that they are 'higher' in Z compared to the rest of the molecule. In comparison, simulations on the larger [-1 6] [6 -2] cell show no such interaction, where instead the molecules are spaced so far apart that they behave as single isolated molecules. In the unstretched [-1 5] [5 -2] cell, the molecules are unrealisticly close, and the phenyl rings rotate almost perpendicular to the surface plane. (Fig: 6.10. c) shows a simulated constant force AFM image using the modified probe particle model described above with an enlarged probe size of 3 Å(approximating the larger ambient AFM probe). Here we see that the brightest regions of the image correspond to the rotated phenyl rings of the ZnTPP molecules. Crucially, we find that the close packing of the phenyl rings from each molecule result in a cluster of these bright features, resulting in a regular pattern of bright features located at the corners of the ZnTPP molecules. This indicates that the bright features in our AFM images do not originate from the central core of each molecule, as originally assumed, but in fact originate from the overlap of the four phenyl rings from adjacent ZnTPP. An overlaid image of the experimental and theoretical data is shown in (Fig: 6.10. d), showing the strong similarities between the data.

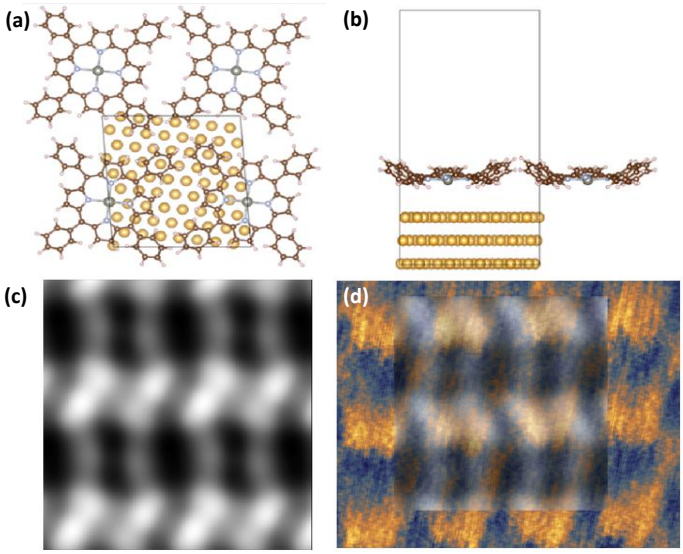

Figure 6.10: **Simulation models constant height NC-AFM.** (a) Top and (b) side views of a schematic representation of the minimum energy configuration for a ZnTPP arrangement bound to a streched [-1 5] [5 2] cell. (c) Simulated constant force AFM measurement of a ZnTPP sample using a 3 Åprobe where the brightest areas correspond to the rotated phenyl rings of the molecules. (d) Superimposition of panel (c) simulated constant force topography with FFT filtered AFM measurement from (Fig: 6.9. f). The overlap of the features confirm the sub-molecular resolution of the experimental data.

Chapter 7

Conclusion

This thesis aimed to demonstrate the on-surface polymerisation on bulk inert and insulating substrates activated by atomic quantum clusters. In this context, the network formation on a surface with low adsorption energy turned out to be of extraordinary scientific relevance as it allowed the analysis and the application of molecular superstructures completely decoupled from the substrate. In fact, the interaction between the substrate and the molecules could induce interference behaviours that could modify the molecular properties, such as structure distortion, orbital broadening, and electrical short-circuits. On the other hand, due to the weak bonding with the substrate, the crosslinking was prevented as the desorption energy resulted favourable than the molecular bond cleavage, hence providing heat to the sample, molecules rather than being thermally activated, tended to diffuse, clump in disordered structures or desorb from the surface. For this reason, reducing the energy activation by employing extrinsic catalysts resulted in a fundamental strategy for the covalent coupling on inert substrates.

Within this framework, this thesis details that Cu_5 clusters activated dehalogenation and subsequent covalent coupling of Br_4TPP molecules at significantly reduced temperatures on metal (Au(111)), semi-metal (HOPG) and insulating surfaces (mica), overcoming the so-called 'desorption problem' [262]. The results were demonstrated by temperature programmed X-ray spectroscopy and supported by calculations of the activation barrier using density functional theory. The XPS analysis confirmed the extraordinary catalytic behaviour of the ACQs even at room temperature, showing that the dehalogenation was at least partially attained and suggesting, by the broadening of the Br 3p peaks, in particular for Au(111)- and HOPG- supported samples, the bond formation with the Cu_5 clusters.

Furthermore, the DFT calculations revealed that compared to a barrier of 1.07 eV for dehalogenation on Au(111), Cu_5 reduced this to as low as 0.35 eV due to significant charge transfer between the Cu_5 and the chemisorbed stabilising oxygen layer.

Contrary to what was expected, the AFM imaging didn't show crosslinked networks similar to the one of (Fig: 5.4. c) obtained on Au(111) substrate without extrinsic catalysis.

Even though the final structures didn't show the general close-packed island formation typical of unreacted molecular arrangements, only for the mica-supported sample the activation-recombination process could be successfully proved; nevertheless, the presence of contaminants in the structures prevented an image resolution high enough to resolve the covalent coupling formation.
Despite the important results achieved with the TP-XPS measurements, the AFM images lead to the conclusion that the spin-coating method deposition of Cu_5 clusters dispersed in solution was not the ideal method for a precise and controlled C-C network architecture. In fact, even though the catalysis was always perfectly achieved, the amount of cluster deposited could vary significantly from one deposition to another even using the same deposition parameters, and the presence of water trapped in the clusters and contaminants over the substrate highly reduced the quality of the molecular network, seldom utterly preventing their development.
In conclusion, a different cluster deposition method that can guarantee the cluster dispersion, of which can be estimated the deposition rate, and that can be entirely performed under UHV conditions, such as the thermal evaporation by K-cells, could improve the network quality and control its formation, highly reducing the presence of contaminants in the sample. Finally, considering the promising results obtained, the ability to tune the catalytic activity of atomic clusters in this way, for example, via cluster size or material, suggests even greater opportunities for directing on-surface polymerisation on a wide range of surface materials previously inaccessible to surface polymerisation.

Furthermore, this thesis research wanted to demonstrate the feasibility of ultra-high resolutions at room temperature and under ambient conditions operating a commercially available atomic force microscope provided by conventional micromachined cantilevers. The resolution of single-molecule and sub-molecular features could be possible only by optimising the PeakForce Tapping mode scanning technique carried out in the ultra-low-noise IsoLab facility. In fact, such a resolution was possible only by the combination of the noise-suppression (acoustic, mechanical, electronic, and thermal fluctuations) achieved by the facility in which the measurement was carried out and a precise operation of the AFM-imaging performed directly controlling the force applied to the sample in a range value of the order of the pN; such forces significantly reduced the chance to deform the molecular sample or compromise the tip sharpness.
Even though the limits of AFM detection and resolution under UHV conditions and at low and ultra-low temperatures are widely documented in scientific literature, the publications under ambient conditions and at room temperature are few, mainly due to the intrinsic limitations concerning these measuring conditions, such as the water layer covering the sample, the sample contamination and deterioration, the high chances to compromise the tip sharpness, and the acoustic and thermal noise. In particular, examples of true atomic/sub-molecular resolution in ambient are few, especially with a commercially available

atomic force microscope, even though investigating the limits of AFM in ambient is crucial. For this reason, among the stable and clean molecular assemblies growth techniques developed in this work, the achievement of single and sub-molecular resolutions was obtained by an instrument optimisation focused on the signal-to-noise ratio maximisation and thermal drift compensation for low force measurements (25-50 pN).

In particular, the AFM resolution capability was proved with a series of experiments characterised by the progressive incremental of the sample complexity. In fact, the resolution of the distinct domains orientations for C_{60}, BipyOPE3, and ZnTPP islands, the concurrent resolution of the two different sizes lattices of a mixed molecular sample (BipyOPE3:ZnTPP), and the molecular details of a disordered structure such as a crosslinked TPP network proved that the aim to attain single-molecule resolution was successfully obtained.

Applying the optimised PeakForce AFM method could improve the imaging quality, resolving the sub-molecular features of a ZnTPP close-packed arrangement. This result was corroborated by Density Functional Theory calculations of the ZnTPP:Au(111) system. The results of the simulations appeared to confirm that sub-molecular constant force imaging is possible, suggesting that contrast in the image was dominated by the rotated phenyl rings from adjacent ZnTPP molecules. This provided good evidence that ambient atomic force microscopy was capable of resolving sub-molecular features that can be meaningfully attributed to real molecular geometry.

Finally, the encouraging results of the optimised PeakForce AFM method suggest that even higher resolutions could be achieved. In fact, several possibilities can be explored to increase the signal-to-noise ratio, such as the implementation of sharper probes and functionalised tips or specific enclosures that guarantee the direct control of humidity and temperature during the measurement to reduce the impact of the external environment further. Furthermore, the direct control of the force and the low force setpoint measurements proved that the optimised PeakForce AFM mode is one of the best methods for analysing fragile samples, such as weak-interacting molecular arrangements.

Bibliography

[1] R. Feynman, "There's plenty of room at the bottom," in *Feynman and computation*, pp. 63–76, CRC Press, 2018.

[2] T. Kudernac, S. Lei, J. A. Elemans, and S. De Feyter, "Two-dimensional supramolecular self-assembly: nanoporous networks on surfaces," *Chemical Society Reviews*, vol. 38, no. 2, pp. 402–421, 2009.

[3] J. V. Barth, G. Costantini, and K. Kern, "Engineering atomic and molecular nanostructures at surfaces," *Nature*, vol. 437, no. 7059, pp. 671–679, 2005.

[4] P. Ruffieux, S. Wang, B. Yang, C. Sánchez-Sánchez, J. Liu, T. Dienel, L. Talirz, P. Shinde, C. A. Pignedoli, D. Passerone, *et al.*, "On-surface synthesis of graphene nanoribbons with zigzag edge topology," *Nature*, vol. 531, no. 7595, pp. 489–492, 2016.

[5] L. Lafferentz, F. Ample, H. Yu, S. Hecht, C. Joachim, and L. Grill, "Conductance of a single conjugated polymer as a continuous function of its length," *Science*, vol. 323, no. 5918, pp. 1193–1197, 2009.

[6] C. Moreno, M. Vilas-Varela, B. Kretz, A. Garcia-Lekue, M. V. Costache, M. Paradinas, M. Panighel, G. Ceballos, S. O. Valenzuela, D. Peña, *et al.*, "Bottom-up synthesis of multifunctional nanoporous graphene," *Science*, vol. 360, no. 6385, pp. 199–203, 2018.

[7] C. Bombis, F. Ample, L. Lafferentz, H. Yu, S. Hecht, C. Joachim, and L. Grill, "Single molecular wires connecting metallic and insulating surface areas," *Angewandte Chemie International Edition*, vol. 48, no. 52, pp. 9966–9970, 2009.

[8] A. Rastgoo-Lahrood, J. Björk, M. Lischka, J. Eichhorn, S. Kloft, M. Fritton, T. Strunskus, D. Samanta, M. Schmittel, W. M. Heckl, *et al.*, "Post-synthetic decoupling of on-surface-synthesized covalent nanostructures from Ag(111)," *Angewandte Chemie International Edition*, vol. 55, no. 27, pp. 7650–7654, 2016.

[9] T. Dienel, J. Gomez-Diaz, A. P. Seitsonen, R. Widmer, M. Iannuzzi, K. Radican, H. Sachdev, K. Müllen, J. Hutter, and O. Gröning, "Dehalogenation and coupling of a polycyclic hydrocarbon on an atomically thin insulator," *ACS nano*, vol. 8, no. 7, pp. 6571–6579, 2014.

[10] G. Binnig, H. Rohrer, C. Gerber, and E. Weibel, "Surface studies by scanning tunneling microscopy," *Physical review letters*, vol. 49, no. 1, p. 57, 1982.

[11] G. Binnig, C. F. Quate, and C. Gerber, "Atomic force microscope," *Physical review letters*, vol. 56, no. 9, p. 930, 1986.

[12] F. Ohnesorge and G. Binnig, "True atomic resolution by atomic force microscopy through repulsive and attractive forces," *Science*, vol. 260, no. 5113, pp. 1451–1456, 1993.

[13] F. J. Giessibl and G. Binnig, "Investigation of the (001) cleavage plane of potassium bromide with an atomic force microscope at 4.2 K in ultra-high vacuum," *Ultramicroscopy*, vol. 42, pp. 281–289, 1992.

[14] L. Gross, F. Mohn, N. Moll, P. Liljeroth, and G. Meyer, "The chemical structure of a molecule resolved by atomic force microscopy," *Science*, vol. 325, no. 5944, pp. 1110–1114, 2009.

[15] J. Repp, G. Meyer, S. M. Stojković, A. Gourdon, and C. Joachim, "Molecules on insulating films: scanning-tunneling microscopy imaging of individual molecular orbitals," *Physical Review Letters*, vol. 94, no. 2, p. 026803, 2005.

[16] J. Repp, G. Meyer, S. Paavilainen, F. E. Olsson, and M. Persson, "Imaging bond formation between a gold atom and pentacene on an insulating surface," *science*, vol. 312, no. 5777, pp. 1196–1199, 2006.

[17] F. Mohn, J. Repp, L. Gross, G. Meyer, M. S. Dyer, and M. Persson, "Reversible bond formation in a gold-atom–organic-molecule complex as a molecular switch," *Physical Review Letters*, vol. 105, no. 26, p. 266102, 2010.

[18] G. Ertl, "Reactions at surfaces: from atoms to complexity (Nobel lecture)," *Angewandte Chemie International Edition*, vol. 47, no. 19, pp. 3524–3535, 2008.

[19] P. Liljeroth, J. Repp, and G. Meyer, "Current-induced hydrogen tautomerization and conductance switching of naphthalocyanine molecules," *Science*, vol. 317, no. 5842, pp. 1203–1206, 2007.

[20] T. Kumagai, F. Hanke, S. Gawinkowski, J. Sharp, K. Kotsis, J. Waluk, M. Persson, and L. Grill, "Controlling intramolecular hydrogen transfer in a porphycene molecule with single atoms or molecules located nearby," *Nature Chemistry*, vol. 6, no. 1, pp. 41–46, 2014.

[21] D. M. Eigler and E. K. Schweizer, "Positioning single atoms with a scanning tunnelling microscope," *Nature*, vol. 344, pp. 524–526, 1990.

[22] M. F. Crommie, C. P. Lutz, and D. M. Eigler, "Confinement of electrons to quantum corrals on a metal surface," *Science*, vol. 262, no. 5131, pp. 218–220, 1993.

[23] A. Heinrich, C. Lutz, J. Gupta, and D. Eigler, "Molecule cascades," *Science*, vol. 298, no. 5597, pp. 1381–1387, 2002.

[24] J. Shi, Y. Hu, S. Hu, J. Ma, and C. Su, "Method and apparatus of using peak force tapping mode to measure physical properties of a sample," Feb. 11 2014. US Patent 8,650,660.

[25] J. V. Barth, G. Costantini, and K. Kern, "Engineering atomic and molecular nanostructures at surfaces," in *Nanoscience and technology: a collection of reviews from Nature journals*, pp. 67–75, World Scientific, 2010.

[26] S. Clair and D. G. de Oteyza, "Controlling a chemical coupling reaction on a surface: tools and strategies for on-surface synthesis," *Chemical reviews*, vol. 119, no. 7, pp. 4717–4776, 2019.

[27] J. V. Barth, "Molecular architectonic on metal surfaces," *Annu. Rev. Phys. Chem.*, vol. 58, pp. 375–407, 2007.

[28] H. Brune, "Microscopic view of epitaxial metal growth: nucleation and aggregation," *Surface Science Reports*, vol. 31, no. 4-6, pp. 125–229, 1998.

[29] R. Gomer, "Diffusion of adsorbates on metal surfaces," *Reports on progress in Physics*, vol. 53, no. 7, p. 917, 1990.

[30] Z. Zhang and M. G. Lagally, "Atomistic processes in the early stages of thin-film growth," *Science*, vol. 276, no. 5311, pp. 377–383, 1997.

[31] I. A. Banerjee, L. Yu, R. I. MacCuspie, and H. Matsui, "Thiolated peptide nanotube assembly as arrays on patterned Au substrates," *Nano letters*, vol. 4, no. 12, pp. 2437–2440, 2004.

[32] N. Nuraje, I. A. Banerjee, R. I. MacCuspie, L. Yu, and H. Matsui, "Biological bottom-up assembly of antibody nanotubes on patterned antigen arrays," *Journal of the American Chemical Society*, vol. 126, no. 26, pp. 8088–8089, 2004.

[33] W. Wang, T. Lee, and M. A. Reed, "Electron tunnelling in self-assembled monolayers," *Reports on Progress in Physics*, vol. 68, no. 3, p. 523, 2005.

[34] B. R. Martin, D. J. Dermody, B. D. Reiss, M. Fang, L. A. Lyon, M. J. Natan, and T. E. Mallouk, "Orthogonal self-assembly on colloidal gold-platinum nanorods," *Advanced Materials*, vol. 11, no. 12, pp. 1021–1025, 1999.

[35] D. L. Allara and R. G. Nuzzo, "Spontaneously organized molecular assemblies. 1. Formation, dynamics, and physical properties of n-alkanoic acids adsorbed from solution on an oxidized aluminum surface," *Langmuir*, vol. 1, no. 1, pp. 45–52, 1985.

[36] P. Gehring, A. Harzheim, J. Spiece, Y. Sheng, G. Rogers, C. Evangeli, A. Mishra, B. J. Robinson, K. Porfyrakis, J. H. Warner, *et al.*, "Field-effect control of graphene–fullerene thermoelectric nanodevices," *Nano letters*, vol. 17, no. 11, pp. 7055–7061, 2017.

[37] J. V. Barth, "Transport of adsorbates at metal surfaces: from thermal migration to hot precursors," *Surface Science Reports*, vol. 40, no. 3-5, pp. 75–149, 2000.

[38] J. Weckesser, J. V. Barth, and K. Kern, "Direct observation of surface diffusion of large organic molecules at metal surfaces: PVBA on Pd(110)," *The Journal of chemical physics*, vol. 110, no. 11, pp. 5351–5354, 1999.

[39] M. Schunack, T. R. Linderoth, F. Rosei, E. Lægsgaard, I. Stensgaard, and F. Besenbacher, "Long jumps in the surface diffusion of large molecules," *Physical review letters*, vol. 88, no. 15, p. 156102, 2002.

[40] J. S. Raut and K. A. Fichthorn, "Diffusion mechanisms of short-chain alkanes on metal substrates: Unique molecular features," *The Journal of chemical physics*, vol. 108, no. 4, pp. 1626–1635, 1998.

[41] K.-Y. Kwon, K. L. Wong, G. Pawin, L. Bartels, S. Stolbov, and T. S. Rahman, "Unidirectional adsorbate motion on a high-symmetry surface: "Walking" molecules can stay the course," *Physical review letters*, vol. 95, no. 16, p. 166101, 2005.

[42] F. Tautz, "Structure and bonding of large aromatic molecules on noble metal surfaces: The example of PTCDA," *Progress in Surface Science*, vol. 82, no. 9-12, pp. 479–520, 2007.

[43] B. Hammer and J. K. Norskov, "Why gold is the noblest of all the metals," *Nature*, vol. 376, no. 6537, pp. 238–240, 1995.

[44] N. Zhu, T. Osada, and T. Komeda, "Supramolecular assembly of biphenyl dicarboxylic acid on Au(111)," *Surface science*, vol. 601, no. 8, pp. 1789–1794, 2007.

[45] S. Stepanow, N. Lin, F. Vidal, A. Landa, M. Ruben, J. V. Barth, and K. Kern, "Programming supramolecular assembly and chirality in two-dimensional dicarboxylate networks on a Cu(100) surface," *Nano letters*, vol. 5, no. 5, pp. 901–904, 2005.

[46] L. Bartels, "Tailoring molecular layers at metal surfaces," *Nature chemistry*, vol. 2, no. 2, pp. 87–95, 2010.

[47] O. Ivasenko and D. F. Perepichka, "Mastering fundamentals of supramolecular design with carboxylic acids. Common lessons from X-ray crystallography and scanning tunneling microscopy," *Chemical Society Reviews*, vol. 40, no. 1, pp. 191–206, 2011.

[48] S. Griessl, M. Lackinger, M. Edelwirth, M. Hietschold, and W. M. Heckl, "Self-assembled two-dimensional molecular host-guest architectures from trimesic acid," *Single Molecules*, vol. 3, no. 1, pp. 25–31, 2002.

[49] R. Gutzler, T. Sirtl, J. F. Dienstmaier, K. Mahata, W. M. Heckl, M. Schmittel, and M. Lackinger, "Reversible phase transitions in self-assembled monolayers at the liquid-solid interface: temperature-controlled opening and closing of nanopores," *Journal of the American Chemical Society*, vol. 132, no. 14, pp. 5084–5090, 2010.

[50] G. Pawin, K. L. Wong, K.-Y. Kwon, and L. Bartels, "A homomolecular porous network at a Cu(111) surface," *Science*, vol. 313, no. 5789, pp. 961–962, 2006.

[51] M. Lackinger, S. Griessl, T. Markert, F. Jamitzky, and W. M. Heckl, "Self-assembly of Benzene- Dicarboxylic acid isomers at the liquid solid interface: steric aspects of hydrogen bonding," *The Journal of Physical Chemistry B*, vol. 108, no. 36, pp. 13652–13655, 2004.

[52] J. A. Theobald, N. S. Oxtoby, M. A. Phillips, N. R. Champness, and P. H. Beton, "Controlling molecular deposition and layer structure with supramolecular surface assemblies," *Nature*, vol. 424, no. 6952, pp. 1029–1031, 2003.

[53] L. Perdigao, E. Perkins, J. Ma, P. Staniec, B. Rogers, N. Champness, and P. Beton, "Bimolecular networks and supramolecular traps on Au(111)," *The Journal of Physical Chemistry B*, vol. 110, no. 25, pp. 12539–12542, 2006.

[54] J. Swarbrick, J. Ma, J. Theobald, N. Oxtoby, J. O'Shea, N. Champness, and P. Beton, "Square, hexagonal, and row phases of PTCDA and PTCDI on Ag-Si(111) $\sqrt{3} \times \sqrt{3}$ R30°," *The Journal of Physical Chemistry B*, vol. 109, no. 24, pp. 12167–12174, 2005.

[55] D. Keeling, N. Oxtoby, C. Wilson, M. Humphry, N. Champness, and P. Beton, "Assembly and processing of hydrogen bond induced supramolecular nanostructures," *Nano Letters*, vol. 3, no. 1, pp. 9–12, 2003.

[56] M. O. Blunt, J. C. Russell, M. d. C. Giménez-López, J. P. Garrahan, X. Lin, M. Schroder, N. R. Champness, and P. H. Beton, "Random tiling and topological defects in a two-dimensional molecular network," *Science*, vol. 322, no. 5904, pp. 1077–1081, 2008.

[57] G. Pawin, K. L. Wong, D. Kim, D. Sun, L. Bartels, S. Hong, T. S. Rahman, R. Carp, and M. Marsella, "A surface coordination network based on substrate-derived metal

adatoms with local charge excess," *Angewandte Chemie*, vol. 120, no. 44, pp. 8570–8573, 2008.

[58] U. Schlickum, R. Decker, F. Klappenberger, G. Zoppellaro, S. Klyatskaya, M. Ruben, I. Silanes, A. Arnau, K. Kern, H. Brune, *et al.*, "Metal-organic honeycomb nanomeshes with tunable cavity size," *Nano letters*, vol. 7, no. 12, pp. 3813–3817, 2007.

[59] S. L. Tait, A. Langner, N. Lin, R. Chandrasekar, O. Fuhr, M. Ruben, and K. Kern, "Assembling isostructural metal-organic coordination architectures on Cu(100), Au(100) and Ag(111) substrates," *ChemPhysChem*, vol. 9, no. 17, pp. 2495–2499, 2008.

[60] A. Langner, S. L. Tait, N. Lin, C. Rajadurai, M. Ruben, and K. Kern, "Self-recognition and self-selection in multicomponent supramolecular coordination networks on surfaces," *Proceedings of the National Academy of Sciences*, vol. 104, no. 46, pp. 17927–17930, 2007.

[61] A. Ulman, "Formation and structure of self-assembled monolayers," *Chemical reviews*, vol. 96, no. 4, pp. 1533–1554, 1996.

[62] A. Cnossen, D. Pijper, T. Kudernac, M. M. Pollard, N. Katsonis, and B. L. Feringa, "A trimer of ultrafast nanomotors: Synthesis, photochemistry and self-assembly on Graphite," *Chemistry–A European Journal*, vol. 15, no. 12, pp. 2768–2772, 2009.

[63] S. Furukawa, H. Uji-i, K. Tahara, T. Ichikawa, M. Sonoda, F. C. De Schryver, Y. Tobe, and S. De Feyter, "Molecular geometry directed Kagome and honeycomb networks: toward two-dimensional crystal engineering," *Journal of the American Chemical Society*, vol. 128, no. 11, pp. 3502–3503, 2006.

[64] S. Lei, M. Surin, K. Tahara, J. Adisoejoso, R. Lazzaroni, Y. Tobe, and S. De Feyter, "Programmable hierarchical three-component 2D assembly at a liquid- solid interface: recognition, selection, and transformation," *Nano letters*, vol. 8, no. 8, pp. 2541–2546, 2008.

[65] K. Tahara, S. Furukawa, H. Uji-i, T. Uchino, T. Ichikawa, J. Zhang, W. Mamdouh, M. Sonoda, F. C. De Schryver, S. De Feyter, *et al.*, "Two-dimensional porous molecular networks of dehydrobenzo [12] annulene derivatives via alkyl chain interdigitation," *Journal of the American Chemical Society*, vol. 128, no. 51, pp. 16613–16625, 2006.

[66] S.-W. Hla, L. Bartels, G. Meyer, and K.-H. Rieder, "Inducing all steps of a chemical reaction with the scanning tunneling microscope tip: towards single molecule engineering," *Physical review letters*, vol. 85, no. 13, p. 2777, 2000.

[67] L. Grill, M. Dyer, L. Lafferentz, M. Persson, M. V. Peters, and S. Hecht, "Nano-architectures by covalent assembly of molecular building blocks," *Nature nanotechnology*, vol. 2, no. 11, pp. 687–691, 2007.

[68] L. Xu, Y. Yu, J. Lin, X. Zhou, W. Q. Tian, D. Nieckarz, P. Szabelski, and S. Lei, "On-surface synthesis of two-dimensional imine polymers with a tunable band gap: a combined STM, DFT and Monte Carlo investigation," *Nanoscale*, vol. 8, no. 16, pp. 8568–8574, 2016.

[69] S. Schlögl, W. M. Heckl, and M. Lackinger, "On-surface radical addition of triply iodinated monomers on Au(111)—the influence of monomer size and thermal post-processing," *Surface science*, vol. 606, no. 13-14, pp. 999–1004, 2012.

[70] Y.-Q. Zhang, N. Kepčija, M. Kleinschrodt, K. Diller, S. Fischer, A. C. Papageorgiou, F. Allegretti, J. Björk, S. Klyatskaya, F. Klappenberger, *et al.*, "Homo-coupling of terminal alkynes on a noble metal surface," *Nature communications*, vol. 3, no. 1, pp. 1–8, 2012.

[71] A. Miura, S. De Feyter, M. M. Abdel-Mottaleb, A. Gesquiere, P. C. Grim, G. Moessner, M. Sieffert, M. Klapper, K. Müllen, and F. C. De Schryver, "Light-and STM-tip-induced formation of one-dimensional and two-dimensional organic nanostructures," *Langmuir*, vol. 19, no. 16, pp. 6474–6482, 2003.

[72] R. Otero, F. Hümmelink, F. Sato, S. B. Legoas, P. Thostrup, E. Lægsgaard, I. Stensgaard, D. S. Galvão, and F. Besenbacher, "Lock-and-key effect in the surface diffusion of large organic molecules probed by STM," *Nature materials*, vol. 3, no. 11, pp. 779–782, 2004.

[73] Y. Okawa and M. Aono, "Nanoscale control of chain polymerization," *Nature*, vol. 409, no. 6821, pp. 683–684, 2001.

[74] J. Lipton-Duffin, J. Miwa, M. Kondratenko, F. Cicoira, B. Sumpter, V. Meunier, D. Perepichka, and F. Rosei, "Step-by-step growth of epitaxially aligned polythiophene by surface-confined reaction," *Proceedings of the National Academy of Sciences*, vol. 107, no. 25, pp. 11200–11204, 2010.

[75] J. Chen, E. Zhu, J. Liu, S. Zhang, Z. Lin, X. Duan, H. Heinz, Y. Huang, and J. J. De Yoreo, "Building two-dimensional materials one row at a time: Avoiding the nucleation barrier," *Science*, vol. 362, no. 6419, pp. 1135–1139, 2018.

[76] L. Lafferentz, V. Eberhardt, C. Dri, C. Africh, G. Comelli, F. Esch, S. Hecht, and L. Grill, "Controlling on-surface polymerization by hierarchical and substrate-directed growth," *Nature chemistry*, vol. 4, no. 3, pp. 215–220, 2012.

[77] J. Cai, P. Ruffieux, R. Jaafar, M. Bieri, T. Braun, S. Blankenburg, M. Muoth, A. P. Seitsonen, M. Saleh, X. Feng, *et al.*, "Atomically precise bottom-up fabrication of graphene nanoribbons," *Nature*, vol. 466, no. 7305, pp. 470–473, 2010.

[78] O. Ourdjini, R. Pawlak, M. Abel, S. Clair, L. Chen, N. Bergeon, M. Sassi, V. Oison, J.-M. Debierre, R. Coratger, *et al.*, "Substrate-mediated ordering and defect analysis of a surface covalent organic framework," *Physical Review B*, vol. 84, no. 12, p. 125421, 2011.

[79] M. Koch, M. Gille, A. Viertel, S. Hecht, and L. Grill, "Substrate-controlled linking of molecular building blocks: Au(111) vs. Cu(111)," *Surface science*, vol. 627, pp. 70–74, 2014.

[80] S. Whitelam, I. Tamblyn, T. K. Haxton, M. B. Wieland, N. R. Champness, J. P. Garrahan, and P. H. Beton, "Common physical framework explains phase behavior and dynamics of atomic, molecular, and polymeric network formers," *Physical Review X*, vol. 4, no. 1, p. 011044, 2014.

[81] H.-Y. Gao, H. Wagner, D. Zhong, J.-H. Franke, A. Studer, and H. Fuchs, "Glaser coupling at metal surfaces," *Angewandte Chemie International Edition*, vol. 52, no. 14, pp. 4024–4028, 2013.

[82] M. Bieri, M.-T. Nguyen, O. Gröning, J. Cai, M. Treier, K. Aït-Mansour, P. Ruffieux, C. A. Pignedoli, D. Passerone, M. Kastler, *et al.*, "Two-dimensional polymer formation on surfaces: insight into the roles of precursor mobility and reactivity," *Journal of the American Chemical Society*, vol. 132, no. 46, pp. 16669–16676, 2010.

[83] C. Dussert, G. Rasigni, M. Rasigni, J. Palmari, and A. Llebaria, "Minimal spanning tree: A new approach for studying order and disorder," *Physical Review B*, vol. 34, no. 5, p. 3528, 1986.

[84] L. Dong, P. N. Liu, and N. Lin, "Surface-activated coupling reactions confined on a surface," *Accounts of chemical research*, vol. 48, no. 10, pp. 2765–2774, 2015.

[85] L. Dong, S. Wang, W. Wang, C. Chen, T. Lin, J. Adisoejoso, and N. Lin, "Transition metals trigger on-surface ullmann coupling reaction: intermediate, catalyst and template," in *On-Surface Synthesis*, pp. 23–42, Springer, 2016.

[86] M. Koch, M. Gille, S. Hecht, and L. Grill, "Steering a cycloaddition reaction via the surface structure," *Surface Science*, vol. 678, pp. 194–200, 2018.

[87] J. Dai, Q. Fan, T. Wang, J. Kuttner, G. Hilt, J. M. Gottfried, and J. Zhu, "The role of the substrate structure in the on-surface synthesis of organometallic and covalent oligophenylene chains," *Physical Chemistry Chemical Physics*, vol. 18, no. 30, pp. 20627–20634, 2016.

[88] N. Kalashnyk, E. Salomon, S. H. Mun, J. Jung, L. Giovanelli, T. Angot, F. Dumur, D. Gigmes, and S. Clair, "The orientation of silver surfaces drives the reactivity and the

selectivity in homo-coupling reactions," *ChemPhysChem*, vol. 19, no. 15, pp. 1802–1808, 2018.

[89] S. Linden, D. Zhong, A. Timmer, N. Aghdassi, J. Franke, H. Zhang, X. Feng, K. Müllen, H. Fuchs, L. Chi, *et al.*, "Electronic structure of spatially aligned graphene nanoribbons on Au(788)," *Physical Review Letters*, vol. 108, no. 21, p. 216801, 2012.

[90] D. Zhong, J.-H. Franke, S. K. Podiyanachari, T. Blömker, H. Zhang, G. Kehr, G. Erker, H. Fuchs, and L. Chi, "Linear alkane polymerization on a gold surface," *Science*, vol. 334, no. 6053, pp. 213–216, 2011.

[91] A. Saywell, J. Schwarz, S. Hecht, and L. Grill, "Polymerization on stepped surfaces: alignment of polymers and identification of catalytic sites," *Angewandte Chemie*, vol. 124, no. 21, pp. 5186–5190, 2012.

[92] J. A. Lipton-Duffin, O. Ivasenko, D. F. Perepichka, and F. Rosei, "Synthesis of polyphenylene molecular wires by surface-confined polymerization," *small*, vol. 5, no. 5, pp. 592–597, 2009.

[93] J. Adisoejoso, T. Lin, X. S. Shang, K. J. Shi, A. Gupta, P. N. Liu, and N. Lin, "A single-molecule-level mechanistic study of Pd-catalyzed and Cu-catalyzed homocoupling of aryl bromide on an Au(111) surface," *Chemistry–A European Journal*, vol. 20, no. 14, pp. 4111–4116, 2014.

[94] X. Zhou, F. Bebensee, Q. Shen, R. Bebensee, F. Cheng, Y. He, H. Su, W. Chen, G. Q. Xu, F. Besenbacher, *et al.*, "On-surface synthesis approach to preparing one-dimensional organometallic and poly-p-phenylene chains," *Materials Chemistry Frontiers*, vol. 1, no. 1, pp. 119–127, 2017.

[95] K. J. Shi, X. Zhang, C. H. Shu, D. Y. Li, X. Y. Wu, and P. N. Liu, "Ullmann coupling reaction of aryl chlorides on Au(111) using dosed Cu as a catalyst and the programmed growth of 2D covalent organic frameworks," *Chemical Communications*, vol. 52, no. 56, pp. 8726–8729, 2016.

[96] R. Zhang, G. Lyu, D. Y. Li, P. N. Liu, and N. Lin, "Template-controlled Sonogashira cross-coupling reactions on a Au(111) surface," *Chemical Communications*, vol. 53, no. 10, pp. 1731–1734, 2017.

[97] R. Gutzler, H. Walch, G. Eder, S. Kloft, W. M. Heckl, and M. Lackinger, "Surface mediated synthesis of 2D covalent organic frameworks: 1, 3, 5-tris (4-bromophenyl) benzene on Graphite(001), Cu(111), and Ag(110)," *Chemical communications*, no. 29, pp. 4456–4458, 2009.

[98] W. Zhao, L. Dong, C. Huang, Z. M. Win, and N. Lin, "Cu-and Pd-catalyzed Ullmann reaction on a hexagonal boron nitride layer," *Chemical Communications*, vol. 52, no. 90, pp. 13225–13228, 2016.

[99] B. Cirera, J. Björk, R. Otero, J. M. Gallego, R. Miranda, and D. Ecija, "Efficient lanthanide catalyzed debromination and oligomeric length-controlled Ullmann coupling of aryl halides," *The Journal of Physical Chemistry C*, vol. 121, no. 14, pp. 8033–8041, 2017.

[100] T. Lin, X. S. Shang, J. Adisoejoso, P. N. Liu, and N. Lin, "Steering on-surface polymerization with metal-directed template," *Journal of the American Chemical Society*, vol. 135, no. 9, pp. 3576–3582, 2013.

[101] P. Olszowski, B. Zapotoczny, J. Prauzner-Bechcicki, M. Vilas-Varela, D. Pérez, E. Guitián, D. Peña, and M. Szymonski, "Aryl halide C-C coupling on Ge(001): H surfaces," *The Journal of Physical Chemistry C*, vol. 119, no. 49, pp. 27478–27482, 2015.

[102] G. Vasseur, M. Abadia, L. A. Miccio, J. Brede, A. Garcia-Lekue, D. G. de Oteyza, C. Rogero, J. Lobo-Checa, and J. E. Ortega, "Π band dispersion along conjugated organic nanowires synthesized on a metal oxide semiconductor," *Journal of the American Chemical Society*, vol. 138, no. 17, pp. 5685–5692, 2016.

[103] X.-H. Liu, C.-Z. Guan, S.-Y. Ding, W. Wang, H.-J. Yan, D. Wang, and L.-J. Wan, "On-surface synthesis of single-layered two-dimensional covalent organic frameworks via solid-vapor interface reactions," *Journal of the American Chemical Society*, vol. 135, no. 28, pp. 10470–10474, 2013.

[104] L. Xu, X. Zhou, Y. Yu, W. Q. Tian, J. Ma, and S. Lei, "Surface-confined crystalline two-dimensional covalent organic frameworks via on-surface Schiff-base coupling," *ACS nano*, vol. 7, no. 9, pp. 8066–8073, 2013.

[105] L. Colazzo, F. Sedona, A. Moretto, M. Casarin, and M. Sambi, "Metal-free on-surface photochemical homocoupling of terminal alkynes," *Journal of the American Chemical Society*, vol. 138, no. 32, pp. 10151–10156, 2016.

[106] C. Guo, Y. Wang, M. Kittelmann, L. Kantorovitch, A. Kühnle, and A. Floris, "Mechanisms of covalent dimerization on a bulk insulating surface," *The Journal of Physical Chemistry C*, vol. 121, no. 18, pp. 10053–10062, 2017.

[107] M. Kittelmann, M. Nimmrich, R. Lindner, A. Gourdon, and A. Kühnle, "Sequential and site-specific on-surface synthesis on a bulk insulator," *ACS nano*, vol. 7, no. 6, pp. 5614–5620, 2013.

[108] R. Lindner, P. Rahe, M. Kittelmann, A. Gourdon, R. Bechstein, and A. Kühnle, "Substrate templating guides the photoinduced reaction of C_{60} on calcite," *Angewandte Chemie International Edition*, vol. 53, no. 30, pp. 7952–7955, 2014.

[109] A. Richter, M. Vilas-Varela, D. Peña, R. Bechstein, and A. Kühnle, "Homocoupling of terminal alkynes on calcite (10.4)," *Surface Science*, vol. 678, pp. 106–111, 2018.

[110] F. Para, F. Bocquet, L. Nony, C. Loppacher, M. Féron, F. Cherioux, D. Z. Gao, F. Federici Canova, and M. B. Watkins, "Micrometre-long covalent organic fibres by photoinitiated chain-growth radical polymerization on an alkali-halide surface," *Nature Chemistry*, vol. 10, no. 11, pp. 1112–1117, 2018.

[111] N. Pavliček, P. Gawel, D. R. Kohn, Z. Majzik, Y. Xiong, G. Meyer, H. L. Anderson, and L. Gross, "Polyyne formation via skeletal rearrangement induced by atomic manipulation," *Nature chemistry*, vol. 10, no. 8, pp. 853–858, 2018.

[112] O. Deniz, C. Sánchez-Sánchez, T. Dumslaff, X. Feng, A. Narita, K. Müllen, N. Kharche, V. Meunier, R. Fasel, and P. Ruffieux, "Revealing the electronic structure of silicon intercalated armchair graphene nanoribbons by scanning tunneling spectroscopy," *Nano letters*, vol. 17, no. 4, pp. 2197–2203, 2017.

[113] O. Deniz, C. Sánchez-Sánchez, R. Jaafar, N. Kharche, L. Liang, V. Meunier, X. Feng, K. Müllen, R. Fasel, and P. Ruffieux, "Electronic characterization of silicon intercalated chevron graphene nanoribbons on Au(111)," *Chemical communications*, vol. 54, no. 13, pp. 1619–1622, 2018.

[114] H. Cheng and L.-S. Wang, "Dimer growth, structural transition, and antiferromagnetic ordering of small chromium clusters," *Physical review letters*, vol. 77, no. 1, p. 51, 1996.

[115] G. H. Guvelioglu, P. Ma, X. He, R. C. Forrey, and H. Cheng, "Evolution of small copper clusters and dissociative chemisorption of hydrogen," *Physical review letters*, vol. 94, no. 2, p. 026103, 2005.

[116] S. Apsel, J. Emmert, J. Deng, and L. Bloomfield, "Surface-enhanced magnetism in nickel clusters," *Physical review letters*, vol. 76, no. 9, p. 1441, 1996.

[117] E. Parks, G. Nieman, K. Kerns, and S. Riley, "Reactions of Ni_{38} with N_2, H_2, and CO: Cluster structure and adsorbate binding sites," *The Journal of chemical physics*, vol. 107, no. 6, pp. 1861–1871, 1997.

[118] A. Halder, L. A. Curtiss, A. Fortunelli, and S. Vajda, "Perspective: Size selected clusters for catalysis and electrochemistry," *The Journal of Chemical Physics*, vol. 148, no. 11, p. 110901, 2018.

[119] E. C. Tyo and S. Vajda, "Catalysis by clusters with precise numbers of atoms," *Nature nanotechnology*, vol. 10, no. 7, pp. 577–588, 2015.

[120] L. Liu and A. Corma, "Metal catalysts for heterogeneous catalysis: from single atoms to nanoclusters and nanoparticles," *Chemical reviews*, vol. 118, no. 10, pp. 4981–5079, 2018.

[121] J. Alonso, "Electronic and atomic structure, and magnetism of transition-metal clusters," *Chemical reviews*, vol. 100, no. 2, pp. 637–678, 2000.

[122] V. N. Popok, I. Barke, E. E. Campbell, and K.-H. Meiwes-Broer, "Cluster-surface interaction: From soft landing to implantation," *Surface Science Reports*, vol. 66, no. 10, pp. 347–377, 2011.

[123] E. Fernández and M. Boronat, "Sub nanometer clusters in catalysis," *Journal of Physics: Condensed Matter*, vol. 31, no. 1, p. 013002, 2018.

[124] E. Fernandez, M. Boronat, and A. Corma, "Trends in the reactivity of molecular O_2 with copper clusters: influence of size and shape," *The Journal of Physical Chemistry C*, vol. 119, no. 34, pp. 19832–19846, 2015.

[125] S. M. Lang, T. M. Bernhardt, R. N. Barnett, B. Yoon, and U. Landman, "Hydrogen-promoted oxygen activation by free gold cluster cations," *Journal of the American Chemical Society*, vol. 131, no. 25, pp. 8939–8951, 2009.

[126] S. Feyel, D. Schröder, X. Rozanska, J. Sauer, and H. Schwarz, "Gas-phase oxidation of propane and 1-butene with [V3O7]+: Experiment and theory in concert," *Angewandte Chemie International Edition*, vol. 45, no. 28, pp. 4677–4681, 2006.

[127] A. W. Castleman, "Cluster structure and reactions: gaining insights into catalytic processes," *Catalysis letters*, vol. 141, pp. 1243–1253, 2011.

[128] N. Vilar-Vidal, J. Rivas, and M. A. López-Quintela, "Size dependent catalytic activity of reusable subnanometer copper(0) clusters," *ACS Catalysis*, vol. 2, no. 8, pp. 1693–1697, 2012.

[129] H. Schwarz, "Chemistry with methane: concepts rather than recipes," *Angewandte Chemie International Edition*, vol. 50, no. 43, pp. 10096–10115, 2011.

[130] F. Dong, S. Heinbuch, Y. Xie, J. J. Rocca, E. R. Bernstein, Z.-C. Wang, K. Deng, and S.-G. He, "Experimental and theoretical study of the reactions between neutral vanadium oxide clusters and ethane, ethylene, and acetylene," *Journal of the American Chemical Society*, vol. 130, no. 6, pp. 1932–1943, 2008.

[131] D. Schröder and H. Schwarz, "C-H and C-C bond activation by bare transition-metal oxide cations in the gas phase," *Angewandte Chemie International Edition in English*, vol. 34, no. 18, pp. 1973–1995, 1995.

[132] Q. Wu, S. Hou, D. Buceta, H. J. Ordoñez, M. A. López-Quintela, and C. J. Lambert, "Tuning the surface states of TiO_2 using Cu_5 atomic clusters," *Applied Surface Science*, vol. 594, p. 153455, 2022.

[133] A. Zanchet, P. López-Caballero, A. O. Mitrushchenkov, D. Buceta, M. A. López-Quintela, A. W. Hauser, and M. Pilar de Lara-Castells, "On the stability of Cu_5 catalysts in air using multireference perturbation theory," *The Journal of Physical Chemistry C*, vol. 123, no. 44, pp. 27064–27072, 2019.

[134] P. Concepcion, M. Boronat, S. Garcia-Garcia, E. Fernandez, and A. Corma, "Enhanced stability of cu clusters of low atomicity against oxidation. effect on the catalytic redox process," *ACS Catalysis*, vol. 7, no. 5, pp. 3560–3568, 2017.

[135] J. Oliver-Meseguer, I. Dominguez, R. Gavara, A. Doménech-Carbó, J. Gonzalez-Calbet, A. Leyva-Pérez, and A. Corma, "The wet synthesis and quantification of ligand-free sub-nanometric au clusters in solid matrices," *Chemical Communications*, vol. 53, no. 6, pp. 1116–1119, 2017.

[136] D. Buceta, S. Huseyinova, M. Cuerva, H. Lozano, L. J. Giovanetti, J. M. Ramallo-López, P. López-Caballero, A. Zanchet, A. O. Mitrushchenkov, A. W. Hauser, *et al.*, "Outstanding nobility observed in cu5 clusters reveals the key role of collective quantum effects," 2021.

[137] K. Novoselov and A. C. Neto, "Two-dimensional crystals-based heterostructures: materials with tailored properties," *Physica Scripta*, vol. 2012, no. T146, p. 014006, 2012.

[138] P. Li and F. Ding, "Origin of the herringbone reconstruction of Au(111) surface at the atomic scale," *Science Advances*, vol. 8, no. 40, p. eabq2900, 2022.

[139] F. Hanke and J. Björk, "Structure and local reactivity of the au (111) surface reconstruction," *Physical Review B*, vol. 87, no. 23, p. 235422, 2013.

[140] S. Hüfner, R. Cohen, and G. Wertheim, "Argon ion sputtering of metallic surfaces for ESCA studies," *Physica Scripta*, vol. 5, no. 1-2, p. 91, 1972.

[141] H.-J. Butt and M. Jaschke, "Calculation of thermal noise in atomic force microscopy," *Nanotechnology*, vol. 6, no. 1, p. 1, 1995.

[142] S. Gould, B. Drake, C. Prater, A. Weisenhorn, S. Manne, G. Kelderman, H.-J. Butt, H. Hansma, P. Hansma, S. Magonov, *et al.*, "The atomic force microscope: a tool for science and industry," *Ultramicroscopy*, vol. 33, no. 2, pp. 93–98, 1990.

[143] F. J. Giessibl, "Advances in atomic force microscopy," *Reviews of modern physics*, vol. 75, no. 3, p. 949, 2003.

[144] S. Kuhn and P. Rahe, "Discriminating short-range from van der Waals forces using total force data in noncontact atomic force microscopy," *Physical Review B*, vol. 89, no. 23, p. 235417, 2014.

[145] U. Hartmann, "Magnetic force microscopy," *Annual review of materials science*, vol. 29, no. 1, pp. 53–87, 1999.

[146] C. Van Oss, D. Absolom, and A. Neumann, "Applications of net repulsive van der Waals forces between different particles, macromolecules, or biological cells in liquids," *Colloids and Surfaces*, vol. 1, no. 1, pp. 45–56, 1980.

[147] J. N. Israelachvili, *Intermolecular and surface forces*. Academic press, 2011.

[148] G. Grosso and G. P. Parravicini, *Solid state physics*. Academic press, 2013.

[149] A. Sweetman and A. Stannard, "Uncertainties in forces extracted from non-contact atomic force microscopy measurements by fitting of long-range background forces," *Beilstein journal of nanotechnology*, vol. 5, no. 1, pp. 386–393, 2014.

[150] M. Bloo, H. Haitjema, and W. Pril, "Deformation and wear of pyramidal, silicon-nitride AFM tips scanning micrometre-size features in contact mode," *Measurement*, vol. 25, no. 3, pp. 203–211, 1999.

[151] K. Kimura, K. Kobayashi, H. Yamada, T. Horiuchi, K. Ishida, and K. Matsushige, "Orientation control of ferroelectric polymer molecules using contact-mode AFM," *European polymer journal*, vol. 40, no. 5, pp. 933–938, 2004.

[152] J. H. Hoh and P. K. Hansma, "Atomic force microscopy for high-resolution imaging in cell biology," *Trends in Cell Biology*, vol. 2, no. 7, pp. 208–213, 1992.

[153] A. Howard, R. Rye, and J. Houston, "Nanomechanical basis for imaging soft materials with tapping mode atomic force microscopy," *Journal of applied physics*, vol. 79, no. 4, pp. 1885–1890, 1996.

[154] Q. Zhong, D. Inniss, K. Kjoller, and V. Elings, "Fractured polymer/silica fiber surface studied by tapping mode atomic force microscopy," *Surface Science Letters*, vol. 290, no. 1-2, pp. L688–L692, 1993.

[155] A. Noy, C. H. Sanders, D. V. Vezenov, S. S. Wong, and C. M. Lieber, "Chemically-sensitive imaging in tapping mode by chemical force microscopy: relationship between phase lag and adhesion," *Langmuir*, vol. 14, no. 7, pp. 1508–1511, 1998.

[156] R. Garcıa and R. Perez, "Dynamic atomic force microscopy methods," *Surface science reports*, vol. 47, no. 6-8, pp. 197–301, 2002.

[157] Y. Martin, C. C. Williams, and H. K. Wickramasinghe, "Atomic force microscope–force mapping and profiling on a sub 100-å scale," *Journal of applied Physics*, vol. 61, no. 10, pp. 4723–4729, 1987.

[158] R. Garcia and E. T. Herruzo, "The emergence of multifrequency force microscopy," *Nature nanotechnology*, vol. 7, no. 4, pp. 217–226, 2012.

[159] I. Medalsy, U. Hensen, and D. J. Muller, "Imaging and quantifying chemical and physical properties of native proteins at molecular resolution by force–volume AFM," *Angewandte Chemie International Edition*, vol. 50, no. 50, pp. 12103–12108, 2011.

[160] C. Reynaud, F. Sommer, C. Quet, N. El Bounia, and T. M. Duc, "Quantitative determination of Young's modulus on a biphase polymer system using atomic force microscopy," *Surface and Interface Analysis: An International Journal devoted to the development and application of techniques for the analysis of surfaces, interfaces and thin films*, vol. 30, no. 1, pp. 185–189, 2000.

[161] N. Guz, M. Dokukin, V. Kalaparthi, and I. Sokolov, "If cell mechanics can be described by elastic modulus: study of different models and probes used in indentation experiments," *Biophysical journal*, vol. 107, no. 3, pp. 564–575, 2014.

[162] O. Marti, M. Holzwarth, and M. Beil, "Measuring the nanomechanical properties of cancer cells by digital pulsed force mode imaging," *Nanotechnology*, vol. 19, no. 38, p. 384015, 2008.

[163] A. Gigler, C. Gnahm, O. Marti, T. Schimmel, and S. Walheim, "Towards quantitative materials characterization with digital pulsed force mode imaging," in *Journal of Physics: Conference Series*, vol. 61, p. 070, IOP Publishing, 2007.

[164] D.-M. Kaimaki, B. E. Smith, and C. Durkan, "On the use of nanomechanical atomic force microscopy to characterise oil-exposed surfaces," *RSC advances*, vol. 8, no. 12, pp. 6680–6689, 2018.

[165] L. Chopinet, C. Formosa, M. Rols, R. Duval, and E. Dague, "Imaging living cells surface and quantifying its properties at high resolution using AFM in QI™ mode," *Micron*, vol. 48, pp. 26–33, 2013.

[166] T. Young, M. Monclus, T. Burnett, W. Broughton, S. Ogin, and P. Smith, "The use of the PeakForceTM quantitative nanomechanical mapping AFM-based method for high-resolution Young's modulus measurement of polymers," *Measurement Science and Technology*, vol. 22, no. 12, p. 125703, 2011.

[167] "Common binding energies for carbon species." https://www.harwellxps.guru/knowledgebase/carbon/. Accessed: 29-08-23.

[168] L. C. Feldman and J. W. Mayer, "Fundamentals of surface and thin film analysis," *North-Holland : Elsevier Science Pub.*, 1986.

[169] Y. Gan, "Atomic and subnanometer resolution in ambient conditions by atomic force microscopy," *Surface Science Reports*, vol. 64, no. 3, pp. 99–121, 2009.

[170] G. Binnig, C. Gerber, E. Stoll, T. Albrecht, and C. Quate, "Atomic resolution with atomic force microscope," *Europhysics Letters*, vol. 3, no. 12, p. 1281, 1987.

[171] T. Albrecht and C. Quate, "Atomic resolution imaging of a nonconductor by atomic force microscopy," *Journal of Applied Physics*, vol. 62, no. 7, pp. 2599–2602, 1987.

[172] T. Schimmel, T. Koch, J. Küppers, and M. Lux-Steiner, "True atomic resolution under ambient conditions obtained by atomic force microscopy in the contact mode," *Applied Physics A*, vol. 68, no. 4, pp. 399–402, 1999.

[173] F. J. Giessibl, "Atomic resolution of the Silicon (111)-(7×7) surface by atomic force microscopy," *Science*, vol. 267, no. 5194, pp. 68–71, 1995.

[174] S.-i. Kitamura and M. I. M. Iwatsuki, "Observation of 7×7 reconstructed structure on the Silicon(111) surface using ultrahigh vacuum noncontact atomic force microscopy," *Japanese journal of applied physics*, vol. 34, no. 1B, p. L145, 1995.

[175] H. Ueyama, M. Ohta, Y. Sugawara, and S. M. S. Morita, "Atomically resolved InP(110) surface observed with noncontact ultrahigh vacuum atomic force microscope," *Japanese journal of applied physics*, vol. 34, no. 8B, p. L1086, 1995.

[176] M. Heuberger, G. Dietler, and L. Schlapbach, "Elastic deformations of tip and sample during atomic force microscope measurements," *Journal of Vacuum Science & Technology B: Microelectronics and Nanometer Structures Processing, Measurement, and Phenomena*, vol. 14, no. 2, pp. 1250–1254, 1996.

[177] A. Buldum, S. Ciraci, C. Fong, and J. Nelson, "Interpretation of long-range interatomic force," *Physical Review B*, vol. 59, no. 7, p. 5120, 1999.

[178] T. Weihs, Z. Nawaz, S. Jarvis, and J. Pethica, "Limits of imaging resolution for atomic force microscopy of molecules," *Applied Physics Letters*, vol. 59, no. 27, pp. 3536–3538, 1991.

[179] R. Pérez, M. C. Payne, I. Štich, and K. Terakura, "Role of covalent tip-surface interactions in noncontact atomic force microscopy on reactive surfaces," *Phys. Rev. Lett.*, vol. 78, pp. 678–681, Jan 1997.

[180] R. Pérez, I. Štich, M. C. Payne, and K. Terakura, "Surface-tip interactions in noncontact atomic-force microscopy on reactive surfaces: Si(111)," *Physical Review B*, vol. 58, no. 16, p. 10835, 1998.

[181] I. Y. Sokolov, G. Henderson, and F. Wicks, "Theoretical and experimental evidence for "true" atomic resolution under non-vacuum conditions," *Journal of Applied Physics*, vol. 86, no. 10, pp. 5537–5540, 1999.

[182] I. Y. Sokolov, "Anomalous increase of friction in the vicinity of nano-size defects," *Tribology Letters*, vol. 12, pp. 131–134, 2002.

[183] I. Y. Sokolov, "Pseudo-non-contact mode: why it can give true atomic resolution," *Applied Surface Science*, vol. 210, no. 1-2, pp. 37–42, 2003.

[184] D. Sarid, *Scanning Force Microscopy*. Oxford University Press, 1994.

[185] F. J. Giessibl, "Forces and frequency shifts in atomic-resolution dynamic-force microscopy," *Physical Review B*, vol. 56, no. 24, p. 16010, 1997.

[186] F. J. Giessibl, "The qPlus sensor, a powerful core for the atomic force microscope," *Review of Scientific Instruments*, vol. 90, no. 1, p. 011101, 2019.

[187] M. Lantz, H. Hug, P. Van Schendel, R. Hoffmann, S. Martin, A. Baratoff, A. Abdurixit, H.-J. Güntherodt, and C. Gerber, "Low temperature scanning force microscopy of the Si(111)-(7×7) surface," *Physical Review Letters*, vol. 84, no. 12, p. 2642, 2000.

[188] T. Eguchi and Y. Hasegawa, "High resolution atomic force microscopic imaging of the Si(111)-(7×7) surface: Contribution of short-range force to the images," *Physical review letters*, vol. 89, no. 26, p. 266105, 2002.

[189] S. Hembacher, F. J. Giessibl, J. Mannhart, and C. F. Quate, "Revealing the hidden atom in graphite by low-temperature atomic force microscopy," *Proceedings of the National Academy of Sciences*, vol. 100, no. 22, pp. 12539–12542, 2003.

[190] F. J. Giessibl, S. Hembacher, H. Bielefeldt, and J. Mannhart, "Subatomic features on the Silicon(111)-(7×7) surface observed by atomic force microscopy," *Science*, vol. 289, no. 5478, pp. 422–425, 2000.

[191] F. J. Giessibl and M. Reichling, "Investigating atomic details of the CaF_2(111) surface with a qPlus sensor," *Nanotechnology*, vol. 16, no. 3, p. S118, 2005.

[192] M. Schmid, J. Mannhart, and F. J. Giessibl, "Searching atomic spin contrast on nickel oxide(001) by force microscopy," *Physical Review B*, vol. 77, no. 4, p. 045402, 2008.

[193] K. Takayanagi, Y. Tanishiro, M. Takahashi, and S. Takahashi, "Structural analysis of Si(111)-7×7 by UHV-transmission electron diffraction and microscopy," *Journal*

of Vacuum Science & Technology A: Vacuum, Surfaces, and Films, vol. 3, no. 3, pp. 1502–1506, 1985.

[194] T. Uchihashi, Y. Sugawara, T. Tsukamoto, M. Ohta, S. Morita, and M. Suzuki, "Role of a covalent bonding interaction in noncontact-mode atomic-force microscopy on Si(111)-7×7," *Physical Review B*, vol. 56, no. 15, p. 9834, 1997.

[195] T. Ichii, M. Fujimura, M. Negami, K. Murase, and H. Sugimura, "Frequency modulation atomic force microscopy in ionic liquid using quartz tuning fork sensors," *Japanese Journal of Applied Physics*, vol. 51, no. 8S3, p. 08KB08, 2012.

[196] B. Hoogenboom, H. Hug, Y. Pellmont, S. Martin, P. Frederix, D. Fotiadis, and A. Engel, "Quantitative dynamic-mode scanning force microscopy in liquid," *Applied Physics Letters*, vol. 88, no. 19, p. 193109, 2006.

[197] S. Rode, N. Oyabu, K. Kobayashi, H. Yamada, and A. Kühnle, "True atomic-resolution imaging of (1014) calcite in aqueous solution by frequency modulation atomic force microscopy," *Langmuir*, vol. 25, no. 5, pp. 2850–2853, 2009.

[198] K. Pürckhauer, A. J. Weymouth, K. Pfeffer, L. Kullmann, E. Mulvihill, M. P. Krahn, D. J. Müller, and F. J. Giessibl, "Imaging in biologically-relevant environments with AFM using stiff qPlus sensors," *Scientific Reports*, vol. 8, no. 1, p. 9330, 2018.

[199] K. Pürckhauer, S. Maier, A. Merkel, D. Kirpal, and F. J. Giessibl, "Combined atomic force microscope and scanning tunneling microscope with high optical access achieving atomic resolution in ambient conditions," *Review of Scientific Instruments*, vol. 91, no. 8, p. 083701, 2020.

[200] D. Klinov, B. Dwir, E. Kapon, N. Borovok, T. Molotsky, and A. Kotlyar, "High-resolution atomic force microscopy of duplex and triplex DNA molecules," *Nanotechnology*, vol. 18, no. 22, p. 225102, 2007.

[201] D. J. Müller, D. Fotiadis, S. Scheuring, C. Möller, and A. Engel, "Conformational changes, flexibilities and intramolecular forces observed on individual proteins using AFM," *Single molecules*, vol. 1, no. 2, pp. 115–118, 2000.

[202] D. J. Müller, D. Fotiadis, S. Scheuring, S. A. Müller, and A. Engel, "Electrostatically balanced subnanometer imaging of biological specimens by atomic force microscope," *Biophysical journal*, vol. 76, no. 2, pp. 1101–1111, 1999.

[203] H. Ooe, D. Kirpal, D. S. Wastl, A. J. Weymouth, T. Arai, and F. J. Giessibl, "Amplitude dependence of image quality in atomically-resolved bimodal atomic force microscopy," *Applied Physics Letters*, vol. 109, no. 14, p. 141603, 2016.

[204] M. R. Uhlig, S. Benaglia, R. Thakkar, J. Comer, and R. Garcia, "Atomically resolved interfacial water structures on crystalline hydrophilic and hydrophobic surfaces," *Nanoscale*, vol. 13, no. 10, pp. 5275–5283, 2021.

[205] D. S. Wastl, A. J. Weymouth, and F. J. Giessibl, "Optimizing atomic resolution of force microscopy in ambient conditions," *Physical Review B*, vol. 87, no. 24, p. 245415, 2013.

[206] D. S. Wastl, A. J. Weymouth, and F. J. Giessibl, "Atomically resolved graphitic surfaces in air by atomic force microscopy," *ACS nano*, vol. 8, no. 5, pp. 5233–5239, 2014.

[207] D. S. Wastl, M. Judmann, A. J. Weymouth, and F. J. Giessibl, "Atomic resolution of calcium and oxygen sublattices of calcite in ambient conditions by atomic force microscopy using qPlus sensors with sapphire tips," *ACS nano*, vol. 9, no. 4, pp. 3858–3865, 2015.

[208] P. Dieška, I. Stich, and R. Pérez, "Reversible short-range electrostatic imaging in frequency modulation atomic force microscopy on metallic surfaces," *Nanotechnology*, vol. 15, p. S55, 01 2004.

[209] P. Dieška, I. Štich, and R. Pérez, "Covalent and reversible short-range electrostatic imaging in noncontact atomic force microscopy," *Physical review letters*, vol. 91, no. 21, p. 216401, 2003.

[210] A. S. Foster, A. Gal, J. Gale, Y. Lee, R. M. Nieminen, and A. Shluger, "Interaction of silicon dangling bonds with insulating surfaces," *Physical review letters*, vol. 92, no. 3, p. 036101, 2004.

[211] A. S. Foster, C. Barth, A. Shluger, and M. Reichling, "Unambiguous interpretation of atomically resolved force microscopy images of an insulator," *Physical Review Letters*, vol. 86, no. 11, p. 2373, 2001.

[212] J. Tóbik, I. Štich, R. Pérez, and K. Terakura, "Simulation of tip-surface interactions in atomic force microscopy of an InP(110) surface with a Si tip," *Physical Review B*, vol. 60, no. 16, p. 11639, 1999.

[213] Y. Sugawara, M. Ohta, H. Ueyama, and S. Morita, "Defect motion on an InP(110) surface observed with noncontact atomic force microscopy," *Science*, vol. 270, no. 5242, pp. 1646–1648, 1995.

[214] A. Schwarz, W. Allers, U. Schwarz, and R. Wiesendanger, "Simultaneous imaging of the In and As sublattice on InAs(110)-(1×1) with dynamic scanning force microscopy," *Applied surface science*, vol. 140, no. 3-4, pp. 293–297, 1999.

[215] M. Ondráček, P. Pou, V. Rozsíval, C. González, P. Jelínek, and R. Pérez, "Forces and currents in carbon nanostructures: are we imaging atoms?," *Physical Review Letters*, vol. 106, no. 17, p. 176101, 2011.

[216] K. Ø. Hanssen, B. Schuler, A. J. Williams, T. B. Demissie, E. Hansen, J. H. Andersen, J. Svenson, K. Blinov, M. Repisky, F. Mohn, *et al.*, "A combined atomic force microscopy and computational approach for the structural elucidation of Breitfussin A and B: Highly modified halogenated dipeptides from Thuiaria Breitfussin," *Angewandte Chemie*, vol. 124, no. 49, pp. 12404–12407, 2012.

[217] C. Moreno, O. Stetsovych, T. K. Shimizu, and O. Custance, "Imaging three-dimensional surface objects with submolecular resolution by atomic force microscopy," *Nano letters*, vol. 15, no. 4, pp. 2257–2262, 2015.

[218] A. Sweetman, S. P. Jarvis, P. Rahe, N. R. Champness, L. Kantorovich, and P. Moriarty, "Intramolecular bonds resolved on a semiconductor surface," *Physical Review B*, vol. 90, no. 16, p. 165425, 2014.

[219] K. Iwata, S. Yamazaki, P. Mutombo, P. Hapala, M. Ondráček, P. Jelínek, and Y. Sugimoto, "Chemical structure imaging of a single molecule by atomic force microscopy at room temperature," *Nature communications*, vol. 6, no. 1, p. 7766, 2015.

[220] F. Huber, S. Matencio, A. J. Weymouth, C. Ocal, E. Barrena, and F. J. Giessibl, "Intramolecular force contrast and dynamic current-distance measurements at room temperature," *Physical Review Letters*, vol. 115, no. 6, p. 066101, 2015.

[221] S. P. Jarvis, A. M. Sweetman, I. Lekkas, N. R. Champness, L. Kantorovich, and P. Moriarty, "Simulated structure and imaging of ntcdi on Si(111)-7×7: a combined STM, NC-AFM and DFT study," *Journal of Physics: Condensed Matter*, vol. 27, no. 5, p. 054004, 2014.

[222] L. Gross, F. Mohn, N. Moll, B. Schuler, A. Criado, E. Guitián, D. Peña, A. Gourdon, and G. Meyer, "Bond-order discrimination by atomic force microscopy," *Science*, vol. 337, no. 6100, pp. 1326–1329, 2012.

[223] V. V. Korolkov, I. G. Timokhin, R. Haubrichs, E. F. Smith, L. Yang, S. Yang, N. R. Champness, M. Schröder, and P. H. Beton, "Supramolecular networks stabilise and functionalise black phosphorus," *Nature Communications*, vol. 8, no. 1, p. 1385, 2017.

[224] V. V. Korolkov, M. Baldoni, K. Watanabe, T. Taniguchi, E. Besley, and P. H. Beton, "Supramolecular heterostructures formed by sequential epitaxial deposition of two-dimensional hydrogen-bonded arrays," *Nature Chemistry*, vol. 9, no. 12, pp. 1191–1197, 2017.

[225] L. Liiró-Peluso, J. Wrigley, D. B. Amabilino, and P. H. Beton, "Submolecular resolution imaging of P3HT:PCBM nanostructured films by atomic force microscopy: Implications for organic solar cells," *ACS applied nano materials*, vol. 5, no. 10, pp. 13794–13804, 2022.

[226] M. Kocun, A. Labuda, W. Meinhold, I. Revenko, and R. Proksch, "Fast, high resolution, and wide modulus range nanomechanical mapping with bimodal tapping mode," *ACS nano*, vol. 11, no. 10, pp. 10097–10105, 2017.

[227] N. Severin, A. Dzhanoev, H. Lin, A. Rauf, S. Kirstein, C.-A. Palma, I. Sokolov, and J. P. Rabe, "Atomic resolution with high-eigenmode tapping mode atomic force microscopy," *Physical Review Research*, vol. 4, no. 2, p. 023149, 2022.

[228] S. A. Sumaiya, J. Liu, and M. Z. Baykara, "True atomic-resolution surface imaging and manipulation under ambient conditions via conductive atomic force microscopy," *ACS nano*, 2022.

[229] A. L. Eichhorn and C. Dietz, "Simultaneous deconvolution of in-plane and out-of-plane forces of HOPG at the atomic scale under ambient conditions by multifrequency atomic force microscopy," *Advanced Materials Interfaces*, vol. 8, no. 20, p. 2101288, 2021.

[230] A. L. Eichhorn and C. Dietz, "Torsional and lateral eigenmode oscillations for atomic resolution imaging of HOPG in air under ambient conditions," *Scientific Reports*, vol. 12, no. 1, p. 8981, 2022.

[231] S. P. Jarvis, S. Taylor, J. D. Baran, D. Thompson, A. Saywell, B. Mangham, N. R. Champness, J. Larsson, and P. Moriarty, "Physisorption controls the conformation and density of states of an adsorbed porphyrin," *The Journal of Physical Chemistry C*, vol. 119, no. 50, pp. 27982–27994, 2015.

[232] S. P. Jarvis, S. Taylor, J. D. Baran, N. R. Champness, J. Larsson, and P. Moriarty, "Measuring the mechanical properties of molecular conformers," *Nature Communications*, vol. 6, no. 1, p. 8338, 2015.

[233] S. Grimme, J. Antony, S. Ehrlich, and H. Krieg, "A consistent and accurate ab initio parametrization of density functional dispersion correction (DFT-D) for the 94 elements H-Pu," *The Journal of chemical physics*, vol. 132, no. 15, p. 154104, 2010.

[234] G. Henkelman, A. Arnaldsson, and H. Jónsson, "A fast and robust algorithm for Bader decomposition of charge density," *Computational Materials Science*, vol. 36, no. 3, pp. 354–360, 2006.

[235] E. Sanville, S. D. Kenny, R. Smith, and G. Henkelman, "Improved grid-based algorithm for Bader charge allocation," *Journal of computational chemistry*, vol. 28, no. 5, pp. 899–908, 2007.

[236] G. Henkelman, B. P. Uberuaga, and H. Jónsson, "A climbing image nudged elastic band method for finding saddle points and minimum energy paths," *The Journal of chemical physics*, vol. 113, no. 22, pp. 9901–9904, 2000.

[237] G. Henkelman and H. Jónsson, "Improved tangent estimate in the nudged elastic band method for finding minimum energy paths and saddle points," *The Journal of chemical physics*, vol. 113, no. 22, pp. 9978–9985, 2000.

[238] J. Kästner and P. Sherwood, "Superlinearly converging dimer method for transition state search," *The Journal of chemical physics*, vol. 128, no. 1, p. 014106, 2008.

[239] G. Henkelman and H. Jónsson, "A dimer method for finding saddle points on high dimensional potential surfaces using only first derivatives," *The Journal of chemical physics*, vol. 111, no. 15, pp. 7010–7022, 1999.

[240] K. Momma and F. Izumi, "VESTA 3 for three-dimensional visualization of crystal, volumetric and morphology data," *Journal of applied crystallography*, vol. 44, no. 6, pp. 1272–1276, 2011.

[241] P. Hapala, G. Kichin, C. Wagner, F. S. Tautz, R. Temirov, and P. Jelínek, "Mechanism of high-resolution STM/AFM imaging with functionalized tips," *Physical Review B*, vol. 90, no. 8, p. 085421, 2014.

[242] P. Jelínek, "High resolution SPM imaging of organic molecules with functionalized tips," *Journal of Physics: Condensed Matter*, vol. 29, no. 34, p. 343002, 2017.

[243] S. P. Jarvis, M. A. Rashid, A. Sweetman, J. Leaf, S. Taylor, P. Moriarty, and J. Dunn, "Intermolecular artifacts in probe microscope images of C_{60} assemblies," *Physical Review B*, vol. 92, no. 24, p. 241405, 2015.

[244] W. Auwärter, D. Écija, F. Klappenberger, and J. V. Barth, "Porphyrins at interfaces," *Nature chemistry*, vol. 7, no. 2, pp. 105–120, 2015.

[245] M. Chen, J. Xiao, H.-P. Steinrück, S. Wang, W. Wang, N. Lin, W. Hieringer, and J. M. Gottfried, "Combined photoemission and scanning tunneling microscopy study of the surface-assisted Ullmann coupling reaction," *The Journal of Physical Chemistry C*, vol. 118, no. 13, pp. 6820–6830, 2014.

[246] Q. Fan, C. Wang, L. Liu, Y. Han, J. Zhao, J. Zhu, J. Kuttner, G. Hilt, and J. M. Gottfried, "Covalent, organometallic, and halogen-bonded nanomeshes from tetrabromo-terphenyl by surface-assisted synthesis on Cu(111)," *The Journal of Physical Chemistry C*, vol. 118, no. 24, pp. 13018–13025, 2014.

[247] A. Batra, D. Cvetko, G. Kladnik, O. Adak, C. Cardoso, A. Ferretti, D. Prezzi, E. Molinari, A. Morgante, and L. Venkataraman, "Probing the mechanism for graphene

nanoribbon formation on gold surfaces through X-ray spectroscopy," *Chemical Science*, vol. 5, no. 11, pp. 4419–4423, 2014.

[248] S. Stolz, M. Di Giovannantonio, J. I. Urgel, Q. Sun, A. Kinikar, G. Borin Barin, M. Bommert, R. Fasel, and R. Widmer, "Reversible dehalogenation in on-surface aryl-aryl coupling," *Angewandte Chemie*, vol. 132, no. 33, pp. 14210–14214, 2020.

[249] S. Huseyinova, J. Blanco, F. G. Requejo, J. M. Ramallo-López, M. C. Blanco, D. Buceta, and M. A. López-Quintela, "Synthesis of highly stable surfactant-free Cu_5 clusters in water," *The Journal of Physical Chemistry C*, vol. 120, no. 29, pp. 15902–15908, 2016.

[250] J. Björk, F. Hanke, and S. Stafstrom, "Mechanisms of halogen-based covalent self-assembly on metal surfaces," *Journal of the American Chemical Society*, vol. 135, no. 15, pp. 5768–5775, 2013.

[251] G. Bussetti, M. Campione, L. Ferraro, L. Raimondo, B. Bonanni, C. Goletti, M. Palummo, C. Hogan, L. Duó, M. Finazzi, *et al.*, "Probing two-dimensional vs three-dimensional molecular aggregation in metal-free tetraphenylporphyrin thin films by optical anisotropy," *The Journal of Physical Chemistry C*, vol. 118, no. 29, pp. 15649–15655, 2014.

[252] G. Bussetti, M. Campione, M. Riva, A. Picone, L. Raimondo, L. Ferraro, C. Hogan, M. Palummo, A. Brambilla, M. Finazzi, *et al.*, "Stable alignment of tautomers at room temperature in porphyrin 2D layers," *Advanced Functional Materials*, vol. 24, no. 7, pp. 958–963, 2014.

[253] E. I. Altman and R. J. Colton, "Nucleation, growth, and structure of fullerene films on Au(111)," *Surface science*, vol. 279, no. 1-2, pp. 49–67, 1992.

[254] J. A. Gardener, G. A. D. Briggs, and M. R. Castell, "Scanning tunneling microscopy studies of C_{60} monolayers on Au(111)," *Physical Review B*, vol. 80, no. 23, p. 235434, 2009.

[255] A. Fartash, "In-plane orientational order across C_{60}(111)/Au(111) interfaces," *Thin solid films*, vol. 323, no. 1-2, pp. 296–303, 1998.

[256] G. Schull and R. Berndt, "Orientationally ordered (7×7) superstructure of C_{60} on Au(111)," *Physical review letters*, vol. 99, no. 22, p. 226105, 2007.

[257] R. Wilson, G. Meijer, D. S. Bethune, R. Johnson, D. Chambliss, M. De Vries, H. Hunziker, and H. Wendt, "Imaging C_{60} clusters on a surface using a scanning tunnelling microscope," *Nature*, vol. 348, no. 6302, pp. 621–622, 1990.

[258] J. Wragg, J. Chamberlain, H. White, W. Krätschmer, and D. R. Huffman, "Scanning tunnelling microscopy of solid C_{60}/C_{70}," *Nature*, vol. 348, pp. 623–624, 1990.

[259] L. Forcieri, S. Taylor, P. Moriarty, and S. P. Jarvis, "Origin of C_{60} surface reconstruction resolved by atomic force microscopy," *Physical Review B*, vol. 104, no. 20, p. 205428, 2021.

[260] S. A. Carabineiro and B. E. Nieuwenhuys, "Reactions of small molecules on gold single crystal surfaces," *Gold Bulletin*, vol. 43, pp. 252–266, 2010.

[261] R. Zuzak, M. Szymonski, and S. Godlewski, "Extended iron phthalocyanine islands self-assembled on a Ge(001): H surface," *Beilstein Journal of Nanotechnology*, vol. 12, no. 1, pp. 232–241, 2021.

[262] M. Lackinger, "Synthesis on inert surfaces," *Dalton Transactions*, vol. 50, no. 29, pp. 10020–10027, 2021.